UNIVERSITY OF CALIFORNIA, SAN DIEGO

Design of an Advanced Positron Emission Tomography Detector System and Algorithms for Imaging Small Animal Models of Human Disease

A dissertation submitted in partial satisfaction of the
requirements for the degree of Doctor of Philosophy

in

Physics

by

Angela Marie Klohs Foudray

Committee in charge:

Professor Craig S. Levin, Co-Chair
Professor Clifford M. Surko, Co-Chair
Professor Carl K. Hoh
Professor Mevlin Y. Okamura
Professor Hans P. Paar

2009

.

The Dissertation of Angela Marie Klohs Foudray is approved, and it is acceptable in quality and form for publication on microfilm and electronically:

_____

_____

_____

_____

Co-Chair

_____

Co-Chair

University of California, San Diego

2009

Dedications

To those loved ones that I have lost during my time in graduate school:

My parent's moms, **Gammy** and **Gramma**
My auntie, **Emmy Lou**
My mother in law, **Deb**
Zach's dad's parents, **Gramps** and **Granny**
Zach's mom's mom, **Virgina**

And loved ones that I have gained:

My wonderful husband, **Zach**
My beautiful baby boy, **Soren**
The kittens; **Niki, Ninja, Kilo,** and **Kiki**
My brothers in law, **Amo** and **Thad**
My sister in law, **Kelly**
My niece, **Fara**
And my cousins; **Jesse, Leah, Dana, Clint** and **Chris**

Epigraph

"A human being should be able to change a diaper, plan an invasion, butcher a hog, conn a ship, design a building, write a sonnet, balance accounts, build a wall, set a bone, comfort the dying, take orders, give orders, cooperate, act alone, solve equations, analyze a new problem, pitch manure, program a computer, cook a tasty meal, fight efficiently, die gallantly. Specialization is for insects."
Robert A. Heinlein, Time Enough for Love

"You may encounter many defeats, but you must not be defeated. In fact, it may be necessary to encounter the defeats, so you can know who you are, what you can rise from, how you can still come out of it."
Maya Angelou

Contents

List of Figures

List of Tables

Symbols and Acronyms

μ linear attenuation coefficient - Section 4.2.1

ϕ the angle a vector makes with respect to the z-axis - Figure 8.7

θ the angle a vector makes with respect to the xy-plane - Figure 8.7

A aspect ratio - Section 2.2.1

ADC analog to digital converter - Section 5.3.4

AlN aluminum nitride - Section 5.2

APD avalanche photodiode - Section 2.3

ASICs application specific integrated chips - Section 9.2.3

axial the direction in a detector system along the central axis of the system (perpendicular to trans-axial and radial) - Section 6.3.2

C counts - Section 1.5.3

CAD computer aided drafting - Section 5.2.3

CBN component based normalization - Section 8.3.2

CFD constant fraction discriminator - Section 5.3.4

COM center of mass, centroid - Section 6.6.3

CT x-ray computed tomography - Section 1.5.3

CTR coincidence time resolution - Section 4.5.3

CTW coincidence time window - Section 6.5

CV coefficient of variaion - Section 8.6.2

CZT cadmium zinc telluride or CdZnTe - Section 2.2.2

dLOR density of lines of response - Section 8.4.3

DN direct normalization - Section 8.3.1

DOI depth of interaction - Section 3.1

ER energy resolution - Section 1.3.4

EW energy window - Section 6.5

FDG fluorodeoxyglucose - Section 1.2.1

FFA fast filter amplifier - Section 5.3.4

FOV field of view - Section 1.4.3

g geometric component based normalization efficiency - Section 8.4.2

GATE GEANT4 Application for Tomographic Emission - Section 6.3.1

Hit an interaction in the detection system - Section 4.4.3

HV high voltage - Section 5.2.1

LOR line of response - Section 1.5.1

LSO lutetium oxyorthosilicate or Lu_2SiO_5 - Section 2.2.1

MIBEC multiple interaction-based electronic collimation - Section 1.5.1

Multiples events with three or more annihilation photons - Section 1.3.4

NC normalization coefficient - Section 8.4.2

NEC noise equivalent counts - Section 6.5

NEMA National Electrical Manufacturers Association - Section 6.2.1

NIM Nuclear Instrumentation Module - Section 5.3.4

oring cylindrical system with modules facing trans-axially - Section 6.4.1

OSEM ordered subset expectation maximization algorithm - Section 1.6.2

PET positron emission tomography - Section 1.1

PMT photomultiplier tube - Section 2.3

PP (photo)peak position - Section 3.2.6

PSAPD position-sensitive avalanche photodiode - Section 2.3

PSF point spread function - Section 4.4.2

psfFWHM point spread function full width at half maximum - Section 4.4.2

PSPMT position-sensitive photomultiplier tube - Section 4.1

PVR peak to valley ratio - Section 4.5.3

QE quantum efficiency - Section 2.2.1

radial the direction in a detector system along the depth of interaction of a head of the system (perpendicular to axial and trans-axial) - Section 6.3.2

Randoms coincidence events formed from annihilation photons produced by separate annihilation events - Section 1.3.4

RMD Radiation Monitoring Devices, Inc. - Section 3.2.3

ROI region of interest - Section 8.6.1

rot/ring cylindrical system with modules facing axially - Section 6.4.1

RSD relative standard deviation - Section 8.6.2

S coincidence detection sensitivity - Section 1.4.1

SA small animal - Section 6.4.1

saPET small animal positron emission tomography - Section 6.4.1

SCA single channel analyzer - Section 4.4.1

Scatters coincidence events formed when one or both annihilation photons have undergone a Compton scattering event in the object being imaged - Section 1.3.4

Singles events with only one annihilation photon - Section 1.3.4

SNR signal to noise ratio - Section 1.4.1

SPECT single photon emission tomography - Section 6.1

TAC time-to-amplitude converter or time-to-amplitude converter produce timing spectrum - Section 4.4.1

TNF tumor necrosis factor - Section 1.2.1

trans-axial the direction in a detector system along the length of a head of the system (perpendicular to axial and radial) - Section 6.3.2

Trues coincidence events containing two annihilation photons that originated from the same annihilation event, neither of which have scattered - Section 1.3.4

U non-uniformity - Section 8.6.1

UFOV useful field of view - Section 1.4.3

w component-based normalization weight - Section 8.4.3

Z atomic number - Section 4.2.1

Acknowledgments

My physics story, and thus my thanks, must begin at the University of Wisconsin, Madison. I don't know how often someone thanks their undergraduate institution in their PhD dissertation - it is just a testament then to its evident dedication to their students and their students' educational experience. Every attempt was made (and in my opinion successfully, I might add) to make a large institution, with all the benefits of a large institution, give everyone the experience of being a part of something big, while still being an individual and recognized as one. Specifically, I would like to thank the members of the Department of Physics for their inclusionary attention to our educational and individual development and for overall real world guidance.

I was lucky enough to interact, study and work with extraordinary individuals at Madison. First and foremost, I have to thank a man whose influence on my decision to become a physicist was at a critical and fragile time. A man who took under his wing a young girl who had no laboratory experience and very little knowledge of the theoretical fundamentals of physics in general (she was a mere sophomore), with a

lot of patience, joi de vivre, excellent lectureship during discussions of new material and general fatherly interest, showed her why physicists are drawn the biz in the first place. Thank you Dr. Donald Peyton Cox for taking a chance. And I'm still waiting for your treatise on armchair Cosmology in published book form.

Another colossal influence throughout my formative physics years was the members of the University Physics Society (a.k.a. UW Madison Physics Club) and Dr. Torsten Schmauder. The first comprised the most disparate bunch of hooligans, each of whom pushed and prodded me in their own way (some more gently than others), towards the physics geek that I have long attempted to embody. You were dear companions, bitter rivals, and much needed sounding boards. How such a fantastic group of people could have amassed at the same point in space and time still boggles my mind. In particular I would like to especially thank Bradford Benson, Lisa (Weltzer) Ward, Jon Nix, Isaac Kunen, Josh Jones, Karen Lewis, Nate Gemelke, Josh Sack, Beth Petrus, Matt Eppleheimer, Andy Szudy, Arthur Kantor, and Matt Pagel. As for Torsten, your confidence-building trust in me independently acquiring abilities and knowledge helped to make me understand the responsibilities and satisfaction in being an independent researcher. You made the 2am beamline data runs something to look forward to after a long day in classes. Not only did you demonstrate with all that you did how to be a good scientist, but also a good human being at the same time. Your twins are lucky to have you as their daddy.

Al Erwin and Theo Alexopoulos in the High Energy Physics division of the Physics

Department gave me a home for a semester to pour over months and months of anti-cascade particle production data from Fermi Lab. Theo, I want to thank you for always being there to discuss anything from data filtering to life as a physicist. Your kind words and modeling of resourcefulness are cherished still today. Dr. Erwin, thank you for your interest in my scholarship and well-being, even long after I was working in your lab. Make sure you are enjoying your well-deserved retirement to the fullest.

I had an exciting and confidence-bolstering summer in the Energy Technology Division of Argonne National Laboratory, and would like to thank Richard Lee in particular - my first imaging mentor. Varied opportunities were afforded to me during that summer - particularly with regards to operating a room-sized scanning electron microscope on a regular basis and being a part of many in-lab and collaborative projects. I think to this day of the times I spent looking at extremely high magnification images of diamond-like carbon, in the dark, with Blue Danube playing in the background. I also have fond memories of Bob Erck and debating mathematical models of surface effects, Ali Erdemir and planning out repairs on the sputtering system, and my uber-supervisor George Fenske.

Every time that I see an instrument wrapped in aluminum foil I think about the years I spent in the MO lab at the Synchrotron Radiation Center in Stoughton, Wisconsin. Marshall Onellion, Shashank Misra, Brad Frazer, and Mike Schneider were indelible figures in my time at Madison. I spent so much time with Marshall

and Brad pouring over or acquiring data - thank you Marshall for all of your stories, experiences and vision. I'd like to give a special nod to the guys in the machine shops in both the SRC and Madison's Physics department - I learned and laughed so much.

I had two summers at Motorola in Plantation, Florida, where I thought I had died and gone to corporate heaven. They were the summers of 1999 and 2000, the golden era. Only 40 hours of work a week, fabulous shiny new equipment, utterly fantastic people, and weekends to play with said people! Matt Nichols, Angela Chou, Kelly Vukad, Wendy Lin, Melissa Light were interns as well, and we attacked Fort Lauderdale with reckless abandon. Well, as much as a bunch of science and engineering nerds can, anyway. Ron Kelley, Steve Pratt, Bob Penisi were among my mentors - they gave me opportunities and projects that were stunningly exciting (sorry, I still think most of them are company secrets), as well as mentorship and seemingly infinite kindness. It was an all around great time of exploration.

On my move to California, being that Zach was starting his Masters program at Madison, I moved into the (in comparison) extremely affordable graduate student housing in Warren College here at UCSD. I shared an apartment with three other girls, all of whom contributed heavily to my initial extreme culture shock. On retrospect, I'm sure this was compounded by the fact that I hadn't spent that much time around non-Physics (Math, Comp Sci, Engineering or otherwise interested in "what is the nature of this?") girls in quite some time. Leslie, Michelle, Susan, and I blossomed into great friends. When Leslie left us for her husband (can't blame her), I got

my partner in crime, Helen (Ing-Wher) Chen (who actually wouldn't even consider passing anyone at 1 mile and hour over the speed limit when I met her - though I cured her of that). Life was beautiful. Thank you Helen for letting me borrow Pumbaa, having your eyes glued to CNN with me at the wee hours of the morn' as the Twin Towers came down, letting yourself be dragged to the Zoo, Balboa park, Moo Time and a movie, etc., etc., and just being there. I still have nightmares that involve my arm broken, a freak snowstorm, a Utah freeway and a snowplow. But I get to say it in print - it was TOTALLY my fault.

During my six months as an Electrical Engineering grad student, I had classes with a bunch of great people, among them: Val Liverini, Jeremy Warner, Naomi Ramos, and Taryn Tomlinson. But I knew my home and my heart was in the Physics department. So I joined up with Doug Smith, Pu Chun Ke, Greg Gemmen, and later Jo Bellanca in the Biophysics portion of the department and learned a great deal about squishy and light emitting things. Thank you Pu-Chun and Jo for throwing me at new problems with a cackle and a warm heart. Jo and Greg, thank you for the companionship and long talks over experiments - though sometimes they were just Greg going on and on about soccer this and soccer that (and me eating up every minute of it).

A shout out to the BioEngineering peeps - especially Joey Russo and Miki Nakajima. Joey - my aunt still talks about you, sitting on her lawn on the Mississippi one afternoon in June, 2004. Oh, the stories. You all were my surrogate family for

long stretches. A huge, crazy, life-loving bunch of people that didn't seem to care too much that I was from some other department entirely.

I was then welcomed into the lab that I would spend the remainder of my time at UCSD - though much of it was spent in our new home at Stanford. Craig Levin, Andrew Dhanasopon, Jon Talcott, Leilani Domingo, Jin Zhang, Frezghi Habte, Garry Chinn, Peter Olcott, Guillem Pratx, Marta Zanchi, Hao Peng, Arne Vanderbroucke and Yi Gu - a lab that started out in a small room at the VA at UCSD and exploded into a basement in the Medical Center of Stanford. Our research expanded to myriads of projects - I wish I would have been able to work with you guys directly more often. Thank you, Craig, for giving me the opportunity to work in a field that straddles so many disciplines. I'd also like to thank Nick Lorang for his friendship and his slaving for multiple days many times to produce amazing beef jerky that he generously handed out afterwards.

During my research in Medical Imaging, I attend conferences, meeting friends that I looked forward to seeing as often as possible. Among these amazing people are Caryl Brzymialkiewicz, Andrew Goertzen, Martin Janecek, Carmen Taylor, Martin Tornai, Magnus Dahlbom, Nicole Detorie, Elena Heckathorne and Jennifer Stickel.

There were people that were there during every step this process - most of them for a major portion of my life. Kristin Hora; Shelley, Scott, Vincent, Leonardo and Kaylee Paulsen; Ed and Janet Davenport; I am indebted to you for your cheerleading, celebrations, and support. I think I would be nearly lost without you.

And last but not least, my amazing family: Gammy Chamberlain, Gramma Klohs, Ted and Linda Klohs; Mike, Kelly, Kilo, Kiki and Fara Klohs; Rodd, Deb, Amo, Thad and Nancy Foudray; Denny, Kathy and Caroline Klohs; Ron, Sonja and Kirby Chamberlain; Ben and Leah Chamberlain; Luke Chamberlain, Jesse Voska, and last but most certainly not least Zach, Soren, Niki, and Ninja Foudray. I could write more than the length of this entire document about you. I needed you all and you were all there for me. One could not imagine a more supportive and loving family. I want to especially thank my parents Ted and Linda Klohs and my husband Zach for helping with any little thing (many things certainly not so little), being there for everything, being who you are, and above all, being my best friends.

Chapter 3, in part, is a reprint of the material as it appears in IEEE Transactions on Nuclear Science, Volume 53, Issue 5, Part 1, Oct. 2006 Page(s):2549 - 2556; and in the Journal of Nuclear Medicine Vol. 44, No. 5, May 2003, p.138. The dissertation author was a primary investigator and author of these papers.

Chapter 6, in part, is a reprint of the material as it appears in Physica Medica 2006. Foudray, AMK, Habte, F, Chinn, G, Zhang, J, Levin, CS. The dissertation author was the primary investigator and author of this paper.

Chapter 8, in part, is a reprint of the material as it appears in Nuclear Science Symposium Conference Record, 2005 IEEE Volume 4, October 23 - 29, 2005 Page(s):2108 - 2111, Foudray AMK, Chinn, G, Levin, CS. The dissertation author was the primary investigator and author of this paper.

Vita

1995-1996	Laboratory Assistant, Dept. of Biochemistry University of Wisconsin, Madison
1996-1997	Executive Officer, Dept. of Housing University of Wisconsin, Madison
1997	Technical Assistant, Div. of Information Technology University of Wisconsin, Madison
1997-1998	Research Assistant, Dept. of Physics (Astrophysics) University of Wisconsin, Madison
1998	Research Participant, Energy Technology Division Argonne National Laboratory
1998-2000	Research Assistant, Dept. of Physics (Solid State) University of Wisconsin, Madison
1999	Research Assistant, Dept. of Physics (High Energy) University of Wisconsin, Madison
1999,2000	Engineer, Adv. Manufacturing Technology Center Motorola, Inc., Plantation, FL
2000	Applied Mathematics, Engineering and Physics (B.S.) 4 Majors: Physics (Honors), Mathematics, Astrophysics, AMEP University of Wisconsin, Madison
2000-2001	Department of Electrical and Computer Engineering Charles Lee Powel Fellowship University of California, San Diego

2001-2003	Research Assistant, Dept. of Physics (Biophysics) University of California, San Diego
2001-2003	Burrows Wellcome Fund La Jolla Interfaces in Science Fellowship University of California, San Diego
2003	Master of Science University of California, San Diego
2003-2004	Research Assistant, Dept. of Radiology (BioMedical Imaging) University of California, San Diego
2004-2007	Research Assistant, Dept. of Radiology (BioMedical Imaging) Stanford University
2004,2005	Nuclear Science Symposium and Medical Imaging Conference Travel Award National Institute of Health
2005	Candidate of Philosophy University of California, San Diego
2005	PEO Scholar Award Recipient PEO International
2005	Molecular Imaging Summer School Tuition and Travel Grant Recipient Molecular-Imaging Integrated Project (European Network)
2006	Nuclear Science Symposium and Medical Imaging Conference Travel Award Merck, Inc.
2007	Full Student Sponsorship (Tuition, Travel, Fees) International Workshop on Bayesian Inference and Maximum Entropy Methods in Science and Engineering
2009	Doctorate of Philosophy University of California, San Diego

Publications

Chinn, G, Foudray, AMK, Levin, CS, "A Method to Include Single Photon Events in Image Reconstruction for a 1 mm Resolution PET System Built with Advanced 3-D Positioning Detectors", Presented at the 2006 IEEE Nuclear Science Symposium and Medical Imaging Conference, San Diego, CA

Chinn, G, Foudray, AMK, Levin, CS, "Accurately Positioning and Incorporating Large-Angle Tissue-Scattered Photons into PET Image Reconstruction", Presented at the 2006 IEEE Nuclear Science Symposium and Medical Imaging Conference, San Diego, CA

Chinn, G, Foudray, AMK, Zhang, J, Levin, CS, "Image reconstruction strategy for a 1 mm resolution dual-panel breast-dedicated PET system that measures photon interaction depth", Oral Presentation at Annual Society of Nuclear Medicine Meeting 2006, San Diego, CA

Chinn, G, Foudray, AMK, Levin, CS, "Comparing Geometries of Systems with Depth of Interaction" Nuclear Science Symposium Conference Record, 2005 IEEE Volume 3, October 23 - 29, 2005 Page(s):1709 - 1712

Dhanasopon AP, Levin CS, Foudray AMK, Olcott PD, Habte F. Scintillation Crystal Design Features for a Miniature Gamma Ray Camera. IEEE Transactions on Nuclear Science Volume 52, Issue 5, Part 1, Oct. 2005 Page(s):1439 - 1446

Erwin, A, et. al., "$\overline{\Xi^0}$, Ξ^0 Polarization at KTeV," Oral Presentation at Hyperon99, Sept. 27-29, 1999, Fermilab.

Habte, F, Olcott, PD, Levin, CS, Foudray, AMK, "Investigation of Scintillation Light Multiplexing for PET Dectectors Based on Position Sensitive Avalanche Photodiodes," Nuclear Science Symposium Conference Record, 2005 IEEE Volume 4, October 23 - 29, 2005 Page(s):2027 - 2030

Habte, F, Olcott, PD, Foudray, AMK, Levin, CS, "Simulation and Measurement of Gamma Ray and Annihilation Photon Imaging Detectors" Nuclear Science Symposium Conference Record, 2004 IEEE Volume 6, 16-22 Oct. 2004 Page(s):4019 - 4022 Vol. 6, submitted to IEEE Transactions on Nuclear Science (undergoing revision, 2005)

Habte, F, Foudray, AMK, Levin, CS, "The Effect of Photon Compton Scatter on Sensitivity in High Resolution Positron Emission Tomography," Presented at the Bio-X Program at Stanford, Watching Life Symposium, March 25, 2005

Habte F, Olcott PD, Levin CS, Foudray AM., "Prototype Parallel Readout System for Position Sensitive PMT based Gamma Ray Imaging Systems," IEEE Transactions on Nuclear Science (in press, 2005)

Habte, F, Levin, CS, Foudray, AMK, "The Optimal Configuration of Detectors for Highest Coincidence Detection Efficiency in High-Resolution Positron Emission Tomography," Presented at the 2005 Academy of Molecular Imaging Meeting, Orlando, FL, March 19-23, 2005. Molecular Imaging and Biology 7(2), p. 132, Feb 2005

Foudray, AMK, Levin, CS, "Bayesian Estimator for Angle Determination: Event Classification in Positron Emission Tomography," Presented at the 27th International Workshop on Bayesian Inference and Maximum Entropy Methods in Science and Engineering, Saratoga Springs, New York, 2007

Foudray, AMK, Habte, F, Levin, CS, Olcott, PD, "Positioning Annihilation Photon Interactions in a Thin LSO Crystal Sheet With a Position-Sensitive Avalanche Photodiode" IEEE Transactions on Nuclear Science, Volume 53, Issue 5, Part 1, Oct. 2006 Page(s):2549 - 2556

Foudray, AMK, Chinn, G, Levin, CS, "Incident Photon Direction Calculation Using Bayesian Estimation for Detector Systems with 3D Positioning Capability", Presented at the 2006 IEEE Nuclear Science Symposium and Medical Imaging Conference, San Diego, CA

Foudray, AMK, Farrell, R, Olcott, PD, Shah, K, Levin, CS, "Characterization of Two Thin Position-Sensitive Avalanche Photodiodes on a Single Flex Circuit", Presented at the 2006 IEEE Nuclear Science Symposium and Medical Imaging Conference, San Diego, CA

Foudray, AMK, Chinn, G, Levin, CS, "Component-Based Normalization for PET Systems with Depth of Interaction Measurement Capability" Nuclear Science Symposium Conference Record, 2005 IEEE Volume 4, October 23 - 29, 2005 Page(s):2108 - 2111

Foudray, AMK, "Algorithm Development for Some Inverse Problems in High-Resolution Positron Emission Tomography Detectors using Monte Carlo Simulation" Oral Presentation at the Molecular Imaging Summer School, Crete, Sept 11-16 2005

Foudray, AMK, "Investigating Positioning Algorithms in a High Resolution Positron Emission Tomography System Capable of Depth of Interaction Measurement" Presented at the Molecular Imaging Summer School, Crete, Sept 11-16 2005

Foudray, AMK, "Event Rejection Techniques for List-Mode Positron Emission Tomography" Presented at the Bio-X Interdisciplinary Initiatives Symposium, August 31st, 2005

Foudray, AMK, Habte, F, Zhang, J, Chinn, G, Levin, CS, "Optimization of a Novel Advanced Positron Emission Tomography System for Imaging Mouse Models of Human Disease" Presented at the 2005 Bio-X Watching Life Imaging Symposium, March 25-26, Stanford University, Palo Alto CA

Foudray, AMK, Levin, CS, Olcott, PD, "Investigating Positioning Algorithms in a High Resolution Positron Emission Tomography System Capable of Depth of Interaction Measurement", Presented at the 2005 Society of Nuclear Medicine Annual Meeting, Toronto, Canada, Journal of Nuclear Medicine, 46 (5), 483P, May 2005

Foudray, AMK, "The Molecular Imaging Instrumentation Laboratory: Dedicated Small Animal Imaging Project", Presented at the San Francisco Exploratorium for the Molecular Imaging Program at Stanford, Sep 2004

Foudray, AMK, Habte, F, Chinn, G, Zhang, J, Levin, CS, Olcott, PD, "Optimization of a PET Breast Imaging System Comprised of Position Sensitive Avalanche Photodiodes Utilizing Monte Carlo Simulation" Presented at the 2004 IEEE Breast Imaging Workshop, Oct 22-23, 2004, Roma, Italy

Foudray, AMK, Habte, F, Chinn, G, Zhang, J, Levin, CS, Olcott, PD, "Optimization of a Box-Shaped PET Breast Imaging System Comprised of Position Sensitive Avalanche Photodiodes Utilizing Monte Carlo Simulation" Physica Medica (in press, 2006)

Foudray, AMK, Habte, F, Levin, CS, Olcott, PD, "Positioning Annihilation Photon Interactions in a Thin LSO Crystal Sheet with a Position-Sensitive Avalanche Photodiode" 2004 IEEE Nuclear Science Symposium and Medical Imaging Conference Record, IEEE, Piscataway, NJ, USA.

Foudray, AMK, Ke, PC, Smith, DE "Microtubule Diffusion in Circular and Linear DNA Polymers Using Fluorescence Probes in Confocal Microscopy", Invited Talk for the La Jolla Interfaces in Science Mini-Symposium, 2002

Foudray, AMK, Gemmen, G, Ke, PC, Smith, DE, "Imaging Mechanisms of Chromatin Assembly Dynamics Using Optical Tweezers," Oral Presentation at the Single Molecule Summer School, Nottingham University, 2002

Foudray, AMK, Ke, PC, Smith, DS "Visualizing ϕ29 Bacteriophage Mechanical Motor Rotation Using Confocal Microscopy," Presented at the Single Molecule Summer School, Nottingham University, 2002

(Foudray) Klohs, AM, Kelley, RJ "Development of a PEM Fuel Cell Membrane Using Carbon Nanotubes" Invited Talk for the Electronics Materials Research Laboratory, Motorola Inc., 2000

(Foudray) Klohs, AM, Kelley, RJ "Correlation of Surface Treatment Optical Properties and Topology as Measured by Profilometry and Atomic Force Microscopy," Invited Talk for the Electronics Materials Research Laboratory, Motorola Inc., 1999

(Foudray) Klohs, AM, Lee, RE, "Using Scanning Electron Microscopy and Energy Dispersive X-ray Spectroscopy to Evaluate Wear in Diamond-like Carbon and Other Novel Materials" Summer Student Research Record, Argonne National Laboratory, 1998

Ke, PC, Foudray, AMK, Gemmen, G, Smith, DE, "Mechanical Study of Histone Modified Chromatin Using Optical Tweezers", Invited Talk for the La Jolla Interfaces in Science Mini-Symposium, 2002

Levin, CS, Farrell, R, Foudray, AMK, et al., "A Thin Position Sensitive Avalanche Photodiode Has Been Fabricated for Ultra-High Resolution PET to Achieve Robust Scintillation Light Collection Efficiency with High Crystal Packing Fraction" Presented at 2004 IEEE Medical Imaging Conference, Oct 16-22, Roma, Italy

Levin, CS, Foudray, AMK, et al, "Impact of High Energy Resolution Detectors on the Performance of a PET System Dedicated to Breast Cancer Imaging." Physica Medica, Volume 21, Supplement 1, 2006, Pages 28-34

Levin, CS, Habte, F, and Foudray, AMK, "Methods to Extract More Light from Minute Scintillation Crystals Used in an Ultra-High Resolution Positron Emission Tomography Detector." Nuclear Instruments and Methods in Physics Research Section A 527 (1-2): 35-40 July 11, 2004.

Levin CS, Foudray AMK, Olcott PD, Habte F., "Investigation of Position Sensitive Avalanche Photodiodes for a New High Resolution PET Detector Design." IEEE Transactions on Nuclear Sciencs 51 (3): 805-810 Part 2, June 2004

Levin, CS, Foudray, AMK and Habte, F, "Novel Detector Prototype for Ultra-High Resolution Positron Emission Tomography" Oral presentation at the 2003 Society of Nuclear Medicine Meeting, New Orleans, LA, June 20-25. Journal of Nuclear Medicine Vol. 44, No. 5, May 2003, p.138

Levin, CS, Foudray, AMK, Habte, F, "Development of a novel technique to extract more light from tiny scintillation crystals used in ultra-high resolution PET detectors" Oral presentation at Second International Conference on Imaging Technologies in Biomedical Sciences: ITBS2003, 26-30 May 2003, Athens and Milos Island, Greece. Paper number:ITBS-1842.

Olcott, PD, Zhang, J, Levin, CS, Habte, F, Foudray, AMK, "Finite Element Model Based Spatial Linearity Correction for Scintillation Detectors that use Position Sensitive Avalanche Photodiodes," Nuclear Science Symposium Conference Record, 2005 IEEE Volume 5, October 23 - 29, 2005 Page(s):2459 - 2462

Olcott, PD, Habte, F, Levin, CS, Foudray, AMK, "Simulation and Measurement of Gamma Ray and Annihilation Photon Imaging Detectors," IEEE Transactions on Nuclear Science (undergoing revision, 2005)

Olcott, PD, Habte, F, Levin, CS, Foudray, AMK, "Performance Characterization of a Miniature, High Sensitivity Gamma Ray Camera". Submitted to IEEE Transactions on Nuclear Science (undergoing revision, 2005).

Olcott, PD, Talcott JA, Levin CS, Habte F, Foudray AMK. "Compact Readout Electronics for Position Sensitive Photomultiplier Tubes" IEEE Transactions on Nuclear Science 52 (1): 21-27 Part 1, Feb 2005

Olcott, PD, Habte, F, Levin, CS, Foudray, AMK, "Characterization of Performance of a Miniature, High Sensitivity Gamma Ray Camera," 2004 IEEE Nuclear Science Symposium and Medical Imaging Conference Record, IEEE, Piscataway, NJ, USA.

Rast, S, (Foudray) Klohs, AM, Frazer, BH, Hirai, Y, Schmauder, T, Gatt, R, "Temperature and wavevector dependence of overdoped $Bi_2Sr_2CaCu_2O_{8+x}$ single crystal samples" Oral Presentation at the 2000 American Physical Society Annual March Meeting, Minneapolis, MN. Session C11, March 20, 103D, MCC

Vandenbroucke, A., Foudray, A. M. K, Lau, F. W. Y., Levin, C. S., Olcott, P. D. and Reynolds, P. D., "Performance Characterization of a New Ultra-High Resolution, 3-D Positioning PET Scintillator Detector" 2008 IEEE Nuclear Science Symposium and Medical Imaging Conference Record, IEEE, Piscataway, NJ, USA.

Zhang, J, Olcott, PD, Foudray, AMK, Chinn, G, Levin, CS, "Monte Carlo Simulation Study of a Dual-Plate PET Camera Dedicated to Breast Cancer Imaging", Nuclear

Science Symposium Conference Record, 2005 IEEE Volume 3, October 23 - 29, 2005 Page(s):1667 - 1671

Zhang, J, Foudray, AMK, Olcott, PD, Levin, CS, "Performance characterization of a novel thin position-sensitive avalanche photodiode-based detector for high resolution PET" Nuclear Science Symposium Conference Record, 2005 IEEE Volume 5, October 23 - 29, 2005 Page(s):2478 - 2482

Zhang, J, Foudray, AMK, Olcott, PD, Levin, CS, "Coincidence Measurements with a 1 mm^3 Resolution Avalanche Photodiode-Based Scintillation Detector for Ultra-High Resolution PET," Oral Presentation at the 2005 Society of Nuclear Medicine Annual Meeting, Toronto, Canada, Journal of Nuclear Medicine, 46 (5), 209P, May 2005

Zhang, J, Olcott, PD, Foudray, AMK, Levin, CS, "Image Quality and Photon Counting Studies with Different Size LSO Crystals on a Dual-Panel PET Camera Dedicated to Breast Cancer Imaging" 2005 IEEE Nuclear Science Symposium and Medical Imaging Conference Record, IEEE, Piscataway, NJ, USA.

Zhang, J, Foudray, AMK, Olcott, P, Chinn, G, Habte, F, Levin, CS, "Development of a Dual-Panel Positron Emission Tomography Camera Dedicated to Breast Cancer Imaging," Presented at the Bio-X Program at Stanford, Watching Life Symposium, March 25, 2005

Zhang, J, Foudray, AMK, Chinn, G, Levin, CS, "Development of Compact PET Camera Based Upon New Detectors for Dedicated Breast Cancer Imaging," Presented at the 2005 Academy of Molecular Imaging Meeting, Orlando, FL, March 19-23, 2005. Molecular Imaging and Biology 7(2), p. 131, Feb 2005

Zhang, J, Foudray, AMK, Habte, F, Olcott, PD, Levin, CS, "Evaluation of a Dual-Head PET Camera Design Dedicated to Breast Cancer Imaging." Presented at the 2004 IEEE Breast Imaging Workshop, Oct 22-23, 2004, Roma, Italy

Zhang, J, Foudray, AMK, Habte, F, Olcott, PD, Levin, CS, "Evaluation of a Dual-Head PET Camera Design Dedicated to Breast Cancer Imaging." Phys Med. 2006, 21, Suppl 1, pp:94-98

Fields of Study

Major Field: Physics

Studies in Microscopy and Imaging.
Doctors George Fenske, Robert A. Erck and Ali Erdemir, Argonne National Laboratory,
Mister Richard H. Lee, Argonne National Laboratory,
Doctor Ronald E. Kelley, Morotola, Inc.,
Professor Richard Prepost, University of Wisconsin, Madison,
Professor Douglas E. Smith,
Professor Craig S. Levin, Stanford University,
Doctor Garry Chinn, Stanford University

Studies in Detector Physics.
Professor Craig S. Levin, Stanford University,

Studies in Signal Processing and Algorithm Development.
Doctor Donald Peyton Cox, University of Wisconsin, Madison,
Doctor Theo Alexopoulos, University of Wisconsin, Madison,
Doctor Ronald E. Kelley, Morotola, Inc.,
Professor Douglas E. Smith,
Professor Craig S. Levin, Stanford University,
Doctor Garry Chinn, Stanford University

Studies in Inverse Problems.
Professor Craig S. Levin, Stanford University,
Doctor Garry Chinn, Stanford University

Studies in Monte Carlo Modeling.
Doctor Donald Peyton Cox, University of Wisconsin, Madison,

Professor Douglas E. Smith,
Professor Craig S. Levin, Stanford University

Studies in High Energy Physics.
Professor Albert Erwin, University of Wisconsin, Madison,
Doctor Theo Alexopoulos, University of Wisconsin, Madison

Studies in Computational Astrophysics.
Professor Donald P. Cox, University of Wisconsin, Madison

Studies in Solid State Physics.
Doctor George Fenske, Argonne National Laboratory,
Professor Marshall Onellion, University of Wisconsin, Madison,
Doctor Torsten Schmauder, University of Wisconsin, Madison

Studies in Optics.
Professor Pu-Chun Ke and Doctor M Josephine Bellanca

Studies in Mechanics and Energy.
Doctor Ronald E. Kelley, Motorola Inc.

Studies in Biology.
Professors Jim Kadonaga and Peter Wolynes
Doctors Karl Haushalter and John Finke

Studies in Biophysics.
Professor Douglas E. Smith,
Professor Philip Williams, University of Nottingham

ABSTRACT OF THE DISSERTATION

Design of an Advanced Positron Emission Tomography Detector System and Algorithms for Imaging Small Animal Models of Human Disease

by

Angela Marie Klohs Foudray

Doctor of Philosophy in Physics

University of California, San Diego, 2009

Professor Craig S. Levin, Co-Chair

Professor Clifford M. Surko, Co-Chair

Detecting, quantifying and visualizing biochemical mechanism in a living system without perturbing function is the goal of the instrument and algorithms designed in this thesis.

Biochemical mechanisms of cells have long been known to be dependent on the signals they receive from their environment. Studying biological processes of cells *in-vitro* can vastly distort their function, since you are removing them from their natural chemical signaling environment. Mice have become the biological system of choice for various areas of biomedical research due to their genetic and physiological similarities with humans, the relatively low cost of their care, and their quick breeding cycle. Drug

development and efficacy assessment along with disease detection, management, and mechanism research all have benefited from the use of small animal models of human disease.

A high resolution, high sensitivity, three-dimensional (3D) positioning positron emission tomography (PET) detector system was designed through device characterization and Monte Carlo simulation. Position-sensitive avalanche photodiodes (PSAPDs) were characterized in various packaging configurations; coupled to various configurations of lutetium oxyorthosilicate (LSO) scintillation crystals. Forty novelly packaged final design devices were constructed and characterized, each providing characteristics superior to commercially available scintillation detectors used in small animal imaging systems: ∼1mm crystal identification, 14-15% of 511 keV energy resolution, and averaging 1.9 to 5.6 ns coincidence time resolution. A closed-cornered box-shaped detector configuration was found to provide optimal photon sensitivity (∼10.5% in the central plane) using dual LSO-PSAPD scintillation detector modules and Monte Carlo simulation. Standard figures of merit were used to determine optimal system acquisition parameters. A realistic model for constituent devices was developed for understanding the signals reported by the detector system and to create event construction and utilization algorithms. To increase quantitative accuracy in the reconstructed images acquired by the system, a component-based normalization algorithm was developed.

Chapter 1

Background

1.1 Introduction

The detection, tracking, and treatment of disease is important to all of us to maintain quality of life. Understanding mechanisms in biological systems can lead to new knowledge about health maintainance and disease prevention. Being that an intact biological system is the best venue for probing biochemical processes; a physically and chemically non-invasive, repeatable, process-specific, high-resolution method for identifying mechanism throughout a living organism could greatly aid research, from basic biology to pharmacology to clinical medicine. Positron emission tomography (PET) is the leading technology accomplishing such tasks. PET dynamically and non-invasively probes a living system with the specificity and resolution necessary to repeatably observe and quantify biochemical function.

The following list is a subset of applications of positron emission tomgraphy:

- Disease management: discovery and staging of disease within a living organism as well as to then observe the progression or recurrence of disease and drug efficacy in a subject.

- Drug development/pharmacology: in pre-clinical trials, the kinetics of concentration of a drug and its elimination from the system can be monitored regularly, not only providing a more rapid and cost effective methodology than the older technique of euthanizing and performing chemical assays on the animals, but also allowing longitudinal studies that show the dynamics of novel drug efficacy and contraindications. Besides reducing the number of animals sacrificed, due to inherent variations that different mice have in their response to a drug, the advantage of in vivo imaging is that the animal can be used as its own control, reducing the number of variables in an experiment. A single animal can be used to track disease development and treatment.

- Disease mechanism research: examine links between end-product systems biology [disease, symptoms (pain, inflamation, etc.), physiological and psychological processes and disorders, etc.] and its constituent building blocks (biochemical molecules and processes).

The manners in which PET systems accomplish these tasks are discussed in the rest of this chapter. The following chapters will describe novel high-sensitivity, high-

resolution positron emission tomography detector system components, designs, as well as algorithms studied using traditional medical imaging figures of merit. The goal of this work was to design the next generation small animal PET detector system in conjunction with the algorithms that would be necessary to utilize the expanded information gathered by such a system.

1.2 Motivation: Disease and Detection

Biochemical mechanisms of cells have long been known to be dependent on the signals they receive from their environment [6]. Studying biological processes *in-vitro* can vastly distort the function of the cell since they have been removed from their normal cell signalling environment. Therefore, host biological systems play a vital role in modern molecular biology research.

1.2.1 Mouse Models of Human Disease

Mice have become the test bed for understanding biochemical function, disease and therapeutic methodologies for use in humans. The many advantages of the mouse as a subject include the genetic and physiological similarities with humans, the relatively low cost of their care, and their quick breeding cycle [15]. Genetic manipulation of mice to develop *in-vivo* (in a living organism) human models have produced a vast array of genetically similar environments in which researchers can study the

mechanism and treatment of human disease.

Metabolism and Biological Processes

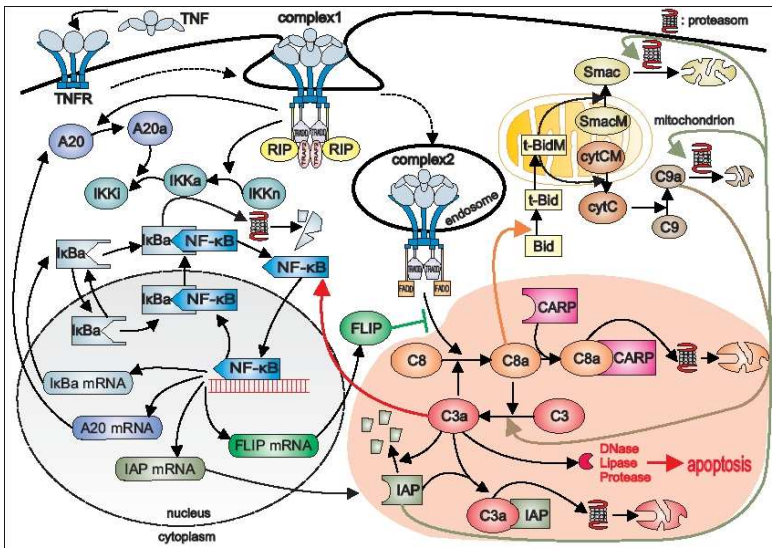

Figure 1.1: An illustration of the Tumor Necrosis Factor (TNF) signal transduction pathway and its qualitative interconnections [183].

The way in which biological function is carried out in an organism is by signaling pathways [16]. One such pathway is shown in Figure 1.1 is for TNF, or Tumor Necrosis Factor [183]. TNF is a pathway for signaling cell death (apoptosis). In this pathway, molecules such as the zinc finger molecule "A20", a regulator of another molcule, "NF-κB" (a transcription factor), are shown using shapes and labelled by their molecular name. The relationship between molecules is identified by directional arrows between the molecules that directly effect one another. The interdependence of the molecules and systems involved in this pathway provide compelling research avenues for drug development by developing compounds that either reduce/block a necessary molecule

for an unwanted process, or increasing a competing molecule, diverting the path to a harmless alternative. Studying the localization of molecules involved in a biochemical process can also aid in (1) understanding the function of the molecule, (2) determining if the process is taking place in the organism at all (detection), or (3) determining if an introduced chemical (drug) is changing the location or production rate of the molecule (therapy).

One of the most successful utilizations of PET to date is detecting or observing the biological process of metabolism. Increased metabolism, and specifically increased glycolysis, throughout the body has been correlated with multiple diseases and/or symptoms. The presence of various tumor types [35, 126, 177, 184], pain [14, 17], myocardial insulin resistance [109, 135], etc. have all been studied using a glucose analog, fluorodeoxyglucose (FDG). FDG's role in molecular imaging will be discussed in Section 1.2.2.

Translational Research

Once a likely molecular candidate for detecting and/or regulating a particular mechanism or disease with specificity has been identified, it can undergo testing to be approved by the FDA for clinical trials. As Reference [124] points out, "the American Physiological Society (APS) has defined translational research as the transfer of knowledge gained from basic research to new and improved methods of preventing, diagnosing, or treating disease, as well as the transfer of clinical insights into hypotheses

that can be tested and validated in the basic research laboratory". This bi-directional learning opportunity enriches both fields, steering further modes of discovery.

1.2.2 Tracer Development and Molecular Imaging

Molecular imaging can only do as well as its tracer. The tracer, or molecular probe, is a biomolecule with a signaling mechanism attached. In the case of PET, the signal is produced from an isotope that emits a positron such as fluorine-18 (^{18}F). The biomolecule is designed to be specific to the process of interest. It is this specificity that is the key to having a successful tracer.

Function Specificity

Specificity in the molecular imaging setting is essentially defined as observing a correlation between a molecule of interest being over- or under-expressed (chemical, molecule) and a single disease process as well as the degree of uptake of the molecular probe in the region of interest of the specific disease process. If other unrelated processes also produce the same molecular binding site, tracer accumulation does not necessarily indicate the process of interest. If a pathway and its constituent biochemical molecules are known, choosing a unique molecule to target within that pathway provides the direction for tracer and drug development.

For instance, reporter probes can be used to track cells modified for use in cell-based therapy. Heart muscle (myocardium) cells can be modified to express a reporter

gene (HSV1-sr39tk) [68]. The modified myocardial cells are then injected into the subject's myocardium. The modified cells and their progeny will then have the ability to express the introduced gene and produce an HSV1-tk enzyme. An external substrate for the HSV1-tk enzyme, injected into the myocardium, is designed to be phosphorylated by the enzyme and thus trapped within the modified myocardial cells. Attached to the external substrate is a positron-emitting molecular probe (18F-FHBG), which used to image the biodistribution of the modified myocardial cells.

Another aspect of specificity is what happens to the tracer after it has found the molecule with which it is meant to interact, which leads to a discussion on biodistribution.

Biodistribution

As mentioned in the beginning of this section, metabolism is a successfully probed process using PET and its most successful tracer is FDG. FDG, a glucose analog, is taken up by the cells, phosphorylated to FDG-6-phosphate (FDG-6-P) by the glucose enzyme hexokinase [147]. Once it has been phosphorylated, the molecule cannot leave the cell[1]. It is this trapping of the molecule that enables PET to image the location (biodistribution) of the process. Because the tracer is trapped over time, the cellular concentration of tracer inside the region of interest is increasing, and the amount of tracer in the full blood volume (throughout the rest of the body) is decreasing.

[1]There is some controversy about further metabolism mechanisms of FDG [77, 132, 164].

This feature enables a powerful contrast mechanism. for detecting, visualizing and quantifying disease in living subjects.

In order to achieve the highest contrast, the tracer is injected into the subject some time before data acquisition is performed (e.g. ∼50-90 minutes). This wait time enables tracer to flow through the subject and over time, be selectively taken up in the cells of tissue of interest by the process of interest, and giving high contrast at the time of image acquisition. A compromise between uptake time and lifetime of the positron emitter determines the time that image acquisition should occur [54, 101, 106, 140].

1.3 The Physics of Positron Emission Tomography

One of the reasons that positron emission tomography (PET) is so successful at non-invasively determining biomolecular function inside a large object of interest is due to the energy of the photons emitted. If an object is sufficiently small or thin in the direction of photon trajectory, two approaches could be useful in regards to choosing the probe's photon emission energy: (1) use numerous low energy photons and strong physical models to calculate a likely photon origin, or (2) use a few high energy photons and simpler models to arrive at a likely photon origin. Bioluminescence and fluorescence use the first photon energy regime to perform studies, but PET and SPECT take advantage of the second. Further modalities use other properties of material being imaged to determine structural or functional information (e.g. computed

tomopgrahy (CT) uses x-ray energy photons, ultrasound uses sound propagation and MRI utilizes the magnetization of nuclei to determine structure and fMRI uses the magnetization of nuclei to determine molecular function).

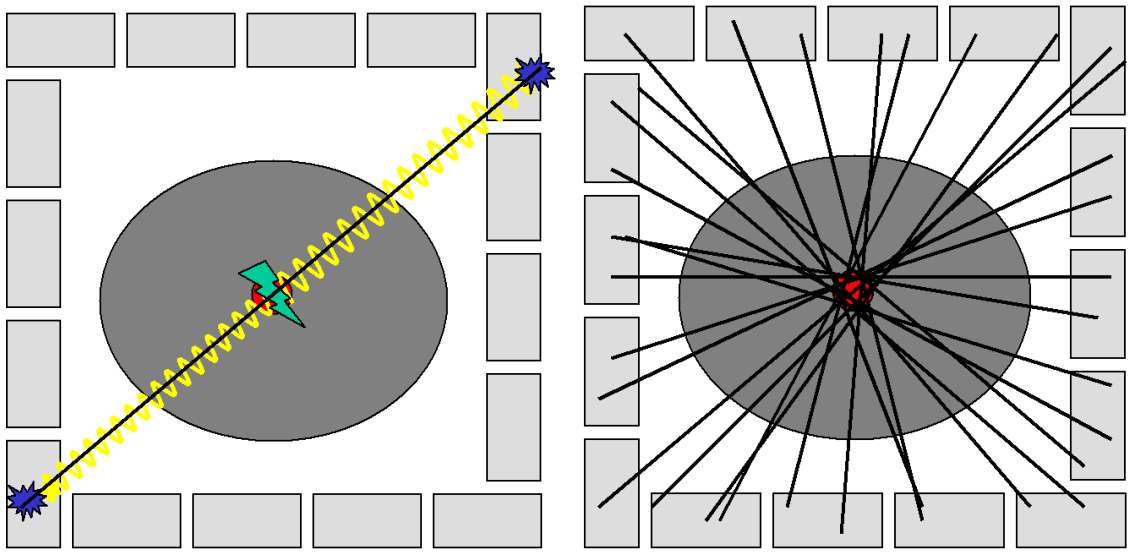

(a) Coincidence line formation

(b) Many coincidence lines: the data used in algorithms for image feature formation

Figure 1.2: (a) an illustration of the tracer uptake (red circle) in the subject (grey oval), positron-electron annihilation (green lightning bolt), annihilation photons generated (yellow wavy lines), interaction locations (blue stars) in the detector (grey boxes) and coincidence line (black line), and (b) an illustration of many coincidence lines (black) crossing through the tracer uptake location (red circle).

Positron emission tomography as an imaging modality takes advantage of the tendency of a positron to annihilate with an electron and produce two 511 keV photons, 180 degrees apart, near the location of the positron emission. The 511 keV photons that are generated have a small chance of interacting in low density matter such as water (of which we are mostly comprised) and a high chance of escaping the body

without interaction. By detecting both photons that are emitted from a single annihilation, it is assumed that the electron-positron annihilation occurred somewhere along a line drawn between the two detected positions.

Therefore, the location of the positron emitter is not directly measured, but rather assigned to a response line. In order to make images, one collects many of these from this double-photon, or coincidence photons, measured from many different angles. These locations of high coincidence-line intersection density are the locations from which the photons were likely generated. The illustrations in Figure 1.2 depict the situation.

The coincidence lines, along with tomographic image reconstruction algorithms, form an accurate tracer distribution image. Understanding some of the details of the processes that the particles (positrons, electrons and photons) involved in PET undergo will help to better understand both the advantages and limitations of the imaging method, as well as possibly give some direction as to how the information that is gathered could be better used.

1.3.1 Positrons

Positron Range

A chosen tracer molecule has attached to it a radionuclide that, for PET, will preferentially emit positrons. The positron, having some kinetic energy from the

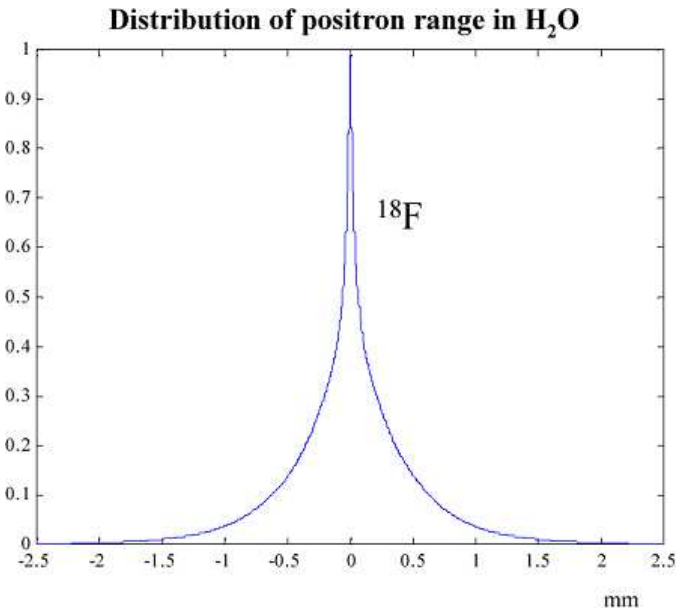

Figure 1.3: The distribution of positron path lengths for ^{18}F-emitted positrons in water [99].

radionuclide decay, must slow down before interacting with an electron. The kinetic energy of the positron has a range (from 0 to 635 keV maximum for ^{18}F), where the released energy from decay is distributed between the positron and a neutrino released simultaneously. The path that the positron takes is tortuous and highly variable in direction and path length. The path length is mainly influenced by the kinetic energy with which the positron is released as well as the composition of the surrounding material. For ^{18}F, the positron emitter used to tag the glucose analog FDG, the absolute value of this range (distribution shown in Figure 1.3) averages $\sim$0.23 mm.

Therefore, positrons are essentially the middle man in PET signaling and detection. Positrons do not, on average, remain at the exact location the tracer was

trapped in the body, nor are they directly detected by the detector system.

Positron Annihilation

Near the end of the positron's path, it interacts with an electron by annihilation, producing two or more photons simultaneously. The most probable number of emitted photons is two (>99% in water [112]) which is exploited by PET[2]. When two photons are produced in the annihilation process, they have nearly (see Section 1.3.1) exactly opposing momenta (collinear, back to back) and energy (511 keV). The collinear, monoenergetic, and simultaneous emission of two annihilation photons is utilized in reconstructing the biodistribution of tracer in the object (see Section 1.5).

Momentum Conservation: Acollinearity

Although positrons slow down before annihilating with electrons, they do not always come to rest in the electron-positron rest frame. Therefore, the remaining energy beyond the rest mass of the positron and electron is converted, via momentum conservation, into a deflection from an exactly π angular separation between the two emitted photons, resulting in acollinearity. The degree of angular deviation is due mainly to the momentum distribution of bound electrons in the surrounding material [107]. For water, the RMS deviation is $\sim$4.5 mradians or 0.26^o [99]. As the diameter of the detector system increases, this angular deviation translates into larger spatial

[2]Some groups have begun looking at the viability of building detectors that also take advantage of three annihilation photon events, as PET is a count-starved imaging modality [5, 78].

deviation in the detected location, producing a system-size dependent uncertainty in the reconstruction of biodistribution.

1.3.2 Annihilation Photons

An overview of the mechanisms of annihilation photon interaction in matter will be discussed here and in more detail in Section 7.2 of Chapter 7.

The interactions of annihilation photons are dependent on photon energy as well as the effective atomic number (Z_{eff}) and density (ρ) of the material with which it interacts [154]. The probability of interaction in a body is also increased by a larger amount of material the annihilation photon must traverse. In other words, a larger volume object increases the chance a photon interacts somewhere along its trajectory.

Some interaction processes lead to annihilation photons being absorbed in a material during interaction, some result in changing the direction of the photon. If interaction occurs in the body before reaching the detector, both of these types of processes can lead to a reduction in the number of annihilation photons that can be detected or kept after signal filters (though a high percentage of interactions, >99%, are due to scattering).

Detector systems, on the other hand, utilize the processes of interaction to absorb and therefore record an annihilation photon. Although the bulk of the energy deposited in a detector interaction occurs at the location of the interaction, the lib-

erated electrons and characteristic x-rays from the interaction processes also go on to deposit energy in the detector. The pathlength of these particles can lead to energy being deposited in neighboring detector elements.

The general trends in parameters that affect photon interaction and signal production are modulated by mechanisms specific to a family of detector materials. The characteristics of common materials used in PET can be found in References [86, 120, 137].

1.3.3 Photon Attenuation

The probability of attenuation along the colinear trajectory of annihilation photons through the object of interest is uniform due to the exponential nature of attenuation of photons through matter. For one of the photons, the probability of the photon emerging along its original path from a depth of x inside the object is:

$$P = 100\% * \frac{I_x}{I_\mathrm{o}} = 100\% * e^{-\mu x} \tag{1.1}$$

where $\frac{I_x}{I_o}$ is the fraction of photons leaving the object, and μ is the material dependent linear attenuation coefficient. For both photons, the probability of both emerging along their original path through an object thickness d is the multiplication of the two probabilities:

$$P = 100\% * \frac{I_x}{\text{o}} * \frac{I_{d-x}}{\text{o}} = 100\% * e^{-\mu x} * e^{-\mu(d-x)} = 100\% * e^{-\mu d} \tag{1.2}$$

where the second photon travels through the rest of the object thickness $(d - x)$ along the LOR path. The result is that the probability of both photons emerging unscattered from the object is independent of the location of the annihilation along the LOR.

1.3.4 Event Classification

Data gathered in an interaction are used, along with inference (see Section 1.5.1 for a discussion on inference) based on the physics of annihilation photon transport from production to detection, to distinguish usable interactions (signal) from interactions that will lead to blur in the image (loosely framed here as "noise"). Usability of events is defined within the framework in which the events are expected to be used. In the case of PET, traditional systems are using the energy and time of an interaction to filter out events that will form lines of response that will reduce contrast in the image.

Noise: Scatters

Finite energy resolution (ERes) in the detection system contributes to the inability to distinguish annihilation photons that have undergone a scattering of small angle before being detected. The photon's energy after a Compton scattering interaction is a function of its pre-interaction energy and the angle at which it scattered (see

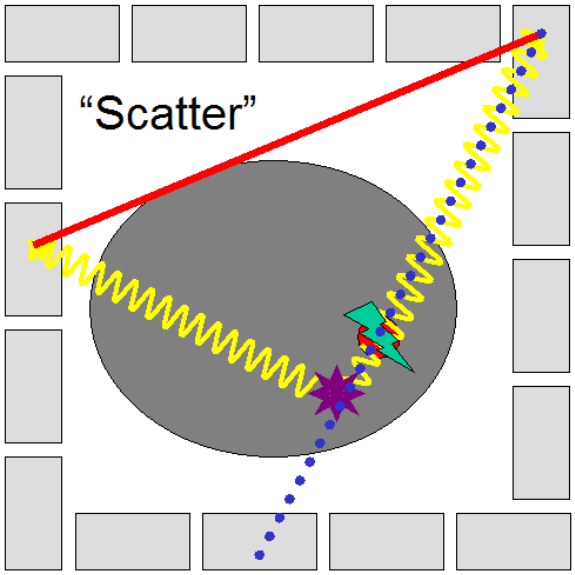

Figure 1.4: An illustration of a detected scattering event. One of the annihilation photons (yellow wavy lines) is detected unaltered and one has undergone one Compton scattering interaction before being detected. The grey rectangles are the detectors, the dark grey oval is the object being imaged, the red circle is a region of dense tracer, the light blue lightening bolt is the annihilation event, the purple star is the Compton scattering interaction location, the red line is the line connecting the two detected interactions, and the blue dotted line is the line that would have resulted if neither annihilation photon had scattered.

Figure 1.5 and Section 7.2.1). Therefore by energy filtering detected events, only annihilation photons that have undergone relatively large angle scatter in the object of interest are rejected (see Section 7.2.1). Table 1.1 shows the upper limit on the scattering angle that would be accepted by a detector system with a given lowest accepted energy threshold.

An event pair that contains annihilation photons that underwent one or more scatter events, but are not filtered out by energy discrimination due to this energy blur or a large acceptance energy window, are called scatter events or just ”scatters”.

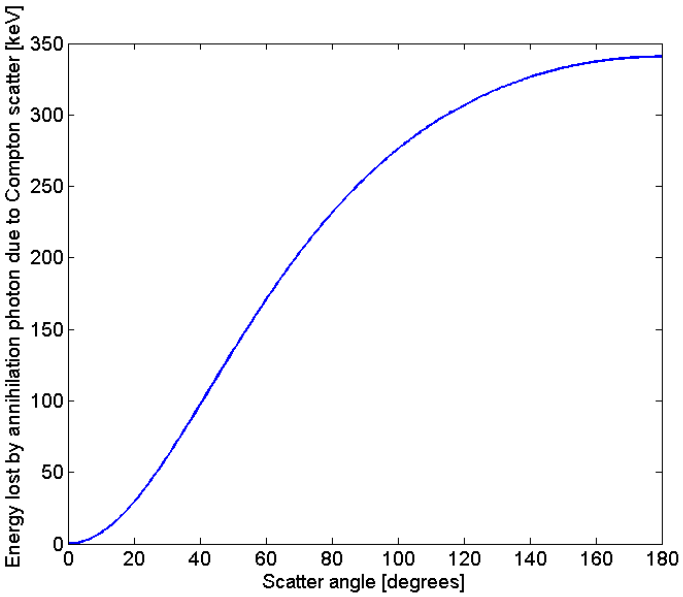

Figure 1.5: Energy lost by an annihilation photon due to a Compton scattering event versus scattering angle.

Table 1.1: Accepted scattering angle for various lowest accepted energy thresholds.

Lowest Accepted Energy [keV]	Lowest Accepted Energy [% 511 keV]	Accepted Scattering Angle Range [degrees]
501	98	0-12
482	94	0-20
451	88	0-30
414	81	0-40
377	74	0-50
308	60	0-70

The larger the (1) volume and (2) density of the material that the annihilation photons must traverse, the greater the likelihood of Compton scattering.

Noise: Randoms

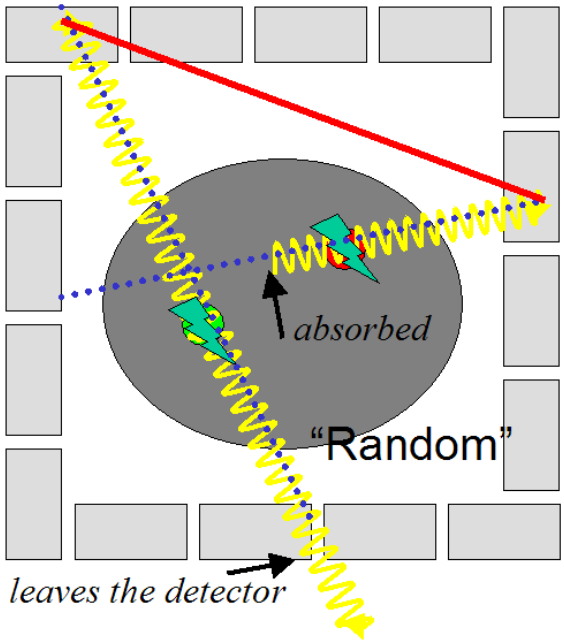

Figure 1.6: An illustration of a detected randoms event. One pair of the annihilation photons (yellow wavy lines) has one detected photon, and one is absorbed. The other pair has one detected photon, while the other passes through the detector undetected. The grey rectangles are the detectors, the dark grey oval is the object being imaged, the red and blue circles are regions of dense tracer, the light blue lightening bolts are the annihilation events, the blue dotted lines are the lines that would have resulted if both annihilation photons of the pairs had been detected and distinguished, and the red line is the line connecting the two detected interactions (notice the red line does not go through either of the regions of the object with high tracer accumulation).

The other major contribution to large scale background in a reconstructed image is the finite time resolution of the constituent detectors in a PET system. Events are constructed from time pairing detected incident photons which are assumed to be from a single photon emission event - an annihilation event produces two photons at precisely the same time. An uncertainty in timing information leads to possible

pairing of detected incident photons from separate annihilations, which incurs large spatial background in the reconstructed image. Events that are paired from photons from separate annihilation events, but are not filtered out by time discrimination techniques due to the temporal uncertainty in the detectors, are call "Randoms". Since all of the annihilation events emit photon pairs isotropically, the "noise" due to the Random coincidences is relatively uniform throughout the field of view [79]. Inclusion of these events degrades contrast, hence degrading quantitative information (functional dependence of intensity in reconstructed image on tumor uptake).

One of a pair of generated photons can go undetected, or filtered out by the energy window meant to discard scatter events, by (see Figure 1.6):

- traveling along a path that is not directed toward detectors (either initially or after being scattered). The bulk of the annihilation photon loss is due to this effect.

- passing through the detectors without (completely) interacting, i.e. the detected energy of the event is less than 511 keV and could thus be removed from the data. This is the second largest effect creating annihilation photons to go undetected.

- being absorbed in the body before getting to the detectors. This is a very rare occurence.

The other factors contributing to Randoms are the activity of the source with

respect to the time resolution and size of the detectors in the system. Annihilation photons are produced via the population-limited Poisson time-distributed emission of positrons from all of the radioisotopes present, with a mean emission rate represented by the current activity of the source. As with scatter events, the random events cannot be labeled in a traditional system, but their rate, after energy and time windowing, can be estimated.

Noise: Multiples

"Multiples" occur when multiple annihilation events have produced three or more detected photons within the coincidence time window. Singles (see definition below) and Multiples can occur for similar reasons as was the case for Randoms - that is, due to photon loss and finite system time resolution - but may be estimated and subtracted from the data. If more about the state of photons as the annihilation photons enter the detector was known; random, single and multiple events could shed some of their ambiguity and contribute with reduced noise to image reconstruction.

Signal: Trues

Taking into consideration the major types of "noise" that contributes to blur or background in the image, then true events are those where all of the following must be true:

- Both annihilation photons from a single annihilation event (that produced only

two annihilation photons) interact in the detector system within the coincidence time window setting.

- Each of the pair of annihilation photons fully deposit there energy in the detector system within the energy window setting.

- Neither of the annihilation photons have scattered in the object before reaching the detector.

Breaking each rule 1) results in or defines different types of noise or 2) illustrates ways in which true counts are reduced. The first rule being broken contributes to random rates, the second rule means the event cannot be distinguished from scatter events (and is thus filtered), and the third rule says that scatter events should be filtered out. As each of the previous "noise" discussions have mentioned, filters are employed as efficiently as possible knowing the signal to noise is increased by using the described filtering methods, but some true events are invariably lost and some blurring events are included due to the finite resolution of the system.

Singles

When only one of a pair of annihilation photons is detected, these events are called "singles". The term "single" is also used when referring to a single photon that is detected above the lower energy threshold of the detection system.

1.4 Key Performance Issues in Positron Emission Tomography

Positron emission tomography systems detect the location, energy and time of annihilation photon interactions in order to produce a map of the locations from which the photons were emitted. This map, or image, corresponds to the biodistribution of the process-specific tracer in the object being studied.

The sharpness and clarity of the tracer map is a function of the efficiency and accuracy of the detector system used. However, intrinsic blurs from positron range and acollinearity (see Sections 1.3.1 and 1.3.1, respectively), which are inherent in the physics of the annihilation process, reduce the accuracy of the overall tracer mapping process. Fundamental limits restrict PET images from achieving perfect representations of the actual biodistribution in the object, hence impacting the ability to quantitatively study disease mechanisms.

The materials and devices used to construct the detection system have traditionally been the major contributor to blurs and artifacts found in the reconstructed image [92, 110, 117, 124, 162, 165, 166, 168]. The major features of detector system driven image limitations are discussed in this section.

1.4.1 Sensitivity

Emission tomography is, by the nature of the method, an inherently counts-starved means to study disease mechanisms in a living subject. The purpose of the method is to assess biological function without perturbing it. Therefore, only trace amounts of chemical tracer are introduced into the system, each molecule having at most one chance of emitting a signal to advertise its location. Therefore, the efficiency with which the system can detect coincident annihilation photon events is of great import.

Detector Photon Sensitivity

Traditional PET systems use only events consisting of the detection of two annihilation photons from a single annihilation event to reconstruct an image (see Section 1.3.4 for a further discussion on event types and Reference [53] for a novel perspective on event-typing). Many factors contribute to the efficiency with which these events are detected. Although there are factors specific to the object being studied that reduce the fraction of annihilation events that result in two detectable annihilation photons. The detector-specific or controllable characteristics will be discussed here.

The major players in detector system efficiency are (see Section 8.3.2 for a further discussion):

- The **solid angle coverage** or geometric efficiency, of the object being studied. Detectors surround the object so that the isotropically directed annihilation

photon pairs are, as often as possible, directed at the detector.

- For those annihilation photons that are directed at the detector, the intrinsic detection efficiency depends on the chance that an incoming photon will be absorbed in the crystal material. This depends upon the Z, density and thickness of the material. Intrinsic detection efficiency determines the fraction of annihilation photons that produce detectable interactions. 511 keV photons have the ability to traverse a non-negligible amount of material before interacting.

- **Intrinsic properties of the components** that are used to construct the system, such as scintillation light output, photodetector quantum efficiency, and coupling mechanisms between the photodetectors and electronics. These factors determine whether an absorbed event will be accepted to be above a given threshold setting. This factor is part of the intrinsic detection efficiency.

The components of detector sensitivity can be broken down further, and are discussed in Section 8.3.2 of Chapter 8.

Data Filters

The position of the detected interactions that are used in final image reconstruction are those from annihilation photons (511 keV interaction energy), desirably from the same annihilation event (simultaneous or coincidence detection). As will be discussed in Section 1.4.2, the resolution with which the position, energy and time is

measured in a detector is not perfect. Therefore, energy and time filters are used to select each detected annihilation photon pair from background coincidence events for reconstruction. These filters reduce the number of detected interactions with the intent to improve the signal to noise ratio (SNR) of the reconstructed image.

1.4.2 Detector Resolution and Linearity

The three characteristics of an interaction that are recorded by the detector are the position, energy and time of the interaction. The energy and the time between two interactions (coincidence time) provide a means to select interaction events to use for image reconstruction.

Position

Because PET uses the interactions from two annihilation photons to make the map of the tracer locations inside the object being imaged, the position resolution and linearity are important detector system considerations. The resolution with which the image map can be made is intrinsically linked to the detector system position resolution. Positioning linearity in the detector also contributes to position resolution in the image in that portions of the object can have artefacts and much lower sampled regions when measured with systems having position detection non-linearities. Section 8.2 explicates how the detector and image spaces are related.

Energy

The energy of an annihilation photon interaction helps to distinguish the event as one arising from annihilation photons. An annihilation photon should deposit 511 keV in the detector. Interactions with more or less than 511 keV are likely to have compromised interaction information, therefore contributing to blurs and artifacts in the reconstructed image. Section 3.2.6 discusses energy resolution when evaluating detectors.

Beyond annihilation photon transport processes contributing to disparate interaction energies, detection systems measure energy with a finite resolution. This energy resolution blurs the distinguishability between unaltered annihilation photon interactions and energy deposited by other means. The inclusion of interactions from scattered photons, for instance, creates a uniform background in the entire image, decreasing the contrast of features.

The energy resolution of current small animal systems existing or under development average ∼17-50% of 511 keV for scintillator-photodetector designs [59, 116, 168, 169, 171, 187, 194], and ∼2-5% for system designs using direct semiconductor photodetection [114, 182].

Interaction and Coincidence Time

The interaction time of an annihilation photon in a detector is used so that it can be paired with the annihilation photon that was most likely to have been emitted during the same annihilation event. Because detectors have finite timing resolution, coupled with the rate at which annihilation events occur in the subject (total activity of the injected tracer), pairing the wrong two annihilation photon interactions occurs at a non-negligible rate. The rate of pairing error is dependent on the following major factors: the detector system, the size and composition of the object being imaged and the amount of activity in the object being imaged. Section 1.3.4 discusses this concept further.

The coincidence time resolution of current small animal systems under development average ∼3-14ns for scintillator-photodetector designs [59, 116, 168, 169, 171, 187, 194], and ∼8-30ns for system designs using direct semiconductor photodetection [114, 182]. These time resolutions do not allow for the detection of the difference in flight times due to dissimilar path lengths of detected annihilation photons from the same event.

Some detectors are able to resolve interactions in the high hundreds of picoseconds (>500ps), too large to be useful in small animal imaging systems, however these detectors are being investigated for larger diameter, full body human imaging systems (∼15 cm in radius [149]) in order to reduce uncertainty in annihilation location along

the annihilation photons' line of trajectory. See Reference [108] for more details.

1.4.3 Sampling

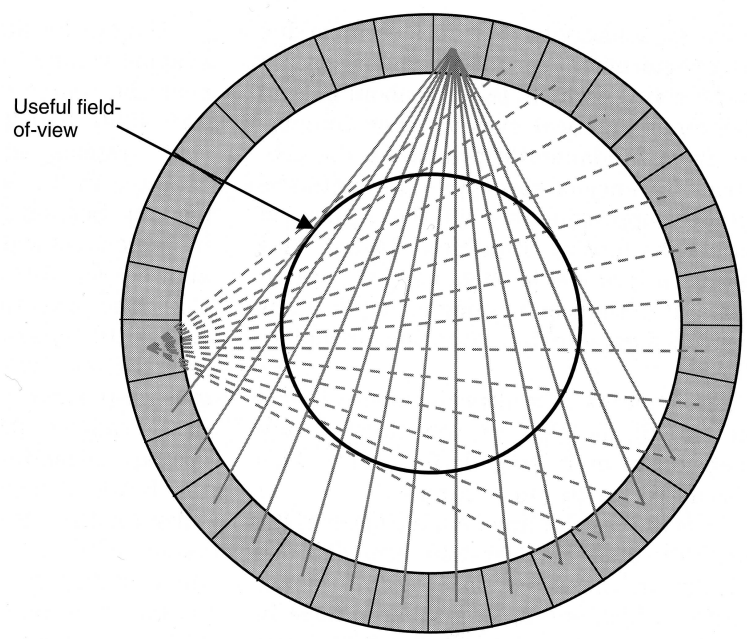

Figure 1.7: An illustration of the coincident detector pair lines and the useful field of view [31].

Because detector elements are only able to discretely measure position in the PET system, the pairs of detectors that are used to form coincident events measure or sample the object being imaged along coincidence lines. The density and linearity of spacing of lines throughout the imaging volume is a major factor in determining the ability of the detector system to uniformly and accurately quantify activity.

Many systems must use a small field of view (FOV), as compared to the inner diameter of the system, to reduce resolution and sampling errors [85, 110, 119]. Un-

fortunately, a small useful field of view increases the cost (more detector is needed to view the same volume) and reduces the photon sensitivity (counts detected in coincidence lines outside the smaller field of view are rejected) of the system. This smaller field of view, or useful field of view (UFOV), is illustrated in Figure 1.7. Another factor, however, also shrinks the useful field of view. A discussion on another major contributor can be found in Section 6.2.1.

1.4.4 Image Quantification

Accuracy in intensity measurement across the reconstructed image is essential to recreating the biodistribution of the tracer in the object being imaged. Intensity measurement for each detector pair should be the same, given the same amount of annihilation photons directed at them. In other words, the efficiency with which a detector pair registers a coincidence event should be the same for all detector pairs. The efficiency map for each detector pair should be measured using known activity distributions and then equalized, a process called normalization. Chapter 8 discusses a novel normalization algorithm developed for the system described in Chapter 6.

Counting Statistics and SNR

The majority of the processes involved in PET detection follow Poisson statistics. Both the decay of an isotope producing a positron as well as photon counting in the detectors are Poisson processes. Poisson noise arguments (where the standard

deviation of counts is equal to the mean which is square root of the counts) show that the local signal to noise ratio (SNR) in the reconstructed image at location (x,y,z) is a function the number of counts in that pixel [186] and the image reconstruction method used.

Therefore, the larger the number of counts, the better the signal to noise ratio will be. This result is a major driving force for increasing photon sensitivity in the detector system and influences how finely discretized the image space can be in reconstruction. A smaller image pixel size will not necessarily result in better image quality unless you have adequate photon statistics in that smaller pixel to maintain high SNR. The two factors in determining the optimal reconstructed pixel size to use are a) the intrinsic resolution of the detector system and b) the number of counts that can be gathered in the acquisition.

Contrast

Besides resolution, the other primary characteristic of feature distinction in reconstructed images is that of contrast. Contrast is essentially the relative intensity in the image due to tracer uptake in the body. Contrast is usually defined in the following way:

$$C_l = \frac{R_\mathrm{l} - R_\mathrm{o}}{R_\mathrm{o}} \tag{1.3}$$

where C_l is the contrast in the lesion or area of interest, R_l is the count rate in the

lesion or area of interest and R_o is the count rate in non-lesion tissue (background). Contrast is used by physicians and researchers to distinguish regions where the chemical process of interest within diseased tissue is taking place from normal tissue. The primary source of contrast is due to the biochemical and molecular mechanisms of uptake of the tracer by the tissue. The ideal tracer would be taken up only by the process of interest, and not at all by the surrounding tissue. Due to the compromise between the kinetics of tracer flowing through the body, the mechanisms of accumulation in the cells of tissue of interest, and the half-life of the radio-isotope attached to the biomolecule, this scenario is extremely difficult to achieve. Therefore, much work is being done on producing high contrast tracers [64, 81, 122, 130]. Algorithms, such as those used in image reconstruction, also play a part in resulting image contrast [25].

1.5 Tomography and Inverse Problems

Because PET detector systems do not directly measure the activity distribution in a body, models and inference must be utilized using information that is measured: the position, energy and time of interactions from annihilation photons.

1.5.1 Input/Output, Likelihood, and Inference

Ultimately, all methods try to achieve the same result: obtaining the origin of the detected photon. The desired output of the models and reconstruction algorithms is the accurate distribution of radionuclide that produced the detection pattern recorded in the detectors. The methods with which information about the photon's origin is determined is discussed in the next section.

Measurements

The major method PET uses to reduce the space from which a single detected photon pair originated is by using electronic collimation, or image-volume filtering using gathered signals (see Figure 1.2). Each interaction characteristic recorded; i.e. position, energy and time; filters the interactions to produce a usable event pair. By this filtering, the event pair was likely from annihilation photons: 1) uncompromised during their transit through the body and 2) that came from the same annihilation event. The coincidence interaction pair locations in the detector system form a line defining the most likely set of locations from which the photons originated in the body. An overview of the coincidence lines, or lines of response (LORs), can be found in Section 1.5.2 and discussed more thoroughly in Sections 1.5.3 and 1.5.5.

Another form of collimation not often employed in modern PET systems is that of mechanical collimation, simply referred to as collimators. Collimators consist of

high atomic number, high density material containing holes that only allow photons from particular angles to enter the detector. This reduction of accepted angles may be achieved by using long, thin, straight, hollow channels which let annihilation photons traveling parallel to the channels pass unabsorbed. Although using collimators descreases blurs due to mis-event-typing, many of the annihilation photons are absorbed in the collimators, drastically reducing system photon detection sensitivity by an order of magnitude or more [31, 84].

Some newer collimation methods are utilizing multiple interactions occurring in the detector per annihilation photon to infer a segment of the volume from which photons may have entered the detector. A standard method employed is using Compton kinematics [36, 133, 172]. Reference [53] discusses a novel algorithm for multiple interaction-based electronic collimation (MIBEC).

1.5.2 Line of Response

Using models, inference, and filters on collected data results in distinguishing the most likely regions of activity in the imaging volume that produced each detection pair. These high likelihood regions generally encompass many image pixels and in PET, are traditionally in the form of a line.

Because it is assumed that annihilation photons are emitted in exactly opposite directions, if they are unhindered during their transit through the object before reach-

ing the detector, the locations of the interactions will form the end points of the line through which the photons traversed. As discussed in Section 1.5.5, the photons have an equal probability of being emitted anywhere along the formed line, or line of response. Therefore, the line of response is the projected representation of the acquired data in image space. See Sections 1.5.3 and 1.5.5 for a more detailed discussion on how lines of response are formed and utilized in image space.

1.5.3 Detector Space

For illustration purposes, suppose there is a 2D detector system made up of two flat plate-like detector heads, and a 2D object between the heads that is uniformly filled with activity (see Figure 1.8). If only the detector pairs that are directly opposing one another in this detection configuration are selected for illustration, the thick black lines in Figure 1.8 represent the parallel lines of response connecting them. Borrowing nomenclature from x-ray computed tomography (CT), t parameterizes the position of a detector pair response line along a given projection oriented at angle theta, and C(t) is the detector-dependent integration of all counts.

Counts are collected for as long as possible to obtain the best counting statistics, allowing all possible detection pairs to gather the most usable information from the detection system. By collecting this data, the activity within the object of interest has been discretely sampled by each detector element pair. As far as detection elements

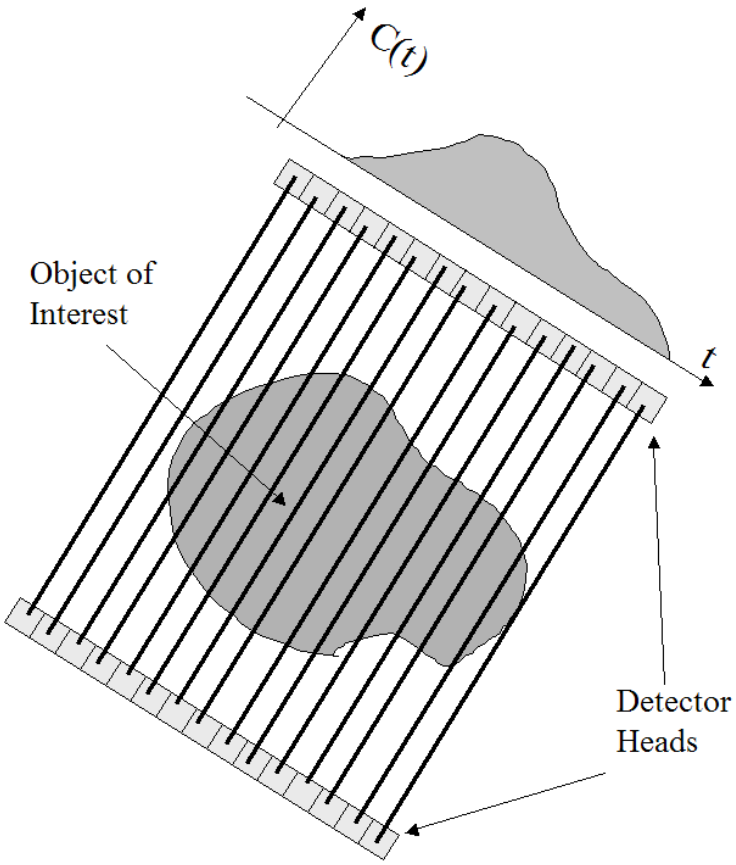

Figure 1.8: Illustration of detected counts from a single angle of the parallel lines of response for a simple dual head detector. This illustration demonstrates one way in which the detected events can be stored (i.e. grouped in parallel lines).

are concerned, an ideal tomographic detector system would be able to (1) sample with infinitesimally small detector elements which would (2) fully cover the 4π surface area surrounding the object; have (3) perfect energy, time and spatial resolution; (4) perfect quantum efficiency, and (5) would have no dead time. This system would still have inherent annihilation and photon interaction physics to take into account such as Compton scatter and scintillation photon production variations, to name just

two. Because none of these idealizations are achieved in PET systems, assumptions and inference must be employed in order to create a likely representation of the radionuclide distribution in the original object. The representation created in this study was in the form of a pixelated image, much like the pixels on your computer screen form images of a family photograph or a character in a video game. How images in this study are formed is described in the following section.

1.5.4 Data Structures

There are two spaces in which information about the object is stored. The first is detector space, commonly referred to in tomographic imaging as "projection space". As discussed previously in this chapter, information is first gathered in this space during acquisition. Section 1.5.4 talks about how acquired data can be sorted for optimal use of computational resources. Section 1.5.2 briefly discussed how these two spaces are linked through physical models of photon transport and detection.

Sinograms Data Sets

Sinograms are not used in any study contained herein; they are briefly discussed here for completeness. The traditional method of storing filtered acquisition data is in the compact form of a sinogram [7, 40, 155, 185]. Sinogram space is parameterized for a particular LOR by: the angle θ a line of response forms in an axial slice of the detector space, the radial distance r of that LOR from the center of an axial slice,

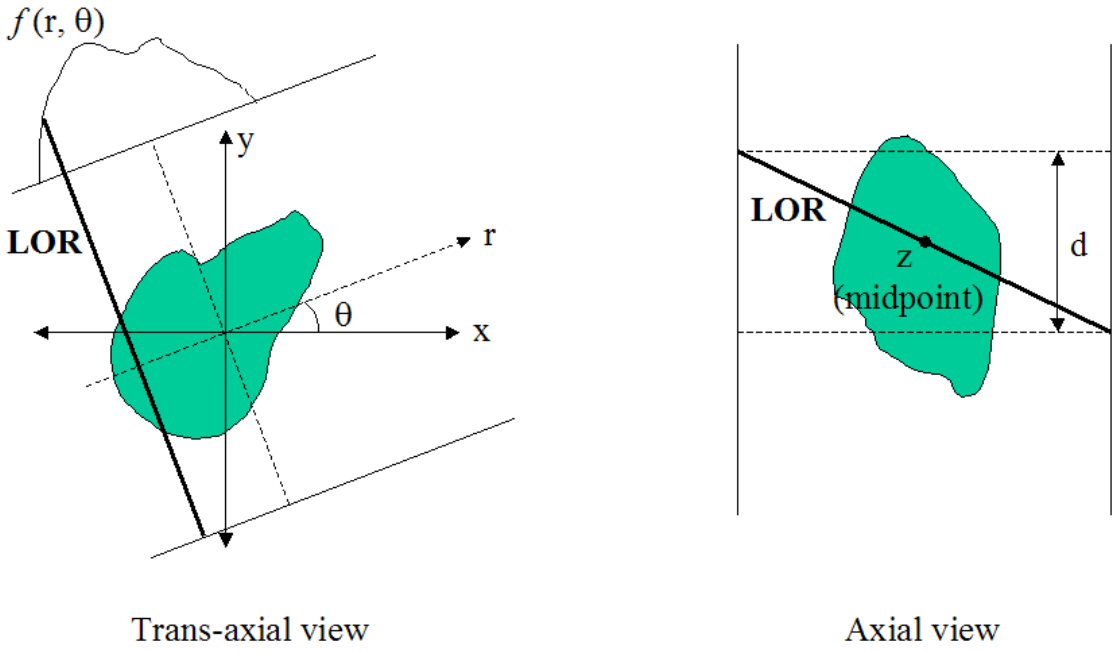

Figure 1.9: Illustration of the nomenclature used to define sinogram space.

the ring difference d or the number of axial slices traversed by that LOR, and the axial slice z of the LOR (see Figure 1.9). The LOR data, binned in four dimensions (r,θ,d,z), can be a dense matrix for detector systems with relatively low numbers of possible detector pairs as compared to the number of collected counts. Reducing the number of calculations by grouping data in this way has traditionally lead to a large speed up in image reconstruction computation time.

List Mode Data Sets

When the possible number of LORs becomes large compared to the number of counts collected in an acquisition, the space used to store collected data may instead

be most efficiently used by storing the individual detector element pairs involved in each event. For instance, the number of possible detector pairs in the small animal system designed in this thesis is $\sim$5x10^9, whereas the number of counts collected is usually $\sim 10^8$. A sparse matrix with an average count density of 0.01 per element does not provide an efficient use of computational resources. Storing each event on a line by line basis can also lead to increased sampling of the detector space as events are not binned to prescribed locations.

1.5.5 Image Space

Section 1.5.4 discusses the methods in which counts acquired by detector pairs can be stored for analysis. Since the method used in this thesis stores each event pair individually in a list, that will be the framework used for the following discussion.

Lines of response formed from the event pair locations traverse the system's field of view, representing the solution space of possible annihilation locations that produced the event. The probability of annihilation photon emission along the line of response is constant when the time resolution of the detectors is large compared to the transit time of the annihilation photons, which was true for the systems described in this work (see Section 1.4.2). This information is transfered to an image space by distributing a weighting factor into the subdivision of image space, which will be described in Section 1.5.5. How the image space itself is subdivided will be discussed in the

following section.

Subdividing Image Space

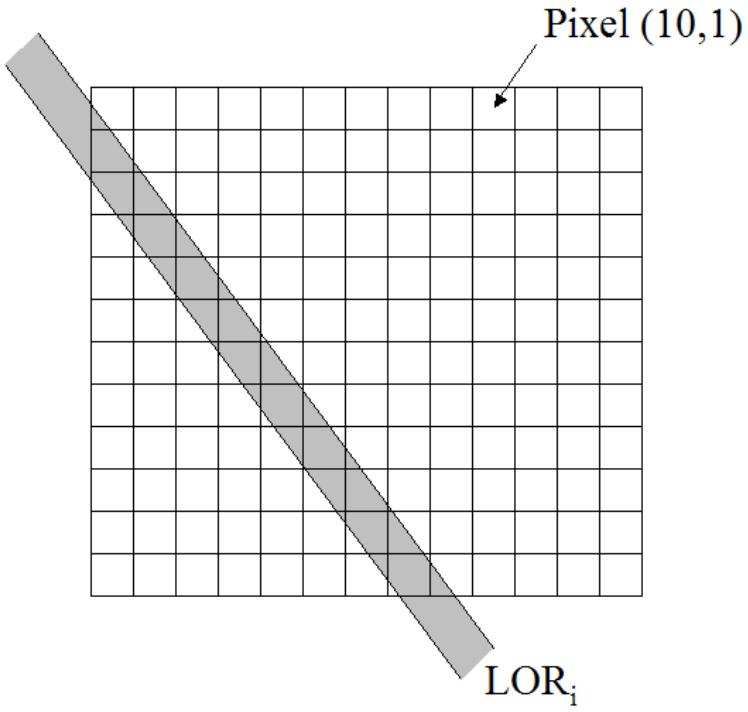

Figure 1.10: Illustration of an event line of response crossing image pixels.

The three dimensional image formed from event counts is constructed from subdivisions in the three coordinates. There are various methods of subdividing image space, though a standard method is to use small cube-shaped divisions or pixels, i.e. discrete image elements that have equal sized edges (see Figure 1.10). Each image pixel dimension represents a physical size in the object. For example, most pixels in

high resolution PET images represent object volumes on the order of $1mm^3$. The pixels are the smallest element in the image, meaning an individual pixel has a value that is uniform across the pixel. Although the LOR in Figure 1.10 traverses the pixels unequally, i.e. the LOR may only graze certain pixels, and completely encompass others, the value of any pixel due to the LOR applies to the whole of that pixel.

Pixel size is chosen based on aspects of the detector system - for instance the system's sampling of the field of view, and the spatial resolution of the detectors. Making smaller pixels in hope of reconstructing images with better resolution will only succeed until the pixels are on the order of the system sampling size. If pixels are too small, counts are stretched too thin per image pixel and counting statistics become low. How the counts from each LOR are distributed to pixels is described in the next section.

Detector Counts Distribution in Image Pixels

The goal of image reconstruction is to recover the original activity density in the object from detector measurements. There are multiple ways to calculate the contribution of a particular line of response to counts in the traversed image pixels. System models specify LOR size, shape, location and cross-sectional profile. The simplest model is illustrated in Figure 1.11, where a constant density, finite thickness line crosses image pixels. The amount of counts distributed to a particular pixel is dependent on the fraction of the pixel that the LOR intersects. The sum of the total

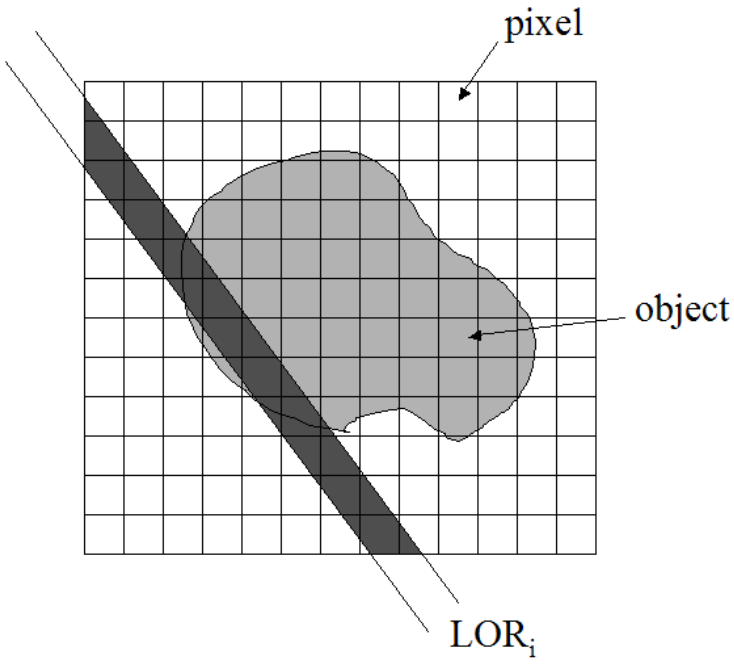

Figure 1.11: Illustration of an event LOR crossing image pixels. The object in light gray is shown for reference.

distributed counts for a single event LOR is normalized to one.

Looking back at the example illustrated in Figure 1.8, it is apparent in this simple model that efficiency differences in detection would lead to mis-representation in the images of the true object activity distribution. Therefore, the relative efficiency differences of the LORs in the system must be determined so that a weight can be applied to normalize LORs with respect to one another. The method of determining this weighting factor is the subject of Chapter 8.

1.6 Reconstruction Algorithms

The image is the representation of the annihilation photon emission distribution, which is the best approximation to the tracer biodistribution. The accuracy of the image with respect to the true radionuclide distribution depends on the detection system, as discussed in Section 1.4, but also on the reconstruction algorithm and its incorporated models.

1.6.1 Reconstruction Methods

Data gathered by a detector system is used to reconstruct an image of the density of annihilation photon emission within the volume imaged by the detectors, and hense the biodistribution of tracer in the object being imaged. The ideas used to reconstruct an image can be shown using the Radon transform in two dimensions. The left hand side of Figure 1.9 illustrates the system space nomenclature used in the Radon transform, and the distance along the LOR will be called t. Then, the Radon transform (R) is defined as [186]:

$$p(r,\theta) = R[f(r,\theta)] = \int_{-\infty}^{\infty} f'(x,y)dt \tag{1.4}$$

This equation states that the number of acquired coincidence pairs for a particular (r,θ) is equal to the sum over all the tracer present along the LOR. This view of the Radon transform is usually called "forward projection" as the events are stored in a

space after they have undergone the "forward" process performed by event collection by the detector, i.e. the data are represented in the space in which they were acquired. The natural structure for the data for application of the Radon transform is the sinogram, discussed in Section 1.5.4.

In order to retrieve the distribution of tracer in image space, the inverse-Radon transform is employed, or by performing the "backprojection" step:

$$R'[g(x,y)] = \int_0^{\pi} p(r,\theta)d\theta \tag{1.5}$$

This step projects the data back into image space along each of the LORs, producing a map of the biodistribution of the tracer.

The ideas in the Radon transform method have been used as a general framework to construct other reconstruction methodologies such as those that include filters to increase accuracy in reconstructed images (e.g. the filtered backprojection algorithm), Fouier and Bayesian methods, as well as maximum-likelihood and other iterative reconstruction techniques.

Optimizing reconstruction techniques is a rich and on-going field of research for PET studies. Information on other techniques can be obtained in References [7, 23, 26, 27, 34, 46, 48, 85, 118, 121, 131, 142–144, 189].

1.6.2 Reconstruction Algorithm: OSEM

The reconstruction algorithm employed in this work is iterative in implementation and uses a likelihood estimator to estimate the most likely image that produced the pattern of recorded detector measurements. Iterative reconstruction algorithms are utilized in PET because of the relatively low number of counts that are used to reconstruct images.

The Ordered Subset Expectation Maximization Algorithm (OSEM) iterative algorithm is based on concepts formed by the maximum-likelihood expectation-maximization (MLEM) algorithm (see Reference [41] for more details). The MLEM algorithm uses previous information about the image to estimate the current image. This is done by first reconstructing data assuming no previous information, or prior. Another image is produced using the same data set by estimating the expectation of the pixel values and then maximizing the likelihood of the image pixel values knowing the pixel values from the previous image. This is iterated many times, ideally until convergence is reached (i.e. the pixel values aren't changing significantly with each successive iteration) [18, 65, 179].

OSEM is also uses previous subsets of the data to form a likelihood map on which further data is then added, but speeds up the iterative process by first breaking data down into subsets [66]. Because the data becomes correlated, the number of subsets in which the data is broken up and the number of times the whole data set is used in

reconstruction (also called iterations), is generally dependent on the amount of data and the complexity of the image. Therefore, the reconstruction parameters (number of subsets, number of iterations), is decided empirically.

1.7 Monte Carlo Simulation Techniques

Monte Carlo simulation algorithms utilize random numbers and known probability distributions to compute outcomes for a defined process. Monte Carlo simulation is utilized in this thesis to generate physically accurate particle transport in modeled PET detector systems. The major advantage of the Monte Carlo technique in the algorithms employed in this work is that it produces and follows each generated particle and secondary particles, effectively modeling the statistical nature of the processes in a built system [67, 152].

Two such Monte Carlo simulation tools are used in this work: one for the annihilation photon and secondary particle transport in the detector system, and the other for the optical transport of the scintillation photons generated from the annihilation photon interactions.

1.7.1 Annihilation Photon and Secondary Particle Transport

Geant4 Application for Tomographic Emission or GATE is a GEANT4 add-on package. GEANT4 is a well-validated simulation tool for the high energy physics

community. GATE was developed for the emission tomography field by a consortium of institutions that actively maintain the simulation package [4]. GATE has been validated with many PET detectors systems that have been constructed [9, 58, 70, 71, 88, 112, 175].

A detailed discussion on the physics that is modeled in GATE and how it is utilized in the system designed in this study can be found in Section 7.2.

1.7.2 Optical Photon Transport

Detect2000 is utilized in many fields as a Monte Carlo simulation tool to study visible spectrum light transport in materials [24, 57, 60, 73, 173]. It is a versatile, fast, easy-to-use tool for studying scintillation light transport in a modeled PET detector module. Section 4.4 discusses how the simulation tool was used in this work, as well as how well it compared to experimental data taken in the same study.

1.8 Directions of this Work

The two fundamental novelties in the detector components developed in this work are: 3 dimensional positioning of events in the detector and using detector components (photodetectors) that can resolve distances on the order of a scattered photon's path length.

These two features lead to two major advances for emission tomography detection:

1) the ability to move beyond previous limitations on how a system must be built; leading to detector configuration versatility, higher sensitivity and sampling; and 2) more information gained per detected photon leading to possible advances in event classification.

These advances then break down the fundamental assumptions about how visualization and quantitation are both measured and realized in PET: detector resolution, sampling, normalization, and event type estimation.

The aim of this work is to begin to utilize these new possibilities to advance each of the key issues in radionuclide emission tomography instrumentation (which are listed in Section 1.4), namely, to improve:

- Detector Resolution and Linearity: identify and characterize improved photodetectors and scintillator geometries (Chapters 3, 4 and 5)
- Sensitivity, Sampling and Image Resolution: design and simulate, using realistic detector models that I developed, improved system configurations (Chapters 6 and 7)
- Image Uniformity and Linearity: the design and implementation of a normalization algorithm to increase image uniformity and linearity (Chapter 8)
- Image Signal to Noise: the design and implementation of novel event classification algorithms for more accurate noise rejection and possibly decreased signal rejection and use of previously discarded information (see Reference [53])

These general ideas can be broken down into the following specific improvements:

1. New concept for scintillation light detection for high resolution PET. A new geometry for scintillation light readout has been investigated and developed and it allow the following features without compromising performance:

- 1 mm intrinsic spatial resolution,
- directly measured depth of interaction,
- high light collection efficiency,
- superior energy resolution ($\sim$12%), and better coincidence time resolution than most APD-based systems ($\sim$2 ns),
- thick detectors for high coincidence detection efficiency without compromising light collection efficiency and other performance parameters,
- and a high photon sensitivty geometrical arrangement of detector modules.

2. Development of a realistic LSO-PSAPD detector system signal model for the following investigated system studies:

- operational system parameter estimation,
- development of positioning techniques for annihilation photons with interactions in multiple photodetectors,

- development of a component-based normalization algorithm for data acquired using detection modules utilizing the new scintillation light readout geometry

Chapter 2

Detectors for PET

2.1 Motivation

The ultimate goal of a positron emission tomography system is to non-invasively detect, visualize and quantify regions of molecular activity within an object of interest. Biologically relevant molecules (see Section 1.2.2) are used as "homing beacons", with up-take preferentially in regions of the studied imaging subject in which a particular biochemical process is taking place. In the case of PET, these homing beacons, or tracers, report their location by emitting positrons. The emitted positrons then undergo annihilation with surrounding electrons, creating annihilation photons. These photons must be accurately detected in order to register the location that the annihilation happened, and thus where the biochemical process is located.

The detectors specific to PET and their physics will be discussed in this chapter.

More focus will be placed on the type of detector studied and utilized in all following chapters of this thesis, i.e. the design comprising scintillation crystal coupled to a photodetector.

2.2 Mechanisms and Characteristics of Detection

2.2.1 Scintillators Coupled to Photodetectors

The most common method of detecting annihilation photons for PET is using a high atomic number, high density material to convert the single 0.511 MeV photons into many photons (∼10,000) with a peak emission spectrum that is a good match to the absorption spectrum of the photodetector [1, 139].

Scintillation

There are many types of materials, natural and engineered, that emit light. Inorganic scintillators are used in high energy photon detection because of their ability to efficiently convert annihilation photons into a shower of photons that are in the high quantum efficiency range of most photo-detectors [91, 105]. The accuracy and efficiency of the photon detection process are dependent on many properties of the material. One such property is the light production process.

Scintillation luminescence in inorganic scintillators occurs along various de-excitation paths, depending on the constituent material of the scintillator. All luminescence is

due to interactions imparting energy into the lattice structure of the material [186].

Photon interactions, or ionization from charged particles, moving through the crystal lattice ionize or excite electrons from the phonon (a quanta of a particular mode of lattice vibration) valence band, creating either unbound electron-hole pairs or pairs that remain bound (excitons). The excitons are then free to move through the lattice until they are trapped and recombine at defects or impurities (intended (dopant) or unintended). Upon recombination, a photon is emitted.

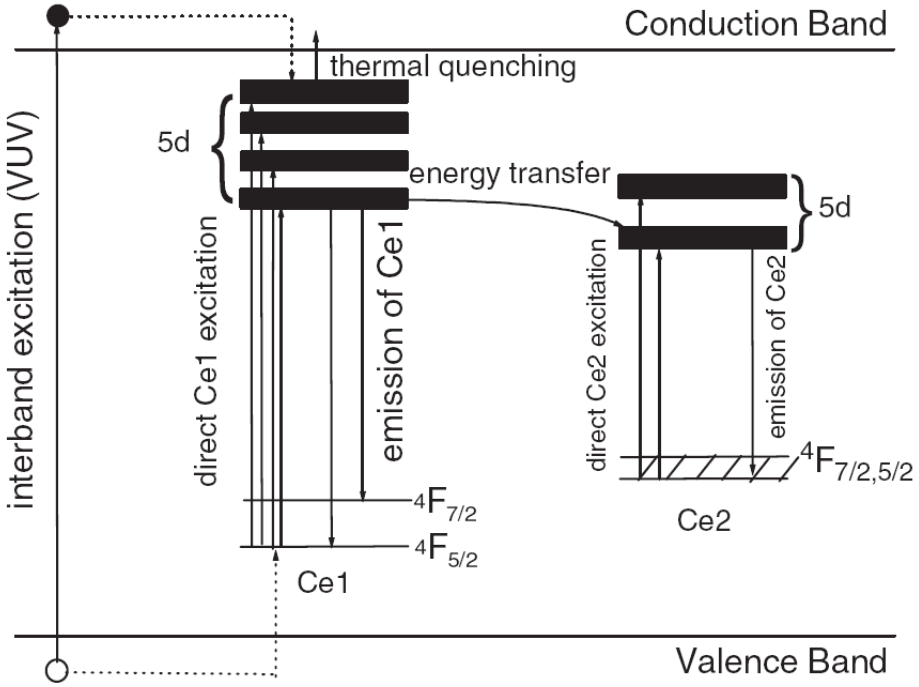

Figure 2.1: An illustration of the band diagram of LSO [103].

Figure 2.1 shows the energy band diagram for one such doped inorganic scin-

tillation crystal, Lutetium Oxyorthosilicate (Lu_2SiO_5 or LSO), doped with Cerium, (LSO:Ce) [103]. LSO is the scintillation crystal studied and utilized throughout Chapters 3-8 of this document. In the case of LSO, the dopant Cerium forms two different structures, labeled Ce1 and Ce2 in the figure, each of which produce slightly different wavelength photons. In fact, there are two such emission bands from the first dopant structure, which peak at 393nm and 422nm. Only one band is emitted from the Ce2 center, which peaks at 462nm. The two observed emission bands from the Ce1 activation center result from the spin-orbit splitting of the two 4f electron energy levels, when de-exciting from the lowest 5d electron energy level.

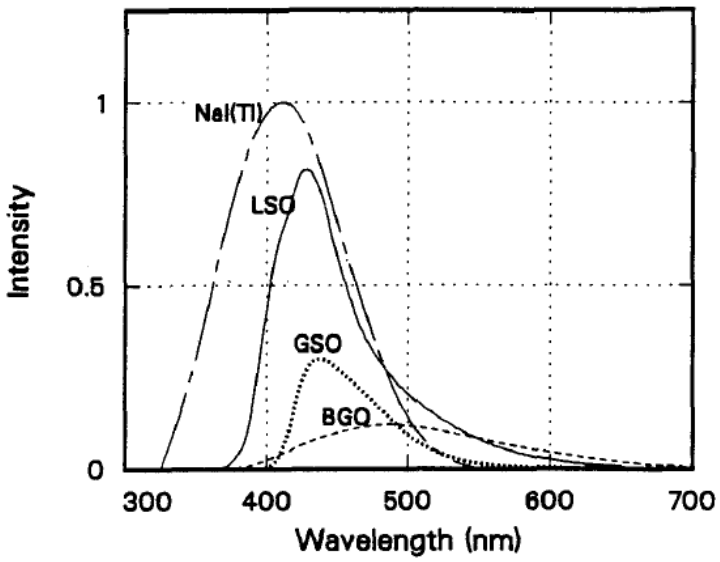

Figure 2.2: An illustration comparing the emission spectra of LSO, BGO, GSO and NaI [111].

The basic processes involved can be broken down into three steps, illustrated in Figure 2.1:

- Excitation - electron-hole pair formation illustrated by the black and white circles on the left of the figure or the upward pointing arrows in the Ce1 and Ce2 centers.

- Thermal relaxation to the bottom of excited state - labeled thermal quenching and by the dotted-lined arrows

- Emission - shown as downward pointing arrows at the two activation centers, Ce1 and Ce2.

The emission bands from the two center types are thermally broadened when measured at room temperature. Figure 2.2 shows the resultant emission spectra of LSO, as well as those of a few other common scintillation crystals [111]. The peak wavelength of LSO is at ∼432nm.

Treating the scintillator as a material whose light output is linearly proportional to the energy of the incident high energy photon, the efficiency of the scintillation response can be written as a product of three efficiencies [80]:

$$\eta = \beta \cdot S \cdot Q \tag{2.1}$$

where β is the conversion efficiency (the ratio of the produced electronhole pairs to the maximum possible), S is the transfer efficiency and Q is the quantum efficiency of luminescence.

Most of the energy introduced into the system by high energy interactions is lost to creating phonons. Because phonons can absorb energies from the exciton before recombination in a continuum of energy ranges, the spectrum of emission from the scintillator is fairly broad in the optical regime.

The number of scintillation photons that are produced per keV of energy deposited into the scintillation crystal during the annihilation photon interaction directly affects the ability of the detector to accurately determine interaction parameters such as energy, position, and time. Following Poisson statistics, when smaller numbers of photons are used for event characteristic estimation, fluctuations due to statistical differences in light production, as well as photon absorption, electronics, etc., produce a larger fractional fluctuation of the interaction parameter. Shot noise, dark noise of the photodetector and the Poisson nature of many of the physical processes in sctillation photon production and detection, also contribute to these fluctuations. Therefore, the larger the number of scintillation photon produced per keV of deposited energy, the smaller the fraction of the signal which will be blurred by statistical fluctuations. The signal-to-noise ratio can be roughly estimated using Poisson statistical arguments:

$$SNR[\%] \sim 100\% \cdot \frac{\sqrt{N}}{N} \tag{2.2}$$

where N is the number of scintillation photons produced

Other factors affect the amount of scintillation light that makes it to the photo-

detector surface. Optical transport properties of the crystal geometry, coupling to the photodetector and index of refraction all play a significant part in the average fraction of produced photons that are collected.

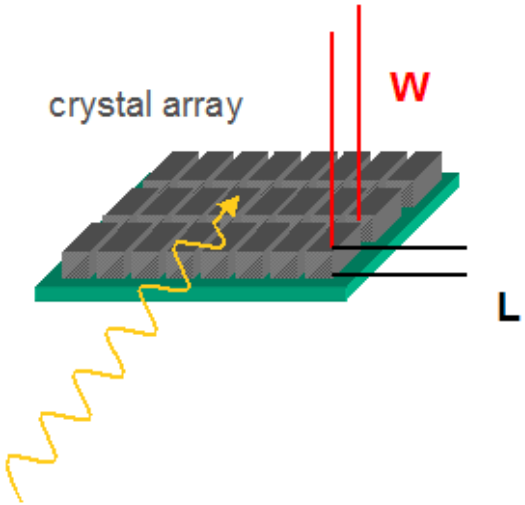

Figure 2.3: An illustration of the nomenclature of crystal coupling aspect ratio.

The aspect ratio of the crystal coupling geometry can greatly affect light collection efficiency. Using the terms shown in Figure 2.3, where L is the height of the crystal in the direction normal to the face of the photodetector and W is the longest width of the crystal parallel to the face of the photodetector, aspect ratio (A) is defined as [95]:

$$A = \frac{W}{L} \tag{2.3}$$

As A increases, the fraction of light produced in the scintillation process increases.

This increase is mainly due to a reduction in the number of surfaces each scintillation photon intercepts on its path to the photodetector, and a reduction in the amount of crystal the scintillation photons must traverse before reaching the photodetector. Each time a scintillation photon impinges a crystal surface, based on the reflection efficiency; i.e. the materials involved, their reflection coefficient, and their index of refraction difference; there is a chance of photon loss.

In general, the reflectance of the material coating the edges of the crystals not coupled to the photodetector, and the index of refraction differences between the crystal and any material with which it is in contact, significantly impact the fraction of produced scintillation light that is collected by the photodetector. Properties of the material coupling each directly read-out crystal and the detection surface of the photodetector also impact light collection efficiency. Reflection and absorption must be kept to a minimum at this intersection, so coupling material properties, such as index of refraction and wavelength dependent opacity, become paramount coupling material features [30].

The initial speed and duration of the scintillation process also affects the ability of the detection system to accurately report the number of photons produced by the scintillation crystal, or ultimately, the energy deposited in the annihilation photon interaction. Figure 2.4 shows the light pulse of LSO, decaying over time [105]. The characteristic decay time of LSO is $\sim$47 ns. The deposited energy in the crystal is best estimated from the integral of the photons over the entire scintillation photon

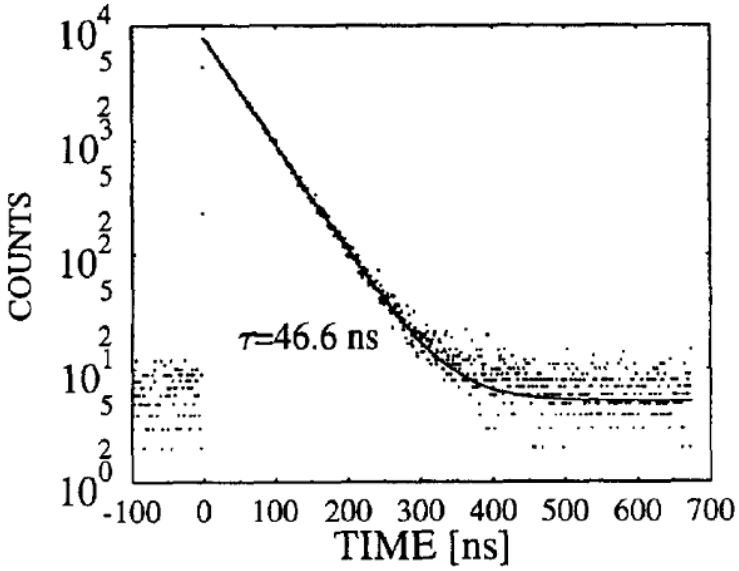

Figure 2.4: The spectrum of the light pulse decay in time for LSO [105].

production process. This integration is performed by the pre-amplifier. The zero-crossing of the rising edge slope of the pre-amplified scintillation pulse determines the time that the interaction occurs.

Therefore, properties such as scintillation crystal photon production rates, optical coupling materials and methods, and (as will be discussed in the next section) photodetector gain and quantum efficiency, all play a significant role in the accuracy of interaction measurement.

Photodetection

The device component in a detector module is a photodetector, which is coupled to the scintillation crystal. The scintillator's job is to provide a material in which

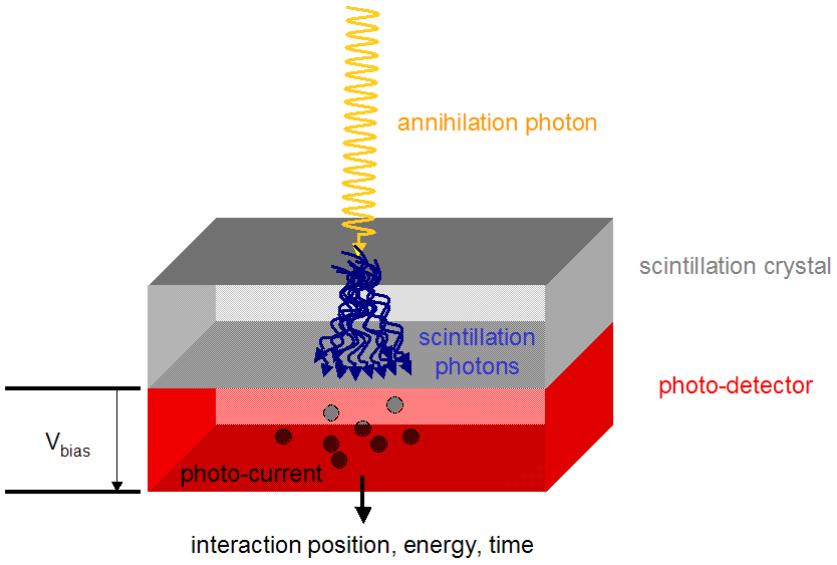

Figure 2.5: An overview of the detection process in the scintillator-photodetector module.

the annihilation photon is to interact and, in turn, produce a spray of near-visible or visible wavelength light. The photodetector collects the scintillation photons that reach the detector surface and coverts them via electron excitation (electron-hole pair liberation into the conduction and valence bands, respectively) into an electrical signal, to be processed and recorded. An illustration of this setup can be seen in Figure 2.5.

The first parameter specific to the photodetector in this design is the efficiency with which the photodetector creates an electron for every scintillation photon that arrives at the photodetector detection surface. This efficiency is called quantum efficiency (QE), and is generally photon wavelength dependent. Figure 2.6 shows the wavelength dependent QE for an avalanche photodiode [158]. Generally, the QE

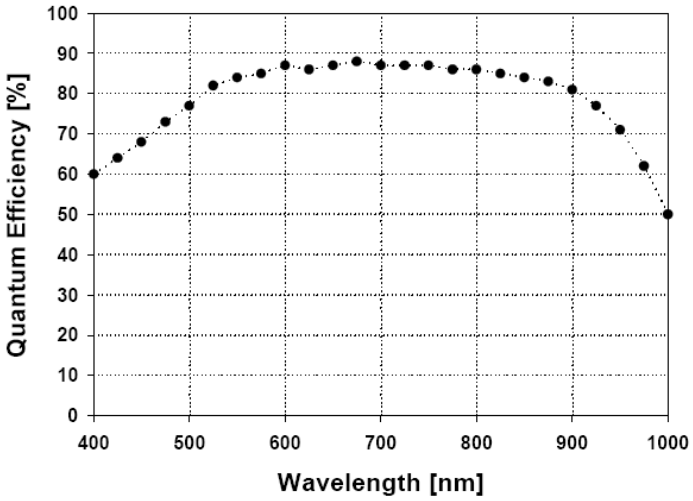

Figure 2.6: A graph of the QE of an APD over a range of photon wavelengths near the visible band [158].

peaks in the visible wavelength region for devices that are coupled to scintillation materials and falls off quickly. The peak QE for photodetection devices can vary greatly, as will be shown for the two types of photodetectors mentioned in Section 2.3.

A feature of most photodetectors is a mechanism to amplify photocurrent produced at the detection surface. The factor used to quantify this amplification is a multiplicative factor, or gain. The gain of photodetection also varies widely from device to device, and can be realized in various ways, nearly all involving high voltage applied across the photodetector ($\geq$1000 V). The gain of the device should not be dependent on the number of photons entering the device in order to preserve the linearity between the output current of the device and annihilation photon interaction

energy.

Electronics process the signals from the photodetectors to extract position, energy and timing information of the interaction. These processes will be described in later chapters in which their measurement and evaluatation will be presented.

2.2.2 Direct Annihilation Photon Photodetectors

All of the studies described in this thesis will have detectors configured in the manner described in the previous two sections pertaining to scintillators and photodetectors. For completeness, another method of detecting annihilation photons is mentioned here.

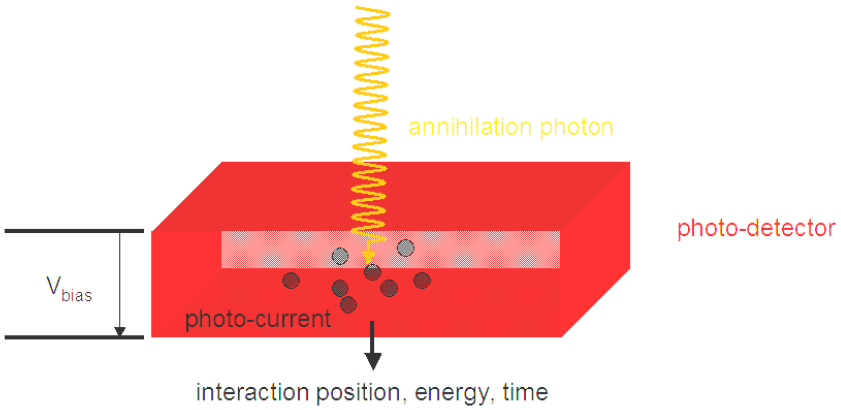

Figure 2.7: An overview of the detection process in the photodetector-only module design.

Instead of making detection a two-step process of scintillation light creation followed by collection and conversion using a photodetector, some devices are adequately sensitive (high density, high atomic number) to be able to directly detect annihilation

photon interactions. One such material is a semiconductor composed of cadmium zinc telluride (CdZnTe or CZT). The device operation of CZT is very similar to the silicon based photodiode described above, but has relatively low leakage current (dark noise) [123].

Because the "middle man" is taken out, many of the loss processes due to photon transport and detector QE no longer apply. Position and energy resolution are very accurately determined in this detection module design. Position accuracy across the face of the detector is essentially customizable down to hundreds of microns, if desired, limited mainly by estimation techniques of charge sharing between read-out anodes. Energy is determined by the sum of the charges read-out, and due to the low leakage current, can be on the order of 1-3% of 511 keV [181]. Interaction time determination, on the other hand, can be more complex to estimate in these devices.

Due to the necessity of the annihilation photons to directly interact in the photodetector, the thickness of the device across which the bias voltage is applied must either be relatively thick, or the system design would require many more thinner detectors and associated read-out channels. However, in the case of CZT, the time of an interaction is depth-dependent. Due to these effects, coincidence time resolutions for CZT have been measured to be $\sim$10 ns FWHM [104,125]. Depth of the interaction in the photodetector must be estimated to increase the accuracy of time of interaction determination. This method relies on knowing the mobility of the charge carriers throughout the device, and is in general, device dependent [104].

2.3 Devices

The photomultiplier tube (PMT) [8, 89, 100, 117] and its position-sensitive variations [19, 150, 151, 162, 190] are still the dominant photodetection devices in the scintillator-photodetector system designs, both commercially and in research settings. Avalanche photodiode (APD) use [158, 160] has recently increased in system designs, with its position-sensitive (PSAPD) variant being actively researched for next generation systems [13, 42, 161, 192]. Both PMTs and PSAPDs will be discussed in the next sections.

2.3.1 Position Sensitive Avalanche Photodiodes

Avalanche photodiodes are semiconductors that can be constructed of various materials such as Indium Gallium Arsenide (InGaAs), Germanium (Ge) and Silicon (Si). The silicon design will be the focus of this discussion. As mentioned in Section 2.3, APDs collect the scintillation light that reaches the detection surface of the device.

Figure 2.8 shows the different regions of the APD that perform the collection, gain, and signal transmission tasks of the device. The p and n regions indicate the portions of the device that are doped (added impurities) with materials producing p- and n-type semiconductors, resulting in relatively more positive (holes) and negative (electrons) charge carrier sections of the APD device, respectively. Essentially, an

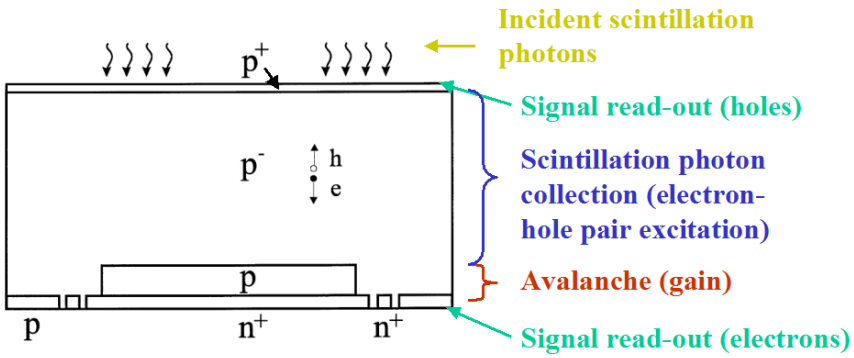

Figure 2.8: An illustration of the doping regions of the APD [136].

n-type (p-type) semiconductor has extra electron (hole) energy levels. Having these added energy levels allows for easier excitation of electrons from the newly created energy levels (in the n-type case) to the conduction band, or from the valence band to the new energy levels (in the p-type case), increasing the number of charge carriers (holes in p-type and electrons in n-type) in the doped region, thereby increasing conduction.

Electron-hole pairs must be produced in the collection region (drift region) of the device, not in the avalanche region (gain or space charge region), or interaction-depth-dependent gain will occur. Avoidance of this nonlinearity is a reason the collection region is constructed to be a large portion of the device. In contrast, the PSAPD device used in this thesis requires only ∼100 microns over which its 1000x gain occurs. A very large bias voltage is applied to the device in order to create this amplification, which accelerates the charge carriers so that they impact and liberate further electron-

hole pairs into the conduction and valence bands, respectively.

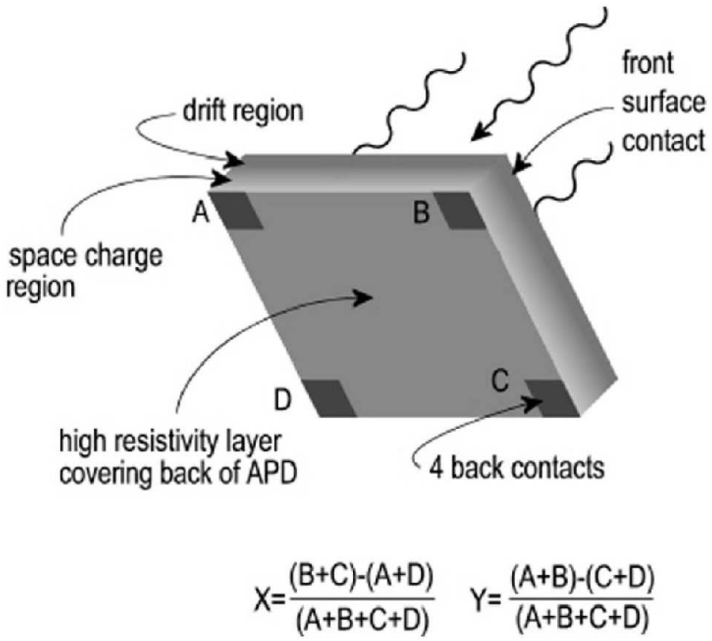

Figure 2.9: Illustration of the four corner positioning anodes (A,B,C and D) and positioning scheme.

The essential difference between an APD and the PSAPDs utilized in this thesis is a resistive coating applied across the entire electron collection side (the bottom anode in Figure 2.8), which shares collected charge between contacts positioned at the four corners of the device. Figure 2.9 shows an illustration of the 5 total signal read-out nodes of the PSAPD, the four positioning anodes and the common (top) anode. Positioning of created charge carriers (scintillation light production and ultimately annihilation photon interaction location) can be achieved using the equations shown in Figure 2.9.

PSAPDs are very compact compared to vacuum tube designs because of the short region (∼100 microns) over which gain is achieved. This compactness will become evident when discussing the PMT avalanche method in the next section.

2.3.2 Photomultiplier Tubes

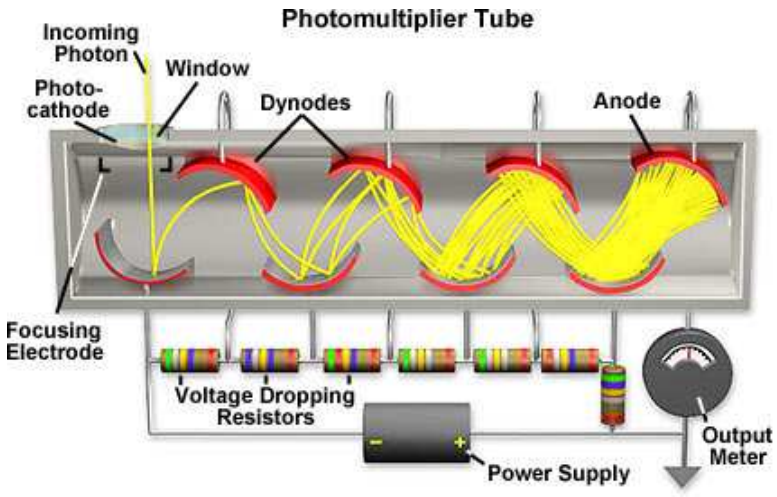

Figure 2.10: An illustration of the gain process of the photomultiplier tube [1].

PMTs are very robust, well-characterized, high gain, photodetector devices. Gain is usually on the order of 10^6 (as opposed to the $\sim 10^3$ gain factor of PSAPDs) and is achieved using high bias voltage just as it is with PSAPDs.

Figure 2.10 shows the method vacuum technology uses to achieve this high gain. Impinging scintillation light creates an electron-hole pair with a wavelength dependent quantum efficiency. The electron-hole pair is accelerated to the first dynode by an applied voltage with respect to the photocathode, and directed by the focusing

(steering) electrode. Voltages are increased at each successive dynode in order to accelerate the electron to the subsequent dynode. Because the electron is accelerated, as it hits the dynode, ∼6 further electron-hole pairs are liberated [31]. This liberation process results in 7^7 or $\sim 10^6$ electrons leaving the anode.

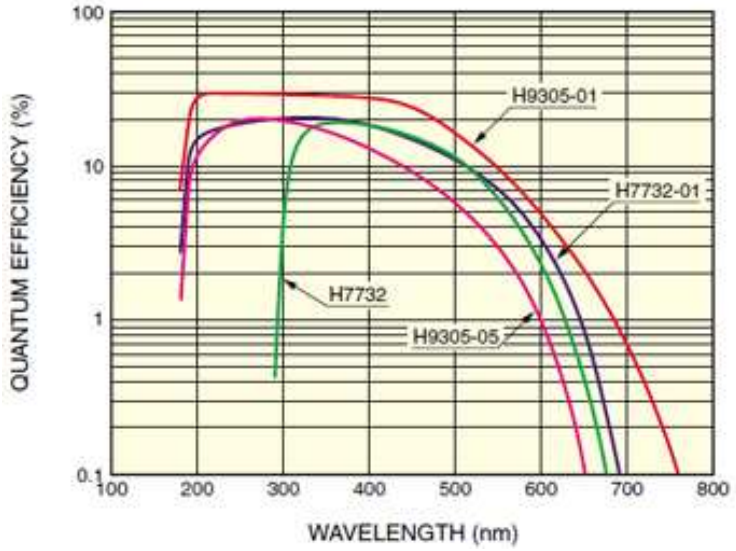

Figure 2.11: Quantum efficiency versus wavelength for various PMTs sold by Hamamatsu.

The quantum efficiency with which the PMT creates an electron-hole pair for various models sold by Hamamatsu can be seen in Figure 2.11. As with PSAPD quantum efficiency, the PMT QE is also wavelength dependent, but peaks around ∼20%, as opposed to the APD's ∼85% peak QE. This reduction in peak efficiency potentially increases the noise in interaction characteristics such as energy determination. Although the signal is higher due to the superior gain, the lower QE increases the statistical noise in the initial scintillation signal. Therefore, using the same scin-

tillation crystal setup, PMTs generally have slightly poorer energy resolution. The gain process of the PMT is, however, simpler and produces less variation in the time that it takes to complete the signal production. The simpler gain process of the PMT is due to the fact that charge carriers travel together through a large potential in vacuum as opposed to through a large potential within a semi-conductor material, as they do in avalanche photodiodes. Therefore PMTs have superior time resolution (as low as hundreds of picoseconds).

2.4 Developed Small Animal PET Detection Systems

Table 2.1 shows a list of small animal PET detection systems for comparison. Many in the list are commercially available, some are systems that are still under development.

Table 2.1: A list of the properties of some small animal PET detection systems.

System Name	Scintillation Material	Photo-Detector	Volume Resolution [μL]	Sensitivity [%]	Reference
MicroPET Focus	LSO	PSPMT	2.5	3.4	[87]
MicroPET II	LSO	PSPMT	0.8	3.3	[170]
RatCAP	LSO	PMT	3.4	0.7	[188]
ClearPET	LYSO/LuYAP	PSPMT	2.5	4	[3]
ATLAS	LGSO/GSO	PSPMT	5.8	1.8	[156]
quad-HIDAC	LSO	PSPMT	0.8	3.3	[113]
Explore Vista	LYSO/GSO	PMT	4	3.3	[2]
Park detector	BGO/Si	PSPMT	0.9	0.0014	[134]
A-PET	GSO/LYSO	PMT	8.7	3.6	[168]
LabPET	LYSO/LGSO	APD	1.8	n/a	[174]

2.5 Conclusion

There are various materials and devices available for consideration when constructing a detection system. Since the advantages of the various technologies reside in different regions of the cost-resolution-compactness-robustness space which designers must navigate, choosing a particular design must therefore be dependent on the utility for which it is built to provide. Table 2.2 briefly summerizes some properties of PET detection schemes and components. The relative advantages of PSAPDs over PMTs and PSPMTs for the application studied in this thesis will be discussed further in Chapter 3, when system design considerations are discussed.

Table 2.2: A list of the properties of some PET detection schemes and components. S/P: scintillator/photodetector, DD: direct detection

Detection Scheme	Components	Degree of Characterization	Cost/Detection Area	Position Resolution [mm]	Energy Resolution [% 511 keV]	Time Resolution [ns]
S/P	LSO/PMT	well established	cheap	>2	∼20	<1
S/P	LSO/PSPMT	established	fairly cheap	>1	∼20	<1
S/P	LSO/APD	relatively novel	fairly expensive	∼1	∼11	∼2
S/P	LSO/PSAPD	novel	expensive	<1	∼11	∼2
DD	CZT	novel	fairly expensive	<1	<3	∼8

Chapter 3

Position Sensitive Avalanche Photodiode Characterization

3.1 Introduction

Chapter 2 discussed the role that materials and devices play in general in positron emission tomography (PET) detection. The detection design used in all studies throughout the rest of this document is the scintillation crystal coupled to a photodetector, in particular, an inorganic scintillator lutetuim oxyorthosilicate (LSO) coupled to a position-sensitive avalanche photodiode (PSAPD). The characterization testing of these two components are broken down into separate chapters: the PSAPD as a photo-detection device is studied in this chapter, and the LSO design is detailed in Chapter 4. The final LSO-PSAPD module design is studied in a further chapter,

Chapter 5.

Although this chapter will focus on device testing of PSAPDs, a brief discussion on the novel detector orientation in which the LSO-PSAPD modules will be utilized in further chapters is necessary to understand the types of devices, and iterations thereof that were characterized.

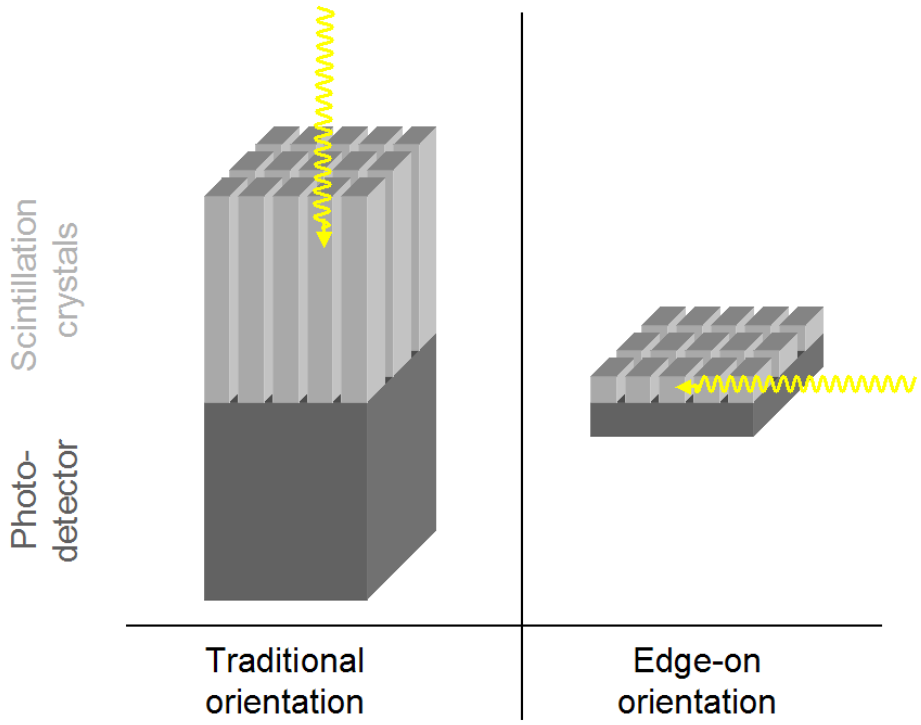

Figure 3.1: An illustration of a traditional and the novel (edge-on) detector orientation. The light grey parallelepipeds represent the scintillation crystal, while the dark grey the photodetector in both designs. The yellow oscillating arrows represent annihilation photons entering the detectors from a likely direction.

Figure 3.1 shows, on the left, a traditional orientation of crystal and photodetector with respect to incoming annihilation photons. In this design, long segmented scintillation crystals are read out on their ends so that annihilation photons directed at

the detection system traverse long distances of crystal. Large volumes of crystal give the annihilation photons a chance to interact before passing through the system undetected. Interactions must occur in the scintillation crystal in these designs, because the photodetector itself has a very low ($\ll 1\%$) chance of interacting in the detector with energy in the desired energy window. The small cross-sectional area coupled to the photodetector gives the crystals an aspect ratio that does not promote optimal light output [95,98]. This coupling geometry results in a compromise between system resolution, light output (effectively energy resolution) and sensitivity [28,74,76,139]. Because crystal interaction position detection, perpendicular to the photodetection surface, is in general not possible[1], this crystal coupling method also results in depth of interaction (DOI) blur. DOI blur has traditionally resulted in PET systems with non-uniform reconstructed spatial resolution when traversing the image in the radial direction away from the center of the system.

Due to the size of the photodetectors used in standard systems, other orientations of detection modules are not practical. In any other orientation, large dead volumes would result where annihilation photons would encounter no scintillation crystal, instead only photodetector material. An advantage of making the photodetector itself very small, on the order of hundreds of microns thick, is that it is feasible to create a multitude of possible detector system orientations and designs. Figure 3.1

[1]Some detector designs include two photodetectors at either end of the long crystals and use a ratio approach to estimate the DOI location [22,45,93]. Other researchers have developed maximum likelihood estimation techniques based on light distribution in the photodetector for estimating DOI location [102,115].

shows on the right side the module orientation that will be featured in this and all subsequent chapters. It will be referred to as the "edge-on" orientation.

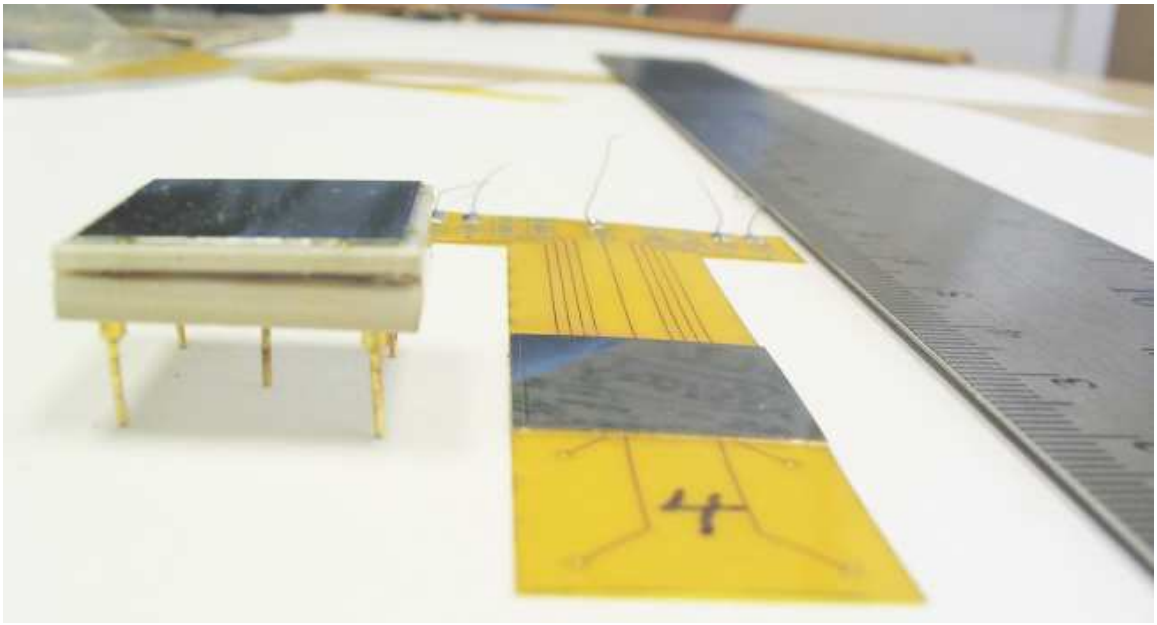

Figure 3.2: A picture of the ceramic device (left) and the novel design (right) with only one PSAPD (black) packaged on the signal readout cable (yellow).

Figure 3.2, left, shows a commercially available PSAPD with ceramic substrate. This device is already much more compact than photomultiplier tubes (PMTs). For example, the dimensions of the position sensitive PMT shown in Figure 3.3 are 52 x 52 x 30 mm^3, with active area 49 x 49 mm^2, and an anode pitch of 6 mm. On the other hand the dimensions of the PSAPD shown on the right of Figure 3.2 are 11 x 11 x 0.4 mm^3, with active area 8 x 8 mm^2, and nearly continuous positioning.

The ceramic substrate device was used as the "gold standard" with which to compare the novel devices. The device on the right of the picture in Figure 3.2 is

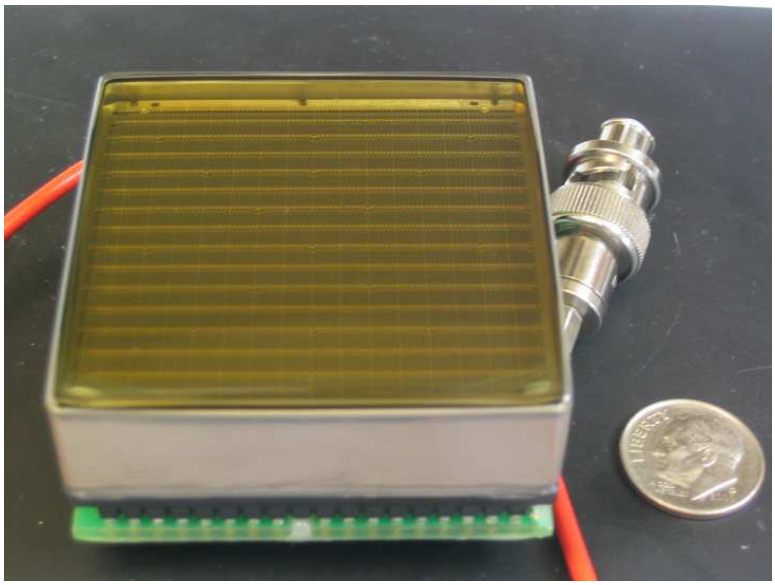

Figure 3.3: A picture of a compact position-sensitive photomultiplier tube.

one of the novel detector designs. A ruler is also shown in the picture for reference. The novel device and its packaging was $\sim 400\mu$m thick. The compact size of the photodetector lended itself to being oriented as shown on the right of Figure 3.1, with small segmented crystals coupled to the photodetector in a high light output configuration. Annihilation photons can then traverse the scintillation crystal parallel to the face of the photodetector. The novel device design on the right of Figure 3.2 had only one PSAPD device connected for testing the capabilities of a single device's operation in the new packaging. Another device can be added to the read-out cable where the number "4" is marked on the cable. Two PSAPDs, each with a scintillation crystal array coupled to them, provided nearly 2 cm of crystal in which the annihilation photon can interact. Two centimeters depth of scintillation crystal

is on par with other small animal PET systems.

Ceramic packaged PSAPDs were first tested to understand the function of the photodetector devices. The envisioned final module design was broken down into design steps, with each new prototype having increasing complexity. Single PSAPDs were tested when packaged with the Kapton flex circuit for signal readout to ensure that the new packaging did not affect device performance. A new PSAPD design was offered by the manufacturer with increased active area, therefore these new PSAPD designs were tested in a single packaging format to compare with previous PSAPD designs. Then two modules were packaged on Kapton flex readout circuits and tested in a similar manner as previous designs as well as for any kind of device cross-talk between both chips on a single readout circuit. Finally, 40 PSAPDs were manufactured, packaged into 20 dual-chip detectors, and tested with a single LSO scintillation crystal array to document inter-detector variability (keeping the crystal array the same). These 5 design steps and the characterization thereof is the subject of this chapter.

Of the performance characteristics mentioned in Section 1.4, the ones that can be tested at a device level are positioning ability (identification, resolution, linearity), as well as energy and coincidence time resolution. These performance characteristics will be explored for all devices tested in this chapter.

3.2 Methods

3.2.1 Crystal Orientation

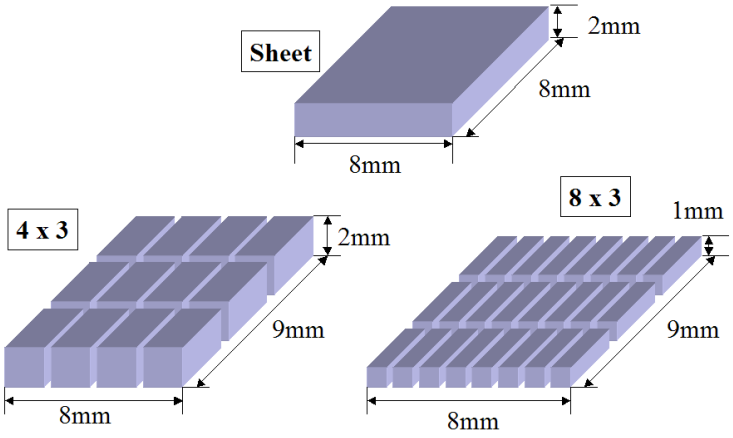

Figure 3.4: 3D illustration of the sizes and layout of the three arrays used in the ceramic PSAPD characterization experiments.

Three crystal array designs were used throughout this chapter, they are illustrated in Figure 3.4. The first was an 8 mm x 8 mm x 2 mm single crystal, the second was a 4 x 3 array made of segmented 2 mm x 2 mm x 3 mm crystals, and the third was a 8 x 3 array comprising 1 mm x 1 mm x 3 mm crystals. To be able to compare the photodetector packaging designs, the same crystals were always used to make up these three arrays. The arrays were coupled to the center of the active area of each device, laying so that their long dimension was optically coupled to the photodetector. Figure 3.5a shows the ceramic PSAPD with the sheet crystal (clear) lying coupling-side-up, wrapped in Teflon (white, opaque) reflector. Figure 3.5b shows the

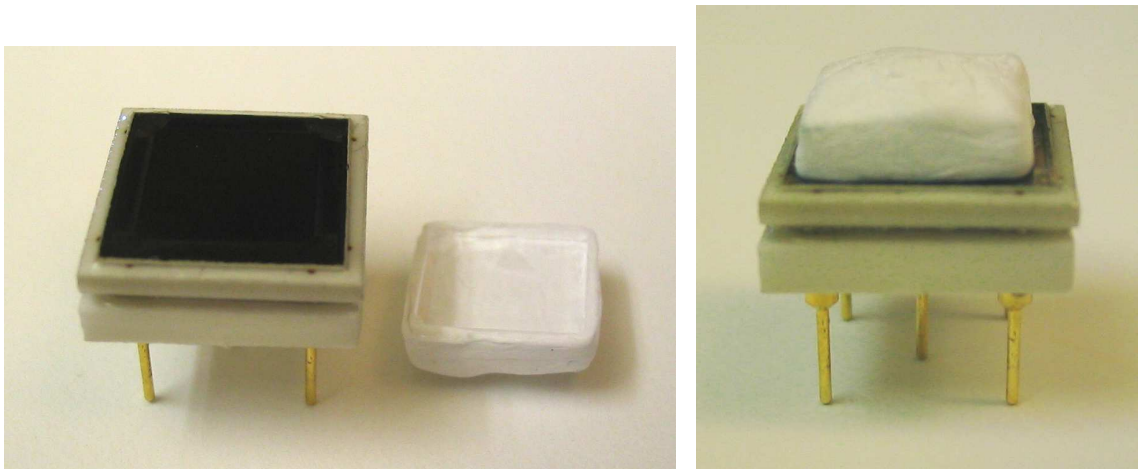

(a) (b)

Figure 3.5: Photographs of the ceramic substrate PSAPD and sheet crystal LSO wrapped in Teflon reflector. The sheet crystal is shown: a) laying on its side wrapped in Teflon reflector to show the crystal inside, b) the side facing up in a) is lying on the active area of the PSAPD.

crystal coupled to the PSAPD, with only the Teflon coating visible.

3.2.2 Four Corner Positioning Schemes

In the devices under study four corner contacts are placed on the backside which is covered by a high resistivity layer. The position of a light flash on the PSAPD front side is calculated using the four corner signals in an Anger-type logic. The energy and timing of each signal may be extracted from the common front surface contact or by summing the four back surface signals (see Figure 3.6).

To calculate the position of the center of mass of the scintillation photons hitting the surface of the PSAPD, the four corner channels shown in Fig. 3.7 were used in

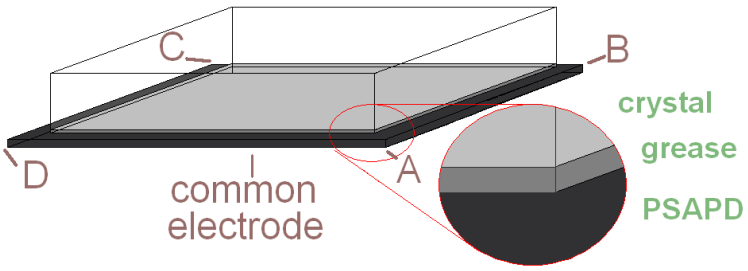

Figure 3.6: Illustration of the optical coupling of the inorganic scintillator (LSO) to the PSAPD with grease. The LSO is then wrapped with Teflon as a reflector material (not shown).

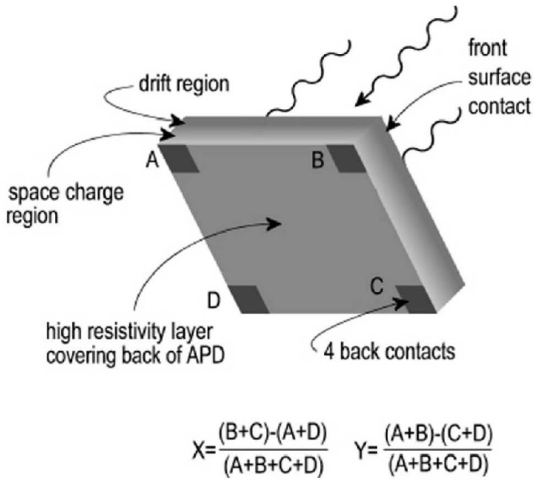

Figure 3.7: An illustration of the four corner and one common contacts of the PSAPD.

the following standard Anger-type logic manner [159]:

$$X = \frac{(A+B)-(C+D)}{A+B+C+D} \tag{3.1}$$

$$Y = \frac{(A+D)-(B+C)}{A+B+C+D} \tag{3.2}$$

where A, B, C, and D are the digitized four corner anode signals of the PSAPD; and X and Y are the coordinates of the scintillation light centroid on the PSAPD surface.

Energy can be obtained from the measurement of all five channels in two ways, either by directly measuring it from the common, or by summing the four corner channels (A,B,C and D). Using the Anger-type logic positioning scheme, flood images always showed significant "pincushion"-like distortion due to the non-linearity of the resistive sheet mediated charge sharing of the device (see Section 3.2.3). In other words, an linear change in interaction position along the face of the detector does not in general translate to a linear change in position the Cartesian map due to non-linear charge sharing in the resistive sheet connecting the four corner electrodes when using the Anger-type logic positioning method.

The rotated coordinate positioning method uses an algorithm developed by Zhang, et al. [193] to reduce the effect of non-linear positioning of the PSAPD. The position is calculated from the four digitized voltages using the data from only the opposing corner anodes of the PSAPD (Figure 3.6) by using the following equations:

$$x' = \frac{B - D}{B + D} \tag{3.3}$$

$$y' = \frac{C - A}{C + A} \tag{3.4}$$

$$x = y' \cdot \cos(\pi/4) - x' \cdot \sin(\pi/4) \tag{3.5}$$

$$y = x' \cdot \cos(\pi/4) + y' \cdot \sin(\pi/4) \tag{3.6}$$

This rotated coordinate positioning method utilizes the four corner electrode signals to provide a more linear position map near the center of the device,. However,

this method over-compensates for crystal configurations that produce a high dynamic range of detected positions, creating a "barrel"-like effect near the edges.

3.2.3 Resistive Coupling Between Corner Anodes

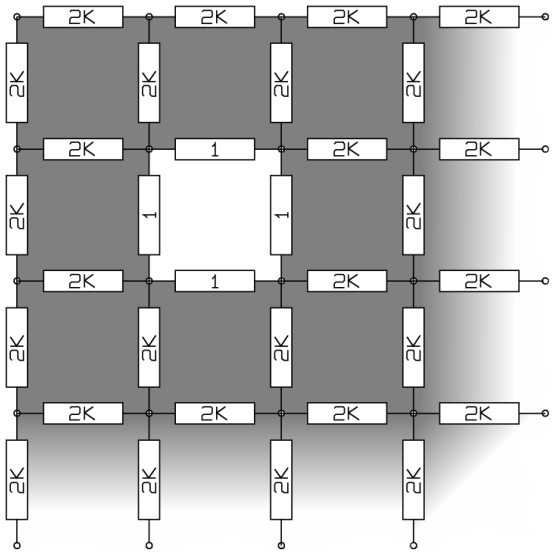

Figure 3.8: An illustration of a model for the resistive positioning sheet on the PSAPDs produced by Radiation Monitoring Devices, Inc..

The four corner anodes are coupled on the back of the PSAPD by a resistive sheet. This resistive sheet distributes the amplified charge gathered on the anode of the device between the four corners. This distribution provides the means for determining the (x,y) location of the charge deposition (and hence annihilation photon interaction) within the device. Models for the resistive sheet have been obtained, a few of which can be found in References [43, 128]. One such method is illustrated in Figure 3.8, where the sheet is modeled as small resistors coupled in a finite element

mesh.

3.2.4 Board Layout

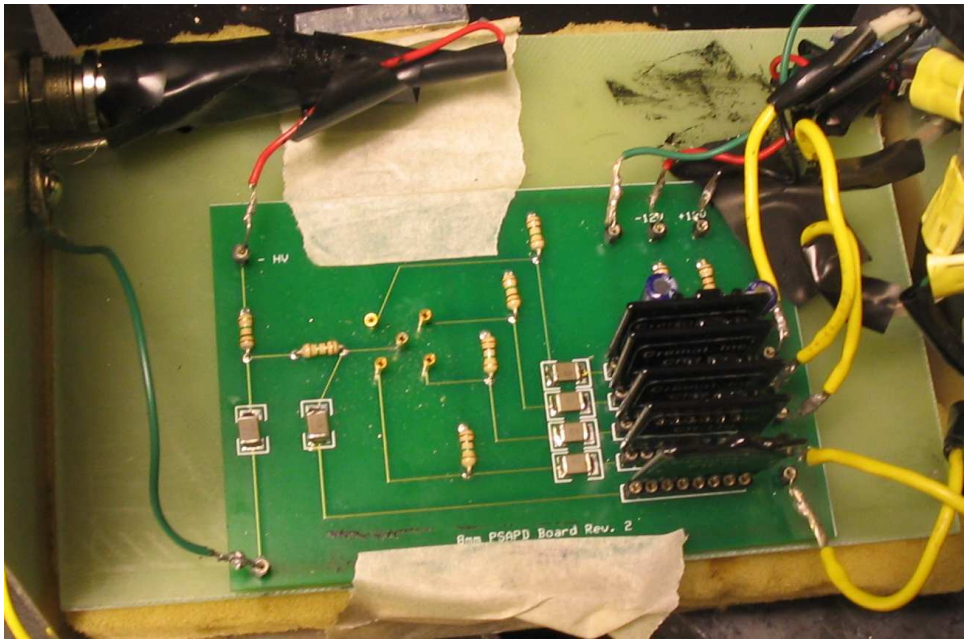

Figure 3.9: A picture of the acquisition board with which all of the single chip designs were tested.

All single chip PSAPD acquisition was performed using the acquisition board shown in Figure 3.9. This board provided the connection from the Kapton flex-circuit of the PSAPD to the pre-amplifiers (Cremat CR-110 - see the preamplifier discussion below). Capacitors on the board provided a capacitive coupling from the PSAPD device to the pre-amps. Bias voltage to the PSAPDs as well as supply voltage to the pre-amplifiers was also input to this board. The board output five pre-ampflied signals: the four corner channels and the single common channel.

This was a prototyping acquisition board and was not sufficient to test the dual-chip PSAPDs. A second prototyping board was built, using the same electronics and setup, but accommodating up to ten output signals, five from each chip, to be acquired at the same time. This second board provided the same bias voltage to both PSAPDs on a single flex, which prevented current arcing between devices under normal operation.

Preamplifiers

The preamplifiers used in all measurements performed are the CR-110 charge-sensitive pre-amps sold by Cremat (see Figure 3.10), which have the characteristics mentioned in Table 3.1.

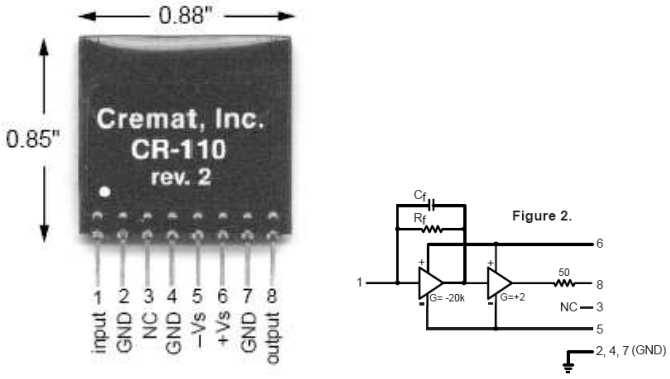

(a) (b)

Figure 3.10: Left: an image of the charge-sensitive pre-amplifier used in all experimental setups. Right: the equivalent circuit of the pre-amplifier.

A picture of the Cremat CR-110 preamplifier used is shown on the left hand

Table 3.1: Characteristics of the CR-110 charge-sensitive pre-amplifiers.

Description	Value	Units
Equivalent Noise Charge RMS	200	electrons
	0.03	fC
Gain	1.4	Volts/pC
Rise Time	7	ns
Decay Time Constant	140	μs

side of figure 3.10 with the device's pinout labeled. An example output pulse of the charge-sensitive preamp can be seen in the right hand side of Figure 3.11. The shape of the pulse determines how it should be proccessed to record the characteristics of an event: namely, how large is the pulse and at what time did it occur. After the initial rise time, the pre-amp acts like a discharging capacitor where the integral of the area under the pulse curve is equal to the total number of electrons from the photodetector, multiplied by the gain of the pre-amp. The number of electrons from the photodetector is proportional to the energy deposited in the detector by the annihilation photon interactions.

The left hand side of Figure 3.11 shows the slope of the rise of the signal. Using the relationship described by Cremat, the 71 pF capacitance of the PSAPD will lengthen this time to about 36 ns [37].

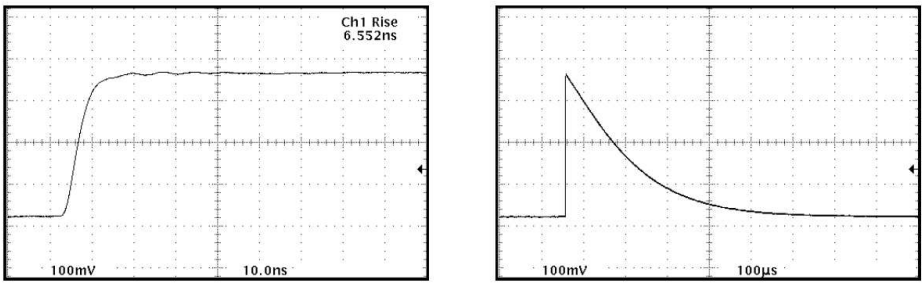

Figure 3.11: Illustration of the pulse shape of the CR-110 preamplifier.

3.2.5 Flood Measurement

When flood irradiated, photon sources were placed sufficiently far (≫5 widths of the active area) away from the center of the photodetector to achieve incoming photon directions that were normal to the face of the photodetector. The four corner anodes were then read to determine positioning and energy information. The fifth electrode, or the common electrode, was not used in flood measurements.

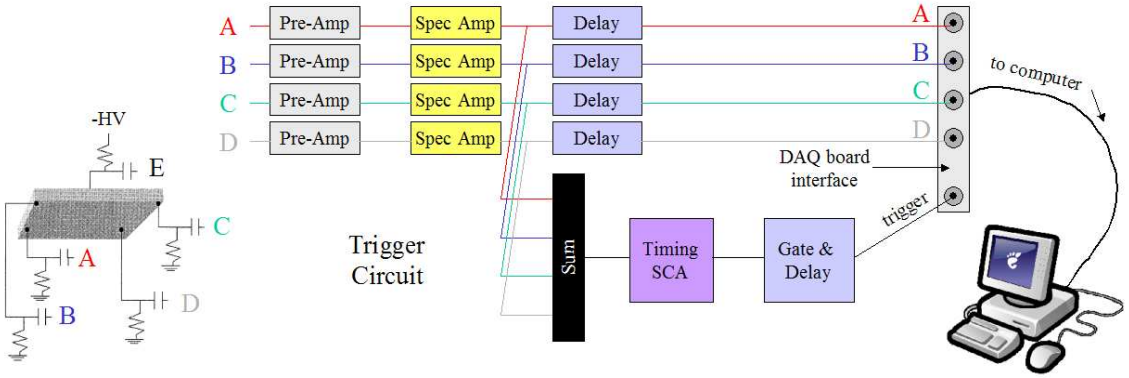

Figure 3.12: An illustration of the shaping electronics used from PSAPD output to acquisition data in the flood measurements.

Figure 3.12 shows all of the shaping electronics used to acquire flood measure-

ments. A picture of the setup can be seen in Figure 3.13.

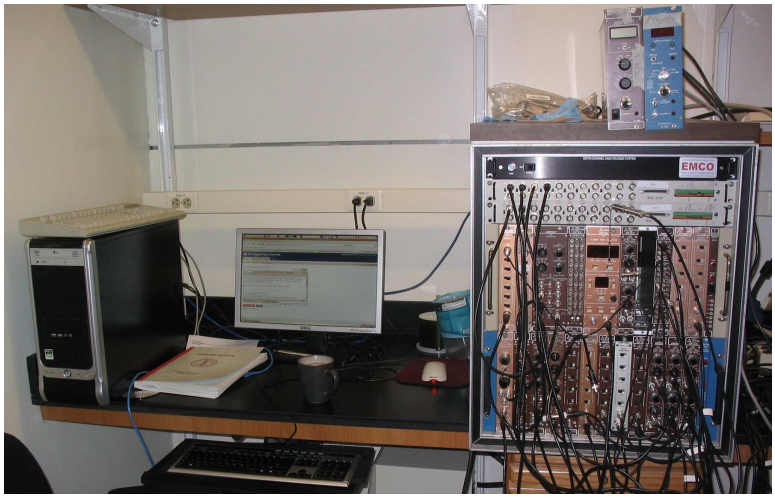

Figure 3.13: A picture of the NIM acquisition electronics used for the flood measurements.

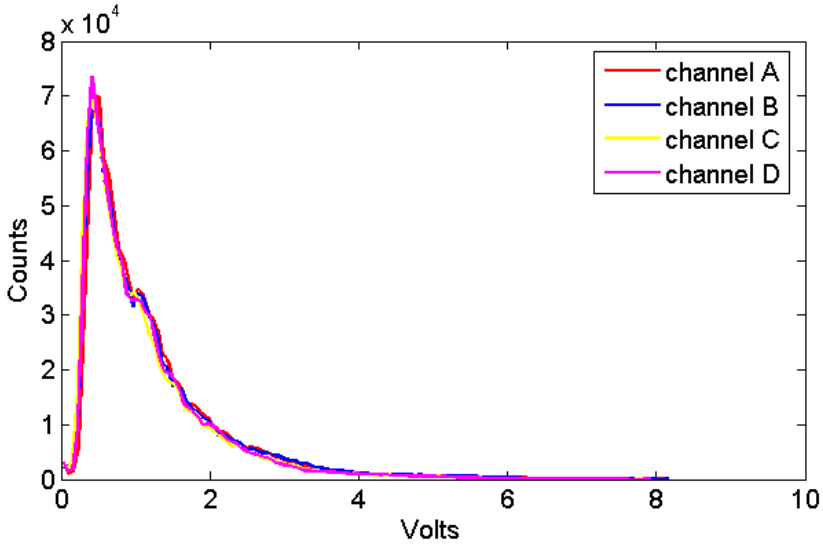

Figure 3.14: An illustration of gain balanced channels.

During each acquisition, the relative gain from each collected corner anode signals was balanced by modifying the gain of the spectrum amplifier (Spec Amp) so that the

histograms of all four corner channels overlapped (see Figure 3.14). This was done so that, for each event, each channel behaved in a similar manner when recording a given amount of charge. Signals were then delayed with respect to the trigger so that each signal would be acquired at the peak of the signal pulse. The trigger for acquisition was formed using a timing single channel analyzer (timing SCA) and a gate and delay generator (gate & delay). The timing SCA's input was the sum of the four channels (essentially an energy signal) and produced a constant height pulse that signified a signal with sufficient amplitude arrived at the timing SCA. The gate and delay generator took the output signal from the timing SCA and produced a TTL signal. The gate and delay also had a controllable delay which could be tuned to line up with the processed four corner anode signals.

During flood measurements, the processed four corner anode signals from a single PSAPD device were acquired for positioning and energy information of the recorded interactions.

3.2.6 Energy Resolution Determination

Energy resolution was estimated from the raw energy spectra by taking the physics of annihilation photon interactions into account. The main sources of energy deposition in the crystal are from Compton scattering and the photoelectric effect. The geometry that was used for most of the energy spectra acquisition was a flood irradi-

ation: bringing the source to a distance at which the entire face of the crystal would be irradiated uniformly. This would give the high energy photons an equal chance of having a first interaction anywhere along the face of the PSAPD. The source that was used in nearly all experiments was a 10 μCi, 500 μm diameter, spherically shaped source of ^{22}Na, which has two methods of decay: beta decay (branching ratio: 90.6%) and electron capture (branching ratio: 9.4%). The beta decay branch emits a positron and a 1275 keV gamma photon.

The main sources of detected events with energies in the vicinity of the photopeak are (see figure 3.15):

- Interactions from a photon initially directed away from the detector module, which get scattered back into the detector by materials surrounding the detector.
- The photon scatters multiple times in the scintillation crystal and then escapes before depositing its fully energy by interacting via photoelectric interaction.
- Natural emission from the 2.6% of the Lutetium that is ^{176}Lu in the LSO scintillation crystal itself.
- The 1275 keV photons have a lower chance of interacting in the same volume of crystal. If they do have an interaction, it is very likely to be a Compton scattering interaction. Therefore a contribution to the background around the photopeak is also due to 1275 keV gamma photon scattering in the crystal.

Most of these effects are dependent on the size and geometry of the crystal array, some on the relative position of the detector with respect to other materials. These effects produce acquired data in a particular crystal that is unique to the crystal's position within the array. All of the effects add up to producing a background on which the Gaussian 511 keV photopeak sits. This background can be thought of as a sum of many Gaussians (each energy being blurred by energy resolution), with tails decaying away from the Compton edge. This trend is traditionally approximated as an exponential.

Fitting the acquired data to obtain the energy resolution is facilitated by performing two separate steps. As seen in Figure 3.15, the photopeak (green line) is riding on a background (red line), which we approximate as an exponential. Points were taken near the Compton edge and far away from the photopeak to fit the exponential function.

The exponential fit is then subtracted from the data in the region around the photopeak. The resulting data represents the 511 keV photopeak. If the energy resolution of the detection process were perfect, the resulting data would be a distribution around 511 keV due to the momentum of the electron and positron at annihilation in the frame of their rest mass. To measure the energy resolution, the positron and electron momentum distribution at annihilation is consdered negligable, and the Gaussian fit to the remaining shape is considered due to the energy blur in the detection process. The full width at half maximum of the Gaussian describes the

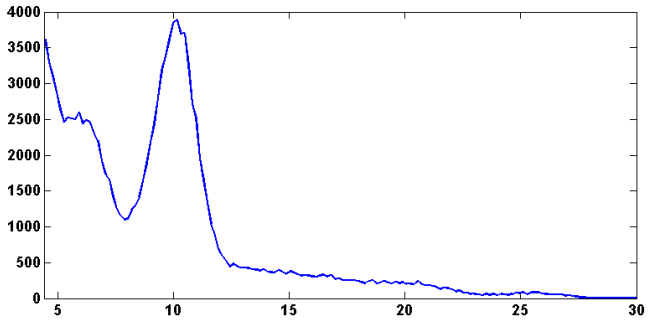

(a)

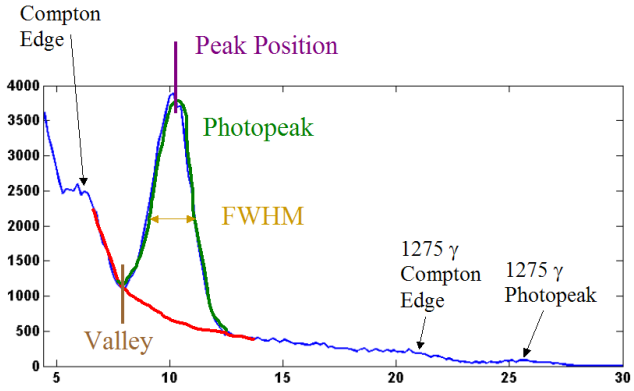

(b)

Figure 3.15: a) an energy spectrum without labeling for clarity and b) an illustration of the nomenclature used for the regions and the values within the energy spectrum for ^{22}Na.

energy resolution of the detection process and must be calibrated in energy units. This is done by using the Gaussian's peak position (PP), which is at 511 keV for PET. Energy resolution is traditionally given in % of the reference energy in keV.

Error bars seen in quantities measured from the energy spectrum such as energy resolution, photopeak position, etc., (e.g. Figure 3.20 in Section 3.3.3) are those of a

95% confidence interval to the fit to the spectrum.

3.2.7 Coincidence Timing Measurement

Experimental Setup

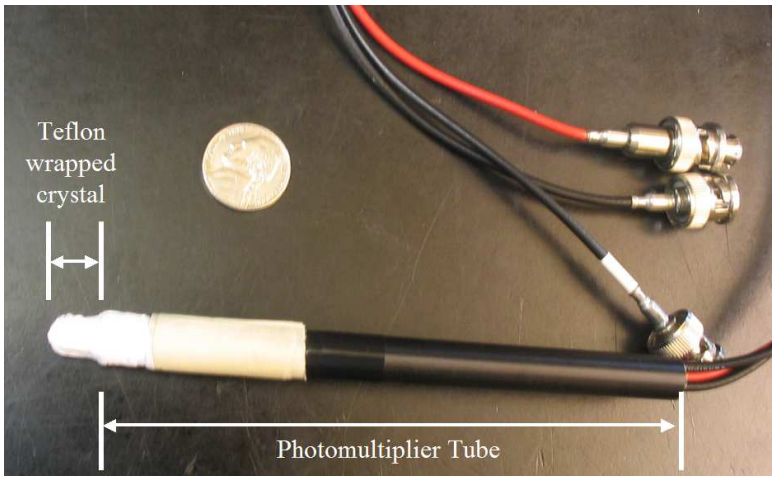

Figure 3.16: A picture of the Hamamatsu 3164 PMT used in the coincidence timing experiments. The photo-detector is shown coupled to 1 cm x 1 cm x 2 cm of LSO, wrapped in 9 layers of Teflon tape.

For the measurements mentioned here, the coincidence time resolution (CTR) was measured for a particular device in coincidence with a compact Hamamatsu 3164 photomultiplier tube (PMT), unless otherwise noted. A picture of this PMT, optically coupled to a 1 cm x 1 cm x 2 cm piece of LSO, is shown in Figure 3.16. The eighth dynode was used for both energy information from the PMT and for triggering.

Figure 3.17 shows the shaping electronics used to acquire coincidence timing measurements. Energy information was acquired from both the PSAPD and the PMT

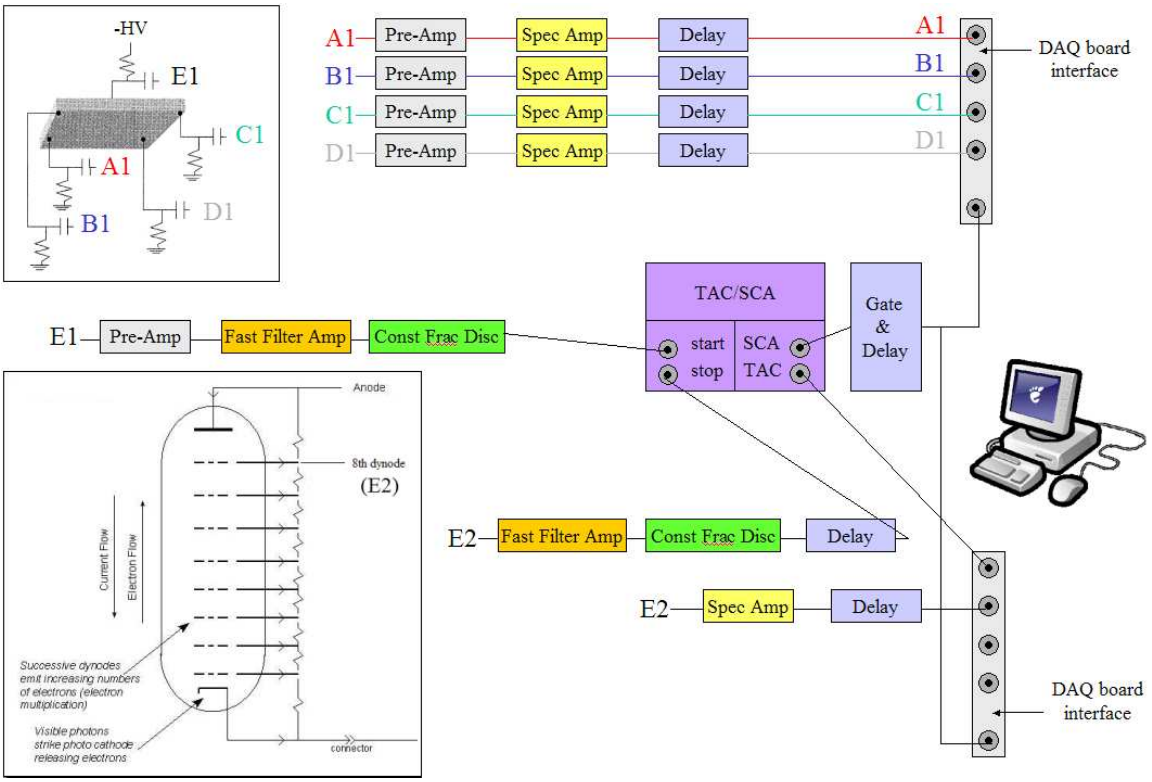

Figure 3.17: An illustration of the shaping electronics used from PSAPD & PMT output to acquisition data in the coincidence timing experiments.

in the same manner as for the flood measurements. The timing information was obtained using a circuit which comprised a fast filter amplifier (FFA), filtering both the PSAPD common and PMT eighth dynode signals, constant fraction discriminator (Cons Frac Disc, or CFD) on the output of each FFA, and a time to amplitude converter (TAC). The FFA provided integration filtering with as little time distortion as possible, and the CFD shaped the signal using standard delayed and attenuation summation techniques forming a signal with a precisely timed zero-crossing. The FFA and CFD processed signals from both the PMT and PSAPD (plus delay) were

used as the start and stop signals, respectively, for the time to amplitude converter. The difference between the zero-crossing times from the PMT and delayed PSAPD was converted into a voltage by the TAC electronics and then read out. The PSAPD signal was delayed a few nanoseconds after the CFD step so that the PSAPD signal always occurred after the PMT signal.

When the PMT and PSAPD signals produced a TAC pulse, the single channel analyzer produced a pulse signifying a coincidence event occurred. This signal was read out by a gate and delay generator and a TTL pulse was produced which provided the trigger for all other signals (the four corner PSAPD signals, the PMT energy signal and the TAC signal) to be read out.

Measurement Calibration

The coincidence timing data was acquired using the methods described in Section 3.2.7 and recorded as a voltage. The manner in which the recorded voltage corresponded to an actual time difference was calibrated using a nanosecond delay module, which shifted the acquired TAC signal in volts. Multiple acquisitions, each with a separate nanosecond delay, were acquired to observe the shifting peak position of the TAC signal. These peak positions were plotted with respect to the delay that was used to produce them. A linear fit to this data produced the calibration factor in ns/V, which could then be applied to the TAC FWHM to find the coincidence timing resolution. An example of this fit is shown in Figure 3.18.

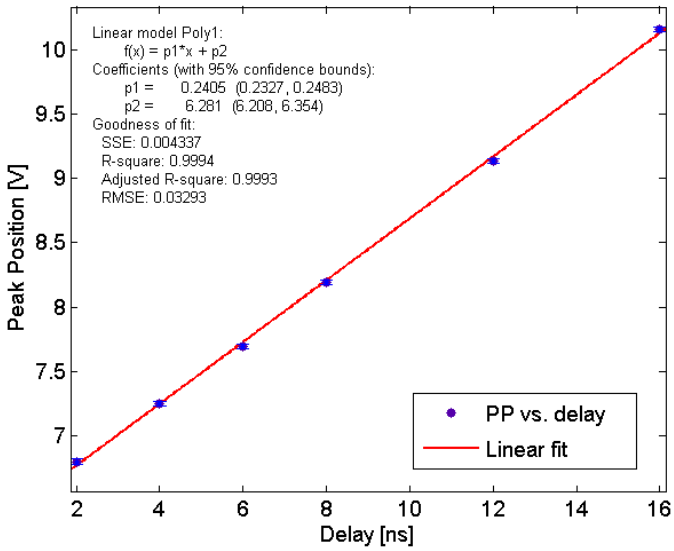

Figure 3.18: An example of the calibration data and fit for a coincidence timing experiment. The error bars are on the order of the size of the markers.

Error bars seen in quantities measured from the coincidence timing spectrum such as peak position, (e.g. Figure 3.26) are those of a 95% confidence interval to the fit of the spectrum.

3.3 Ceramic Substrate PSAPDs

3.3.1 Introduction

The bulk of the data in this section was previously published in Reference [96]. The devices characterized in this section were commercial devices, sold by Radiation Monitoring Devices, Inc. in Watertown, Massachusetts. These devices were characterized not only to discover their ability to resolve interaction events in position, energy and time, but as a gold standard for the characterization of the various prototypes in the sections to follow. The goal of these experiments is to provide that standard.

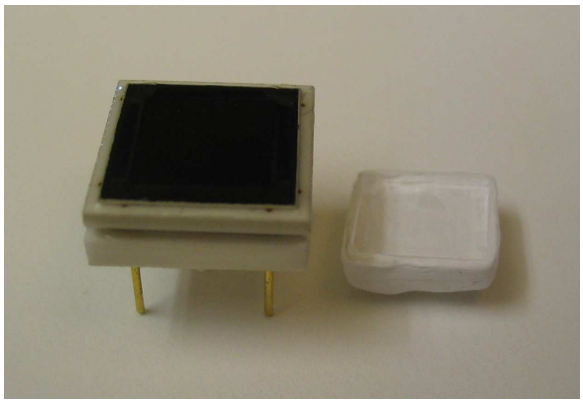

Figure 3.19: Photograph of (left) the 8 mm x 8 mm ceramic substrate PSAPD and (right) a Teflon wrapped sheet crystal with the side that would be coupled to the photodetector face up.

The off-the-shelf ceramic substrate PSAPD photodetectors studied in this section were not considered for use in the final detector system design, though they have been investigated as-is for use in similar applications in this field [13,21,22,42,45,192]. The

aim of this design is to optimize the inter-crystal packing fraction of the detection system by compacting as much of the volume not directly involved in annihilation photon interaction such as the substrate and read-out electronics. Figure 3.19 shows the scale of the material that is used in photodetection, and the materials that are housing signal traces. Everything below the black silicon chip on this photodetector ($\sim$250 μm in thickness) is either a signal trace (the gold pin-outs, on which the device is shown standing) or the trace's packaging (the off white ceramic substrate). It is indeed exciting to imagine the device packaged in a much more compact way, freeing up the ways in which this photodetector could be used.

3.3.2 Materials and Methods

Specifications

Many of the mechanical and electrical characteristics of the device can be found in Table 3.2 [159].

Table 3.2: Ceramic Substrate PSAPD Specifications for both the 8 mm x 8 mm and 14 mm x 14 mm active area devices. HV_{opt} is optimal operational bias voltage. *LSO peak emission wavelength.

Attribute	Value (8 mm)	Value (14 mm)	Units	Notes
Gain	$\sim$1000	$\sim$1000	x	at HV_{opt}
Quantum Efficiency	65	65	%	at 420nm*
Capacitance	85	202	pFarads	
Leakage Current	300-600	600-1000	nAmps	
Noise (erms)	140	210	electrons	

Scintillation Crystal Configurations

Three scintillation crystal configurations were studied for characterizing the two sizes of ceramic PSAPD photodetectors for energy resolution and spatial crystal identification. Illustrations of the arrays are shown in Figure 3.4.

As mentioned in Section 3.2.1, the crystals in these arrays were coupled side-on to the PSAPD photodetectors for optimal scintillation light collection. Surface treatment has been shown to be a factor in the fraction of light collected by the photodetector [44]. All of the segmented crystal arrays (4 x 3 and 8 x 3 arrays) had a mechanically ground (as-cut) surface treatment on all faces, and the sheet crystal was polished on all faces. All arrays were wrapped with Teflon reflector on every side that was not coupled to the PSAPD photodetector. There was no reflector used between any of the crystals in either segmented crystal array.

Energy and Coincidence Time Resolution

Energy and coincidence time resolution were acquired and analyzed in the manner described in Sections 3.2.6 and 3.2.7, respectively.

Bias Voltage Optimization

The optimal operational high voltage bias was determined using three characteristics that are important for signal detection and event classification. Figure 3.15 shows the portions of the energy spectrum used for these measurements.

- Peak to valley ratio (PVR) is a measure of the detector to distinguish the photopeak from events that don't deposit 511 keV. This measurement is calculated by taking the value of the peak height of the photopeak divided by the value of the background counts at the base of the photopeak. This measurement can also be an indication of other processes, such as the degree of light coupling of the scintillator to the photodetector.

- Photopeak position (PP) is a measure of the gain of the device. Inefficiencies in scintillation light generation, scintillation light collection, photodetector quantum efficiency, etc., can cause variations in gain. The mean of the photopeak position should be linearly related to the energy deposited in the detector by the annihilation photon, and hense a measure of the gain of the detection scheme. See Section 4.2 for a detailed description of the processes involved in this signal value.

- Full-width at half-maximum (FWHM) of the photopeak is a measure of variance in the detection process of measuring energy. Because the size of the crystal is small, annihilation photons that first interact in the scintillation crystal as a Compton scattering interaction, generally scattering out of the crystal before interacting again (the solid angle of the crystal is small). Therefore, by and large, the signals generated and recorded for this setup are from single interactions, Compton or photoelectric. Because of the nature of Compton Scattering,

only a fraction of the total energy of the photon can be deposited in a single interaction, up to $\frac{2}{3}$ of a 511 keV annihilation photon. This leads to a discernable "forbidden energy region" called the Compton edge. Therefore, if no other interactions could take place, only a single Compton or single photoelectric, a histogram would reveal a mono-energetic spike at 511 keV and then a continuum starting from 0 keV and ending at $\frac{2}{3}$ of 511 keV or about 341 keV. There are further complications on this simple model, but as a first approximation, this tells us that we can use the variance of the spectrum at the photopeak for measuring the detector's ability to repeatedly report energy.

All measurements are made in volts as the charge pulses generated by the PSAPD are first processed by charge sensitive preamplifiers, which integrates the charge and sends out a voltage pulse with a fast rise time and relatively slow decay time (see Section 3.2.4 for more details).

3.3.3 Results

Bias Voltage Optimization

Because the gain of these avalanche photodiodes depends on the bias voltage applied, a PSAPD is likely to have the best position, energy and coincidence time resolution near the limits of its linear gain region. To find this optimal voltage, both the 8 mm x 8 mm and 14 mm x 14 mm active area ceramic devices were

biased at a wide range of voltages and their photopeak full width at half maximum (FWHM), photopeak position (PP), energy resolution (ER) and photopeak-to-valley ratio (PVR) values were measured.

Figure 3.20 shows two figures with different ranges of bias voltages tested using the 8 mm x 8 mm ceramic PSAPD. The top figure shows the characterized values over a large range of voltages (1700-1760V, 2V steps), looking for a voltage region to observe operating characteristics more finely. A low value of energy resolution and a high value of PVR were used to determine the region observed in the figure to the right. The bottom graph of Figure 3.20 shows a smaller region of voltages (1736-1743V) over which characteristics were determined with 1V steps between them. Although gain is still increasing over this region, the bias voltage with the best compromise between PVR and ER is 1740 V. This is the bias voltage applied to this device for the rest of the experiments.

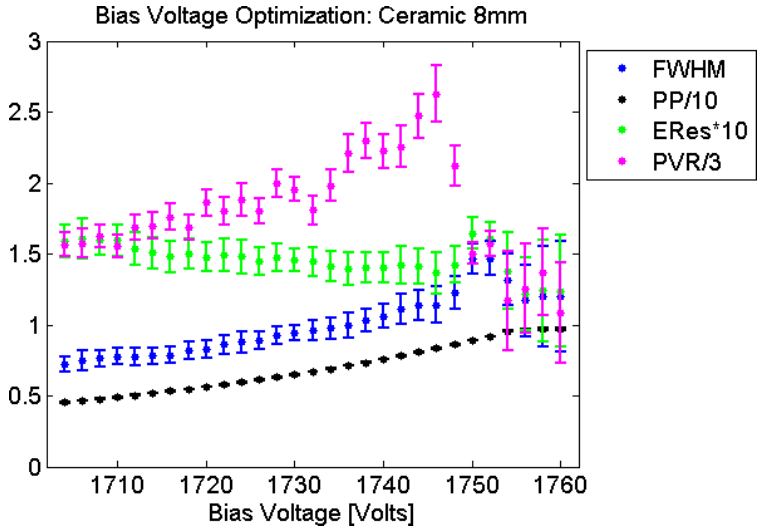

(a)

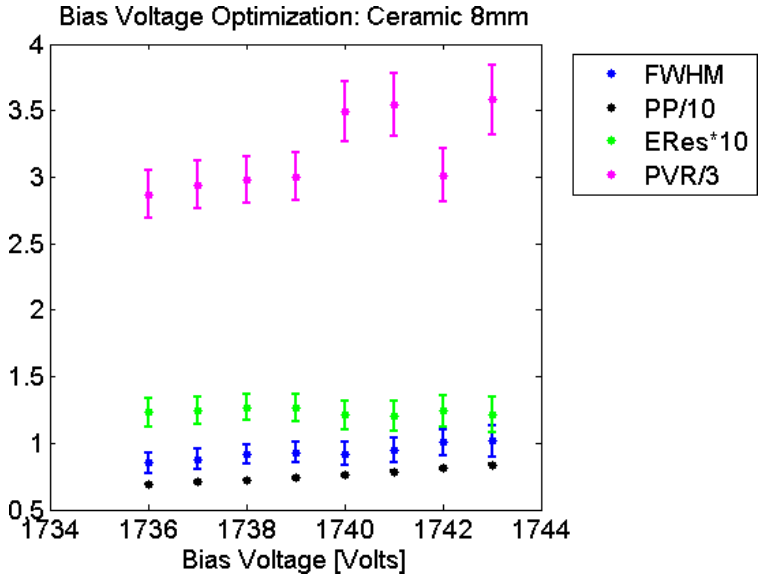

(b)

Figure 3.20: Optimization of bias voltage for the 8 mm x 8 mm ceramic PSAPD, (top) over a large range of voltages, and (bottom) windowed in on the region of best performance. FWHM is in Volts, PP is in Volts, ER is in percent, and PVR is unitless. Measurements shown in the first graph were taken seperately from the second graph.

Also, for the 14 mm x 14 mm devices, a large range (Figure 3.21 top) and an interesting smaller range (Figure 3.21 bottom) were studied to find the optimal bias voltage. The bottom graph shows, as with the 8 mm x 8 mm active area device, a good compromise between low values of ER and locally high values of PVR can be found around 1740 V. This is the bias voltage applied to this device for the rest of the experiments.

Crystal Identification - 8 mm x 8 mm Device

Two arrays were assessed for the ability of the 8 mm x 8 mm active area ceramic detector to identify the position of individual crystals using flood irradiation. A 4 x 3 array constructed of 2 mm x 2 mm x 3 mm crystals, and an 8 x 3 array constructed of 1 mm x 1 mm x 3 mm crystals were used in these studies..

Figure 3.22 shows the flood images (upper left); profile (lower left); and individual, mean and standard deviation of the position peak to valley ratio (right) for both crystal arrays studied.

Crystal Identification - 14 mm x 14 mm Device

As with the other ceramic device, two arrays were assessed for the ability of the 14 mm x 14 mm active area ceramic detector to identify the position of individual crystals using flood irradiation. A 4 x 3 array constructed of 2 mm x 2 mm x 3 mm crystals, and an 8 x 3 array constructed of 1 mm x 1 mm x 3 mm crystals were used

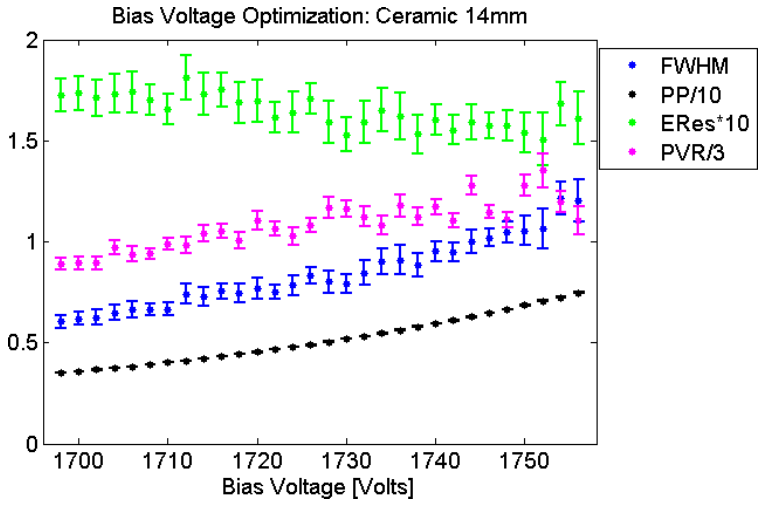

(a)

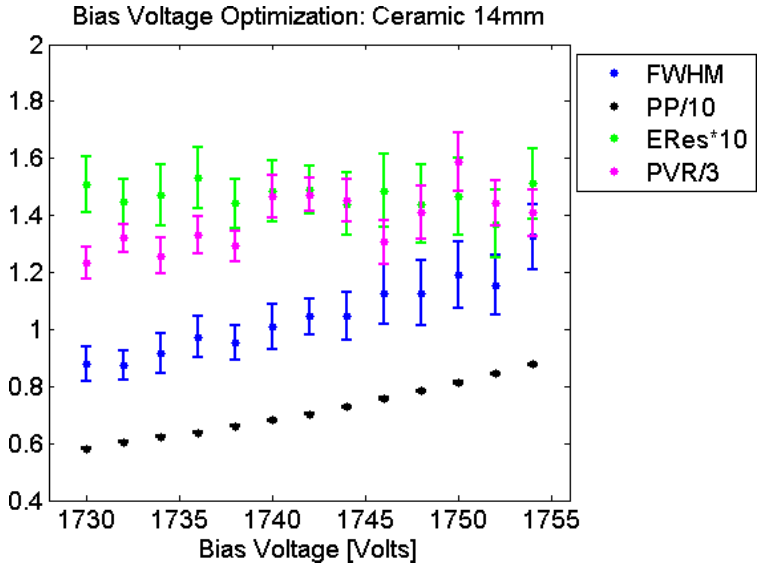

(b)

Figure 3.21: Optimization of bias voltage for the 14 mm x 14 mm ceramic PSAPD, (top) over a large range of voltages, and (bottom) windowed in on the region of best performance. FWHM is in Volts, PP is in Volts, ER is in percent, and PVR is unitless. Measurements shown in the first graph were taken seperately from the second graph.

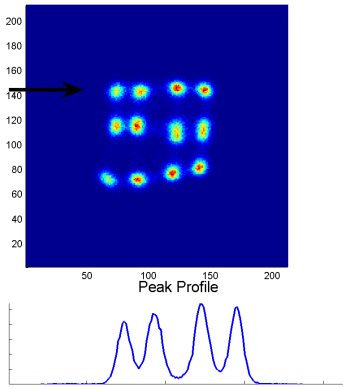

Peak	PVR
1	4.27
2	11.90
3	13.49
4	5.99
Mean	8.91
StDev	4.47

(a)

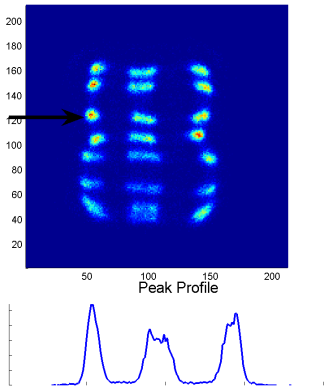

Peak	PVR
1	31.57
2	15.00
3	34.29
Mean	26.96
StDev	10.44

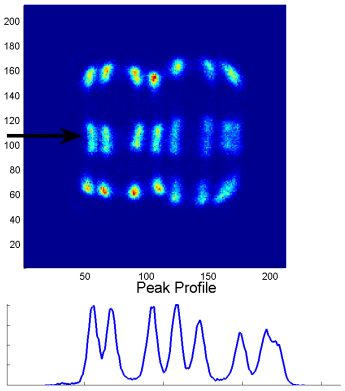

Peak	PVR
1	3.08
2	14.53
3	6.18
4	5.00
5	4.13
6	9.98
7	5.55
8	0.92
Mean	6.17
StDev	4.27

(b) (c)

Figure 3.22: Flood image and profile for (top) 4 x 3 array along the 4 crystal direction, and (bottom) 8 x 3 array along the (left) 3 and the (right) 8 crystal direction.

in these studies.

Figure 3.23 shows the flood images (upper left); profile (lower left); and individual, mean and standard deviation of the position peak to valley ratio (right) for both crystal arrays studied.

Comparing each of the measurements in Table 3.3, the 8 mm x 8 mm active

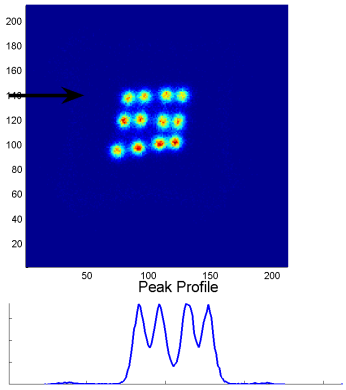

Peak	PVR
1	2.19
2	4.40
3	4.52
4	2.17
Mean	3.32
StDev	1.32

(a)

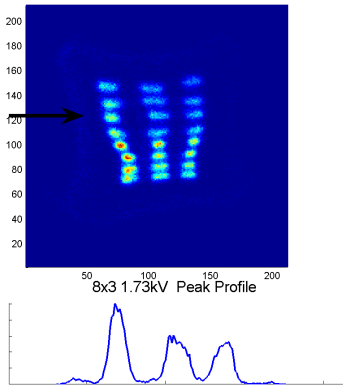

Peak	PVR
1	35.59
2	12.93
3	12.11
Mean	20.21
StDev	13.32

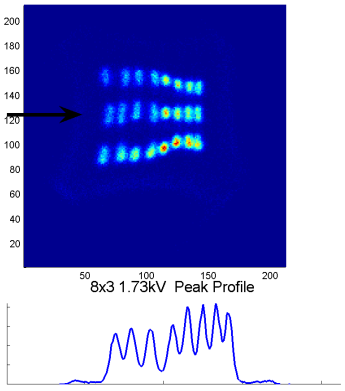

Peak	PVR
1	2.02
2	3.15
3	4.06
4	1.98
5	2.48
6	2.63
7	2.29
8	1.64
Mean	2.53
StDev	0.77

(b) (c)

Figure 3.23: Flood image and profile for (top) 4 x 3 array along the 4 crystal direction, and (bottom) 8 x 3 array along the (left) 3 and the (right) 8 crystal direction.

Table 3.3: Peak to valley ratio (PVR) for both 8 mm x 8 mm and 14 mm x 14 mm devices, comparing the same three profile direction measurements. 4C: 4 x 3 array along the 4 crystal direction, 3C: 8 x 3 array along the 3 crystal direction and 8C: 8 x 3 array along the 8 crystal direction.

Profile direction	PVR, 8 mm x 8 mm device	PVR, 14 mm x 14 mm device
4C	8.9±4.5	3.3±1.3
3C	27.0±10.4	20.2±13.3
8C	6.17±4.3	2.5±0.8

area ceramic device out-performs the 14 mm x 14 mm active area ceramic device in identifying crystals in the same array. The 8 mm x 8 mm device had 168%±84%, 33%±13%, and 144%±100% better peak to valley ratios for crystal profiles in the 4 x 3 array along the 4 crystal direction, 8 x 3 array along the 3 crystal direction, and 8 x 3 array along the 8 crystal direction, respectively.

Energy Resolution - 8 mm x 8 mm Device

Two arrays were assessed for the 8 mm x 8 mm active area detector's energy resolution capabilities. A 4 x 3 array constructed of 2 mm x 2 mm x 3 mm crystals, and an 8 x 3 array constructed of 1 mm x 1 mm x 3 mm crystals were used in these studies.

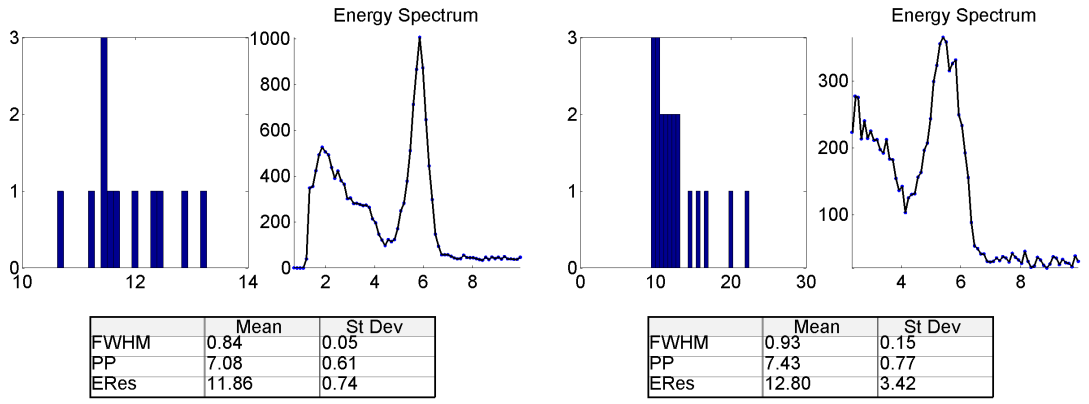

	Mean	St Dev
FWHM	0.84	0.05
PP	7.08	0.61
ERes	11.86	0.74

	Mean	St Dev
FWHM	0.93	0.15
PP	7.43	0.77
ERes	12.80	3.42

(a) 4 x 3 array

(b) 8 x 3 array

Figure 3.24: 8 mm x 8 mm device: individual crystal energy resolution for (left) the 4 x 3 array and (right) the 8 x 3 array.

Figure 3.24 shows energy spectral analysis of the 8 mm x 8 mm active area device

results for both the 4 x 3 array and the 8 x 3 array. Both subfigures have (upper left) a histogram of the individual crystal resolution values, (upper right) a representative energy spectra and (bottom) the mean and standard deviation of the photopeak full width at half maximum (FWHM) in Volts, photopeak position (PP) in Volts, and the energy resolution (ER).

Energy Resolution - 14 mm x 14 mm Device

The same two arrays were assessed for the 14 mm x 14 mm active area detector's energy resolution capabilities of individual crystals. A 4 x 3 array constructed of 2 mm x 2 mm x 3 mm crystals, and an 8 x 3 array constructed of 1 mm x 1 mm x 3 mm crystals were used in these studies.

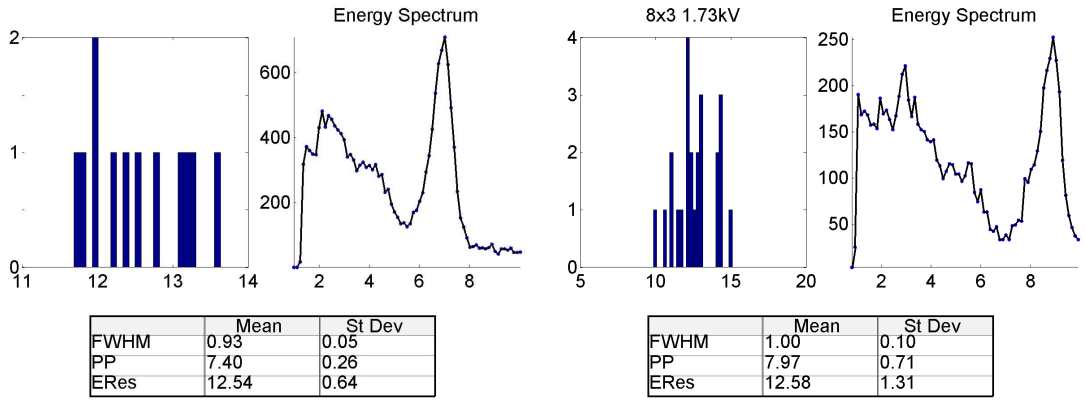

	Mean	St Dev
FWHM	0.93	0.05
PP	7.40	0.26
ERes	12.54	0.64

	Mean	St Dev
FWHM	1.00	0.10
PP	7.97	0.71
ERes	12.58	1.31

(a) 4 x 3 (b) 8 x 3

Figure 3.25: 14 mm x 14 mm device: individual crystal energy resolution for (left) the 4 x 3 array and (right) the 8 x 3 array.

Figure 3.25 shows energy spectral analysis of the 14 mm x 14 mm active area

device results for both the 4 x 3 array and the 8 x 3 array. Both subfigures have (upper left) a histogram of the individual crystal resolution values, (upper right) a representative energy spectra and (bottom) the mean and standard deviation of the photopeak full width at half maximum (FWHM) in Volts, photopeak position (PP) in Volts, and the energy resolution (ER).

Table 3.4: Photopeak full width at half maximum (FWHM), photopeak position (PP) and energy resolution (ER) means and standard deviation values for both 8 mm x 8 mm and 14 mm x 14 mm devices, and both 4 x 3 and 8 x 3 arrays tested.

Device	Array	FWHM	PP	ER
8 mm x 8 mm	4 x 3	0.8±0.1	7.1±0.6	11.9±0.7
8 mm x 8 mm	8 x 3	0.9±0.2	7.4±0.8	12.8±3.4
14 mm x 14 mm	4 x 3	0.9±0.1	7.4±0.3	12.5±0.6
14 mm x 14 mm	8 x 3	1.0±0.1	8.0±0.7	12.6±1.3

Comparing each of the measurements in Table 3.4, the 8 mm x 8 mm active area ceramic device is comparable to the 14 mm x 14 mm active area ceramic device in energy resolution performance.

Coincidence Timing Resolution - 8 mm x 8 mm Device

A single 8 x 8 x 2 mm^2 sheet crystal was used to determine the coincidence time resolution of the 8 mm x 8 mm active area ceramic PSAPD device, using the method described in Section 3.2.7.

Figure 3.26 shows a representative TAC spectrum − this one was collected using a 0 ns delay between the PSAPD and the stop input of the TAC/SCA. The coincidence time resolution was measured to be 2.0 ± 0.3 ns.

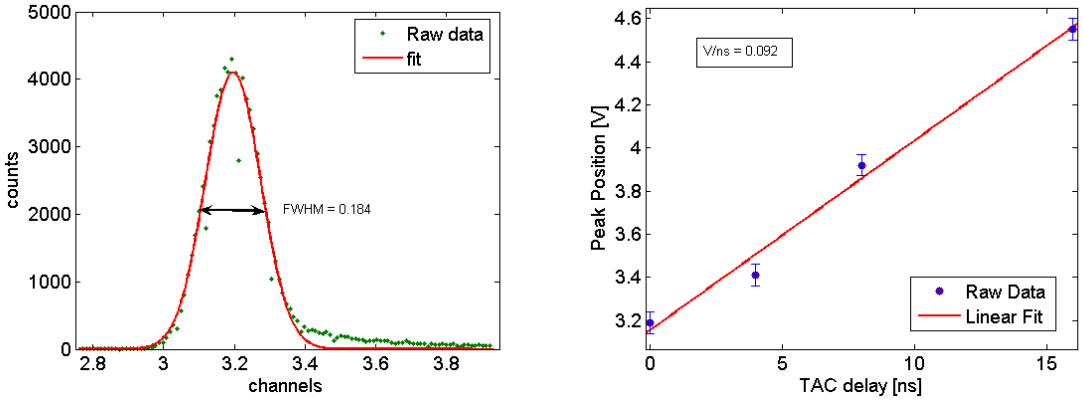

(a) (b)

Figure 3.26: Coincidence timing resolution measurement and calibration (8 mm x 8 mm device). a) A representative TAC spectra, b) voltage to nanosecond calibration graph.

Coincidence Timing Resolution - 14 mm x 14 mm Device

The same single 8 x 8 x 2 mm^2 sheet crystal was used to determine the coincidence time resolution of the 14 mm x 14 mm active area ceramic PSAPD device as well, in the method described in Section 3.2.7.

Figure 3.27 shows a representative TAC spectrum, this one was collected using a 0 ns delay between the PSAPD and the stop input of the TAC/SCA. The coincidence time resolution was measured to be 3.3 $\pm$ 0.34 ns.

Comparing the two devices, the 8 mm x 8 mm active area device showed 39% lower coincidence time blur as compared to the 14 mm x 14 mm device.

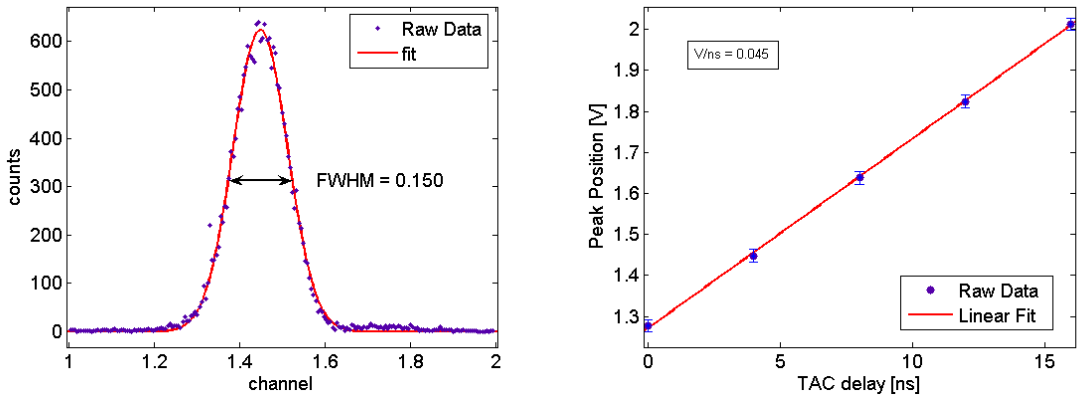

(a) (b)

Figure 3.27: Coincidence timing resolution measurement and calibration (14 mm x 14 mm device). a) A representative TAC spectra, b) voltage to nanosecond calibration graph.

3.3.4 Conclusions

Both the crystal identification and coincidence time resolution of the 8 mm x 8 mm active area ceramic packaged PSAPD were superior to the 14 mm x 14 mm active area device. The 8 mm x 8 mm device acheived a < 1 mm crystal feature size FWHM (see Figure 3.22c), and coincidence time resolution of 2 ns. On the other hand, the 14 mm x 14 mm device showed a ~ 1 mm crystal feature size FWHM (see Figure 3.23c), and a coincidence time resolution of 3.3 ns. The 511 keV photopeak energy resolution of the two devices were comparable (10-12% of 511 keV). Further packaging designs are not likely to improve on these results because the ceramic packaging substrate provides a well-isolated environment for the PSAPD chip. Nonetheless, both active area designs will be tested in the next design step to better understand the effect of

packaging on device operation characteristics.

3.4 Single-Chip Flex Modules with a Dead Perimeter of 1.5 mm

Four novel Kapton flex circuit packaged module prototypes were tested with a single PSAPD chip packaged on each circuit. Each PSAPD chip had a dead perimeter of 1.5 mm around all the edges, as with the ceramic packaged PSAPD chips tested in Section 3.3. Two of these devices had a 8 x 8 mm^2 active area, the other two had a 14 x 14 mm^2 active area. These chips had the same electrical properties (gain, leakage current, noise, etc.) as the ceramic packaged PSAPDs tested in Section 3.3. The goal of these tests was to understand the effect of the novel Kapton circuit packaging method on the operational properties of the PSAPDs.

A single crystal array was used in each of the experiments performed in this section: the 4 x 3 array comprising segmented 2 mm x 2 mm x 3 mm crystals. Bias voltage optimization as well as position, energy and coincidence time measurements were performed using the methods described in Section 3.2 of this chapter.

3.4.1 Bias Voltage Optimization

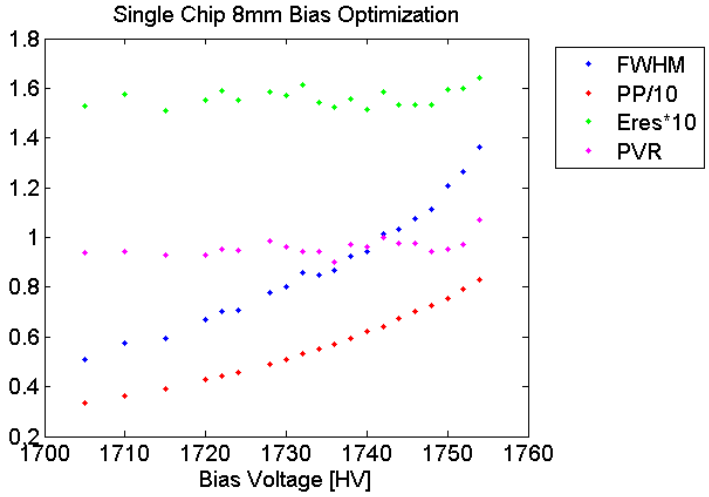

Figure 3.28: Photopeak full width at half maximum (FWHM), photopeak position (PP), energy resolution (ER), and photopeak-to-valley ratio (PVR) versus bias voltage for the position-sensitive 8 mm x 8 mm active area device.

Initial flood maps were taken on each device at the bias voltage at which the ceramic chips were optimal. Of the two 8 mm x 8 mm active area devices, only the second had positioning capabilities, so it was used for bias voltage optimization. Figure 3.28 shows characteristics of the operation of the device at various bias voltages. Photopeak FWHM (labeled FWHM), photopeak position (labeled PP), energy resolution (labeled Eres), and energy photopeak to (Compton) valley ratio (labeled PVR) are all plotted at each acquired bias voltage.

Flood maps were also taken near the optimal bias voltages for evaluating the device function in position space. Figures 3.30-3.36 show the flood maps with corresponding data measured: center of crystal separation distance in pixels between the

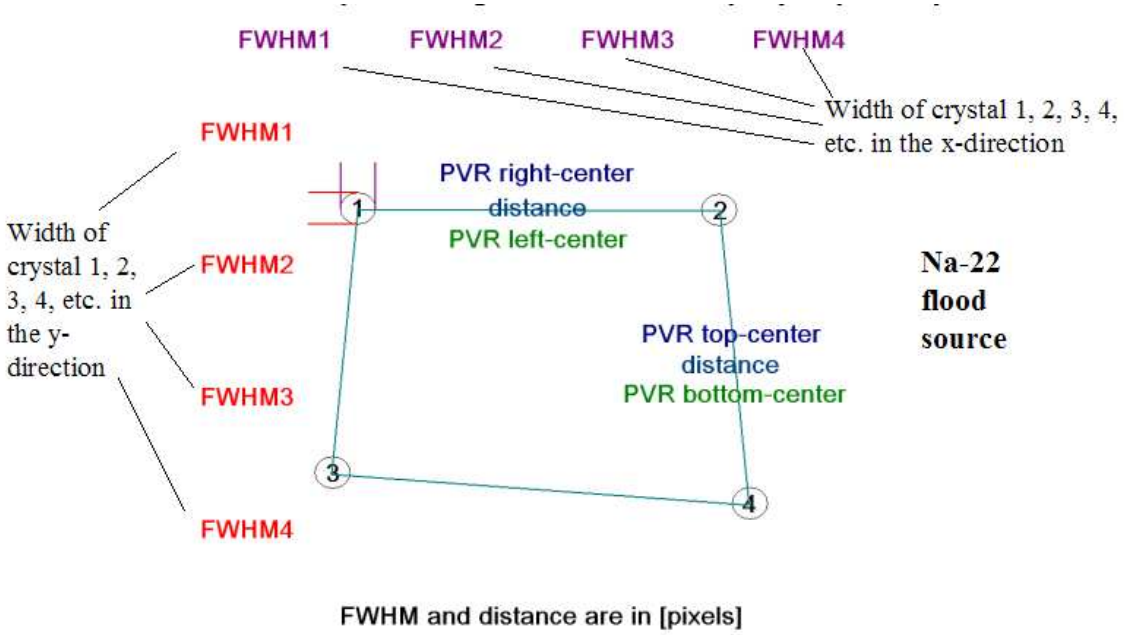

Figure 3.29: An illustration of the location of data within the flood images used for bias voltage optimization.

connected crystals (labeled distance), FWHM of crystal features in horizontal and vertical directions (labeled FWHM1, etc. in figure 3.29 and is ordered by crystal number), and peak counts to valley counts in each neighboring inter-crystal direction (PVR top-center, bottom-center, right-center and left-center). For instance, the peak to valley ratio (PVR) defined as "top-center" finds the peak height at the center of the crystal directly "north" of the number, the valley height between the "north" and the "south" crystals, and divides them. The data is shown in each of Figures 3.30-3.36 in the format illustrated in Figure 3.29.

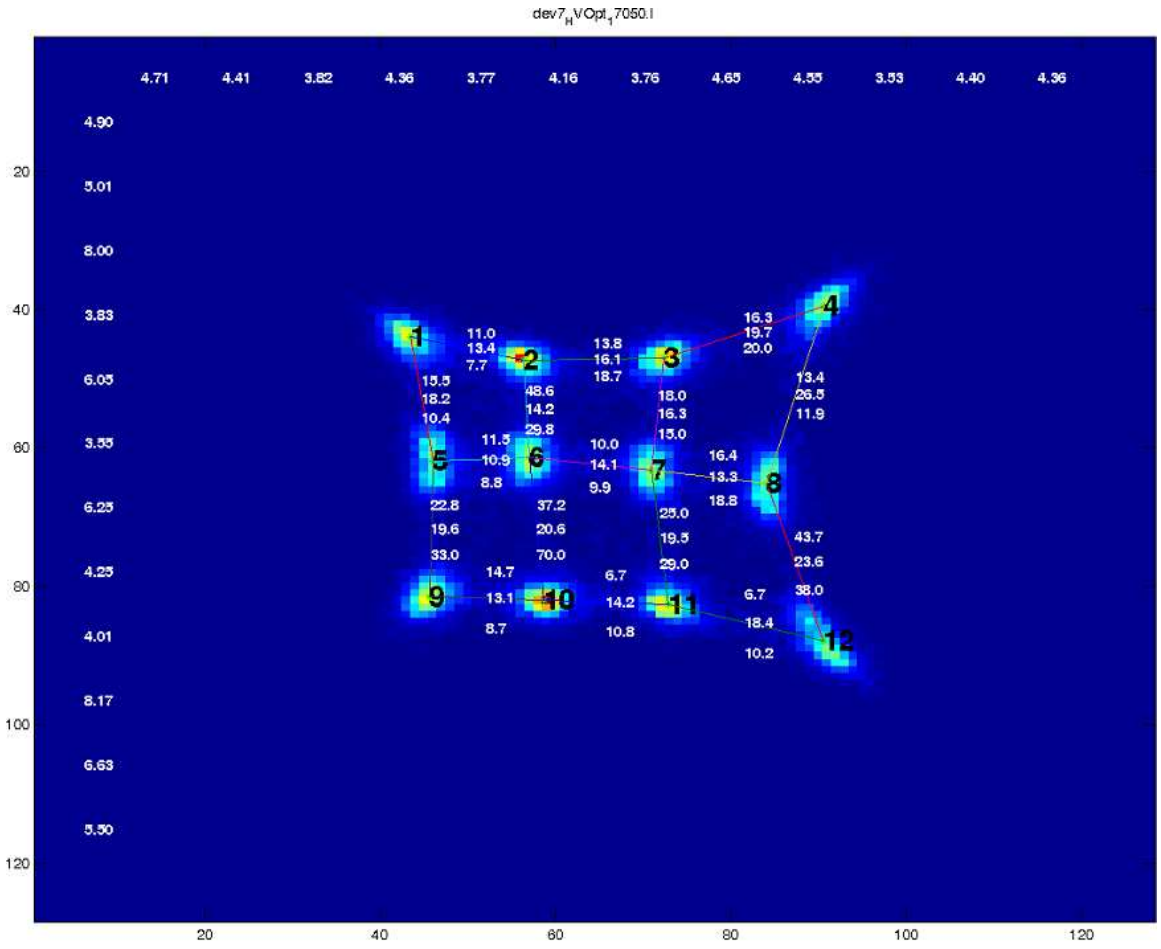

Figure 3.30: Flood image for 8 mm x 8 mm ceramic packaged single chip PSAPD at bias voltage = 1705 V

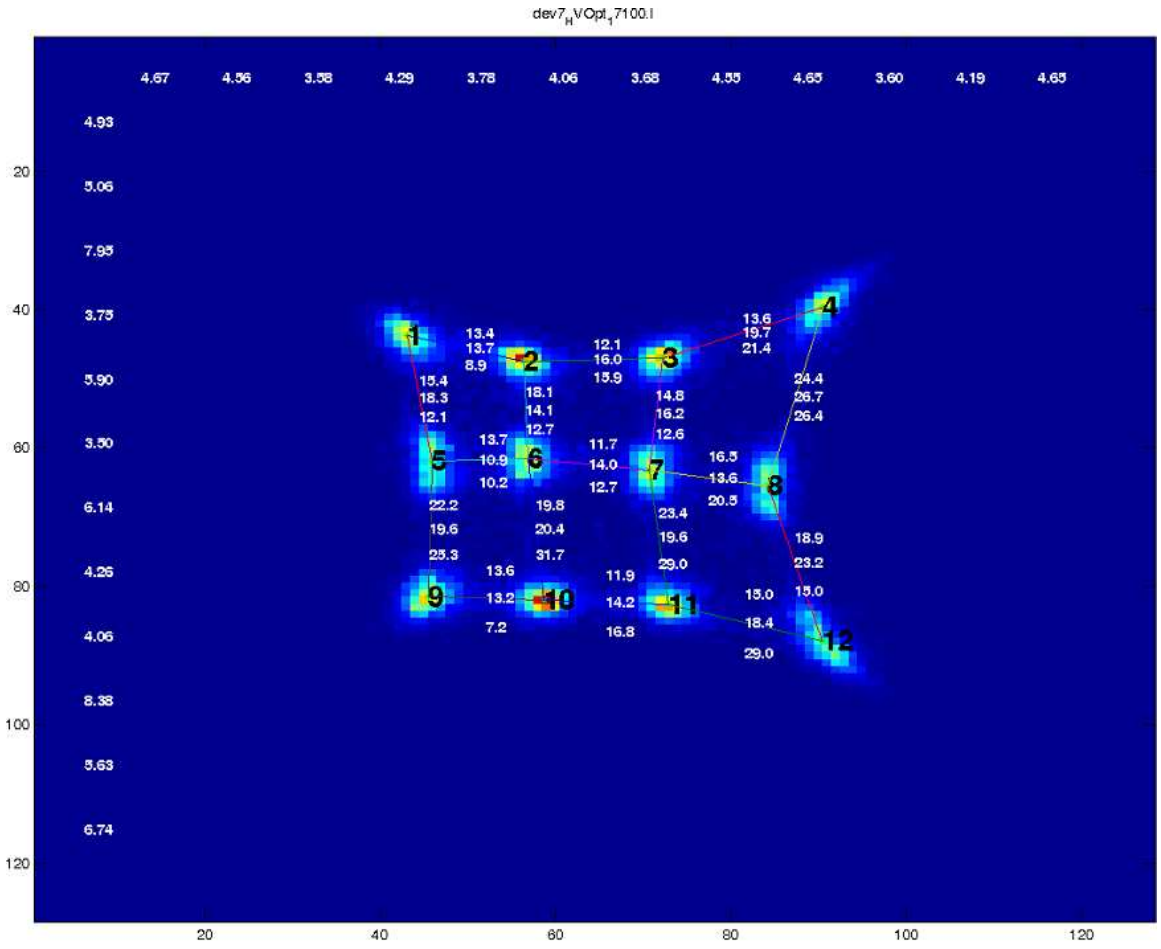

Figure 3.31: Flood image for 8 mm x 8 mm ceramic packaged single chip PSAPD at bias voltage = 1710 V

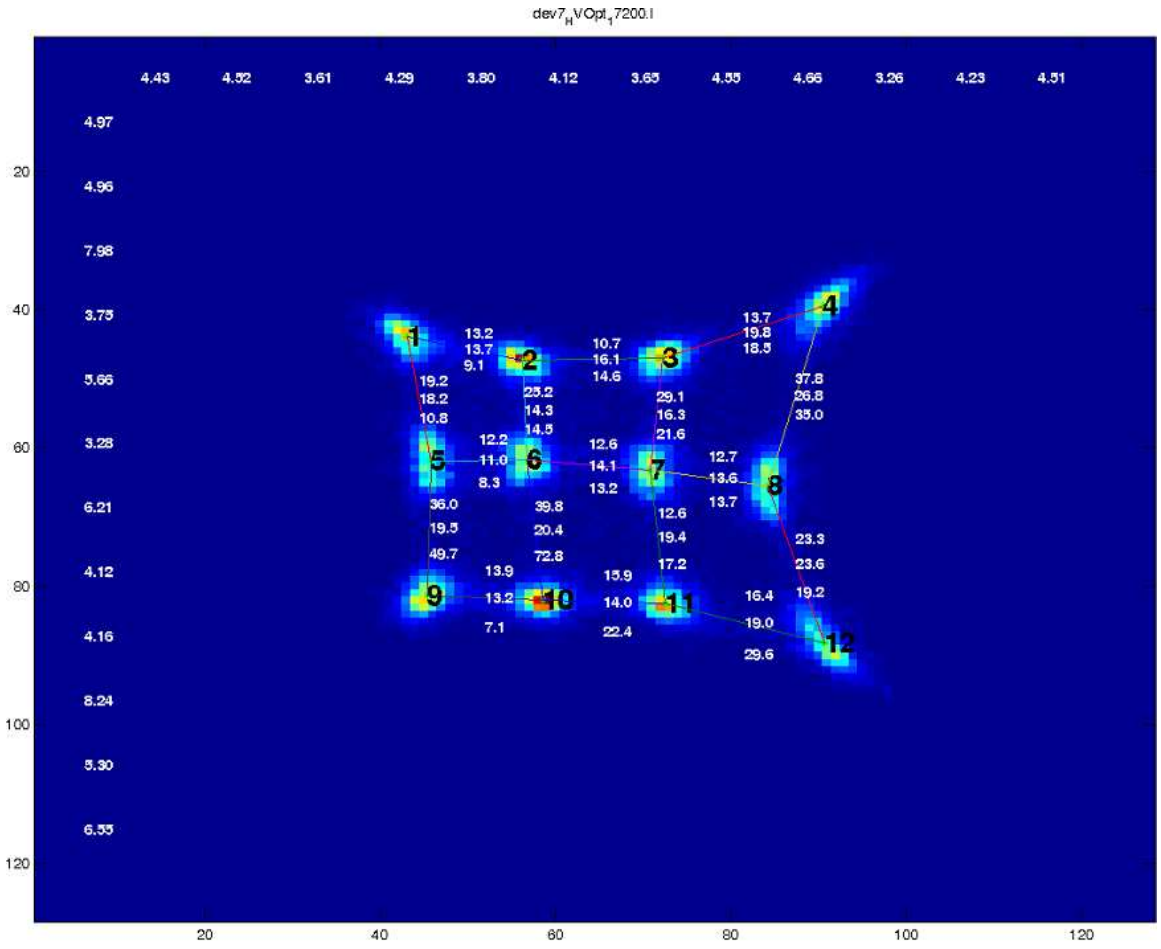

Figure 3.32: Flood image for 8 mm x 8 mm ceramic packaged single chip PSAPD at bias voltage = 1720 V

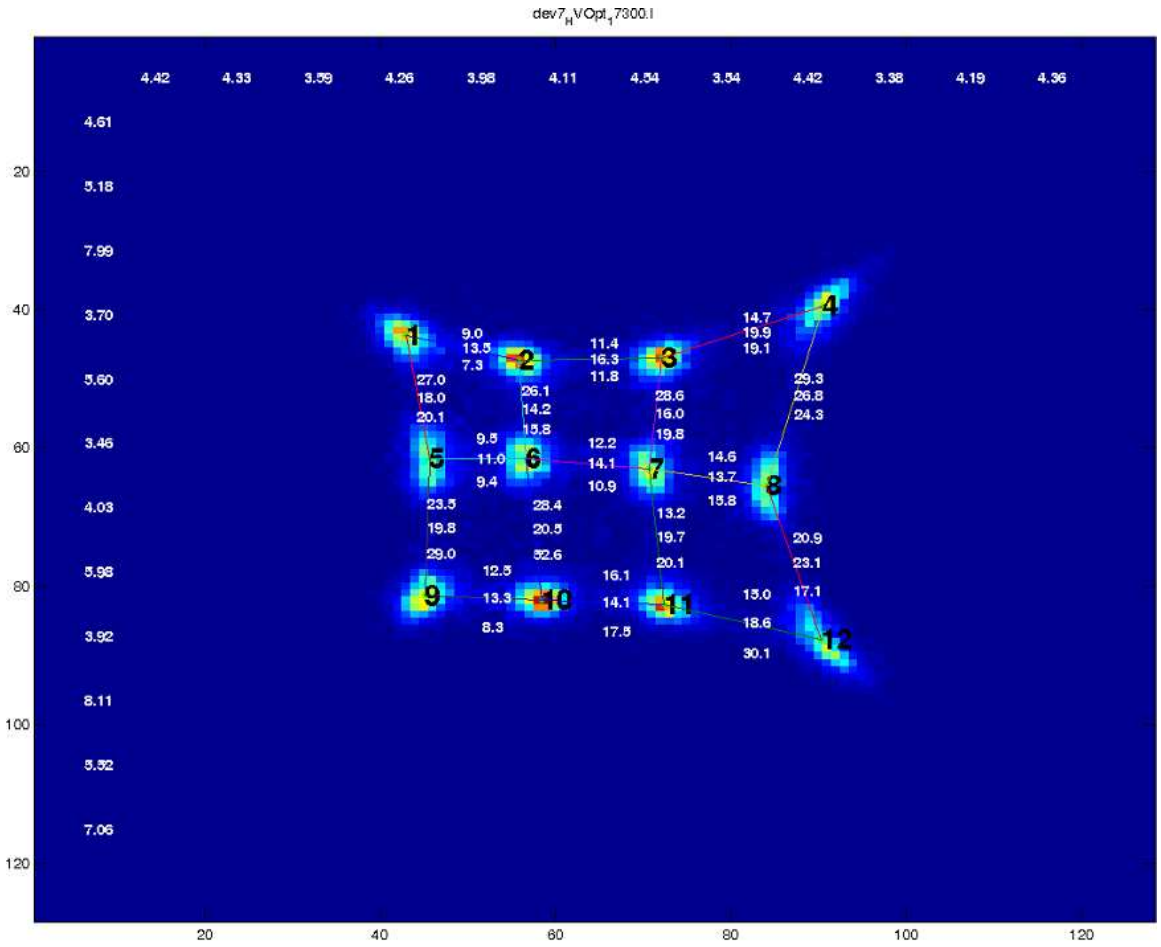

Figure 3.33: Flood image for 8 mm x 8 mm ceramic packaged single chip PSAPD at bias voltage = 1730 V

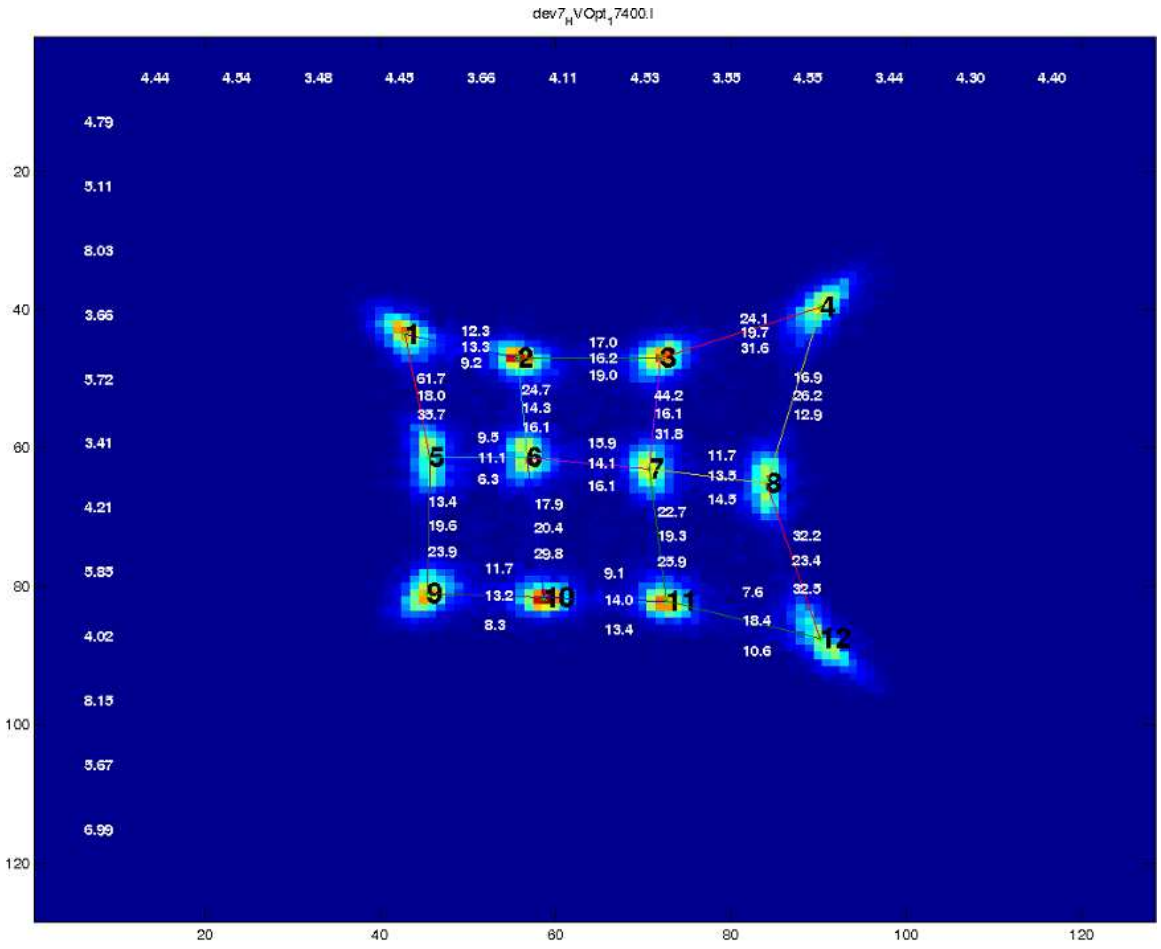

Figure 3.34: Flood image for 8 mm x 8 mm ceramic packaged single chip PSAPD at bias voltage = 1740 V

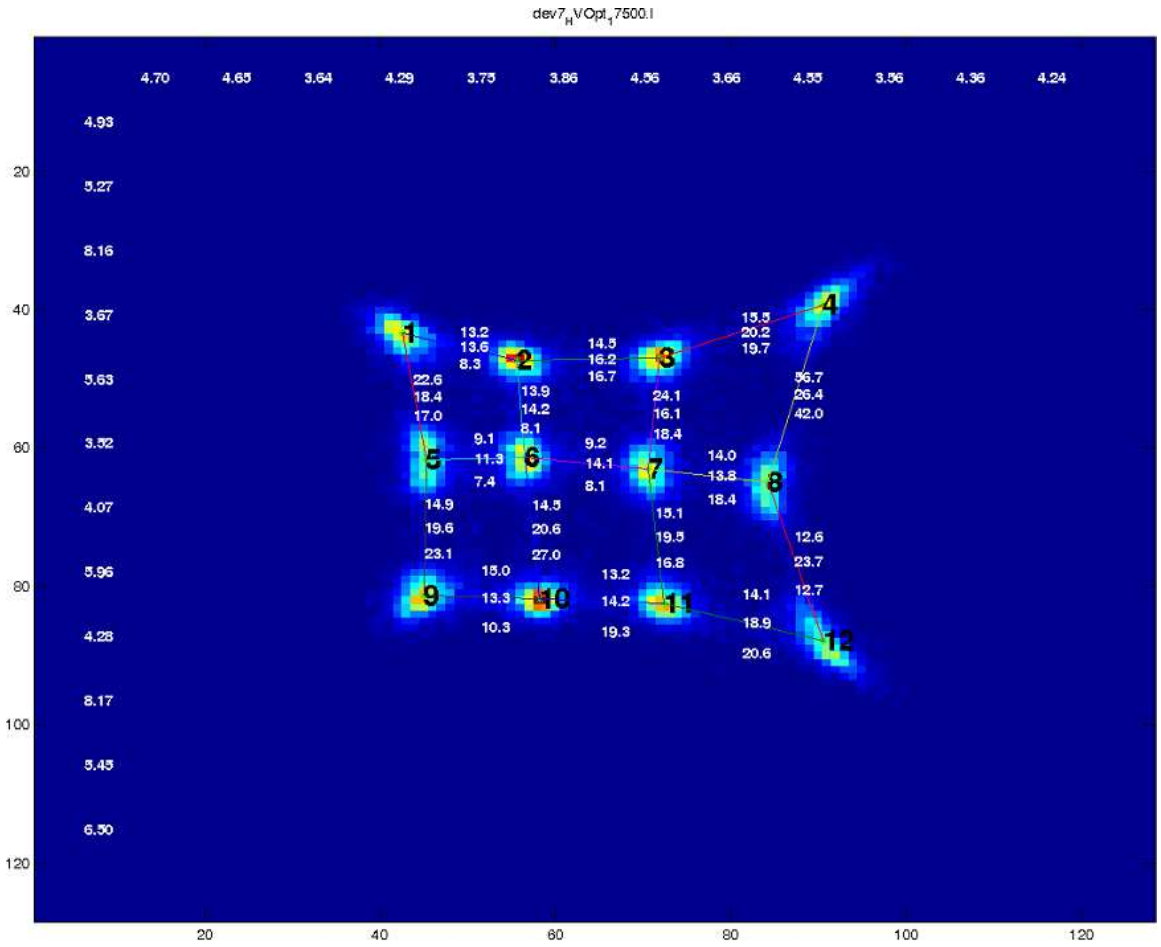

Figure 3.35: Flood image for 8 mm x 8 mm ceramic packaged single chip PSAPD at bias voltage = 1750 V

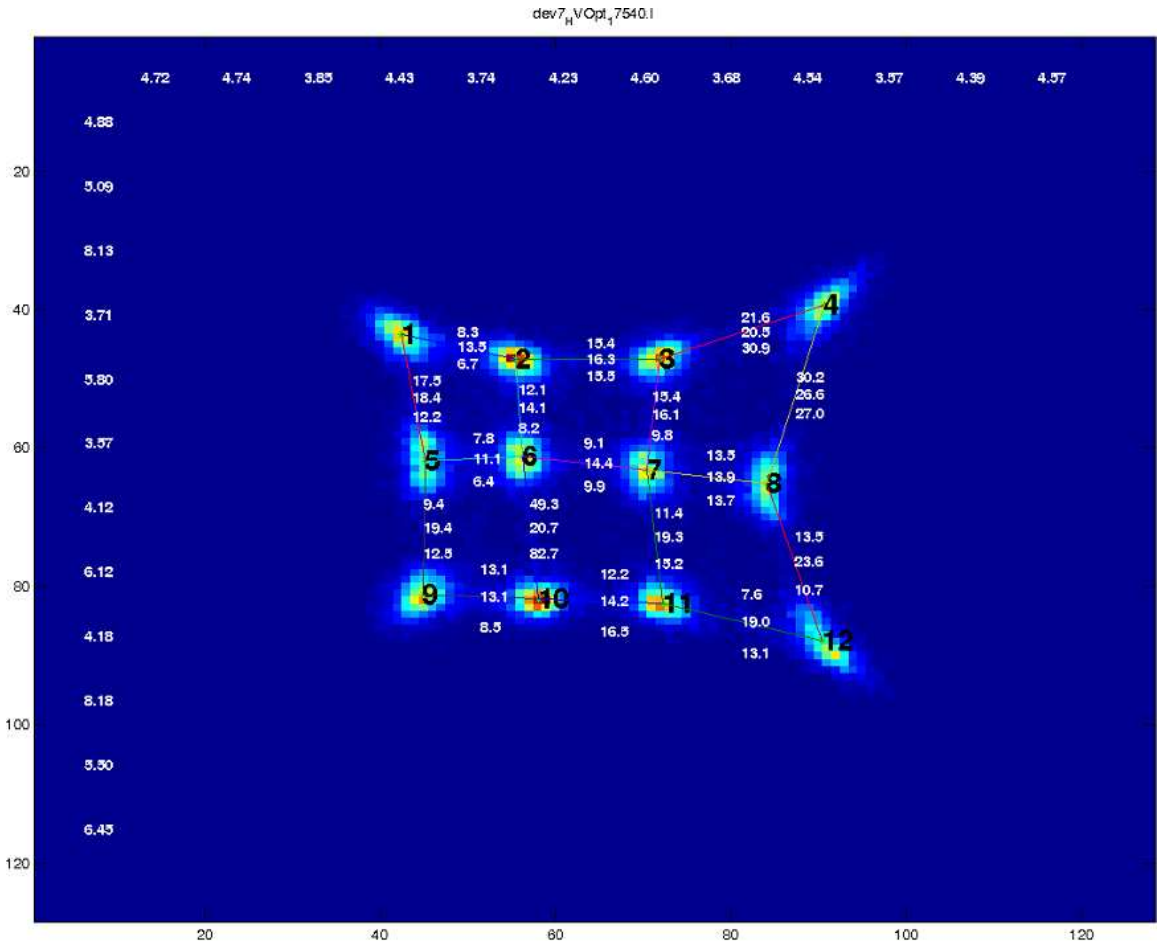

Figure 3.36: Flood image for 8 mm x 8 mm ceramic packaged single chip PSAPD at bias voltage = 1754 V

A summary of the 8 mm x 8 mm active area device data shown in each of the figures can be found in Table 3.5.

From the summary data shown in Table 3.5; inter-crystal distance, crystal size FWHM, and peak-to-valley ratio remains about the same across voltage steps. A large inter-crystal distance and a high PVR can signify better crystal resolution and crystal feature size should be small to resolve smaller crystals. Therefore, having slightly

Table 3.5: Position characteristics for the 8 mm x 8 mm active area 1.5 mm dead perimeter PSAPD single flex device at operating bias voltages in the neighborhood of optimal energy resolution.

Bias Voltage	Mean Inter-crystal Distance [pixels]	Mean FWHM [pixels]	Mean PVR
1705	17.2±4.1	4.9±1.3	19.8±14.2
1710	17.2±4.1	4.9±1.3	17.2±6.2
1720	17.2±4.1	4.8±1.3	21.2±13.7
1730	17.2±4.1	4.8±1.3	18.9±9.1
1740	17.3±4.0	4.8±1.3	20.5±11.5
1750	17.3±4.1	4.8±1.3	17.2±9.6
1754	17.3±4.1	4.9±1.3	16.7±14.5

better PVR and mean inter-crystal distance, 1740 V was chosen for all subsequent measurements on devices.

3.4.2 Flood Measurements and Crystal Identification

The flood measurements for all four devices with 1.5 mm-width dead perimeter are shown in Figure 3.37, each taken at an operating bias voltage of 1740 V. Note that the first of the 14 mm x 14 mm active area devices and the second of the 8 mm x 8 mm active area devices were not able to produce position-resolved images. Bias voltages throughout the safe operating regime were tested for the first and fourth devices shown in Figure 3.37, but no operating voltages which produced spatial resolution. The devices were operated at 1740 V to produce the displayed flood images for direct comparison. For the devices with no available spatial characterization, as flood image results could not be obtained, only coincidence time resolution studies

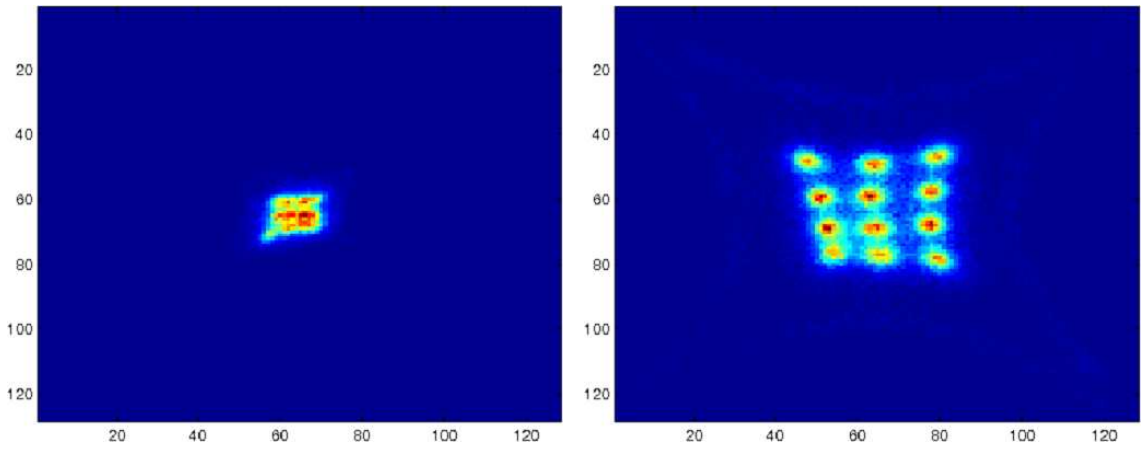

(a) first device with 14 mm x 14 mm active area (b) second device with 14 mm x 14 mm active area

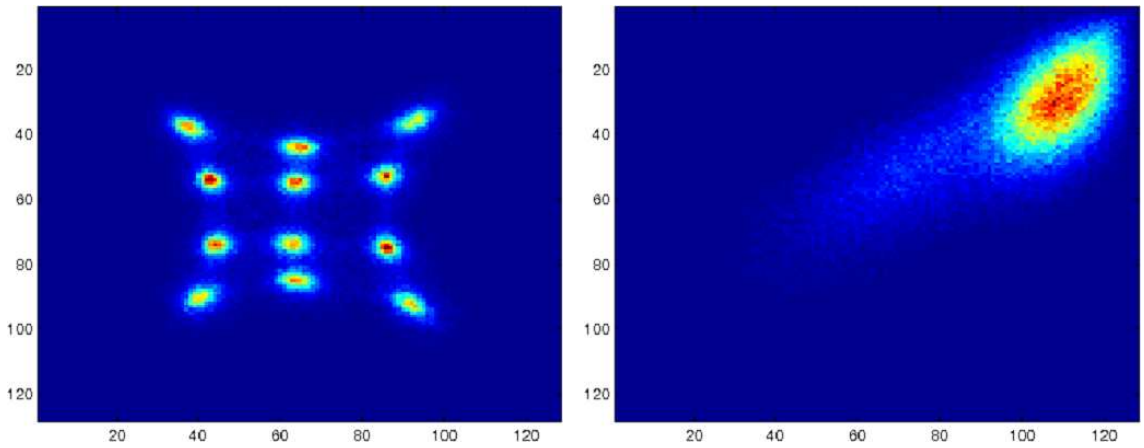

(c) first device with 8 mm x 8 mm active area (d) second device with 8 mm x 8 mm active area

Figure 3.37: Flood images of the four single chip on flex circuit, 1.5 mm-width dead perimeter, PSAPD devices tested.

were performed.

For comparison with the 8 mm x 8 mm active area position characterization data, the flood map from the 14 mm x 14 mm active area single chip module with a 1.5 mm dead perimeter was also studied for spatial characteristics at 1740 V. Figure 3.38

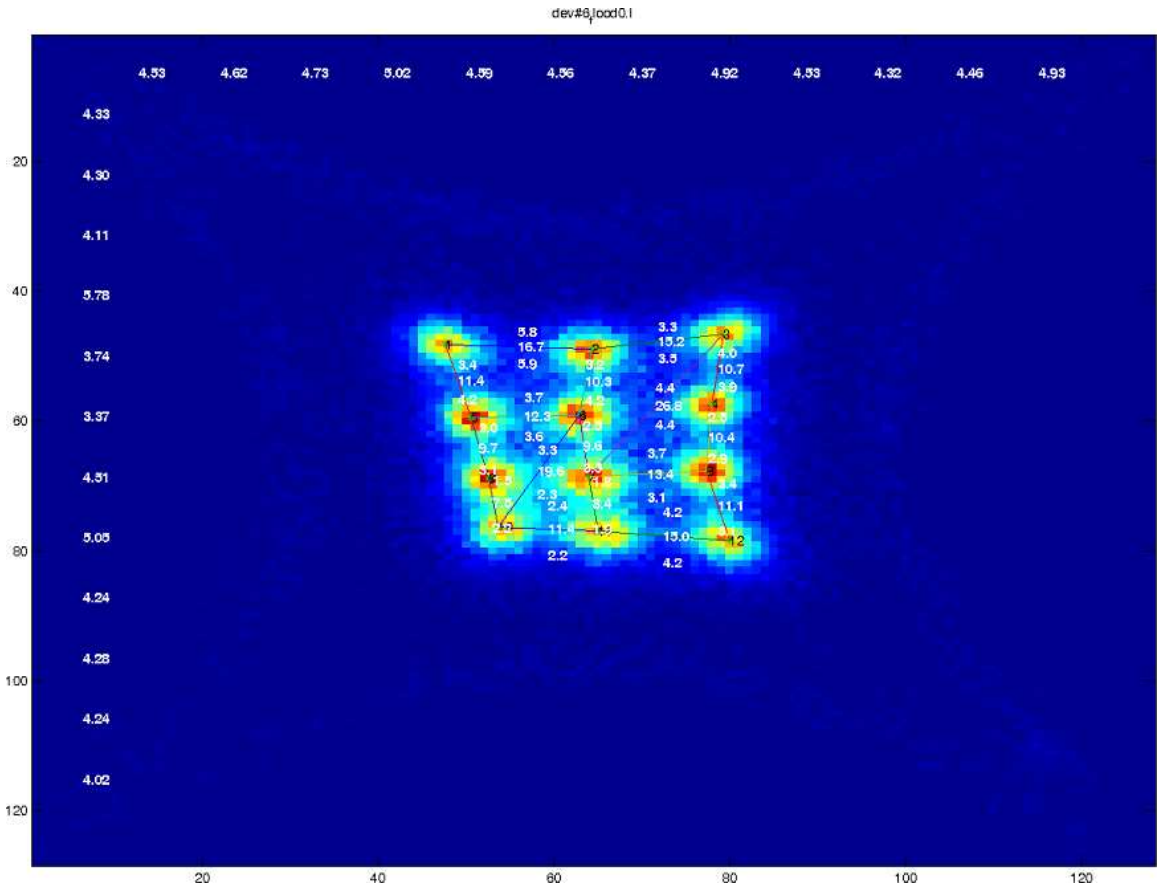

Figure 3.38: Analyzed flood image for the 14 mm x 14 mm, 1.5 mm-width dead perimeter, position-sensitive active area device.

shows the flood map with associated measurements. Note the smaller dynamic range of the flood image for the 14 mm x 14 mm active area single chip module versus that of the 8 mm x 8 mm active area single chip module (see Figure 3.37 for comparison). Figure 3.39 shows the portion of the flood map with just the positioned crystals. The data obatained from crystals that were not neighboring one another were discarded (indicated by diagonal lines). The mean inter-crystal distance was 11.6±2.6, the mean crystal FWHM was 4.5±0.5 and the mean peak to valley ratio was 3.4±1.0.

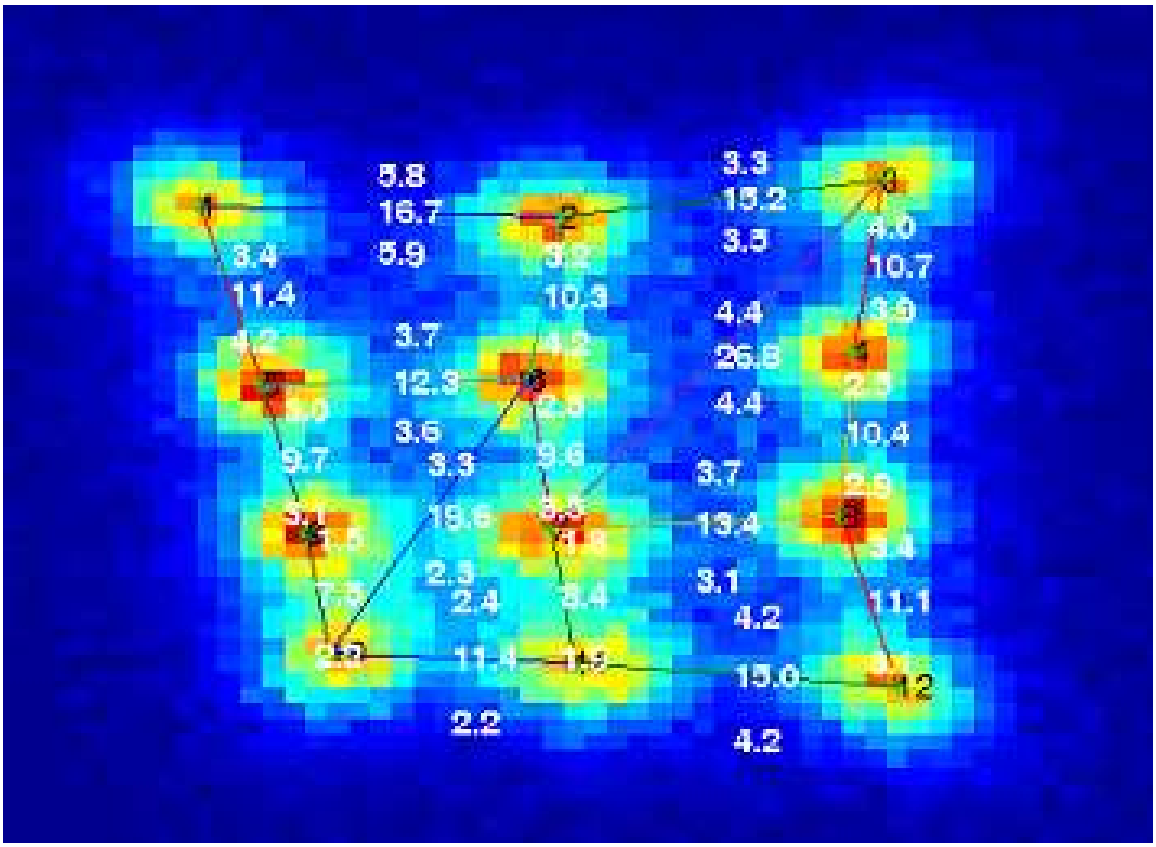

Figure 3.39: Expansion of the positioned crystal region in the flood image for the 14 mm x 14 mm, 1.5 mm-width dead perimeter, position-sensitive active area device.

Comparing the 8 mm x 8 mm active area device data, while operating at the same 1740 V, to the results for the 14 mm x 14 mm device, the 8 mm x 8 mm device had nearly 50% higher crystal separation, with a 6.9% larger crystal FWHM, and a 508% larger peak to valley ratio. These results indicate that the 8 mm x 8 mm active area device can better determine interaction location within the device.

3.4.3 Energy Resolution

Per-crystal energy resolution was assessed for the two devices that produced position-resolved flood maps. Table 3.6 shows the per-crystal energy characteristics measured using the 14 mm x 14 mm active area device, and 3.7 shows the same information measured using the 8 mm x 8 mm active area device.

Table 3.6: Energy characteristics for the 14 mm x 14 mm active area 1.5 mm dead perimeter PSAPD single flex device at operating bias voltages in the neighborhood of optimal energy resolution.

Crystal	Peak Position [V]	Energy Res. [%]	PVR
1	3.2	14.3	8.5
2	3.4	13.8	8.6
3	3.4	14.2	7.9
4	3.3	14.2	7.3
5	3.3	13.7	8.6
6	3.3	13.2	7.9
7	3.2	14.1	7.1
8	3.3	14.3	7.4
9	3.3	14.7	9.5
10	2.9	16.3	7.0
11	3.2	15.7	6.2
12	3.2	14.4	6.2

The mean peak position for the results for the 14 mm x 14 mm active area device shown in Table 3.6 was 3.2±0.1 V, the energy photo peak to valley ratio was 7.7±1.0, and the energy resolution was 14.4±0.9%.

The mean peak position for the results for the 8 mm x 8 mm active area device shown in Table 3.7 was 3.7±0.2 V, the energy photo peak to valley ratio was 8.2±1.8, and the energy resolution was 11.9±1.1%. Therefore, the mean energy resolution for

Table 3.7: Energy characteristics for the 8 mm x 8 mm active area 1.5 mm dead perimeter PSAPD single flex device at operating bias voltages in the neighborhood of optimal energy resolution.

Crystal	Peak Position [V]	Energy Res. [%]	PVR
1	3.8	11.8	7.1
2	4.0	10.4	7.0
3	3.7	12.5	6.7
4	3.8	11.0	9.3
5	3.9	10.7	11.7
6	3.6	12.5	6.8
7	3.7	11.9	8.2
8	3.9	10.7	10.6
9	3.6	13.4	6.6
10	3.4	13.4	6.8
11	3.7	11.7	9.7
12	3.5	13.1	7.3

the 8 mm x 8 mm active area device was 17.2% smaller, and the photopeak to valley ratio was 6.1% higher. These results show that the 8 mm x 8 mm device can better determine energy.

3.4.4 Coincidence Timing Measurements

Coincidence timing measurements were made using the method described in Section 3.2.7. These measurements were performed for all four single chip 1.5 mm-width dead perimeter PSAPD devices.

Converting voltage into nano seconds for each of the devices, using the results shown in Figure 3.40, the mean coincidence FWHM was 4.1±0.4 ns, 10.9±0.3 ns, 5.0±0.2 ns, and 4.7±0.2 ns, for the first through fourth device respectively. Therefore,

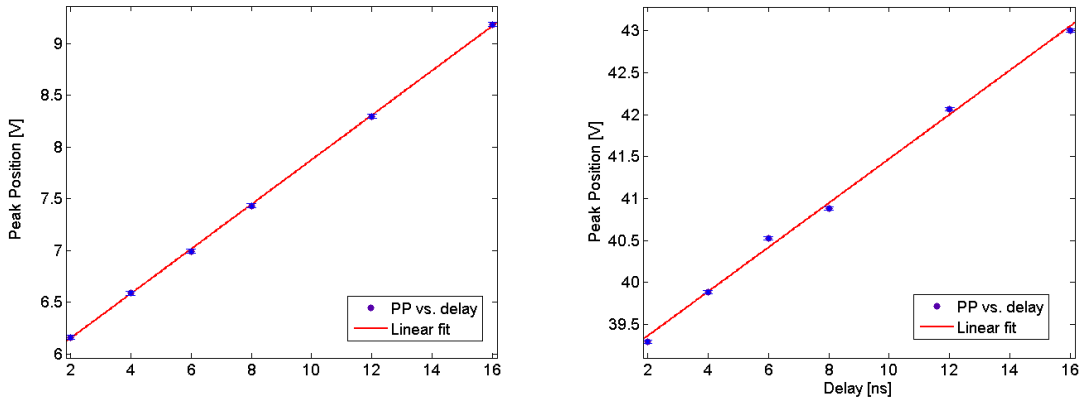

(a) first device with 14 mm x 14 mm active area (b) second device with 14 mm x 14 mm active area

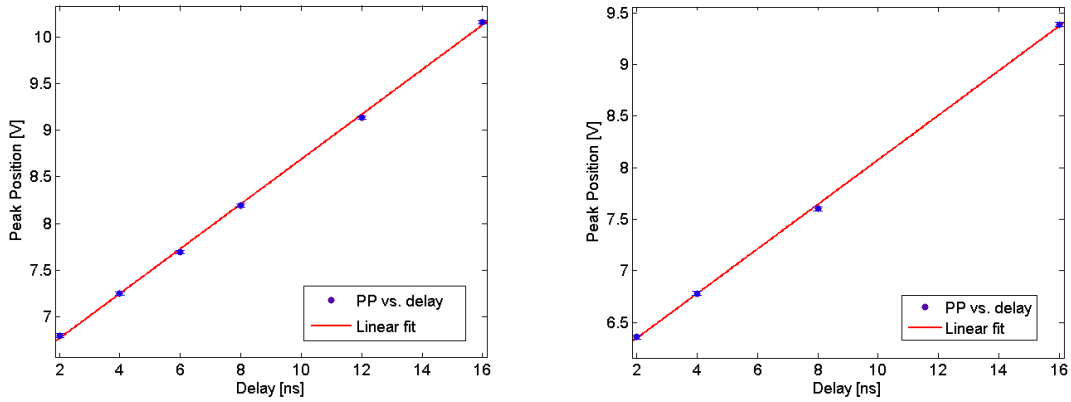

(c) first device with 8 mm x 8 mm active area (d) second device with 8 mm x 8 mm active area

Figure 3.40: Coincidence timing calibration data for the four single chip on flex circuit, 1.5 mm-width dead perimeter PSAPD devices tested.

for the two devices with positioning capability, the 8 mm x 8 mm active area device had 54% of the coincidence time resolution value. Consequently, the 8 mm x 8 mm device had superior performance determining interaction time.

3.4.5 Discussion

In each of the tested categories: position, energy and coincidence time properties, the 8 mm x 8 mm active area device outperformed the 14 mm x 14 mm active area device. These results confirmed the findings in the same two active area designs tested on the ceramic substrate. The 8 mm x 8 mm active area device was chosen as the design with which all further experiments were performed.

3.5 Single-Chip Flex Modules with a Dead Perimeter of 1.0 mm

3.5.1 Introduction

A new device was introduced by Radiation Monitoring Devices, Inc.[2] (RMD) during the characterization effort which reduced the dead area around the outer edge of the chips from a 1.5 mm thick perimeter to a 1 mm thick perimeter. The active area of the devices remained about the same, so the total surface area of the new devices were 10 mm x 10 mm and 16 mm x 16 mm. This reduction in dead area ultimately increases the packing fraction of the detector system, increasing the stopping power of the detector per volume, but this reduction in dead-area then requires a greater number of devices in order to cover the same detection volume.

[2]Radiation Monitoring Devices, Inc., 44 Hunt Street, Watertown, MA 02472 Phone: 617-668-6800, 800-LEAD-RMD (800-532-3763), Fax: 617-926-9980, Email: info@rmdinc.com

The results of the characterization work on these devices are summarized below, but can be found in their entirety in Reference [193].

3.5.2 Investigated Features and Results

Energy Resolution

Both 4 x 3 and 8 x 3 arrays were investigated and the results are summerized in the following Table 3.8:

Table 3.8: Energy Spectra Characteristics for the 1 mm dead perimeter PSAPD single flex device.

Array	Attribute	Value	Units
4 x 3	Peak Position	5.1±0.0	Volts
	Counts	2293±49.5	photons
	Energy Resolution	10.9±0.7	% at 511 keV
	Best Energy Res	10.0	% at 511 keV
	Worst Energy Res	11.9	% at 511 keV
8 x 3	Peak Position	5.7±0.0	Volts
	Counts	1604±53.8	photons
	Energy Resolution	12.9±1.2	% at 511 keV
	Best Energy Res	10.0	% at 511 keV
	Worst Energy Res	17.4	% at 511 keV

Coincidence Time Resolution

The measured coincidence time resolution with FWHM energy gating was 2.0±0.3 ns.

Position Gated Information

The sum of raw scanning data showed that the polished crystals have higher light output than the ground crystals. The 1 mm dead perimeter flex PSAPD clearly resolved the entire 8 x 3 crystal array in the sum image. Analysis showed the polished crystals also had better average ER, 12.5±1.2% vs 14.7±1.3%, than ground crystals.

Along the 1 mm length of the crystals in the array, the average FWHM of raw PSFs was 1.3±0.1 mm. With photon beam size deconvolution, the intrinsic SR was 1.1±0.1 mm.

Along the 3 mm length of the polished and ground crystals, the average FWHM of the point spread functions for the ground and polished crystals were 3.0±0.1 mm and 3.0±0.1 mm, respectively. The difference in CSR for the ground and polished crystals were due most likely to the smaller size of polished crystals.

Discussion

The 1 mm dead perimeter, flex circuit mounted, PSAPD had comparable energy and time resolutions to the ceramic packaged standard PSAPD, and it also generated ∼40% higher photopeak pulse height. The 1 mm dead perimeter Kapton-packaged PSAPD also showed better crystal identication ability than the 1.5 mm dead perimeter ceramic device. Energy resolution and coincidence time resolution measurements were comparable.

3.6 Dual-Chip Flex Modules

3.6.1 Introduction

The data and results of this section were previously published in Reference [50]. The small size, high quantum efficiency, and high spatial resolution of semiconductor photodetectors when coupled to the high-Z scintillator crystals commonly used in positron emission tomography (PET) have made them good candidates for use in detector systems. A novel position-sensitive avalanche photodiode (PSAPD) [159] has been developed by RMD and studied when packaged individually on a flex-cable readout circuit in our previous work [193].

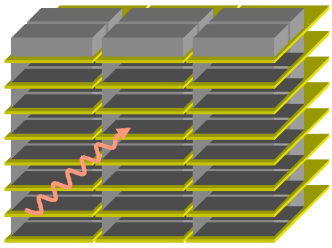

Figure 3.41: Shown is a portion of the designed system; 8 modules are stacked and then repeated in three columns. In the figure a red photon is incident, the modules consist of grey LSO crystal sitting atop two dark grey PSAPDs (1 cm x 1 cm) and yellow flexcable. The top row of crystals is opaque, showing their relative location; and the rest of the levels are transparent, showing the PSAPD underneath. In this geometry, incoming photons see a minimum of 2 cm thick LSO.

In order to increase the stopping efficiency and effective photon sensitivity of a detector system based on this technology, a module that consists of two thin PSAPDs mounted on a single flex cable readout circuit was designed and tested (see illustration

of a portions of the system in Fig. 3.41).

Figure 3.42: Picture of two silicon chip PSAPDs (black squares) on one flex cable (yellow material). The module is mounted to glass with tape to rigidly secure the structure during movement and coupling to acquisition electronics.

Previously, a flex-circuit with a single PSAPD chip mounted on a flex-cable read-out circuit [193] was tested. In this study, two chips mounted on a single flex-cable were tested as well as the degree of inter-device cross-talk due to their close-proximity. In a single module, the chips are only $\sim 50\mu$m apart, both sensitive to ambient EM fields, and require approximately 1700 Volts of biasing voltage. It was not obvious that the performance characteristics of each of the PSAPDs on this dual-chip version would be the same as that achieved by one PSAPD chip mounted on the flex-circuit. Energy, spatial and coincidence time resolution were measured with both devices biased. One of the modules tested is pictured in Figure 3.42.

3.6.2 Methods

A high-voltage supply and readout board was constructed to read-out and deliver bias to the two PSAPDs through the single flex-circuit. Positioning for the PSAPD is calculated using signals from the four corner anodes in the traditional manner.

All measurements were made using a 10 μCi, 500μm diameter, ^{22}Na point source. The same array of 1 x 1 x 3 mm^3 lutetium oxyorthosilication (LSO) crystals was optically coupled to both of the PSAPDs on the flex cable for each study performed. The crystals were coupled by one of their 1 x 3 mm^2 faces, to form a 8 x 3 crystal array, 8 mm x 9 mm in area, on the face of the device. The array was wrapped in 12 layers of Teflon to provide a reflective surface, but had no reflective material between the individual crystal elements. For each measurement, both devices were biased together, with the same voltage supply. Parameter optimization experiments have determined optimal device operation is obtained with a bias between 1680 and 1760 V.

Spatial crystal identification was measured for the devices by using flood irradiation and by acquiring the four spatial channels of the irradiated device. Events were triggered by the sum of the four corner channels. Energy resolution was determined by fitting two Gaussians to the photopeak - one for 511 keV events, and one for 511 keV - 63 keV events where the 63 keV x-ray produced in the photoelectric interaction escaped the crystal. As these crystals are tiny, the occurrence of an x-ray escaping

the crystal of interaction happens a measurable amount of the time.

Coincidence time resolution was measured using the same ^{22}Na point source between the PSAPD, in alignment with a 1 cm diameter Hamamatsu H3164 photomultiplier tube (PMT), which had a 3 mm x 3 mm x 8 mm piece of LSO crystal attached as the scintillation material. The events were triggered by a timing separation of less than 50 nanoseconds between an energy gated common signal of the PSAPD and an energy gated 8th (last) dynode signal of the PMT.

Cross talk was measured in two ways: (1) by acquiring spatial signals for one of the devices on a flex-circuit while irradiating a crystal array coupled to the other PSAPD and (2) by acquiring spatial signals from the irradiated device as well as the common channel of the unirradiated device.

3.6.3 Results and Discussion

Crosstalk

Cross talk between the two devices was measured and is compared in Figure 3.43 with the data acquired in both PSAPDs for the same acquisition time. The number of events recorded in the non-irradiated compared to the irradiated PSAPD was three orders of magnitude lower across all energies, including in the photopeak. This is an indicator that the devices are electrically isolated relatively well from one another, i.e., in general, readout or current generation from one device will not in general

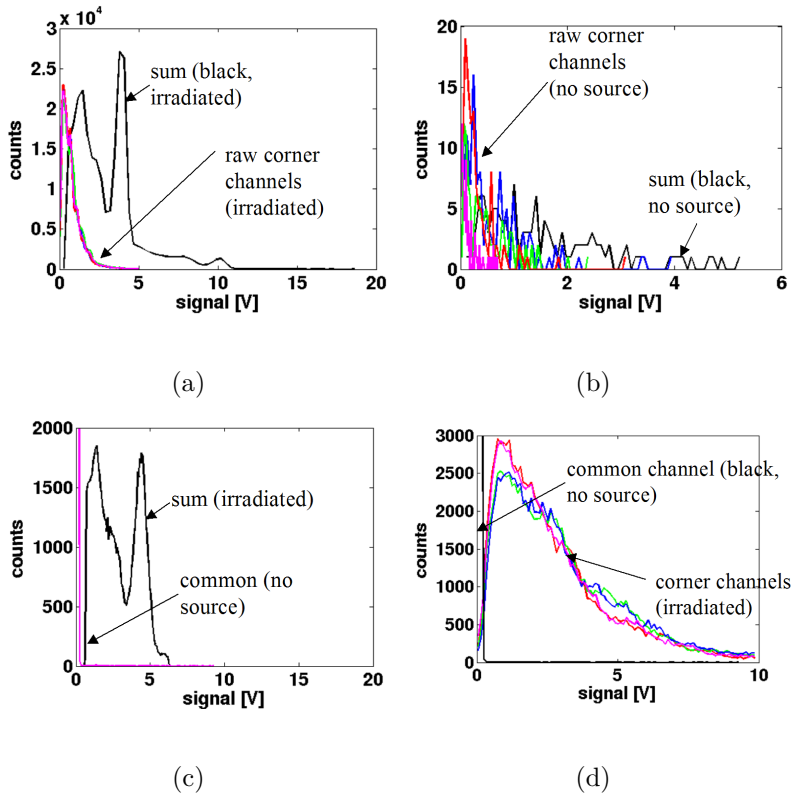

Figure 3.43: Top, Left: Signals from the corner anodes for the irradiated device with an LSO array of 2 x 2 x 3 mm^3 crystals and, Top, Right: adjacent PSAPD chip device with no LSO crystal coupled to it. The black line is the sum of the four corner anodes, which are shown in magenta, red, green and blue. Bottom, Left: The sum of the corner signals (black), compared to the common signal from the un-irradiated device with no crystal coupled (magenta). Bottom, Right: Signals from the 4 corner channels compared to the common channel (black) of the un-irradiated device.

trigger a spurious event from the neighboring chip.

Crystal Identification

Shown in Fig. 3.44 are typical results of flood irradiation of segmented LSO arrays optically coupled to one of the PSAPD chips with both chips biased. Figure 3.44 is an 8 x 3 array of 1 x 1 x 3 mm^3 crystals, with no inter-crystal reflector, coupled to

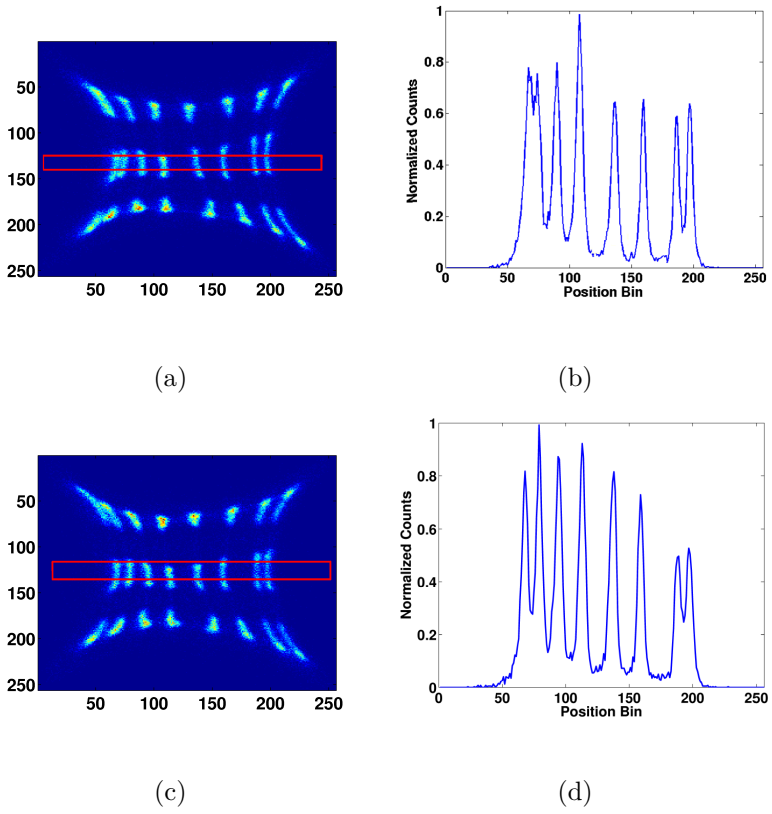

Figure 3.44: Array of 1 x 1 x 3 mm^3 crystals with no inter-crystal reflectors. Left: Histogrammed position from a flood irradiated LSO array coupled to one of the PSAPDs. Right: Profile through the bins bounded in the red box shown in the figure on the left. Top: array irradiated on the PSAPD closest to the signal leads (inner), Bottom: array irradiated on the PSAPD farthest from the signal leads (outer).

each of the PSAPDs on one dual-chip module. Crystals are identified and results are comparable to previous results achieved with one PSAPD per module. Profiles were taken through the middle row of each array shown on the left hand side of Fig. 3.44. The average peak to valley ratio for the inner chip was 11.3 and was 10.9 for the outer chip.

For comparison, a segmented crystal array manufactured by Agile Engineering,

made of LSO, each crystal having a size of ∼1 mm on a side, was coupled to the inner PSAPD on the flex circuit (Fig. 3.45). This array has a thin layer of reflective material between the crystals, and the exposed edges of the array that was not coupled to the PSAPD were wrapped in 12 layers of Teflon. The average peak-to-valley ratio was 5.5, with the minimum PVR being 3.

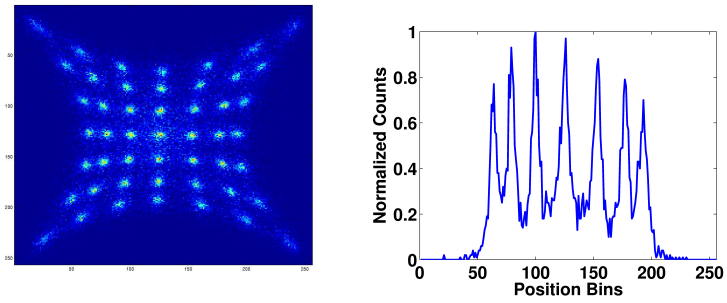

(a) (b)

Figure 3.45: a) Flood histogram of a 7 x 7 array with inter-crystal reflector, and b) profile through the center row of crystals.

Energy Spectra Features per Crystal

Energy spectra were extracted for each crystal in the array coupled to the PSAPD. Figure 3.46a and 3.46b show the individual energy spectra for the array coupled to the inner and outer PSAPDs, respectively. Figure 3.46c shows the energy spectrum of a common crystal in the array after compton edge subtraction. The average counts per crystal were 960±98 for the inner PSAPD and 921±104 for the outer PSAPD. The average ER at 511keV for the 24 crystals was 10.0±4.5%, very similar to previous

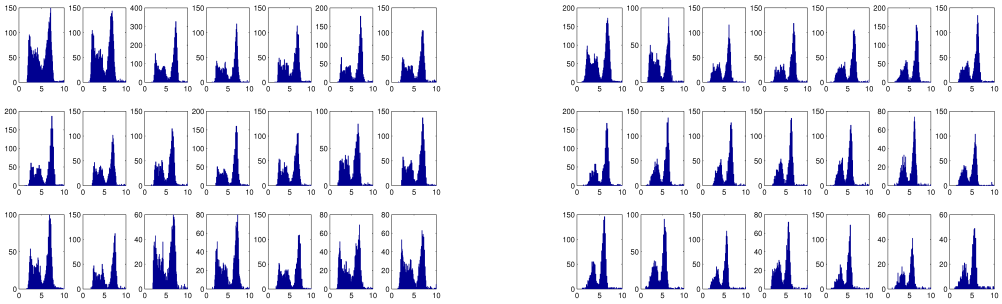

(a) (b)

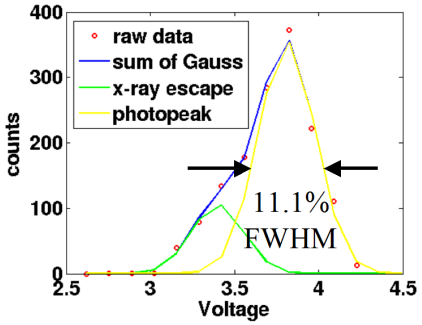

(c)

Figure 3.46: Individual energy spectra for each crystal on the a) inner and b) outer PSAPD. c) Two Gaussian fit to energy spectra data from a typical crystal in the 8 x 3 array. The yellow Gaussian indicates the distribution when all energy from the photoelectric interaction is deposited into the crystal, the green Gaussian shows the events where the x-ray produced in the PE interaction escaped from the crystal.

measurements.

The photopeaks were very well resolved from the Compton edge, and the photopeak-to-valley ratios for the position gated energy spectra were very high: 32 $\pm$ 16.5 and (with the smallest being 13) and 31 $\pm$ 24 (with the smallest being 8) for the outer and inner PSAPD respectively.

Coincidence Timing Resolution per Crystal

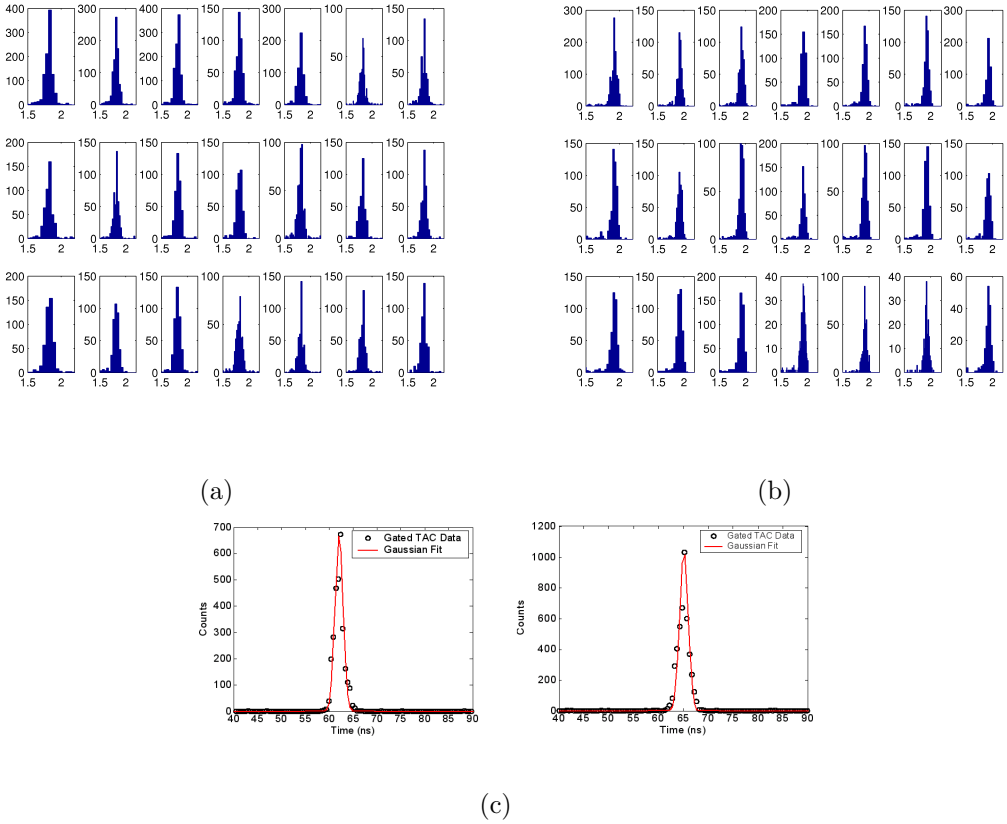

Figure 3.47: Individual coincidence timing spectra for each crystal on the a) inner and b) outer PSAPD. c) A typical coincidence timing spectrum and its Gaussian fit.

Coincidence timing was measured for both the inner and outer PSAPDs on both modules, for each individual crystal, with the PMT and PSAPD energy gate applied for that particular crystal. The inner PSAPD had an average coincidence time resolution of 3.7 ns $\pm$ 0.3 ns, with a peak position standard deviation of 0.14 ns. For the outer PSAPD, the average coincidence time resolution was 3.8 ns $\pm$ 0.3 ns, with a peak position standard deviation of 0.16 ns. The peak position varied a small fraction

(∼5%) of the full width half maximum for all crystals on both the inner and outer chip, making the coincidence time parameters (resolution and window offset) on the face of the chip nearly independent of position.

3.6.4 Conclusions

In most of the performance parameters measured, the results from the PSAPDs on the dual-chip flex-cable mounted modules tested were comparable to results obtained when only one PSAPD was packaged per module, and both chips on one module were comparable to each other. Spatial crystal identification and energy resolution for an 8 x 3 array of LSO crystals were very similar to one-PSAPD results, with the average energy resolution of 10.0%±4.5% and peak to valley ratio of 11 across the chips. Coincidence timing resolution measurements showed a higher jitter in the timing spectra compared to the ceramic ([96] and Section 3.3) and 1 mm dead perimeter single chip flex modules previously tested ([193] and Section 3.5), but similar to the 1.5 mm dead perimeter single chip flex modules (Section 3.4), with an average timing resolution of approximately 3.75 ns. Improvements in timing acquisition and shaping electronics parameters may be possible however, because directly observing the jitter of the PSAPD timing signals on the oscilloscope showed less than 1.8 ns time width.

3.7 Conclusions

The commercial ceramic-packaged position sensitive avalanche photodiodes coupled to lutetium oxyorthosilicate scintillation crystal were shown to provide excellent spatial identification (∼1 mm), energy resolution (10-12% of 511 keV), and coincidence time resolution (2-3.3 ns). Two designs were tested, differing in electrical properties most notibly in capacitance and hence dark current noise. This capacitance difference is likely the cause of the superior performance by the smaller active area PSAPD (8 mm x 8 mm versus 14 mm x 14 mm) in position, energy and coincidence time experiments.

The same two chip designs were tested alone in novel packaging, where a Kapton polyimide flex circuit provided electrical coupling between supply bias voltage to the chips as well as signal read-out from all anodes of the chip. These tests showed that nearly all figures of merit tested; e.g., bias voltage optimization (1740 V), position identification (∼1 mm), and energy (10-12.6% of 511 keV); showed similar results to the ceramic-packaged devices. Coincidence time resolution had a higher blur (4-9 ns), but this was likely due to a deficit in the optimization of new test equipment. These tests were duplicated with a further iteration of the PSAPD design structure with the chosen 8 mm x 8 mm active area feature, and the coincidence time resolution was restored to the ceramic-packaged value (∼2 ns - see Section 3.5).

Kapton packaged flex circuits with two PSAPD detectors electrically coupled were

then tested in the same manner as the previous design steps. Position identification, energy resolution, and coincidence time resolution were all similar to previous measurements. Cross-talk between the two devices on a single read-out circuit was tested, with very little inter-chip signal triggering observed. Read-out or current generation from one device, in general, will not trigger a spurious event from the neighboring chip. Moisture did prove to be a problem with this new design and devices had to be tested in a dry Nitrogen environment. Further designs have been made to the flex circuit and chip mounting procedure which will optimistically reduce the environment controls necessary to operate the device.

Chapter 3, in part, is a reprint of the material as it appears in IEEE Transactions on Nuclear Science, Volume 53, Issue 5, Part 1, Oct. 2006 Page(s):2549 - 2556; and in the Journal of Nuclear Medicine Vol. 44, No. 5, May 2003, p.138. The dissertation author was a primary investigator and author of these papers.

Chapter 4

Scintillation Crystal Characterization and Selection

4.1 Introduction

The studies contained in this chapter were performed to design a high-sensitivity, high-resolution small animal positron emission tomography (PET) system for studying the kinetics and mechanisms of human disease in small laboratory animal models. Most high-resolution imaging systems in use as well as those in development are incorporating increasingly smaller pixellated scintillation crystals to try to improve system resolution [97, 170]. In order to increase the detection efficiency of the annihilation photons, the crystals were made long in the direction of the incoming photons. In standard PET detector designs, the photodetector is coupled to the thin crystals on

the side with the smallest cross-sectional area, giving them an aspect ratio that does not promote optimal light output [95, 98]. This coupling geometry results in a compromise between system resolution, light output (effectively energy resolution) and sensitivity [28, 74, 76, 139].

Traditionally, PET detectors are made using scintillation crystals coupled to photomultiplier tubes (PMTs). Both segmented arrays, as well as continuous scintillation crystals, have been coupled to PMTs and position-sensitive PMTs (PSPMTs) to achieve high detector spatial resolution. For example, in the work by Simon Cherry, et al. [32], continuous crystals are coupled to an array of photomultiplier tubes to determine continuous positioning. PMTs and PSPMTs, however, are large and resulting system configurations compromise either system solid-angle coverage or crystal packing fraction. There are definite advantages to this technology including that they are well characterized and relatively low in cost.

Recently developed detectors such as very thin position-sensitive avalanche photodiodes (PSAPDs) devices (described more thoroughly in Chapter 3) allow a compact detector system, including photodetectors and the necessary electronics for signal acquisition. The thin PSAPD presented in Chapter 3 allows more advantageous scintillator coupling geometries and detector orientations, which significantly improve the sensitivity, energy resolution and spatial resolution (Figure 4.1). With such small detectors, the packing fraction does not change significantly for various detector orientations. Crystals can then be coupled so that the aspect ratio is high (the PSAPD

surface normal is perpendicular to the incoming photon direction), without reducing intrinsic sensitivity.

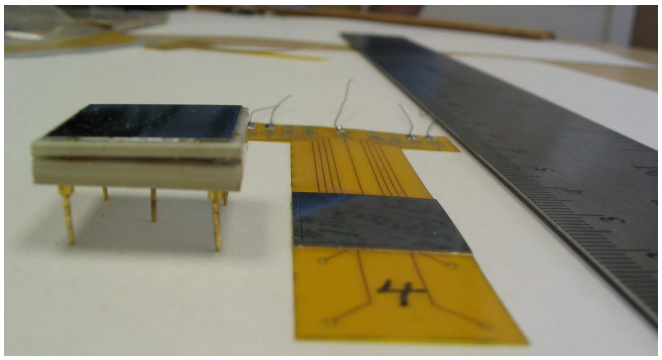

Figure 4.1: Left: the studied prototype PSAPD, center: the thin PSAPD to be used in system construction.

A pixellated crystal design facilitates spatial linearity across the entire face of the position-sensitive detector [167]. If the photo-detector has a higher intrinsic spatial resolution, the use of a continuous scintillator might provide superior spatial resolution to a discrete crystal design. A continuous scintillator also reduces manufacturing complexity and increases mechanical robustness of the detector system. Both designs will be evaluated in this chapter.

The system described throughout this document uses the detection configuration mentioned in Section 2.2.1, i.e. a scintillator coupled to a photodetector. In this detection method, the scintillation material is used to convert high energy annihilation photons into lower energy, traditionally visible photons. Photons produced by the scintillator ideally lie entirely in a high quantum efficiency wavelength band of the selected photodetector.

Features to consider when selecting a scintillator are discussed in the next section. Analysis methods used to choose between scintillator configurations can be found in Section 4.3. The analysis methods section is followed by results from experiments performed on various designs. Discussion of the results and future directions can be found in the last two sections of this chapter.

4.2 Scintillator Design

Physical aspects both on the microscopic and macroscopic scale contribute to the performance of scintillators. Atomic and lattice considerations are discussed in Section 4.2.1 and crystal shape and coupling configurations can be found in Section 4.2.2.

4.2.1 Material Selection

This section focuses on the aspects affecting absorption and production of light in lutetium oxyorthosilicate (Lu_2SiO_5 or LSO), as compared to other common inorganic scintillators used in PET. A discussion of the general interaction model for photons with energies above 1 keV in materials can be found in Section 7.2.

Interaction Properties

The effective atomic number (Z) and density (ρ) of a material plays a substantial role in the stopping power (linear attenuation coefficient) of materials (see Section 7.2). Recall that, for photon energies involved in PET, the cross-section (τ) for interaction is proportional to the fourth to fifth power of Z (depending on photon energy), and that linear attenuation coefficient (μ) is proportional to $\tau\rho$. Values of ρ, μ, and effective Z for various materials are shown for comparison in table 4.1 [31].

Table 4.1: Density, effective atomic number and linear attenuation coefficient at 511 keV for various materials. Scintillation crystal values from Reference [31], and the lead μ value is obtained from a rational fit (cubic over quadratic polynomial) using values obtained from NIST.

	NaI(Tl)	BGO	GSO(Ce)	LSO(Cs)	Lead
$\rho\ [\frac{g}{cm^3}]$	3.67	7.13	6.7	7.4	11.34
Z_{eff}	51	75	59	66	82
μ @ 511 keV $[\frac{1}{cm}]$	0.34	0.95	0.70	0.88	1.77

Lutetium oxyorthosilicate (LSO) has a relatively high μ at the annihilation photon energy, requiring smaller amounts of costly crystal than Thallium doped Sodium iodide (NaI(Tl)) or Cerium doped Gadolinium oxyorthosilicate (GSO(Ce)), and similar amounts as Bismuth germanate (BGO). All listed scintillators are commonly used in PET systems, with NaI being the most prevalent.

Further important considerations are the types of interactions photons will undergo in a material. The energy dependent photon cross-section for LSO is shown in Figure 4.2, showing contributions from scattering, photoelectric and total attenuation.

Photoelectric interactions are the most prevalent throughout the lower portion of the energy range, with the likelihood of photoelectric and Compton scattering equal at approximately 400 keV. At 511 keV in LSO, Compton scattering is 62%, photoelectric 32% and coherent scattering 6% of all initial annihilation photon interactions. Any annihilation photon that deposits all of its energy in the detector system undergoes a photoelectric interaction as the final interaction.

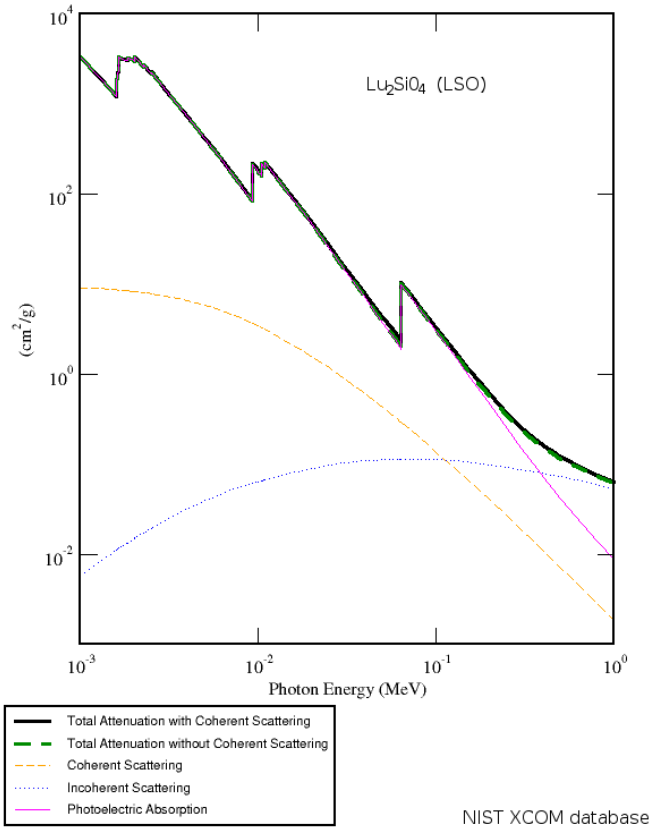

Figure 4.2: Photon cross section for LSO versus photon energy. Figure from the NIST XCOM database.

After considering annihilation photon interactions in scintillation materials, light production characteristics of the scintillator are the next key features to examine.

Scintillation Light Production

The light produced by a scintillator from an interaction must have the following features:

- (1) The number of scintillation photons produced must be proportional to the energy deposited by the interaction.
- (2) The light produced must be in a wavelength range in which the scintillator is transparent - or the scintillation photons will be absorbed before being detected.
- (3) The light produced during scintillation should be as short as possible so that further interactions in the crystal are not effected by previous interactions.
- (4) The number of scintillation photons produced must be large so that errors in counting photons (i.e. determining the energy deposited or the time at which an event occurred) are not large.
- (5) The index of refraction of the material is close to the index of refraction of the photodetector surface so that transmission into the detector is high.
- (6) The emission wavelength band of the scintillator is well matched to the wavelength band of the photodetector where the quantum efficiency is high.
- (7) The robustness of the material and its imperviousness to environmental conditions (such as humidity) is high.

Not all scintillators have all of the properties listed above. The comparison of various scintillators, in terms of: produced light pulse decay times, number of photons produced by an interacting photon per keV, index of refraction, peak emission wavelength (λ), and whether or not the material is hygroscopic are shown in table 4.2 [31].

Table 4.2: Light production parameters for various scintillators used in PET. Values obtained from Reference [31].

	NaI(Tl)	BGO	GSO(Ce)	LSO(Cs)
Decay time [ns]	230	300	60	40
Photon yield [per keV]	38	8	12-15	20-30
Index of refraction	1.85	2.15	1.85	1.82
Peak emission λ [nm]	415	480	430	420
Hygroscopic	Yes	No	No	No

Relating the index of refraction of LSO (1.82) to the materials used in the studies in this document, the optical coupling compound between the LSO and the position sensitive avalanche photodiode (PSAPD) photodetector was 1.465 and the PSAPD although made of silicon has a thin silicon dioxide entrance layer with index of refraction 1.46.

The emission spectra for various scintillators can be seen in Figure 4.3. The quantum efficiency plot as a function of wavelength for all of the PSAPDs[1] studied in this thesis is shown in Figure 4.4 [111, 158]. These data show that average quantum efficiency (QE) for LSO coupled to a PSAPD should be $\geq$60%. This can be compared

[1]Although the reference uses non-position-sensitive avalanche photodiodes for testing, the PSAPDs analyzed in this thesis were modified from this design in a region beyond the scintillation photon absorbing region. The quantum efficiency of the devices were therefore not affected.

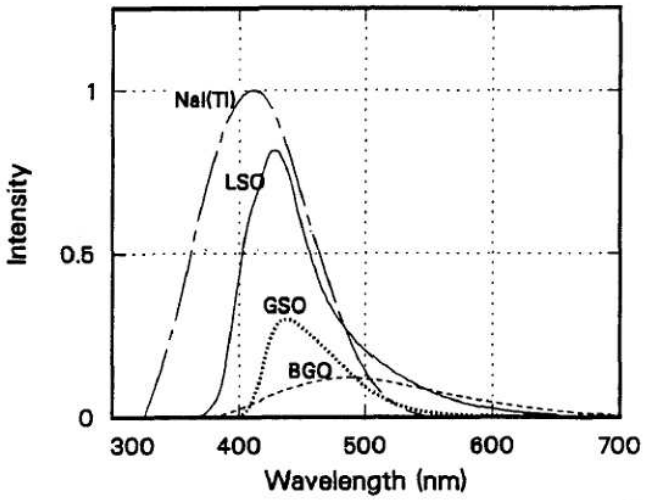

Figure 4.3: Plot of the emission spectra for scintillators listed in table 4.2. Plot obtained from Reference [111].

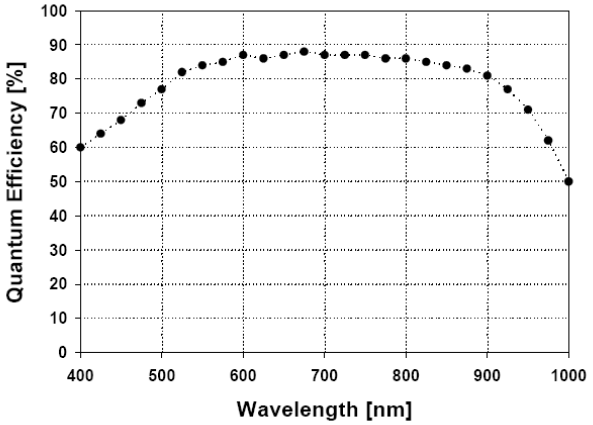

Figure 4.4: Plot of the quantum efficiency of tested PSAPDs in the emission range of LSO. Plot obtained from Reference [158].

to LSO coupled to a photomultiplier tube (PMT), which would have a QE of about 7-14% [29].

Combining the properties from tables 4.1 and 4.2, LSO stands out as a well rounded material. Its linear attenuation coefficient, decay time, and photon yield make LSO the material of choice for most up and coming PET systems.

4.2.2 Geometry

The size and shape of individual crystals, as well as how they are placed with respect to other crystals, affects a scintillator's ability to transfer light to a photodetector. A poor coupling geometry can lead to fewer counted scintillation photons. Another consideration is that inter-crystal cross-talk can lead to scintillation photons being absorbed at surfaces spread out over a large area of the photodetector. A brief discussion of these topics is contained in this section, but a more detailed account can be found in References [55, 98, 138, 195].

Scintillation light arriving at the photodetector undergoes a Possion process when producing a photocurrent, with an average efficiency of conversion given by the photodetector's quantum efficiency [55, 195]. The resulting shot noise is reduced proportionally as the number of scintillation photons per interaction increases. Energy, position, and time of an interaction are all estimated from the signal pulse produced by photocurrent production. Therefore, low efficiency transmission of scintillation light to the photodetector reduces the signal processing electronics' ability to estimate signal parameters (signal peak height, start time, etc.) and hense determine

these all-important values [138]. Care must be taken then in the design of coupling geometry, scintillator-photodetector adhesion mechanism, reflector placement, etc., to ensure optimal light transfer.

Coupling geometry has been shown to affect light output to photodetectors [98]. Aspect ratio is defined as the size of the largest dimension of the crystal along the face of the coupled photodetector divided by the dimension normal to the face of the detector, or width over height. When the aspect ratio of the crystal is high, the scintillation light does not reflect off the surfaces of the crystal many times, on average, as it travels through the volume of the crystal towards the detection surface.

Reflective material used on the edges of the crystal can help to keep scintillation light from exiting the crystal in which it was produced. Keeping light contained within the original crystal of interaction aids in keeping scintillation photons directed at the same section of the photodetector, decreasing edge effects (centroid overlapping, etc. - see an example in Section 4.4.4), light loss due to escape and absorption through surfaces, and reduction of variance due to counting and positioning non-linearities across the face of the photodetector.

All of the above mentioned factors point to short (in the direction normal to the face of the detector) crystal geometries. Two such geometries were investigated; a single sheet crystal coupled to the entirety of the face of the photodetector, and an array of segmented crystals.

4.3 Methods

4.3.1 Experimental Setup and Analysis

The methods used in the majority of this chapter are described thoroughly in Section 3.2 of Chapter 3, specifically measurement techniques (Section 3.2), positioning techniques (Section 3.2.2), and the devices used (Section 2.3). Acquisition electronics are described in Section 3.2.5. Some analysis concepts are introduced in this chapter, and will be discussed in the sections to which they are relevant.

4.4 Sheet Crystal

The data and results in this section were perviously published in Reference [52]. Using scintillation crystal sheets instead of discrete crystal arrays in high-resolution PET has the immediate advantage of reduced complexity as well as a potential for increased sensitivity. In order to evaluate the positioning capability of a position sensitive avalanche photodioide (PSAPD) using a sheet Lutetium Oxyorthosilicate (LSO) crystal scintillator, the dependence of detected event position versus the known source position was studied. In particular, positioning in a continuous 8 mm x 8 mm LSO sheet coupled to a PSAPD with an 8 mm x 8 mm active area was experimentally studied, optical transport in the sheet crystal was studied with Monte Carlo simulation, and two positioning methods were used to evaluate PSAPD "pincushioning" effects (see Section 3.2.2 for a discussion on device positioning and "pincushion"). Both collimated ^{57}Co 122keV and coincidence-triggered ^{22}Na 511keV sources were used in the experiments performed. Energy resolution, sensitivity, photopeak position and spatial resolution were analyzed as a function of source position.

4.4.1 Experimental Study

Figure 4.5 shows the collimation configuration that was used for each of the two sources. Physical collimation for the 122 keV ^{57}Co source was relatively straightforward using a few centimeters of lead (Figure 4.5a), whereas the 511 keV ^{22}Na source

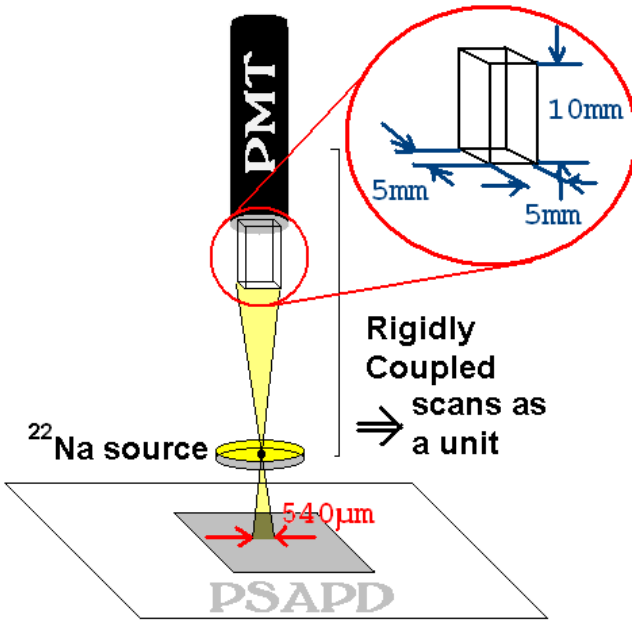

(a)

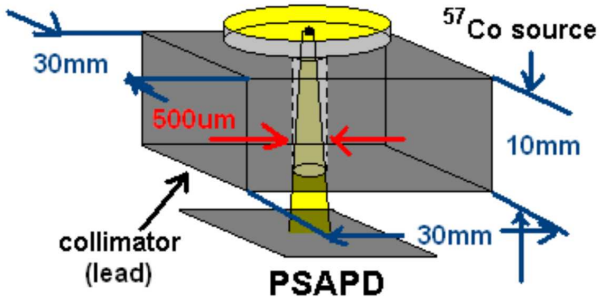

(b)

Figure 4.5: The acquisition setup for a) coincidence-collimated ^{22}Na annihilation photon detection with spot size ∼500 μm and b) lead collimated ^{57}Co gamma photon detection with spot size ∼500 μm.

required electronic collimation as the same lead collimator did not attenuate more than 10% of the 511 keV photons.

Common Setup

The ceramic PSAPD developed by RMD, Inc. with an active region of 8 mm x 8 mm (Figure 4.1, left) [97] was used in this study. An 8 mm x 8 mm x 1 mm LSO continuous crystal was coupled to the PSAPD with silicon optical grease (∼10 μm thick) and seven layers of Teflon were wrapped around the crystal to provide a reflector along the array surfaces not in contact with the PSAPD. A LabView-controlled, motorized, National Aperture MM-4M-EX-140 micro-stage was used to automate and accurately control the positioning steps across the detector. ^{57}Co (122 keV gamma) and ^{22}Na (511 keV annihilation photons) point sources were used to study the point spread function and spatial linearity of the PSAPD.

^{22}Na Setup

The highly energetic 511 keV photons from the 10 μCi, 500 μm diameter, ^{22}Na point source were electronically collimated using a coincidence setup which was constructed using a Hamamatsu H3164 photomultiplier tube (PMT) that was coupled to a Teflon-wrapped 5 mm x 5 mm x 10 mm LSO crystal with silicone optical grease (see Figure 4.5a). The LSO-PMT detector was mechanically coupled to the source at a distance of 190 mm and moved with the micro-stage in 160 μm steps. The source-to-PSAPD distance was kept at a constant 1.5 mm. The geometry of the setup resulted in a ∼540 μm spot size projected onto the face of the PSAPD, evaluated using the

following relationship:

$$\frac{5\text{mm}}{190\text{mm}} = \frac{x}{1.5\text{mm}} \tag{4.1}$$

where x is the additional extent of the spot size due to the width of the scintillation crystal coupled to the PMT.

The coincidence circuit comprised Fast Filter Amplifiers, Constant Fraction Discriminators, a TAC/SCA (time-to-amplitude converter/single channel analyzer), and Gate and Delay Generator NIM modules to trigger the four-channel PSAPD event acquisition.

^{57}Co Setup

The ^{57}Co source was collimated using a 30 mm x 30 mm x 10 mm block of lead with a 500 μm hole (Figure 4.5b). The geometry of the setup resulted in a $\sim$560 μm spot size on the face of the PSAPD. The four anode signals were acquired and processed in the same manner as the ^{22}Na setup − one spectrum amplifier and one delay amplifier per anode out to an acquisition board. The events were triggered by the signal from the common electrode (see Figure 3.6).

4.4.2 Positioning

Methods

Due to the non-linear nature of the charge distribution process over the face of the PSAPD detector, the calculated position map suffered from pincushion distortion when using traditional position calculation methods [159]. In order to help study the effect of pin cushioning, positions were calculated from the four digitized PSAPD channels using a rotated coordinate Anger-type method as well as the traditional method of Anger-type logic, both of which are described in Section 3.2.

The range for the corner anodes was [0,10] volts; the range for x and y using the Anger-type or rotated coordinate position method was [-1,1] (unitless). The energy for each event, using either method, is calculated from the sum of the corner signals and had a range of [0, 20] volts. The units of position, and therefore the point spread function full width at half maximum (psfFWHM), as well as the average energy, are all reported in the range of the positioned events for conciseness: [-0.3, 0.3].

Method Assessment

A point spread function (PSF) is a measure of a system of interest's (materials, devices, electronics, data processing algorithms, etc. evaluated together) ability to determine a known quantity, such as position. For instance, the position PSF of a detector, its associated electronics and positioning schemes can be determined by ir-

radiating the detector at a single point in a known location, and plotting the resultant position spread. This calculated position spread is called the position PSF.

To understand characteristics of positioning using both the traditional Anger-logic and rotated coordinates methods, the shape of the calculated PSF was modeled as an ellipse. Its position-dependent size, orientation, and calculated location was quantified using standard image processing methods which computes the second moment of the image. The angle that the major axis makes with the x-axis of the image is calculated in the following manner [69]:

$$M_{xx} = \frac{\sum x^2}{\sum x}, M_{\mathrm{yy}} = \frac{\sum y^2}{\sum x}, M_{\mathrm{xy}} = \frac{\sum \mathrm{xy}}{\sum x} \tag{4.2}$$

$$\theta = atan(\frac{M_{\mathrm{yy}} - M_{\mathrm{xx}} + \sqrt{(M_{\mathrm{yy}} - M_{\mathrm{xx}})^2 + 4M_{\mathrm{xy}}^2}}{2M_{\mathrm{xy}}}) \tag{4.3}$$

The variables that were included for characterizing the resulting calculated PSF ellipse were: angle θ, major axis "a", and minor axis "b", which were measured across the face of the detector for both positioning methods.

4.4.3 Monte Carlo Study

In the following Monte Carlo simulations, only optical transport in the continuous LSO crystal is modeled in the positioning of events. To compare the experimental results with a system that does not involve positioning affects due to the PSAPD, we utilized two standard simulation packages to model both high energy and light

photon interactions in the LSO scintillation crystal. Interaction mechanisms of the high-energy annihilation photons were simulated with GATE [72], which is a medical imaging specific Monte Carlo add-on package to the high energy physics GEANT4 software. Subsequent scintillation photon transport and interactions were carried out using the DETECT2000 package [62].

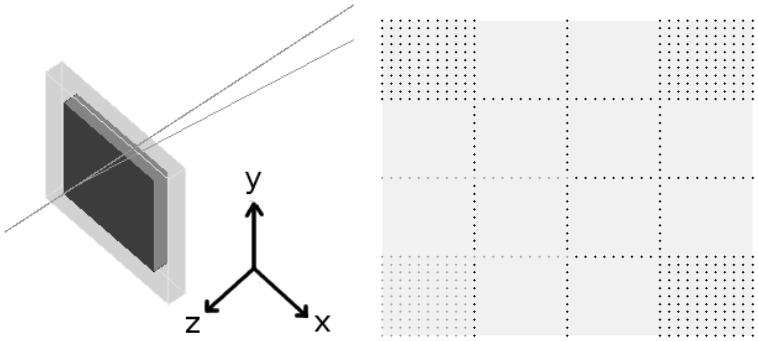

(a) (b)

Figure 4.6: (a) Screen capture of the LSO-PSAPD detector during GATE simulation, (b) the locations of the source relative to the face of the detector.

Figure 4.6(a) shows a screen shot of the LSO-PSAPD module during GATE simulation. The LSO-PSAPD module here is the volume occupied by a single LSO crystal and PSAPD chip. In Figure 4.6(a), the dark gray parallel-piped represents LSO crystal, the light gray parallel-piped shows the volume of the module, and the gray lines illustrate representative high-energy photon trajectories. Photons were simulated originating at various location across the face of the detector. The high-energy photons were collimated, as in the experimental setup, directed at the detector, nor-

mal to its surface. In Figure 4.6(a), the origin of the photons was to the left of the LSO, and to the right of the LSO shows the track of the photons that were transmitted. Figure 4.6(b) shows the source positions that were simulated (dark gray dots) relative to the face of the detector. Simulating and analyzing data taken at locations represented by the dark gray dots, the behavior at the light gray positions is known by symmetry of the PSAPD device (the geometry of the crystal and photodetector are equivalent under rotation or reflection). The light gray area represents the active area of the PSAPD.

GATE

To simulate similar conditions as seen in the ^{22}Na experimental coincidence study, GATE was used to obtain Compton scattering, Photoelectric and characteristic X-ray interaction positions in the LSO scintillation crystal. A 20 μm radius sphere containing 511 keV activity was placed 5 mm from the surface of an 8 mm x 8 mm x 1 mm single LSO crystal, emitting normal to the surface of the crystal (Figure 4.6a). Each interaction with the crystal was recorded by GATE into a "hits" file, which gives specific information including the energy, three-dimensional position, and annihilation event number. In order to probe the location-dependent response and light spread, the source sphere was stepped at 200 μm increments at the locations on the face of the detector - shown in Figure 4.6b as dark gray dots. The position, energy and event number were passed, for each "hits" interaction to DETECT2000, which simulated

optical transport within the crystal.

DETECT2000

The interactions determined by GATE were modeled as a point process, i.e., the scintillation photons modeled by DETECT2000 for a particular GATE interaction ("hit") were all given the same initial location determined in the "hits" file. DETECT2000 requires as an input a location and number of photons to generate. It outputs the detection location on the photodetector surface for each scintillation photon. The energy given in the GATE "hits" file was converted to a number of photons to generate for the DETECT2000 step assuming an average LSO conversion efficiency of 25 photons per keV. Generating a constant number of photons per keV for each interaction limits the factors affecting energy resolution of the detector to optical transport effects: absorption, scatter, transmission, reflection, as well as material index of refraction.

The two materials simulated are shown in Figure 3.6: an 8 mm x 8 mm x 1 mm LSO crystal, with index of refraction 1.82, and a 10 μm thick optical grease layer with the same cross-section and an index of refraction of 1.465. The surface finish on the five faces of the scintillation crystal not in contact with the optical grease were considered ground, and the sixth connecting face, polished. These surface definitions were mirrored in the grease layer, except for the side considered in contact with the PSAPD. This contact side was defined as the "detect" layer. Scintillation

photons that come in contact with this detect layer are considered detected and the position and location are automatically written out. The centroid of these locations were calculated in post-processing and averaged to compare to results obtained in experiment.

4.4.4 Results

Experimental Results

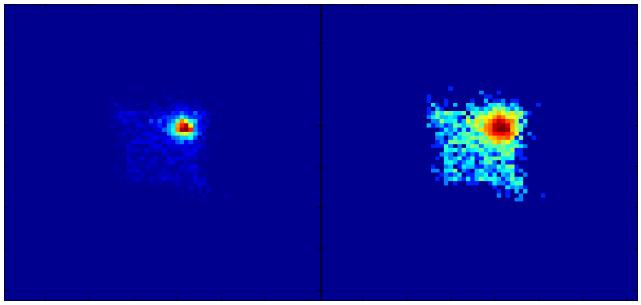

(a) Point spread function for ^{22}Na

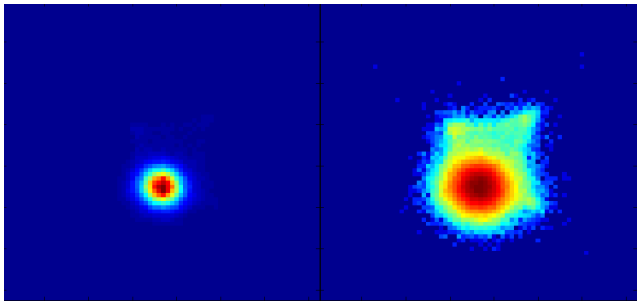

(b) Point spread function for ^{57}Co

Figure 4.7: Collimated point spread functions.

For a single source position, Figure 4.7 shows (left) the measured PSF and (right)

the log of the histogram values (enhance the visualization of the dynamic range). All images use the traditional Anger-type logic positioning algorithm.

Figure 4.7 uses the traditional positioning method and shows the measured PSF at a position near the right edge using the ^{22}Na coincidence setup (Figure 4.7a) and a position to the left of center for the ^{57}Co collimation setup (Figure 4.7b). Both images shown in a) are of the same data set. The left hand image shows the raw histogrammed counts, and the right hand image shows the log of the counts. The log of the counts is shown to visualize the relative position spread of the PSF with respect to the size of the possible position locations of the crystal, or the dynamic range. The same procedures were used to produce the images in b).

Figure 4.8 shows the position, photopeak location, counts and energy resolution for both (a) ^{22}Na and (b) ^{57}Co. All quantities are in volts, except for counts. Energy resolution, photopeak location and counts are scaled to visualize all data in one graph. Error bars for photopeak location, counts, and energy resolution are equal to the standard deviation of 3 measurements. Positioning error is calculated using the bootstrap method. In (b), the error bars are smaller than the data point symbol size.

Data were gathered for 2000 seconds (33 min) at each location using the ^{22}Na setup and for 120 seconds for the ^{57}Co. Although the acquisition times for the ^{22}Na setup were an order of magnitude longer, the number of recorded events were lower because electronic coincidence was used for collimation ($\sim$1000 events after energy gating at full width fifth max for ^{22}Na, versus >30,000 for the collimated ^{57}Co source). The

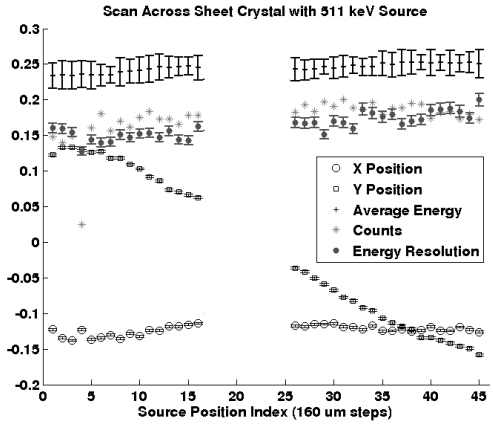

(a)

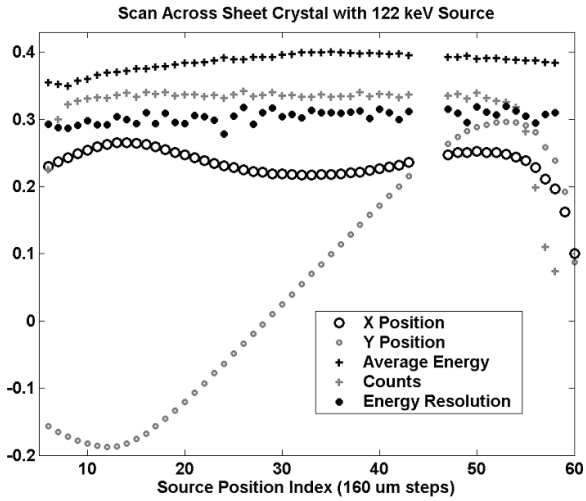

(b)

Figure 4.8: (a) ^{22}Na and (b) ^{57}Co scan results

centroid of the positions of the events for a particular source location was calculated and plotted along with the number of counts, average energy, and energy resolution (Figure 4.8). During the portion of the acquisition of the ^{22}Na coincidence data when the source was directly over the center of the crystal, a large deviation in spatial

linearity was recorded for both the direction in which the source was moving, "x", as well as perpendicular to it, "y" (Figure 4.8a). This anomaly was believed to be due to a portion of the moving PMT-source structure becoming impeded during a few millimeters of its motion. The linearity of the calculated position versus known source position resumed after the anomaly. There was a short period during the acquisition using the ^{57}Co source (Figure 4.8b) that a scheduled software process took priority over acquisition and resulted in three data points being lost.

The dynamic range was compressed in these studies due to light spread across the whole face of the PSAPD [97] for every event. Note also that the average photopeak position did not remain constant at the edge of the detector, and could potentially provide a fifth positioning parameter to resolve positioning difficulties at the edge. The average raw FWHM energy resolution for ^{57}Co was 24.5% $\pm$ 0.2% at 122keV and 17.3% $\pm$ 1.1% at 511 keV for ^{22}Na within 2 mm of the center. Within 2 mm of the edges, the uncorrected FWHM energy resolution for ^{57}Co was 24.9% $\pm$ 0.2% at 122 keV and 15.2% $\pm$ 1.2% at 511 keV for ^{22}Na. The error given is equal to the standard deviation of all the measurements for a group of data.

Figure 4.9 shows the two dimensional histrograms for a ^{57}Co source, location index 15 (1.28 mm from the left edge), using both positioning methods. The white pincushioned outlines show the range of positioning on the PSAPD for each method. Note: the range is larger for positioning method 1 (see Figure 4.10). The light gray

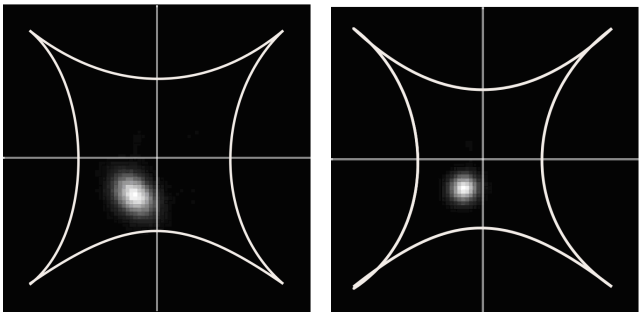

(a) (b)

Figure 4.9: Visually comparing point spread function using the (a) rotated coordinates and (b) traditional Anger-type positioning methods (see Section 3.2.2).

cross-hair lines show the center of the PSAPD. Both images have the same dynamic range: [-1.5, 1.5], but notice the dynamic range difference (location of the center of the spot in the image) and the difference in spot shape and distribution.

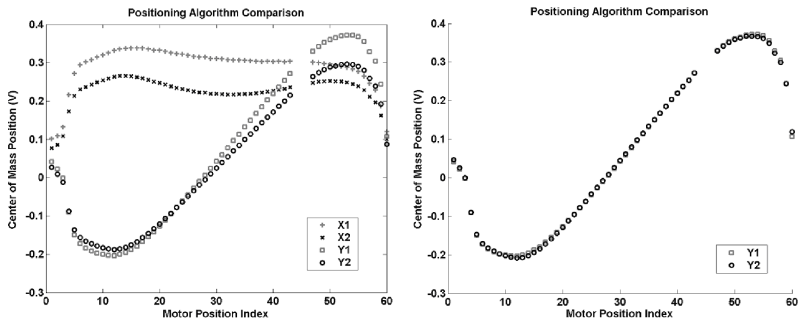

(a) (b)

Figure 4.10: (a) Centroid positions of the point spread function using the positioning algorithm method 1 (X1,Y1) and method 2 (X2,Y2). (b) Y2 scaled to Y1.

The measured psfFHWM, using the traditional positioning method, averaged 2.9 mm for ^{57}Co and 1.23 mm for ^{22}Na. Deconvolving the finite size of the source, 500 μm was used as a conservative value for both the ^{57}Co and ^{22}Na case. Using a first

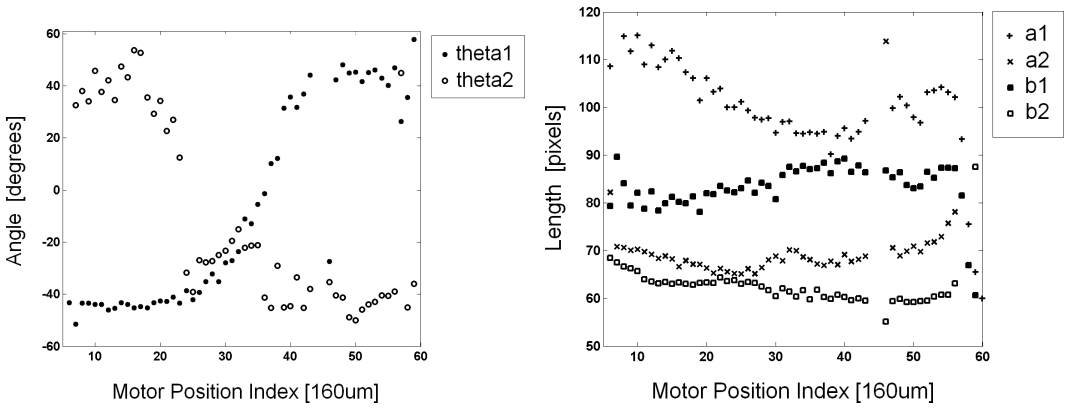

(a) (b)

Figure 4.11: PSF characterization using the (a) rotated coordinates and (b) traditional Anger-type positioning methods.

approximation sqrt((meas. psfFWHM)^2 - (500μm)^2) gave 2.86 mm FWHM for ^{57}Co and 1.12 mm FWHM for ^{22}Na. The positioning linearity for the central 6 mm had an R^2-value of 0.965 for ^{22}Na (not including the points taken during impeded source motion) and 0.9995 for ^{57}Co.

Positioning Method Results

Using positioning methods 1 (rotated coordinates) and 2 (traditional Anger-type logic), the area of the PSF was modeled as an ellipse. Figure 4.11(a) plots the angle between the major axis of the PSF ellipse and the x-axis of the image (theta) is plotted for both methods across the face of the detector, where theta1 and theta2 are calculated using positioning methods 1 and 2 respectively. Figure 4.11(b) plots the FWHM of the ellipse along the major axis "a" and minor axis "b" for both methods

across the face of the detector; where a_1 and b_1 are calculated using positioning method 1, and a_2 and b_2 are calculated using positioning method 2.

Looking at the major and minor axes lengths, the first positioning algorithm produced a PSF with a larger FWHM in both directions. Note also the elongation of the PSF at a single position (shown in Figure 4.9a) using positioning method 1 as opposed to the relatively circular shape of the PSF when using positioning method 2 (Figure 4.9b).

Although both positioning methods had similar ranges of orientation angles, the degree to which the second positioning algorithm was non-circular was much reduced. This can be seen by the smaller difference between the major and minor axis lengths for the second positioning algorithm (Figure 4.9a).

Looking at the centroid locations in x and y, using both positioning methods, as a function of source position index (Figure 4.10), an increase in dynamic range when using positioning method one (Figure 4.10a) was observed. When rescaling and translating the centroid positions calculated using positioning method two to cover the same range as positioning method one, the centroid locations were found to be very similar (Figure 4.10b). Therefore, the positioning algorithm which reduces the pincushion distortion did not affect the positioning degeneracy near the edges of the detector.

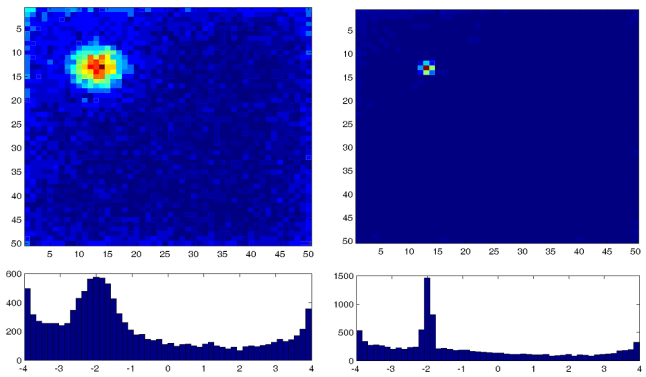

(a) (b)

Figure 4.12: Results illustrating the light spread differences due to interactions that occur far from (left) and near to (right) the detection surface.

Simulation Results

Figure 4.12 shows 2D and 1D histograms of the individual scintillation photons from one "hits" interaction which originated (a) z = 0.63 mm and (b) z = 0.16 mm from the photodetector surface inside the crystal. Both events had the same energy and (x,y) position within the crystal (coordinate system defined in Figure 4.6).

Figure 4.12 shows the effect of annihilation photon interaction depth (measured from the surface of the crystal to the detector) on the light spread within the crystal. Not to be confused with Figure 4.7, Figure 4.12 shows histograms of the locations of the individual scintillation photons detected from one annihilation event. The centroid of the positions shown in Figure 4.12 makes up one event in the histogram of Figure 4.7.

The energy surface at the corner of the crystal sheet (the 10 x 10 location patch

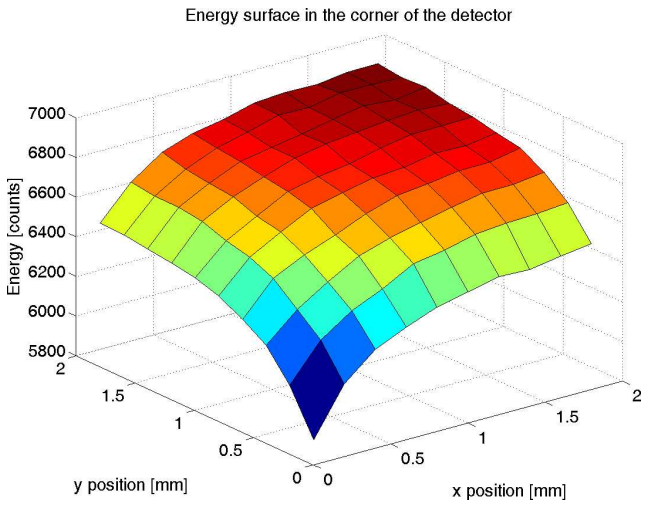

Figure 4.13: Average energy at locations in the corner of the crystal sheet.

shown in Figure 4.6b) is shown in Figure 4.13. The calculated position plotted (Figure 4.14a) was the mean of the centroids of the photons from an event over the entire crystal. The average energy (number of scintillation photons) is shown in Figure 4.14b. Averages were calculated from 300 GATE simulated events for each interaction location used in the experimental study.

Figure 4.14 shows the comparison of experimental (exp) and simulated (th) calculated (a) position and (b) energy vs. source position. The experimental data were the ^{22}Na and ^{57}Co data plotted in Figure 4.8. The simulated source locations are seen in Figure 4.6b as dark gray dots. Note that for locations within 1.2 mm from the edge of the sheet crystal in both simulated and experimental data, there is not a one-to-one correspondance between the calculated position and source irradiation location maps. In other words, a calculated position near the edge of the sheet crystal

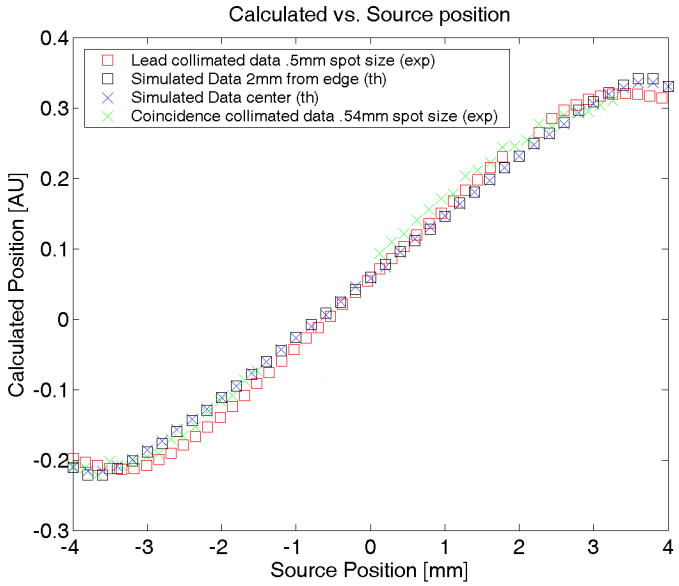

(a)

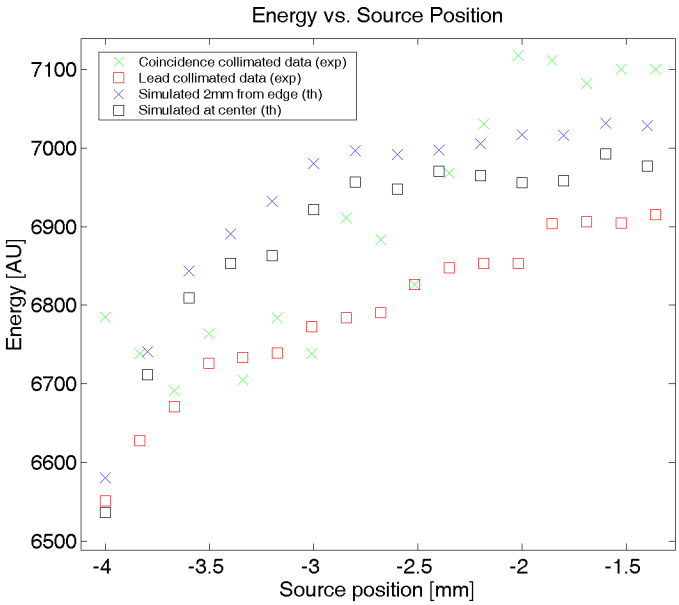

(b)

Figure 4.14: Experimental and Monte Carlo simulated position and energy results for the scanning experiment.

could correspond to two interaction locations (the function is somewhat sinusoidal), i.e. the edge positions are degenerate.

The PSAPD resistive surface was not modeled to simulate pincushion effects. Pin-cushioning adds non-linear distortions in the position estimates [159]. There is a larger region over which the experimentally calculated position for the 122keV ^{57}Co data is non-linear possibly due to more interactions happening closer to the top of the crystal, i.e. farther from the detector surface.

4.4.5 Conclusion

The experimental and simulated results agree quite well − both show that the calculated positions from events whose centroids are within 1.2 mm from the edge of the sheet crystal are degenerate. A positioning method that reduced the pincushion distortion was employed to reduce non-linearities in positioning on the surface of the PSAPD, but did not succeed in reducing the region of positioning degeneracy. Therefore, the degeneracy appeared to be due to the edge effects within the scintillation crystal − a sizable portion of the scintillation photons reflect off the surface of the sides of the crystal. Because of these reflections, some photons are lost through transmission and absorption, which changes the average energy of events positioned at the edge as compared to events at the center of the detector. The percentage change in energy within 1.2 mm from the edge is about 5%. If energy resolution

in the detection process were better than this 5% change near the edges, perhaps a positioning algorithm that uses energy as well as position may be able to resolve positions near the edge. However, the energy resolution of our characterized PSAPD with this scintillator is 10-12%.

A summary of the scanning position resolution experiments performed by Zhang, et al. using 1 x 1 x 3 mm^3 segmented crystals packed in an 8 x 3 (8 mm x 9 mm) array coupled to the PSAPD detector can be found in Reference [193]. The average energy resolution at 511 keV was comparable: 12.61% and the average deconvolved FWHM of the PSF was 1.09 mm, also comparable to the results found in this study. On the same photodetector device with the segmented crystals, Reference [193] mentions the difficulty in resolving the array crystals near the edge - this is where degeneracy in the sheet crystal was also observed. However, this difficulty was greatly reduced when studying the spatial resolution capabilities of the new thin photodetector introduced in Section 3.5.

Further efforts to utilize all the information collected from the four anode channels to reduce degeneracy might involve maximum-likelihood position estimation algorithms. Future experiments will include positioning accuracy of events near the edge of the PSAPD active area when the continuous crystal is larger than the PSAPD active area. The increased sensitivity [51, 193] of these larger crystals and potential decrease in crystal edge-effect positioning problems suggests further study.

4.5 Segmented Crystal Array

4.5.1 Array Designs

Multiple segmented array designs were tested in order to assess factors such as crystal feature position and overlap (commonly assessed herein as peak to valley ratio), energy resolution per crystal, and coincidence timing resolution per crystal. Crystal geometry effects the amount of light collected by the photodetector as well as light distribution across the photodetection surface, both of which may influence any of the PET-relevant parameters mentioned (feature position, energy and coincidence time resolution). The crystal sizes ranged from a dimension of 1 mm to 3 mm coupled to the face of the detector. A conservatively designed array comprising crystals of dimensions 2 mm x 2 mm x 3 mm was first investigated to learn the extent to which crystal features for relatively large segmented crystals within an array were seperable in a flood image (crystal peak count to inter-crystal valley count ratio). As investigations proceeded, arrays containing crystals of size 1 x 1 x 1 mm^3 were investigated. The results of these experiments are given in this section.

4.5.2 4 x 3 and 8 x 3 Arrays

The detailed results from the 4 x 3 and 8 x 3 arrays coupled to the commercially available ceramic PSAPD can be found in Section 3.3. The results are summarized below.

Table 4.3: Summary of results for 4 x 3 and 8 x 3 LSO crystal arrays coupled to the 8 x 8 mm^2 active area ceramic device.

	8 x 3 array	4 x 3 array
Energy Resolution [%]	15.5	17.4
Crystal Identification	yes	yes
Coincidence Time Resolution [ns]	12.5	15.3

4.5.3 10 x 10 Array - No Reflector

Positioning Schemes

Crystal identification and profile peak to valley ratio (PVR) were examined for both positioning schemes while taking flood measurements of the 10 x 10 LSO array with no inter-crystal reflector. Flood measurements were taken, acquiring each of the four corner channels. The traditional Anger-type logic and rotated coordinate positioning methods were applied to the same data set (see Section 3.2.2 for a discussion of positioning methods). The flood images and the results of the profile PVR measurements can be seen in Figure 4.15 using the (left) Anger and (right) rotated positioning algorithms.

A 10 x 10 LSO array comprising crystals, of size 1 mm on each side, covered an area larger than the 8 mm x 8 mm active area of the position sensitive avalanche photodiodes. Each crystal in the array that was at least partially positioned over the active region of the PSAPD was identified using both positioning schemes. Although the rotated coordinate positioning method did decrease the barrel distortion found using the Anger-type logic positioning method, the peak to valley ratio results did

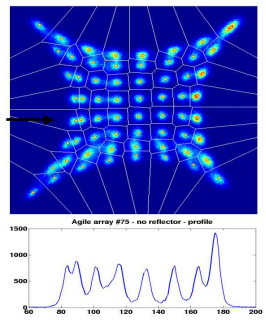

1	1.28
2	3.84
3	2.18
4	8.44
5	7.51
6	11.45
7	6.45
8	3.63
Mean	5.60
StDev	3.46

(a)

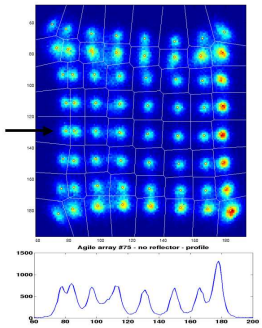

1	1.29
2	3.76
3	2.17
4	8.93
5	9.08
6	9.82
7	5.94
8	3.75
Mean	5.59
StDev	3.34

(b)

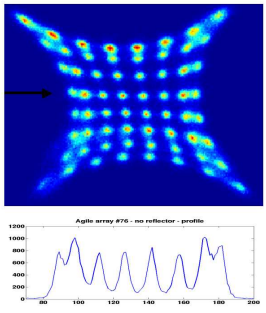

1	1.41
2	4.20
3	6.11
4	7.69
5	7.93
6	8.19
7	6.35
8	1.41
Mean	5.41
StDev	2.78

(c)

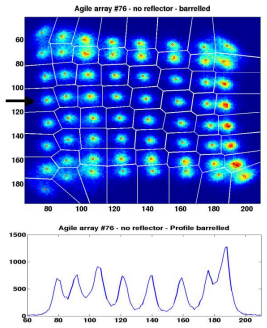

1	1.43
2	4.25
3	5.42
4	7.47
5	8.32
6	6.20
7	5.96
8	1.37
Mean	5.05
StDev	2.57

(d)

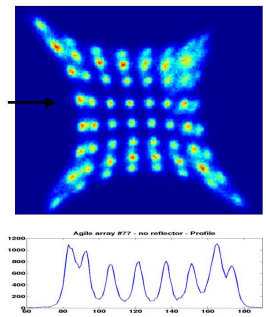

1	1.50
2	6.81
3	7.38
4	6.97
5	7.08
6	5.85
7	4.38
8	1.42
Mean	5.19
StDev	2.46

(e)

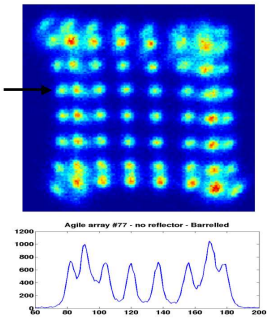

1	1.62
2	2.56
3	6.70
4	7.72
5	7.32
6	11.16
7	3.63
8	1.25
Mean	5.25
StDev	3.51

(f)

Figure 4.15: Figures a)-f) show the flood (upper left), profile (lower left), and PVR (right) of three 10 x 10 Agile crystal arrays with no inter-crystal reflector. Figures on the same line are from the same crystal array (i.e. Figures a),b) are produced using data from the same crystal array). Figures on the left (right) use traditional Anger-type logic (rotated coordinates) position schemes.

not change significantly.

Energy Resolution

Individual crystal energy resolution was evaluated for the 8 x 8 crystals coupled to the active region of the PSAPD (figure 4.16, left). Shown in each image in the left-hand column of Figure 4.16 is a histogram of all crystal energy resolutions (upper left), a representative energy spectrum of one of the crystals (upper right), and a summary of the results in the lower half. The mean energy resolution for the arrays was 12.8% with a standard deviation of 0.6% and the mean standard deviation within the arrays was 3.1 ± 0.5.

Because the area of the crystal array was at least two crystals larger in each dimension than the active area of the PSAPD, degredation in energy resolution in the outer ring of crystals from scintillation photon loss is likely. Therefore, individual crystal energy resolution was also evaluated for the 6 x 6 crystals that were completely coupled to the active area of the PSAPD (see Figure 4.16, right). The images on the right-hand column of Figure 4.16 show the histogram of the individual crystal energy resolutions of the inner 6 x 6 crystals (upper right) and a summary of the results for the array in the lower portion of the image. The mean energy resolution for the inner 6 x 6 crystal arrays was 12.7% with a standard deviation of 0.3% and the mean standard deviation within the arrays was 1.2 ± 0.3. Looking at only the inner 6 x 6 crystals resulted in no significant mean energy resolution change from the full

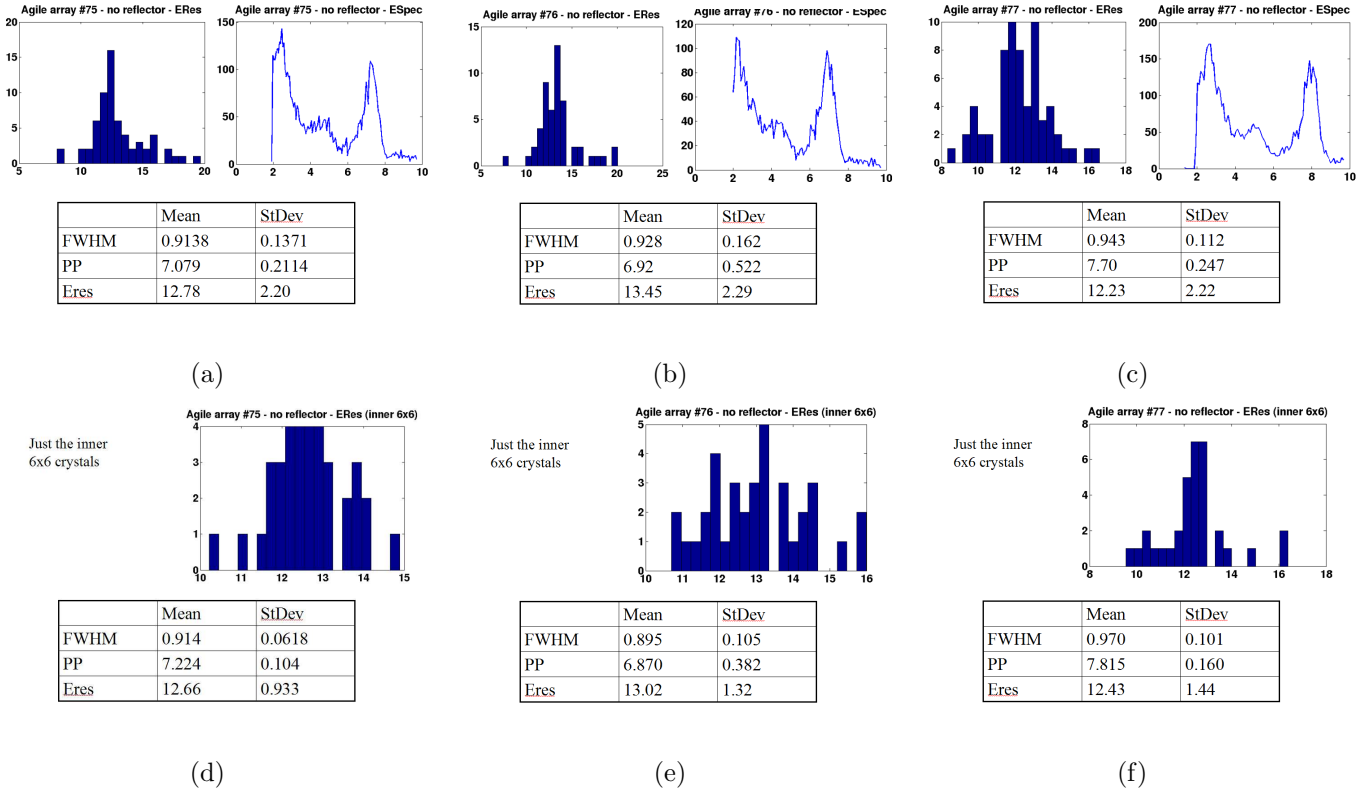

	Mean	StDev
FWHM	0.9138	0.1371
PP	7.079	0.2114
Eres	12.78	2.20

(a)

	Mean	StDev
FWHM	0.928	0.162
PP	6.92	0.522
Eres	13.45	2.29

(b)

	Mean	StDev
FWHM	0.943	0.112
PP	7.70	0.247
Eres	12.23	2.22

(c)

	Mean	StDev
FWHM	0.914	0.0618
PP	7.224	0.104
Eres	12.66	0.933

(d)

	Mean	StDev
FWHM	0.895	0.105
PP	6.870	0.382
Eres	13.02	1.32

(e)

	Mean	StDev
FWHM	0.970	0.101
PP	7.815	0.160
Eres	12.43	1.44

(f)

Figure 4.16: Figures a)-f) show various aspects of energy resolution for three 10 x 10 Agile crystal arrays with no inter-crystal reflector. Figures in teh same column are from the same crystal array (i.e. Figures a) and d) are data from the same crystal array). Figures a)-c) show energy resolution histograms for all 64 crystals coupled to the active area of the PSAPD (bar plot, upper left), a typical energy spectrum (blue line plot, upper right), and the mean and standard deviation of energy parameters (bottom table). Figures d)-f) show a histogram of the energy resolution data for the inner 6 x 6 crystals in each array (upper right) and the mean and standard deviation of energy parameters (bottom table). Note that the scales are different in the histograms.

array value but an improvement of the standard deviation of the mean of 50.8%, an improvement of the mean of the standard deviation within an array of 60.8%, and improvement of the standard deviation of the standard devation within an array of 46.0%.

Coincidence Time Resolution

Coincidence time resolution (CTR) measurements, between a representative array and a PMT using the coincidence method described in Section 3.2.7, were performed. A representative TAC spectrum is shown in the upper right hand side of Figure 4.17, along with the fitted data used to calculate the coincidence time resolution (left and lower portion of the image). The CTR for the 8 x 8 array with no inter-crystal reflector was 5.3 ns $\pm$ 0.1 ns.

The coincidence acquired energy spectrum for the PSAPD and the PMT are shown in Figure 4.18. On the left side of the image are the spectra for an open TAC window (all data). On the right side of Figure 4.18, the energy spectra for the PSAPD and PMT for a gated TAC window are shown. The gate had a width of two times the fitted full width at half maximum (FWHM) value and was centered on the peak of the TAC spectrum.

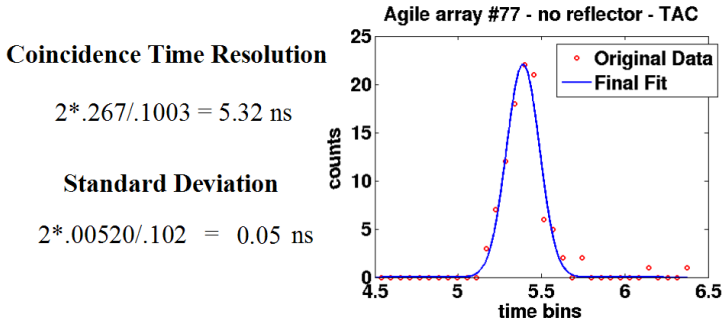

Delay [ns]	Peak Position	FWHM
22	5.09 +/- 0.01	0.27 +/- 0.03
24	5.19 +/- 0.01	0.27 +/- 0.02
28	5.39 +/- 0.01	0.27 +/- 0.02

Figure 4.17: Coincidence time resolution measurement for an 10 x 10 Agile crystal array without inter-crystal reflector.

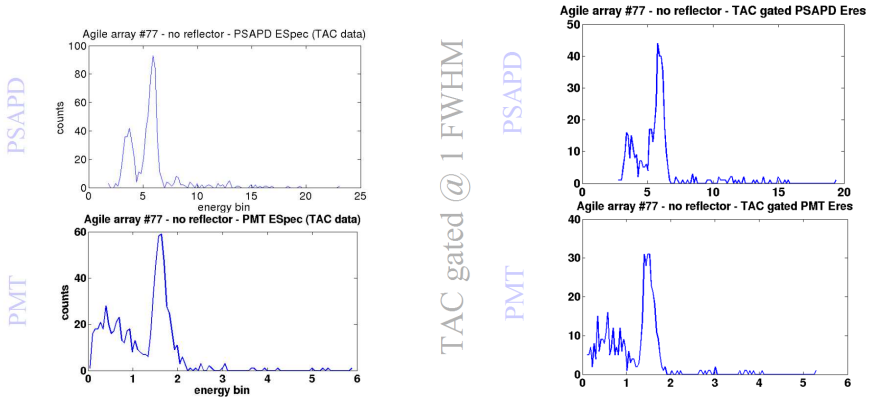

(a) (b)

Figure 4.18: Coincidence energy spectra for both the PSAPD (top row) and PMT (bottom row) with (right) and without (left) gating on the FWHM of the TAC (timing spectra) signal for an 10 x 10 Agile crystal array without reflector.

Summary

4.5.4 10 x 10 Array - VM2000 Reflector

Crystal identification and profile peak to valley ratio (PVR) were examined for both positioning schemes while taking flood measurements of the 10 x 10 LSO array

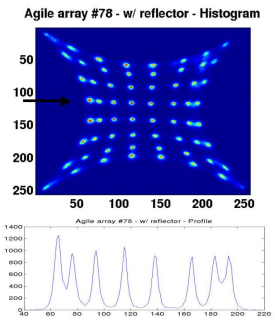

1	3.62
2	14.51
3	22.76
4	35.12
5	24.81
6	38.85
7	15.67
8	2.03
Mean	19.67
StDev	13.38

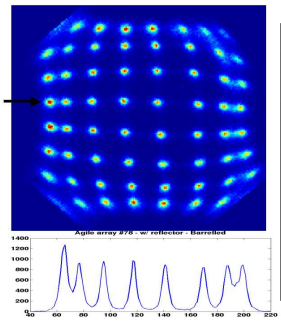

1	3.58
2	10.85
3	22.10
4	29.64
5	27.24
6	25.64
7	10.90
8	1.87
Mean	16.48
StDev	11.00

(a) (b)

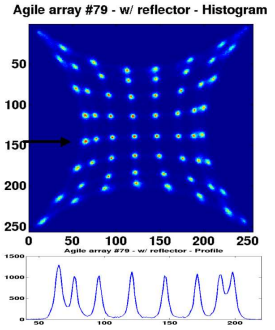

1	4.23
2	14.55
3	30.33
4	26.47
5	30.87
6	25.42
7	13.46
8	1.90
Mean	18.40
StDev	11.49

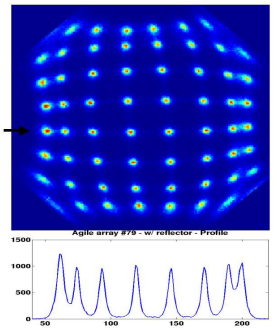

1	4.22
2	14.79
3	24.76
4	34.54
5	32.38
6	33.62
7	13.85
8	1.87
Mean	20.00
StDev	13.18

(c) (d)

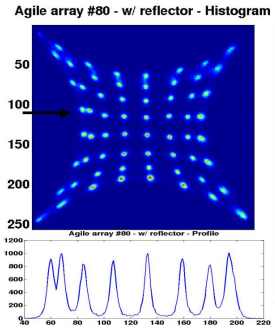

1	2.10
2	10.36
3	21.95
4	37.92
5	32.53
6	38.85
7	18.12
8	6.30
Mean	21.02
StDev	14.31

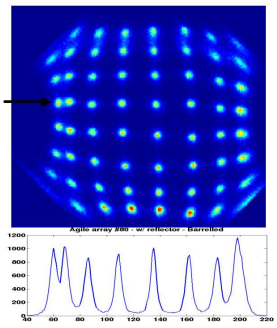

1	2.11
2	8.60
3	17.85
4	29.76
5	27.40
6	21.28
7	14.37
8	6.09
Mean	15.93
StDev	9.99

(e) (f)

Figure 4.19: Figures a)-f) show the flood (upper left), profile (lower left), and PVR (right) of three 10 x 10 Agile crystal arrays with VM2000 inter-crystal reflector. Figures on the same line are from the same crystal array (i.e. Figures a),b) are produced using data from the same crystal array). Figures on the left (right) use traditional Anger-type logic (rotated coordinates) position schemes.

Table 4.4: Summary of characteristics of 10 x 10 Agile crystal arrays with no inter-crystal reflector. Rotated and Anger are the rotated coordinate and Anger-like logic positioning methods, respectively.

Characteristic	Mean	St Dev
PVR (rotated)	5.4 ± 0.2	2.9 ± 0.5
PVR (Anger)	5.3 ± 0.3	3.1 ± 0.5
Energy Res.	12.8 ± 0.6	2.2 ± 0.1
Counts	518880 ± 588	

with 3M's VM2000 inter-crystal reflector. Flood measurements were taken, acquiring each of the four corner channels. The traditional Anger-type logic and rotated coordinate positioning methods were applied to the same data set. The flood images and the results of the profile PVR measurements can be seen in Figure 4.19 using the (left) Anger and (right) rotated positioning algorithms.

A 10 x 10 LSO array comprising crystals 1 mm on a side, plus inter-crystal reflector, covered a larger area than the 8 mm x 8 mm active area of the position sensitive avalanche photodiodes. The array was centered on the PSAPD detection surface, so only the interior 6 x 6 crystal were fully coupled to the active region of the PSAPD. Each crystal in the array that was positioned at least partially over the active region of the PSAPD was identified using both positioning schemes. The rotated coordinate positioning method did decrease the barrel distortion found using the Anger-type logic positioning method, and the peak to valley ratio improved from 17.47 using the traditional method to 19.70 using the rotated coordinate positioning method.

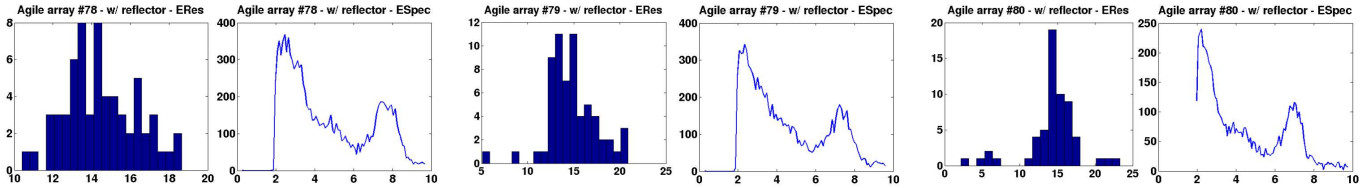

	Mean	StDev
FWHM	1.12	0.190
PP	7.611	0.601
Eres	15.14	2.94

(a)

	Mean	StDev
FWHM	1.15	0.212
PP	7.83	0.499
Eres	14.89	3.28

(b)

	Mean	StDev
FWHM	0.939	0.324
PP	6.597	1.638
Eres	15.16	3.19

(c)

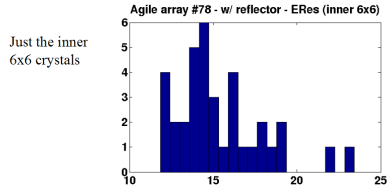

	Mean	StDev
FWHM	1.223	0.2163
PP	7.967	0.300
Eres	15.35	2.655

(d)

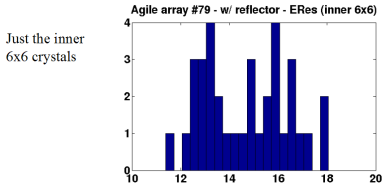

	Mean	StDev
FWHM	1.210	0.160
PP	8.154	0.287
Eres	14.86	2.063

(e)

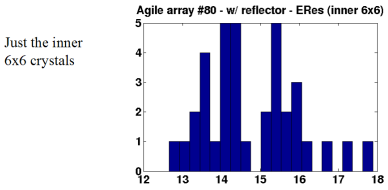

	Mean	StDev
FWHM	1.027	0.127
PP	6.954	0.542
Eres	14.76	1.185

(f)

Figure 4.20: Figures a)-f) show various aspects of energy resolution for three 10 x 10 Agile crystal arrays with VM2000 inter-crystal reflector. Figures in teh same column are from the same crystal array (i.e. Figures a) and d) are data from the same crystal array). Figures a)-c) show energy resolution histograms for all 64 crystals coupled to the active area of the PSAPD (bar plot, upper left), a typical energy spectrum (blue line plot, upper right), and the mean and standard deviation of energy parameters (bottom table). Figures d)-f) show a histogram of the energy resolution data for the inner 6 x 6 crystals in each array (upper right) and the mean and standard deviation of energy parameters (bottom table). Note that the scales are different in the histograms.

Energy Resolution

Individual crystal energy resolution was evaluated for the 8 x 8 crystals coupled to the active region of the PSAPD (Figure 4.20, left). Shown in each image in the left-hand column of Figure 4.20 is a histogram of all crystal energy resolutions (upper left), a representative energy spectrum of one of the crystals (upper right), and a summary of the results in the lower half. The mean energy resolution for the arrays was 15.1% with a standard deviation of 0.2%. The mean standard deviation within the arrays was 3.1 ± 0.2.

Because the area of the crystal array was at least two crystals larger in each dimension than the active area of the PSAPD, degredation in energy resolution in the outer ring of crystals from scintillation photon loss is likely. Therefore, individual crystal energy resolution was also evaluated for the 6 x 6 crystals that were completely coupled to the active area of the PSAPD (see Figure 4.20, right). The images on the right-hand column of Figure 4.20 show the histogram of the individual crystal energy resolutions of the inner 6 x 6 crystals (upper right) and a summary of the results for the array in the lower portion of the image. The mean energy resolution for the inner 6 x 6 crystal arrays was 15.0% with a standard deviation of 0.3% and the mean standard deviation within the arrays was 2.0 ± 0.7. This resulted in a mean energy resolution improvement of 0.5% with an increase of the standard deviation of the mean of 113%, an improvement of the mean of the standard deviation within

an array of 37.3%, and increase of the standard deviation of the standard deviation within an array of 306%.

Coincidence Time Resolution

Coincidence time resolution (CTR) between a representative array and a PMT, using the coincidence method described in Section 3.2.7, was performed. A representative TAC spectrum is shown in the upper right hand side of Figure 4.21, along with the fitted data used to calculate the coincidence time resolution (left and lower portion of the image). The CTR for the 8 x 8 array with no inter-crystal reflector was 8.7 ns ± 0.1 ns.

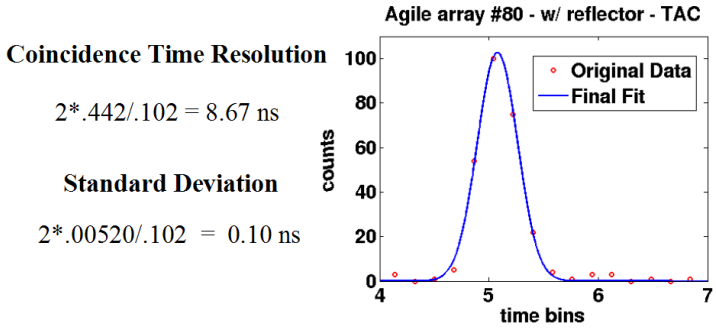

Delay [ns]	Peak Position	FWHM
22	5.08 +/- 0.02	0.44 +/- 0.04
24	5.18 +/- 0.02	0.45 +/- 0.04
26	5.28 +/- 0.02	0.44 +/- 0.04

Figure 4.21: Coincidence time resolution measurement for an 10 x 10 Agile crystal array with VM2000 inter-crystal reflector.

The coincidence acquired energy spectrum for the PSAPD and the PMT are shown

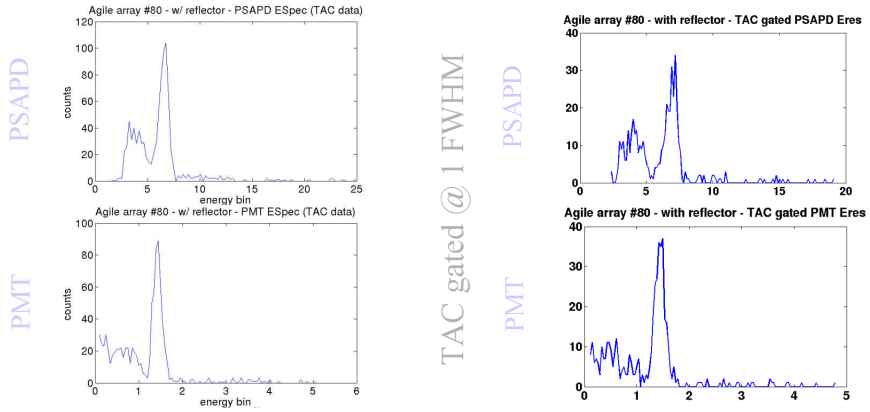

(a) (b)

Figure 4.22: Coincidence energy spectra for both the PSAPD (top row) and PMT (bottom row) with (right) and without (left) gating on the FWHM of the TAC (timing spectra) signal for an 10 x 10 Agile crystal array with VM2000 inter-crystal reflector.

in Figure 4.22. On the left side of the image are the spectra for an open TAC window (all data). On the right side of Figure 4.22, the energy spectra for the PSAPD and PMT for a TAC-gated window. The TAC gate had a width of two times the fitted full width at half maximum (FWHM) value and was centered on the peak of the TAC spectrum.

Summary

Table 4.5: Summary of characteristics of 10 x 10 Agile crystal arrays with VM2000 reflector.

Characteristic	Mean	St Dev
PVR (rotated)	19.7 ± 1.3	13.1 ± 1.4
PVR (Anger)	17.5 ± 2.2	11.4 ± 1.6
Energy Res.	15.1 ± 0.2	3.1 ± 0.2
Counts	506300 ± 3589	

4.5.5 Discussion

Looking at the results comparing 10 x 10 segmented arrays with and without inter-crystal reflector, a particular design does not stand out as a clear winner. Arrays without inter-crystal reflector showed superior energy resolution and coincidence time resolution, whereas those with inter-crystal reflector showed higher light output and far superior crystal separation (PVR). Therefore, moving forward, the final design dual chip modules were assembled using half of each design.

4.6 Segmented Arrays for Final Design Dual-Chip Modules

Forty position sensitive avalanche photodiodes were to be used to assemble 20 dual-chip PSAPD modules. Each module was read out using a single Teflon flex circuit. Since the results of testing segmented crystals with and without reflector did not signify a clearly optimal design, these 40 PSAPDs were divided in half, resulting in 10 dual-chip modules of each crystal segmentation design. Before coupling the arrays to the PSAPDs, each were tested for energy resolution and crystal identification, assuring the integrity of the arrays before incorporating them permanently into the modules. The results after coupling the crystals can be found in Chapter 5. This section discusses the results from the crystals all coupled to the same device used in

testing the 10 x 10 crystal arrays.

4.6.1 8 x 8 Arrays with No Inter-Crystal Reflector

Crystal Identification

Crystal identification and profile peak to valley ratio (PVR) were examined for each of the 20 arrays using the rotated coordinates positioning scheme on data taken using flood measurements of each of the four corner channels of the PSAPD. The rotated coordinate positioning scheme provided simpler segmentation for the arrays but accentuated any small gain differences seen by the corner channels, gain differences unobservable in a visual inspection of the histogrammed corner data during test runs before long acquisitions.

Individual flood, profile and peak to valley ratio data for each of the 20 crystal arrays can be found in Figures A.1-A.5 in Appendix A. The left portion of the sub-images show the flood histogram and profile on which PVR was calculated, and the right portion of the sub-images show the results for individual, mean and standard deviation PVR values. All 64 crystals were resolved in each of the arrays. The mean PVR over all arrays was 7.6 $\pm$ 1.4 and the mean variance within an array, over all arrays was 4.4 $\pm$ 1.5. The average number of counts acquired for each array was 119671 $\pm$ 8380.

Energy Resolution

Energy resolution was evaluated for each crystal in the 8 x 8 array, for each array (Figures A.6-A.10 in Appendix A). Each sub-image shows the results for a particular array. On the left side of each sub-image of Figures A.6-A.10 is a histogram of all crystal energy resolutions (upper left), a representative energy spectrum of one of the crystals (upper right), and a summary of the results in the lower half. The mean energy resolution for the arrays without reflector was 14.3% with a standard deviation of 0.2% and the mean standard deviation within the arrays was 1.4 $\pm$ 0.1.

Energy resolution histograms, example energy spectra, and the mean and standard deviation of energy parameters obtained from the 64 crystals for each of the 20 crystal arrays can be found in Figures A.6-A.10 in Appendix A.

4.6.2 8 x 8 Arrays with VM2000 Inter-Crystal Reflector

Crystal Identification

Crystal identification and profile peak to valley ratio (PVR) were examined for each of the 20 arrays using the traditional positioning scheme on data taken using flood measurements of each of the four corner channels of the PSAPD. The Anger-type logic positioning scheme provided simpler segmentation for the arrays with inter-crystal reflector.

Individual flood, profile and peak to valley ratio data for each of the 20 crystal

arrays can be found in Figures A.11-A.15 in Appendix A. The left portion of the sub-images show the flood histogram and profile on which PVR was calculated, and the right portion of the sub-images show the results for individual, mean and standard deviation PVR values. All 64 crystals were resolved in each of the arrays. The mean PVR over all arrays was 19.4 ± 4.5 and the mean variance within an array, over all arrays was 10.5 ± 4.1. The average number of counts acquired for each array was 106265 ± 7329.

Energy Resolution

Energy resolution histograms, example energy spectra, and the mean and standard deviation of energy parameters obtained from the 64 crystals for each of the 20 crystal arrays can be found in Figures A.16-A.20 in Appendix A. Each sub-image shows the results for a particular array. On the left side of each sub-image of Figures A.16-A.20 is a histogram of all crystal energy resolutions (upper left), a representative energy spectrum of one of the crystals (upper right), and a summary of the results in the lower half. The mean energy resolution for the arrays without reflector was 15.3% with a standard deviation of 0.4% and the mean standard deviation within the arrays was 1.9 ± 0.3.

4.6.3 Summary and Discussion

Table 4.6 shows the summary of results for the two crystal array designs.

Table 4.6: Mean and standard deviation (StDev) of the peak to valley ratio, energy resolution and counts for the arrays with no inter-crystal reflector (noR) and with VM2000 inter-crystal reflector (R).

	Mean	StDev
Peak to Valley - noR [%]	7.6 ± 1.4	4.4 ± 1.5
Peak to Valley - R [%]	19.4 ± 4.5	10.5 ± 4.1
Energy Resolution - noR [%]	14.3 ± 0.2	1.4 ± 0.1
Energy Resolution - R [%]	15.3 ± 0.4	1.9 ± 0.3
Counts - noR [%]	119671 ± 8380	
Counts - R [%]	106265 ± 7329	

These results follow the same trend as those seen in Sections 4.5.3 and 4.5.4 in the 10 x 10 array case;

- All crystals are resolved in arrays with both designs, though the peak to valley ratio in the arrays with inter-crystal reflector are far superior (157% improvement on average).

- The energy resolution in the arrays without inter-crystal reflector are superior to those with VM2000 between crystals, though the improvement is only about 6% on average.

- The number of counts acquired with the arrays without inter-crystal arrays is higher (12.6% in the case of the 40 8 x 8 arrays) due to the slightly higher amount of crystal in the array.

Coincidence timing resolution was not measured in this study. The results of the coincidence timing data for these crystals were found after they were assembled into the final modules (see Chapter 5).

4.7 Discussion

Multiple crystal structure designs were tested for crystal identification, energy resolution and coincidence time resolution. Although the sheet crystal design has a high crystal packing fraction and would be practical to manufacture, non-linearities in positioning near the edge of the crystal make interaction location determination difficult in large regions of the active area of the detector.

The segmented crystal array results, however, did not show a clearly superior crystal design. In general, arrays constructed without inter-crystal reflector had better energy resolution, coincidence time resolution and sensitivity (counts collected per acquisition time). Arrays with inter-crystal reflector, on the other hand, had far superior peak to valley ratio (crystal separation), potentially leading to better position resolution. Both designs were investigated in the final module design discussion in Chapter 5.

Chapter 5

Final Module Design

5.1 Introduction and Considerations

Incorporating the results from Chapters 3 and 4, the final module design and the study thereof took into consideration issues that presented themselves in previous designs. Moisture in the position sensitive avalanche photodiode (PSAPD), the attachment mechanism of the Kapton flex cable to the pre-conditioning board, and the structural integrity of the copper traces within the flex cable after continual testing, all proved to be major impediments to the testing of PSAPD chips.

The new design also had to incorporate specifications for the modules so that they could be used in the final built system. These specifications determined that it was necessary to incorporate components to provide thermal coupling to the PSAPD and structural components for module robustness and ease of system assembly.

The ways in which the previous issues and the final specifications were resolved involved five major subprojects: (1) the design and construction of a test fixture which provided expedited coupling between a dual-chip flex module and the pre-conditioning board, (2) the design and construction of an experimental enclosure which provided a light-tight, low moisture, and low radio-frequency environment in which to test the modules, (3) the re-design and construction of the Kapton flex-circuit, (4) the design and construction of a structure component for thermal dissipation, mechanical structure and mechanical robustness, and (5) the assembly and testing of the final module design.

Each of the major sub-projects listed above is discussed in this chapter.

5.2 Module Design

The modules comprised two PSAPD photodetectors, each with an LSO scintillation crystal array coupled to it, read out by a thin Kapton flex-cable, and structurally and thermically stabilized by ceramic Aluminum Nitride (AlN). Three out of the four components can be seen in Figure 5.1, and an example of the crystal arrays can be seen in Figure 5.2. Each of the components, their function, and how they were assembled in the module are described in the rest of this section.

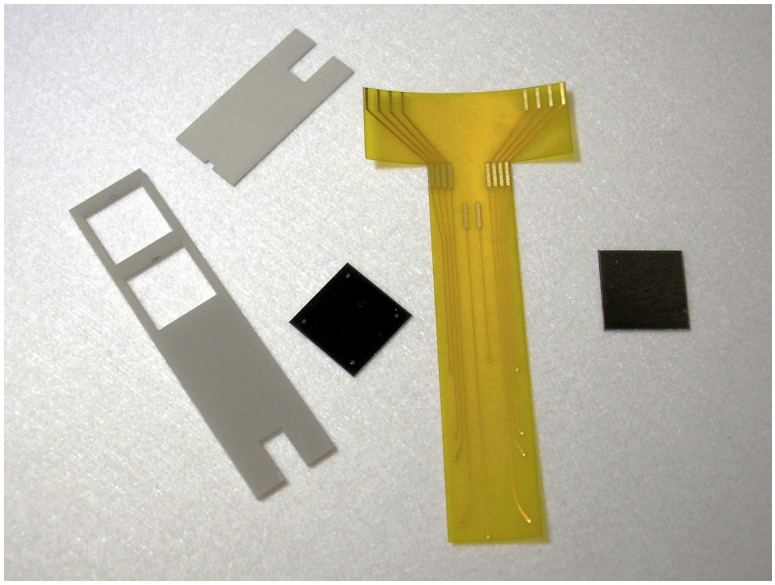

Figure 5.1: A picture of nearly all of the components of a single module. Missing are the two crystal arrays, which are shown in Figure 5.2.

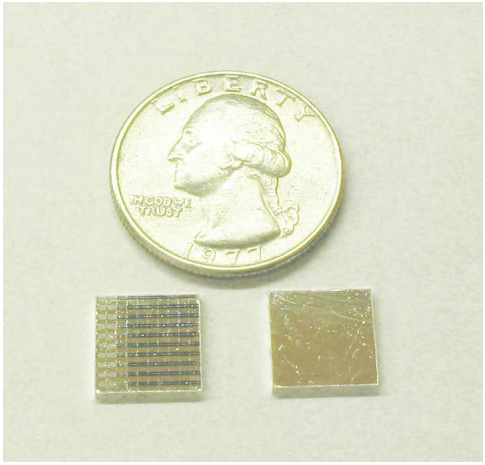

Figure 5.2: A picture of two arrays, left: with the segmentation side up (the side that it coupled to the photodetector and right: with the reflector side up. A quarter is shown for size reference.

5.2.1 Kapton Flex Circuit

The Kapton flex circuit was redesigned to overcome three issues faced in assembly and testing with the previous design, as well as to facilitate the incorporation of the

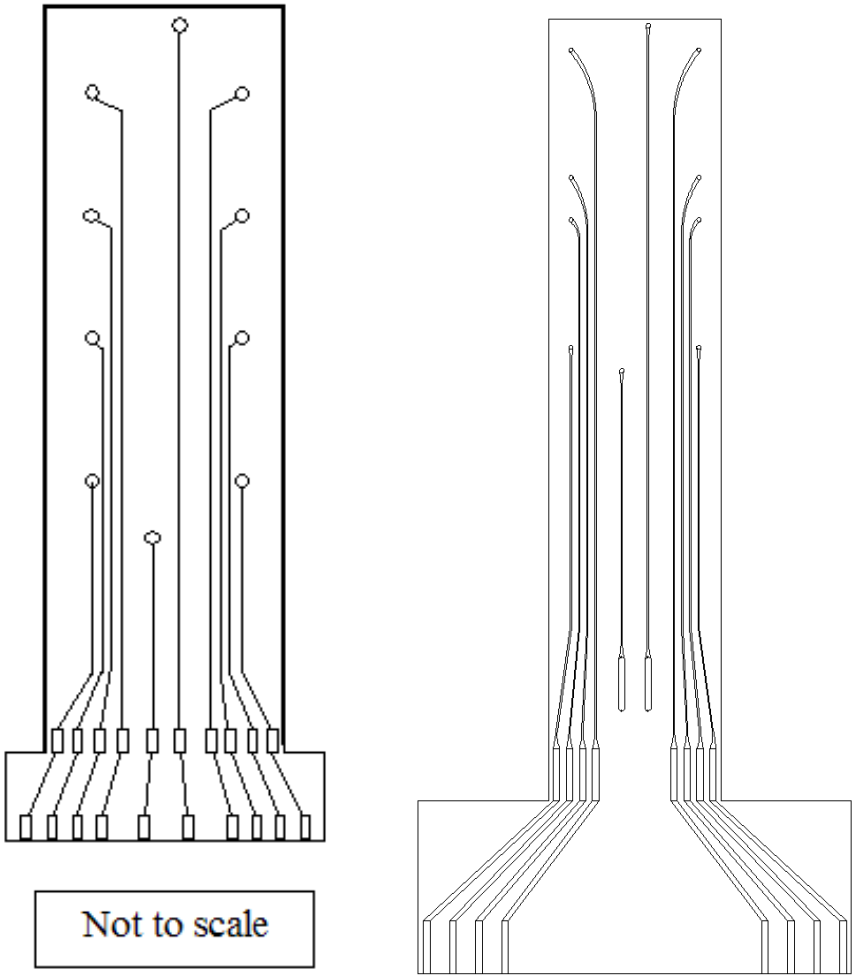

(a) (b)

Figure 5.3: The old and new versions of the Kapton flex circuit.

tested modules into the final system. The specifications for re-design can be broken down into four groups of structural changes:

- **Increased width of the Kapton.** Moisture from humidity in the air was leaking through the edges of the Kapton flex-circuit and interacting with the

PSAPDs, creating a complete absence of positioning ability of the device after as little as 22 minutes of operation. In the re-design, a widening of the Kapton flex circuit in the plane of the surface of the PSAPD provided a region to increase the amount of epoxy used to couple and seal the PSAPD to the Kapton, reducing the amount of moisture that could enter by 99.5% (based on diffusion estimates evaluated by Radiation Monitoring Devices).

- **Modifying the copper trace junctions.** Straight-edge narrowing and sharp cornering of traces at junctions between straight trace lines produced high stress and weak link regions in the copper traces. These regions, upon repeated handling of the Kapton flex circuits, eventually failed and in turn produced modules with unreadable signals. The copper traces were redesigned so that any change in trace direction or changes in width were done using a smooth, Bezier curve to bridge between points.

- **Restructuring of pads for removal of test region.** There were two sets of connection pads for reading out signals. The set of pads on the thin neck of the module, closer to the PSAPDs, were moved so that their location did not extend beyond the width of the PSAPD. This set comprised pads that were to be used by the built system. These pads were modified for high module packing and efficient electronic coupling. The second set of pads, further from the PSAPDs, were available only for the module testing phase. The test pad

set was spread out for facilitated connection options without electrical bridging between pads. The second set of pads were not to be used once the system was constructed, so a simple removal strategy was necessary. Ideally, the test region of the Kapton circuit would be removed by cutting away the circuit just before it widened. Since the high voltage (HV) pads would be more difficult to pacify after cutting, HV pads were not included in the test portion of the circuit for the redesign. The low voltage pads would then be pacified by a high dielectric sealant.

- **HV pad placement for arcing minimization.** The arcing between low and high voltage pads was reduced by moving the HV pads further up the flex circuit towards the PSAPDs. The pads' edges were also smoothed to reduce sharp edges, where arcing tended to occur.

5.2.2 Position Sensitive Avalanche Photodiodes

The PSAPD design and fabrication method was not altered from the design used in the devices tested in Chapter 3. The evolution (Sections 3.3-3.6) details of the PSAPDs can be found in Chapter 3.

5.2.3 Support Structure

Two structures, made of Aluminum Nitride (AlN), were designed and incorporated into the module to perform multiple functions. AlN is a ceramic that has a high thermal conductivity ($140 - 180\ \frac{W}{m \cdot K}$) and a high dielectric strength ($20\ \frac{kV}{mm}$). Its thermal expansion coefficient (AlN, $4.5 \cdot 10^{-6}/^{o}\mathrm{C}$) matches very well to that of the PSAPD (silicon, $2.6 \cdot 10^{-6}/^{o}\mathrm{C}$). AlN is also a hard ceramic, though fairly brittle and difficult to machine. These mechanical, thermal and electrical properties make AlN a common choice for silicon chip manufacturers for heat sinks and substrates for packaging. These were also the functions that the AlN provided in the module design described here.

Two dimensional computer aided draft (CAD) drawings of the AlN structures can be seen colored in green in Figure 5.5. Because the AlN material could not be manufactured with a step change in thickness, two pieces were necessary. The first piece (left AlN piece in Figure 5.5) was designed to be the same thickness as the silicon PSAPD chips and the same width as the Kapton flex circuit. It couples directly to the Kapton flex in the region between the two chips and the flex-circuit's signal read-out pads. The first piece of AlN functions effectively as a spacer to provide an even surface across the whole of the flex circuit, but ends before the signal pads.

The second AlN piece (right AlN piece in Figure 5.5) covers the whole of the flex circuit, though also ends before the signal pads so that the pads are still exposed. The

second piece provides structural support across the flex circuit for system assembly. This longer second piece also provides alignment of the LSO scintillator arrays by means of two windows directly over the active region of the PSAPDs. The second AlN structure also provides thermal coupling of the PSAPDs to the system structure because it is directly coupled to the PSAPDs in the frame-type region around the scintillation crystals.

5.2.4 Scintillation Crystal Array

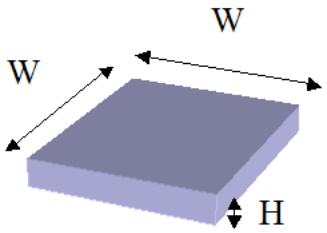

Figure 5.4: An illustration of the nomenclature for the dimensions of the crystal array.

Two scintillation crystal designs were chosen for study in the final design, one with inter-crystal reflector, one without. Both arrays:

- needed to fit in the same sensitive area on the PSAPD – an 8 mm x 8 mm region in the center of the chip.
- the maximum height could not exceed the height of the window of the AlN support structure. This height requirement was necessary so that the crystal

arrays did not produce a point of contact with the module stacked above them in an assembled system.

- utilized 3M brand VM2000 specular reflector on 5 of the 6 exposed faces of the assembled array. The face that was not covered was the 8 mm x 8 mm face coupled to the PSAPD so that light transmission to the photodetector was not impeded.

- had 64 crystals, arranged in an 8 x 8 configuration.

Because both types of arrays had to fit in the same active area of the PSAPD photodetector (i.e. to have the same outer dimensions), and the inter-crystal materials were different (i.e. one had two layers of epoxy sandwiching the reflector, and the other had only a layer of epoxy), the constituent crystals of the two designs had different dimensions. The design with VM2000 inter-crystal reflector and two layers of coupling material on either side of the reflector resulted in arrays that required crystals smaller in width.

5.2.5 Assembly

Assembly of the modules was done by the manufacturer of the PSAPD devices, Radiation Monitoring Devices Inc. The constituent pieces, in the order of placement, can be seen in Figure 5.5. The PSAPDs were first coupled to the Kapton flex circuit using the same silver epoxy used in previous flex-circuit designs. A non-conductive

epoxy was then used to fuse the smaller of the two AlN pieces to the flex to provide a base for the second AlN piece. Figure 5.6 shows the module at this point in assembly. The second AlN piece was adhered to the PSAPD and lower AlN piece using an electrically insulating, thermally conductive epoxy. A picture of an assembled module without crystal arrays can be seen in Figure 5.7. The LSO crystals were then placed into the AlN windows and adhered to the PSAPD using an index of refraction matching coupling material. The finished modules can be seen in the nitrogen storage enclosure in Figure 5.8.

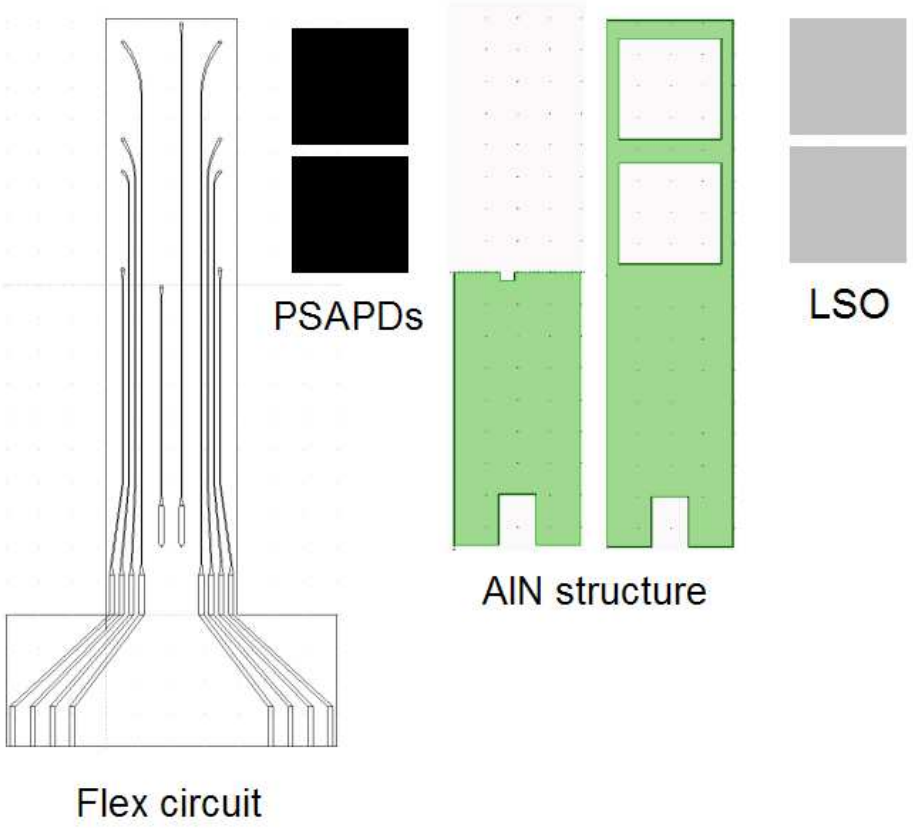

Figure 5.5: An illustration of the pieces and their relative locations in the assembled module.

5.3 Experimental Setup

5.3.1 Enclosure

An aluminum enclosure was designed and built to provide a dark, low-humidity, low ambient radio-frequency environment in which to test the modules. Thick walls (∼0.5 inch) and sufficiently strong, adjustable clamps were utilized so that nitrogen could be used to fill the chamber to one atmosphere gauge pressure (above ambient

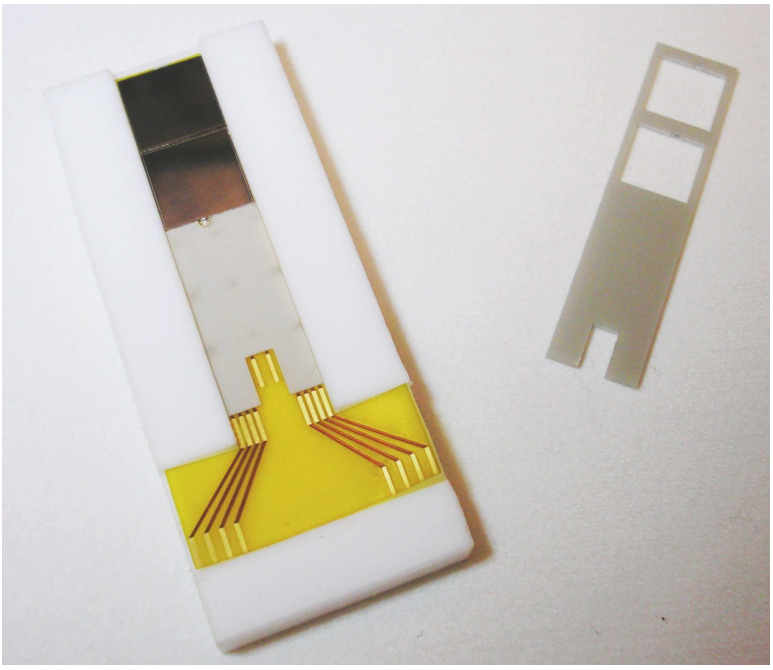

Figure 5.6: A picture of the PSAPDs and first AlN piece assembled on the Kapton flex circuit.

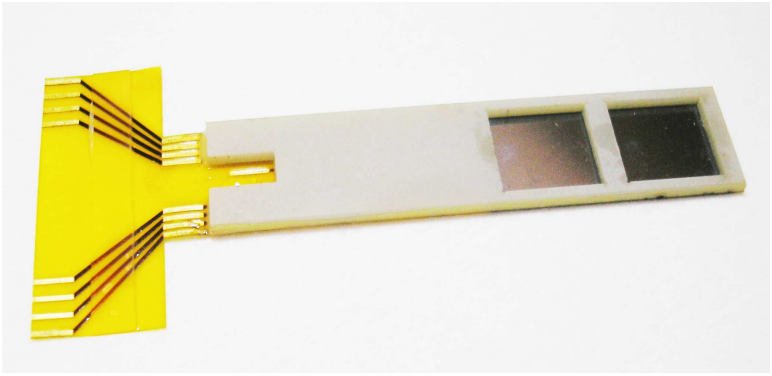

Figure 5.7: A picture of the PSAPDs and both AlN pieces assembled on the Kapton flex circuit.

pressure) in order to run long experiments. Because humidity was a prominent concern in past flex-cable experiments, a nitrogen storage chamber was also designed and built to house modules before and after experiments. This storage chamber can be

Figure 5.8: A picture of 19 of the 20 tested modules in the nitrogen storage chamber.

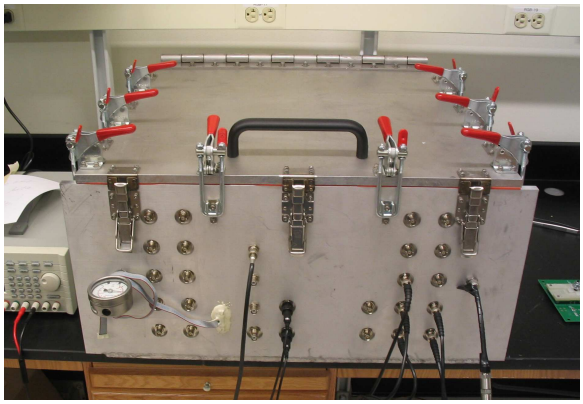

Figure 5.9: An illustration of the nitrogen environment enclosure used to test all final design modules.

seen in Figure 5.8.

5.3.2 Test Fixture

In order to facilitate coupling of the PSAPD flex-cable module to the signal pre-conditioning board, a test fixture was designed and built. This fixture provided a simple, re-usable, rigid coupling mechanism between the module and the pre-conditioning

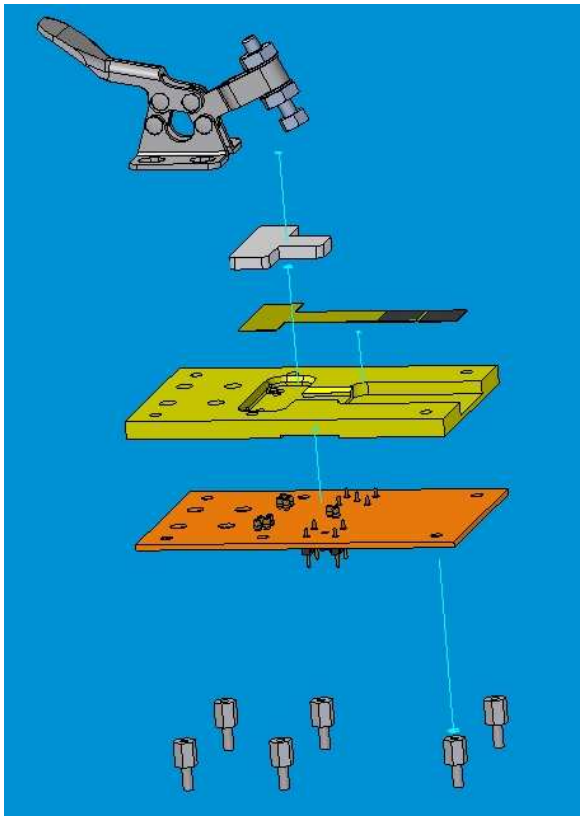

Figure 5.10: An illustration of the components in the reusable test fixture and how all layers were assembled.

board. It also facilitated alignment during the coincidence scanning experiment by securing the orientation of the modules with respect to the pre-conditioning boards. The assembly procedure is illustrated in Figure 5.10.

A clamping mechanism secured the flex module in place, where the pressure from the clamp (the top-most component in Figure 5.10) was distributed by a "T" shaped plastic bar over all contact pads (the component shown beneath the clamp in Figure 5.10). The dual-PSAPD flex module (shown as the third component in the same figure) was placed with its contact pads facing down, where spring loaded pogo pins

mounted through the yellow plastic tray (fourth component) made an adjustable contact with the exposed contact pads on the module. The orange component shown as the fifth piece in Figure 5.10 was the circuit board which coupled the pogo pins to the signal output pins. The output pins were oriented downwards so that they could fit into the input connectors on the pre-conditioning board. The last pin-like pieces, shown as the sixth component, are stand-offs which provided room for non-flush electronics and the output pins while still providing support once the test fixture is coupled to the pre-conditioning board.

5.3.3 Test Pre-Conditioning Board

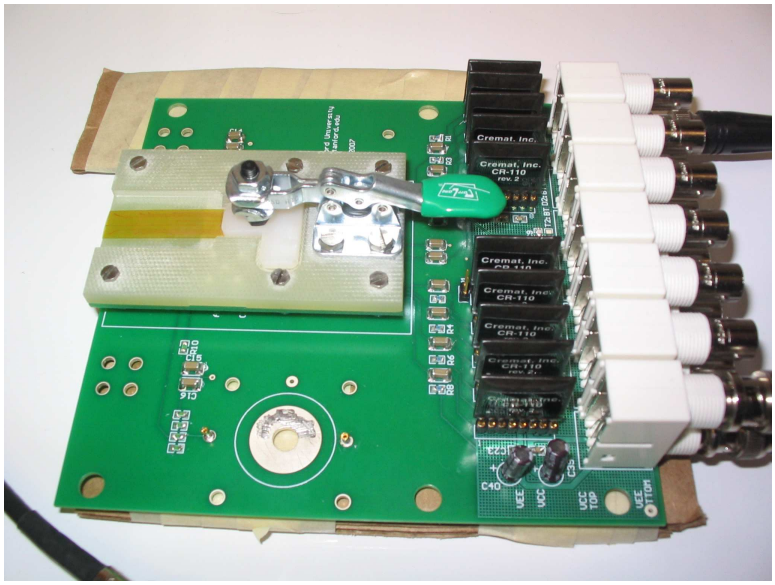

Figure 5.11: A picture of the test pre-conditioning board, including pre-amps. The figure shows the PSAPD module clamped into the test fixture, which is plugged into the test pre-conditioning board.

A pre-conditioning board was constructed which provided bias voltage to the flex module, capacitive coupling from the output of the flex module to the input of pre-amplifiers (pre-amps), the charge sensitive pre-amplifiers themselves, and the power required to run the pre-amps (see Figure 5.11). The flex module was coupled to this pre-conditioning board through the test fixture described in Section 5.3.2.

The outputs of the board were the pre-amplified signals from the four corner channels and the top common channel of both PSAPD devices on the flex cable. The output connections were 50 Ω BNC cables which were coupled to the bulkhead BNC connectors on the nitrogen environment enclosure in order to connect to the acquisition electronics.

5.3.4 Electronics

Nuclear Instrumentation Module (NIM) electronics were used for shaping and processing signals from the PSAPDs acquired in coincidence. The signal paths are illustrated in Figure 5.12. Two PSAPDs were in coincidence at a time. The four corner positioning channels A, B, C and D, as well as the top common channel E (see the two inserts in Figure 5.12) were continuously read out during the acquisition. The first PSAPD's corner signals A1, B1, C1, and D1 were processed in the traditional manner with pre-amplifiers, spectrum amplifiers, and a delay to line up the signal in time with the trigger. The four corner channels were used after acquisition to

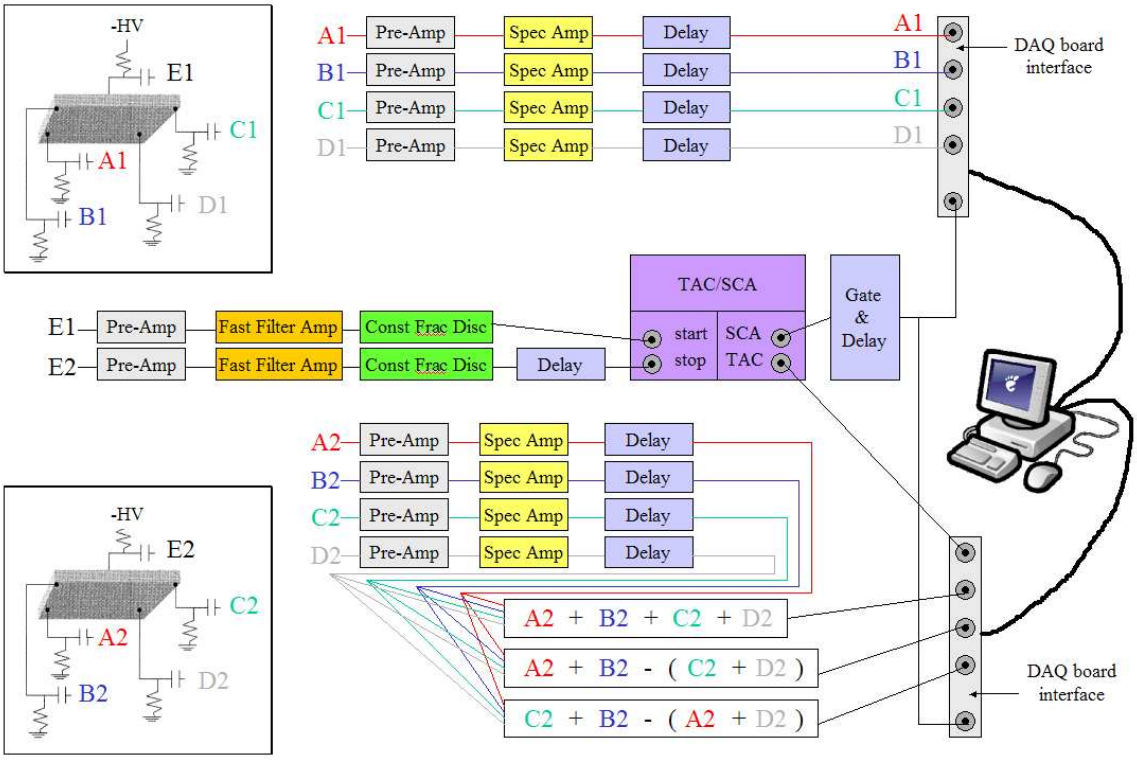

Figure 5.12: An illustration of the coincidence scan acquisition electronics.

calculate the position and energy of the acquired event.

The second PSAPD's corner signals were first processed in the same manner, and then underwent sum and invert processing to directly compute the coordinates for the position of the interactions (X2, Y2) and energy of the event for acquisition. This further processing step reduced the number of acquired channels to determine position and energy from 4 to 3. This reduction in number of signal channels was necessary because only 8 analog to digital converters (ADCs) were available to acquire signals at any time. The final signal that was necessary was the TAC signal, or the time

difference signal between the two PSAPDs. This signal was necessary for filtering the acquired data to an acceptable time window, producing good quality coincidence events.

The trigger for the coincidence events was produced by a fast coincidence electronics setup. Fast Filter Amplifiers (FFAs) were used to integrate and differentiate the signal to attain good signal quality with the least amount of processing to introduce as little smoothing as possible. Constant Fraction Discriminators (CFDs) were employed to accurately determine the time of the event, independent of signal amplitude. The CFDs provided a short duration signal for indicating the time an interaction occurred in the PSAPD. Coincidence was determined using a Time to Amplitude Converter/Single Channel Analyzer (TAC/SCA). The start of the coincidence was the output of the CFD from the first PSAPD. The stop signal was determined from the delayed output of the CFD processing of the second PSAPD. The added delay was constant (18 ns) which translated the TAC signal from a Gaussian centered near 0 ns to one centered near 18 ns, depending on the inherent delays associated with each PSAPD due to the RC constant (resistance-capacitance) of the individual device. The two outputs of the TAC/SCA were: (1) the time difference of the start and stop signal, or the TAC signal, and (2) a constant height signal specifying in a binary nature whether a coincidence was formed (5V coincidence, 0V no coincidence). The SCA signal was processed through a gate and delay generator, which provided the trigger for all 8 channels (A1, B1, C1, D1, X2, Y2, S2, TAC), where S2 is the

sum of all corner channels from the second PSAPD (i.e. S2 = A2 + B2 + C2 + D2).

The acquisition of this eight channel set (8-tuple) provided the ability to determine interaction position, position dependent energy, and position dependent time of each event in both PSAPDs for each coincidence event. The coincidence-acquired (1) energy spectral analysis, (2) crystal identification, (3) point spread function, and (4) crystal pair coincidence time resolution were evaluated using this data acquisition setup.

5.3.5 Scanning

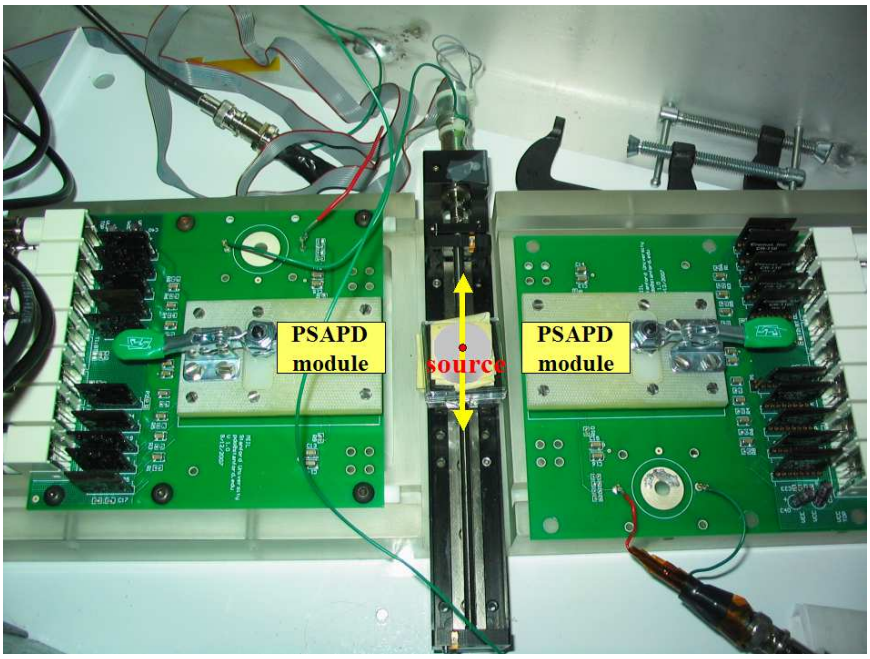

Figure 5.13: A picture of the dual-chip PSAPD coincidence scan setup. The two green PCB test boards (see Section 5.3.3) provide power, pre-processing electronics and mechanical support to the white test fixture (see Section 5.3.2). The test boards hold the coincident PSAPDs in the same plane as the scanning source. The source scans in a line using the electronically controlled positioning stage (black).

For each experiment, two modules were aligned using the setup shown in Figure 5.13. An electronically controlled micro-positioning stage was used to translate a 100 μCi ^{22}Na point source at 165 μm steps across the faces of the two modules. The two PSAPD modules faced each other, equidistant from the source, separated by 6 cm. The point source remained at each location for 25 minutes and acquired ~20,000 coincidence events for each step. The data were written out so that each acquired 8-tuple was on a separate line (list mode format).

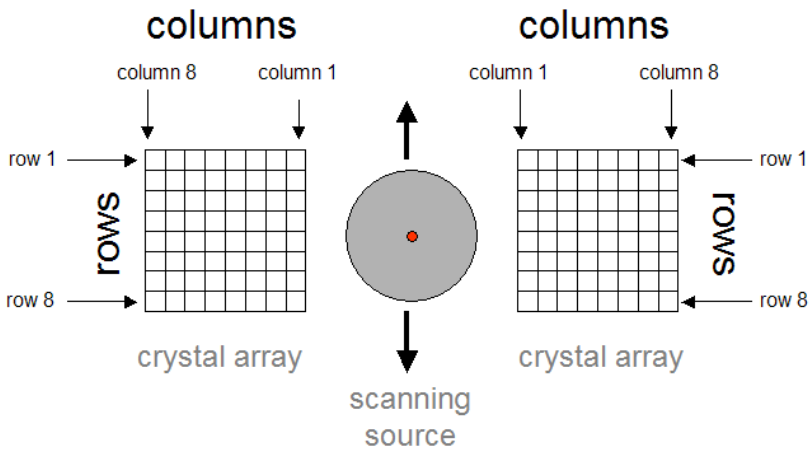

Figure 5.14: An illustration of the nomenclature used to name crystals within the coincident arrays. The arrays and the source are in the same plane throughout the entire scan.

Two experiments were performed: (1) using two modules where both did not have inter-crystal reflectors, and (2) using two modules where both had inter-crystal reflector. Coincidence was made between the front PSAPDs in both modules for each experiment. The methods and results of these experiments will be discussed in the next sections.

Results will be discussed for crystal groups called "rows" and "columns" within the array. An illustration of this naming scheme is shown in Figure 5.14.

5.4 Results: Crystal Identification

Coincidence position histograms were obtained by including all of the events gathered during the entire scan experiment into one two-dimensional position image.

These data indicate the ability to identify crystals in the coincident arrays. Separable crystal regions usually correlate with separable individual crystal point spread functions.

5.4.1 Without Intercrystal Reflector

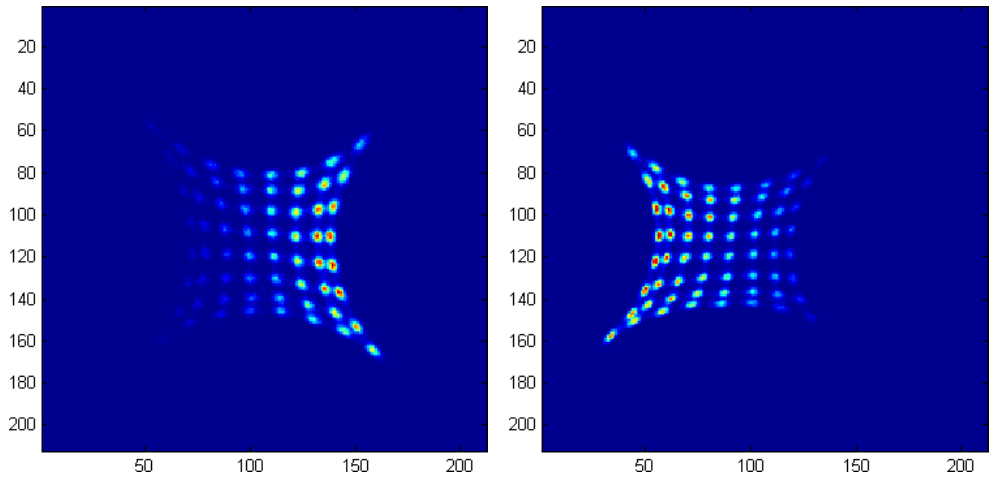

(a) (b)

Figure 5.15: Coincidence flood for the whole array.

The images in Figure 5.15 show globally energy windowed coincidence position histograms for all crystals in the coincident arrays. The images in Figure 5.16 show individual crystal energy gated positions for each crystal in the first three columns of crystals, where the bulk of the coincident interactions took place. The orientation of the arrays was the same as shown in Figure 5.13, i.e. the source was scanned between the shown arrays (i.e. vertically, in both figures). All crystals locations were

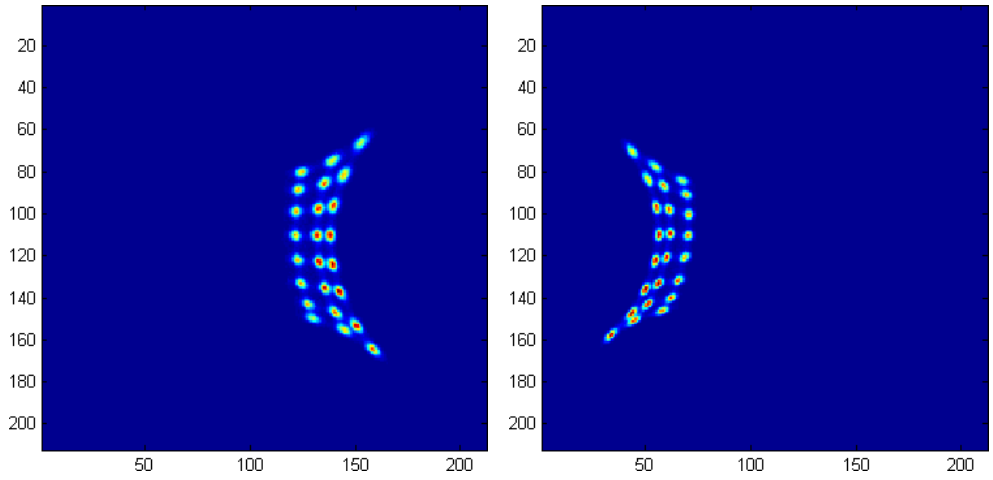

(a) (b)

Figure 5.16: Energy gated coincidence flood for the first three columns of crystal closest to the ^{22}Na point source.

identified and crystal regions were well separated.

5.4.2 With Intercrystal Reflector

The images in Figure 5.17 show globally energy windowed coincidence position histograms for all crystals in the coincident arrays. The images in Figure 5.18 show individual crystal energy gated positions for each crystal in the first three columns of crystals, where the bulk of the coincident interactions took place. The orientation of the arrays was the same as shown in Figure 5.13, i.e. the source was scanned between the shown arrays, vertically.

All crystals locations were identified and crystal regions were even better separated than the arrays without inter-crystal reflectors. Note also that the dynamic range of

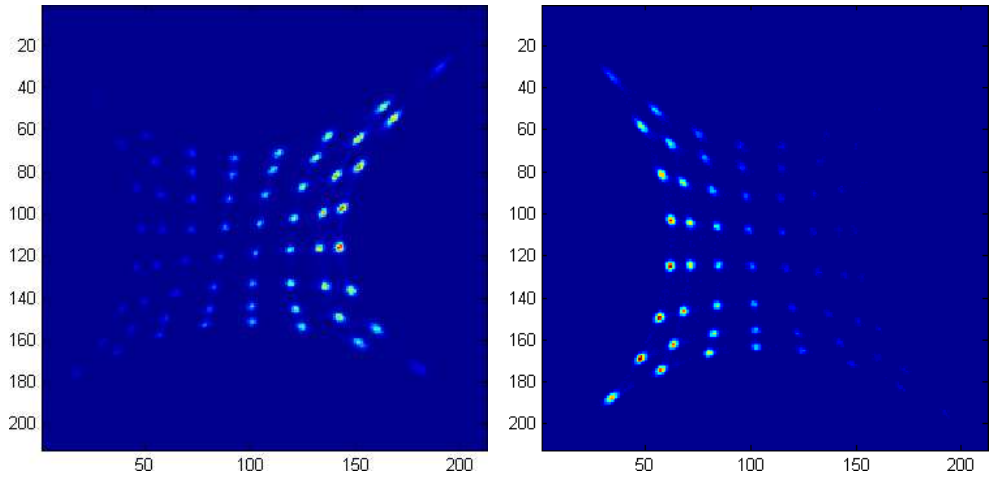

(a) (b)

Figure 5.17: Coincidence flood for the whole array.

the crystal locations is increased in the coincidence position histograms for the arrays with inter-crystal reflector. These results followed the trend seen when evaluating crystal identification using a flood measurement.

5.5 Results: Energy Spectral Analysis

Energy resolution and photopeak position were evaluated for both with inter-crystal and without inter-crystal reflector experiments for each crystal in the array. Energy spectra were obtained for each crystal by including all of the events gathered during the entire scan experiment. Per crystal energy spectra were evaluated for energy resolution and photopeak position. Representative energy spectra are also included in this section.

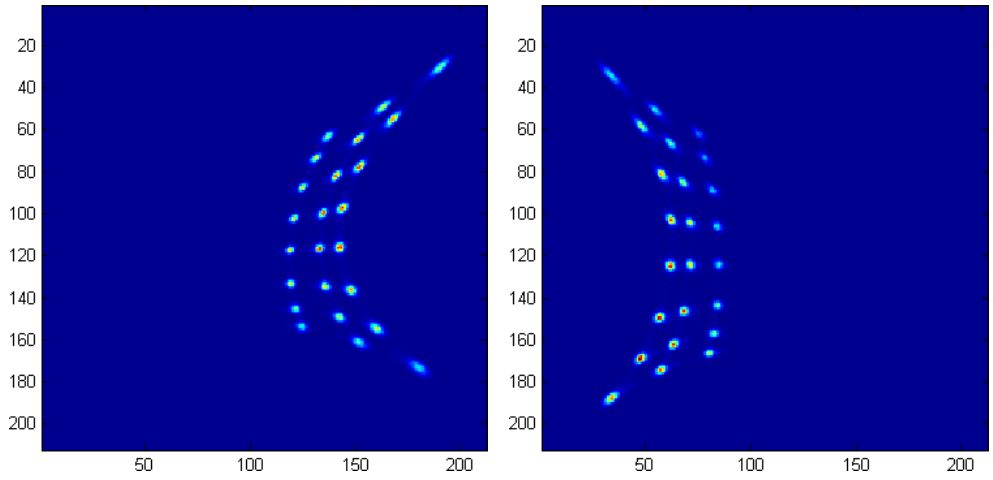

(a) (b)

Figure 5.18: Energy gated coincidence flood for the first three columns of crystal closest to the ^{22}Na point source.

5.5.1 Arrays Without Intercrystal Reflector

Energy Resolution

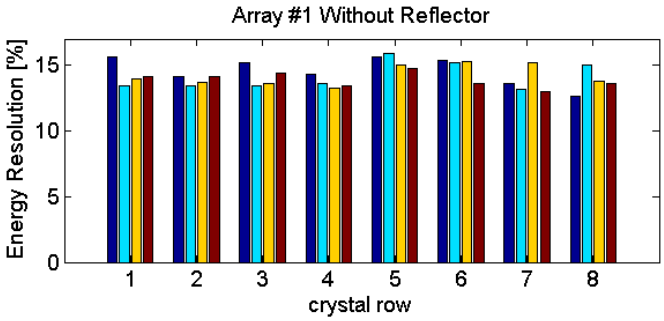

Figure 5.19: Energy resolution for each of the 32 crystals in the front 4 columns of crystals of array 1 without inter-crystal reflector. Column 1: dark blue, column 2: light blue, column 3: yellow, column 4: red (see figure 5.14 for an illustration of row and column nomenclature).

Figures 5.19 and 5.20 show the energy resolution for the front 4 columns of crystals

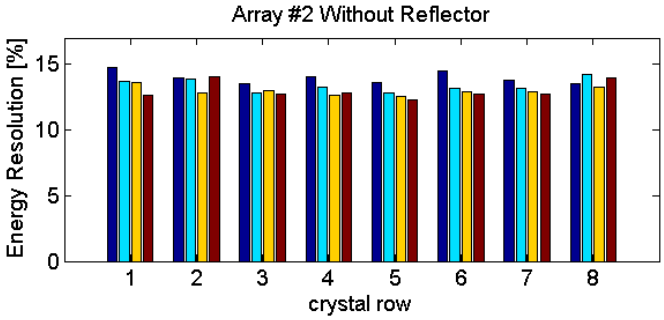

Figure 5.20: Energy resolution for each of the 32 crystals in the front 4 columns of crystals of array 2 without inter-crystal reflector. Column 1: dark blue, column 2: light blue, column 3: yellow, column 4: red (see figure 5.14 for an illustration of row and column nomenclature).

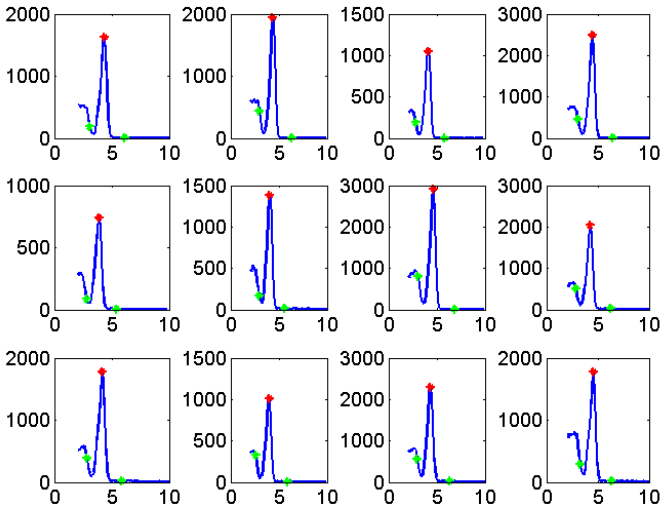

Figure 5.21: Energy spectra for 12 crystals without inter-crystal reflector. Shown for each crystal is gathered data in the region surrounding the 511 keV photopeak, where the peak position is signified by the red star. The green stars define the region over which the data were fit.

in each of the arrays in coincidence. The figures group the crystals in the same row of the array to the same x-coordinate and differentiate the four columns of the array by the color of the bar. Red, orange, light blue, and dark blue represent the first through

fourth columns respectively. The data were fit with an exponential plus Gaussian function to determine peak location and FWHM of the photopeak. The first crystal array had an average per crystal energy resolution of 14.2% with a standard deviation within the array of 0.6%. The second crystal array had an average per crystal energy resolution of 13.3% with a standard deviation within the array of 0.9%.

Figure 5.21 shows 12 representative energy spectra for the modules without inter-crystal reflector. The photopeak was well resolved from the exponentially decreasing tail (which is due to multiple and single Compton interactions). This result was likely due to the coincidence requirement for acquisition, i.e. very few if any acquired events were due to scattering in surrounding material before interaction in the LSO array. The red marker in each spectrum of Figure 5.21 shows the fitted Gaussian peak location (see Section 5.5.1), and the green markers indicate the regions over which the data were fit.

Peak Position

Photopeak position, which corresponds to the signal height in Volts of 511 keV interactions, is an indication of the cumulative gain of the acquisition process. Figures 5.22 and 5.23 show the peak position of the photopeak for the front 4 columns of crystals in each of the arrays in coincidence. The figures group the crystals in the same row of the array to the same x-coordinate and differentiate the four columns of the array by the color of the bar. Red, orange, light blue, and dark blue again

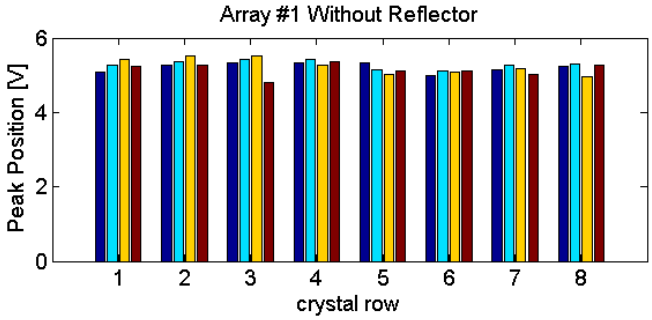

Figure 5.22: Peak position for each of the 32 crystals in the front 4 columns of crystals of array 1 without inter-crystal reflector. Column 1: dark blue, column 2: light blue, column 3: yellow, column 4: red (see figure 5.14 for an illustration of row and column nomenclature).

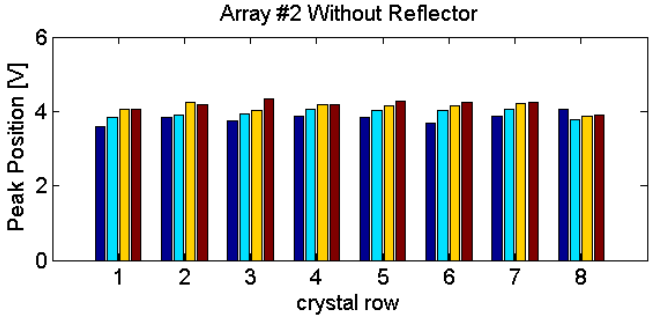

Figure 5.23: Peak position for each of the 32 crystals in the front 4 columns of crystals of array 2 without inter-crystal reflector. Column 1: dark blue, column 2: light blue, column 3: yellow, column 4: red (see figure 5.14 for an illustration of row and column nomenclature).

represent the first through fourth columns respectively. As mentioned previously, the data were fit with an exponential plus Gaussian function to determine peak location of the photopeak. The average peak position for the first array was 5.23 Volts with a standard deviation within the array of 0.16 Volts. The average peak position for the second array was 4.01 Volts with a standard deviation within the array of 0.19 Volts.

5.5.2 Arrays With VM2000 Intercrystal Reflector

Energy Resolution

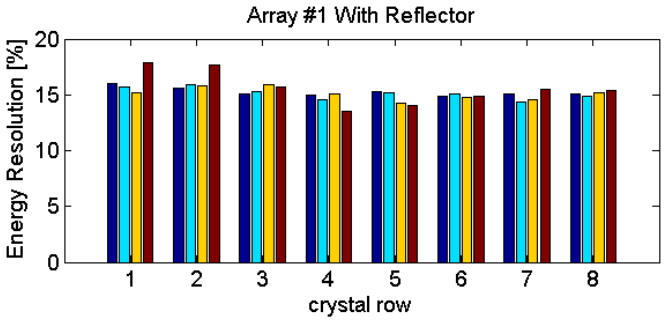

Figure 5.24: Energy resolution for each of the 32 crystals in the front 4 columns of crystals of array 1 with VM2000 inter-crystal reflector. Column 1: dark blue, column 2: light blue, column 3: yellow, column 4: red (see figure 5.14 for an illustration of row and column nomenclature).

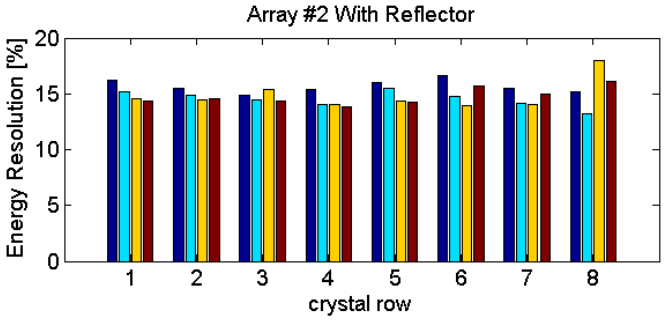

Figure 5.25: Energy resolution for each of the 32 crystals in the front 4 columns of crystals of array 2 with VM2000 inter-crystal reflector. Column 1: dark blue, column 2: light blue, column 3: yellow, column 4: red (see figure 5.14 for an illustration of row and column nomenclature).

Figures 5.24 and 5.25 show the energy resolution for the front 4 columns of crystals in each of the arrays in coincidence. The figures group the crystals in the same row of the array to the same x-coordinate and differentiate the four columns of the array by

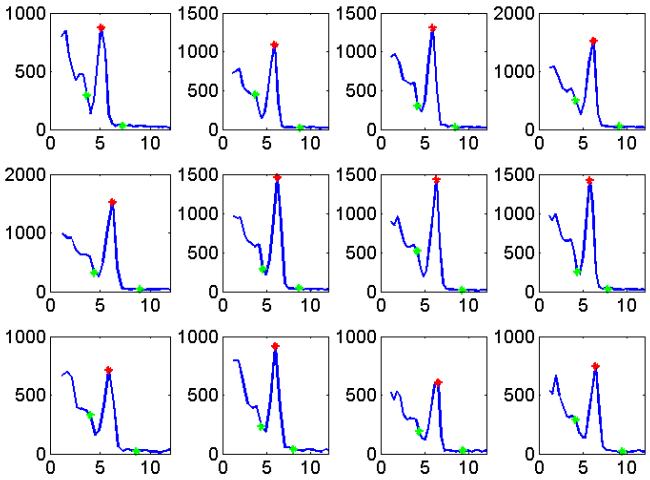

Figure 5.26: Energy spectra for 12 crystals with VM2000 inter-crystal reflector. Shown for each crystal is gathered data in the region surrounding the 511 keV photopeak, where the peak position is signified by the red star. The green stars define the region over which the data were fit.

the color of the bar. Red, orange, light blue, and dark blue represent the first through fourth columns respectively. The data were fit with an exponential plus Gaussian function to determine peak location and FWHM of the photopeak. The first crystal array had an average per crystal energy resolution of 15.3% with a standard deviation within the array of 0.9%. The second crystal array had an average per crystal energy resolution of 15.0% with a standard deviation within the array of 1.0%.

Figure 5.26 shows 12 representative energy spectra for the modules without inter-crystal reflector. The photopeak was well resolved from the exponentially decreasing tail (which is due to multiple and single Compton interactions). This result was likely due to the coincidence requirement for acquisition, i.e. very few if any acquired events

were due to scattering in surrounding material before interaction in the LSO array. The red marker in each spectra of Figure 5.21 shows the fitted Gaussian peak location (see Section 5.5.1), and the green markers indicate the region over which the data were fit.

Peak Position

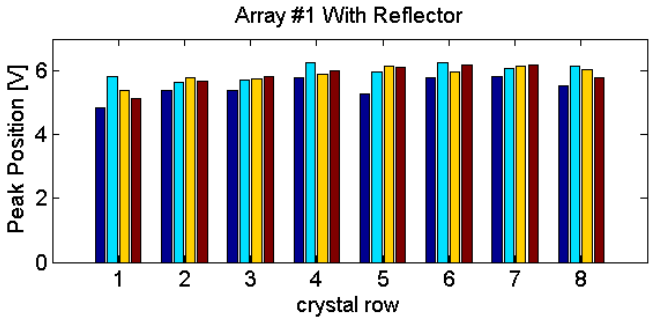

Figure 5.27: Peak position for each of the 32 crystals in the front 4 columns of crystals of array 1 with VM2000 inter-crystal reflector. Column 1: dark blue, column 2: light blue, column 3: yellow, column 4: red (see figure 5.14 for an illustration of row and column nomenclature).

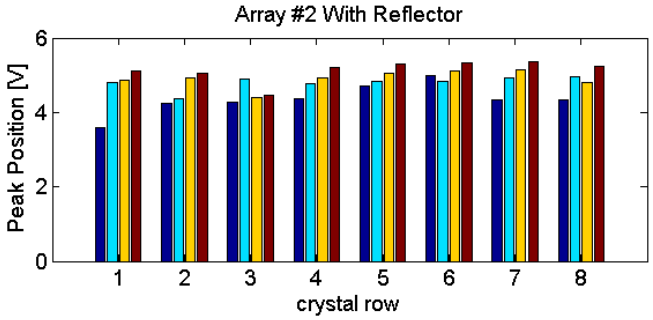

Figure 5.28: Peak position for each of the 32 crystals in the front 4 columns of crystals of array 2 with VM2000 inter-crystal reflector. Column 1: dark blue, column 2: light blue, column 3: yellow, column 4: red (see figure 5.14 for an illustration of row and column nomenclature).

Figures 5.27 and 5.28 show the peak position of the photopeak for the front 4 columns of crystals in each of the arrays in coincidence. The figures group the crystals in the same row of the array to the same x-coordinate and differentiate the four columns of the array by the color of the bar. Red, orange, light blue, and dark blue again represent the first through fourth columns respectively. As mentioned previously, the data were fit with an exponential plus Gaussian function to determine peak location of the photopeak. The average peak position for the first array was 5.81 Volts with a standard deviation within the array of 0.35 Volts. The average peak position for the second array was 4.80 Volts with a standard deviation within the array of 0.40 Volts.

5.6 Results: Coincidence Scanning

5.6.1 Point Spread Function

Scanning was performed by acquiring scanning data from the PSAPDs closest to the source ("front" PSAPD) for the modules in coincidence (see Section 5.3.5). Data were gathered for all crystals coupled to the coincident PSAPDs at each source location. Position resolution was measured for the cases with and without inter-crystal reflector by plotting the number of counts observed at each scan step for only the parallel line coincident set of crystals (i.e. rows). For instance, only crystals in row 1 of array 1 were considered for coincidence with row 1 in the opposing crystal

array, array 2. The counts distribution that each set produced indicated the physical space over which coincidence events were acquired and therefore would be considered the same location by the system, i.e. from the same crystal row. In other words, if coincidence counts were registered between the crystals in row 2 of each array over a range of step positions, all of those counts would be positioned at the line of response between the front two crystals of row 2. The spatial distribution formed by counting coincidence events at each step is called the point spread function (PSF). All PSFs shown have been energy filtered by the individual crystal energy window.

Two point spread functions will be shown for both experiments. The first is the point spread function for coincidence between only the front crystals, closest to the scanning point source. The second PSF is showing the distribution for coincidence between the front crystal from one array and all crystals in the same row of the opposing array (which has been labelled "front-row" in the figure title).

Without Intercrystal Reflector

Figure 5.29 shows the fitted point spread function for each front crystal pair. In the legend, xx1 is the source position (in steps) and yy1-yy8 are the first through eigth rows of the coincident arrays, respectively. The markers indicate the measured counts at each scan step and the solid lines indicate a single Gaussian fit to each crystal pair distribution. The average FWHM width of the Gaussians was 2.6 mm $\pm$ 0.7 mm.

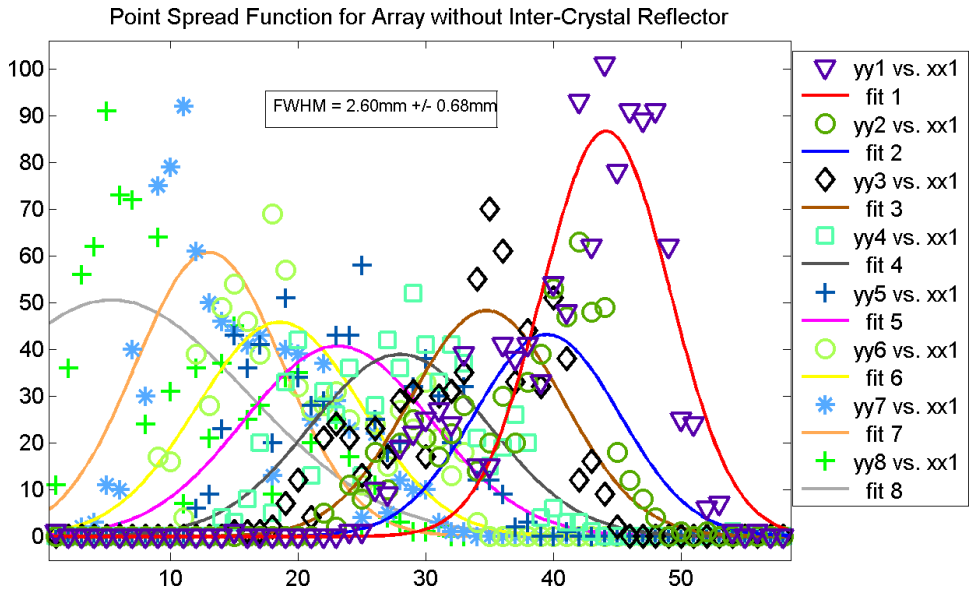

Figure 5.29: Fitted point spread function for the front crystal pairs without inter-crystal reflector.

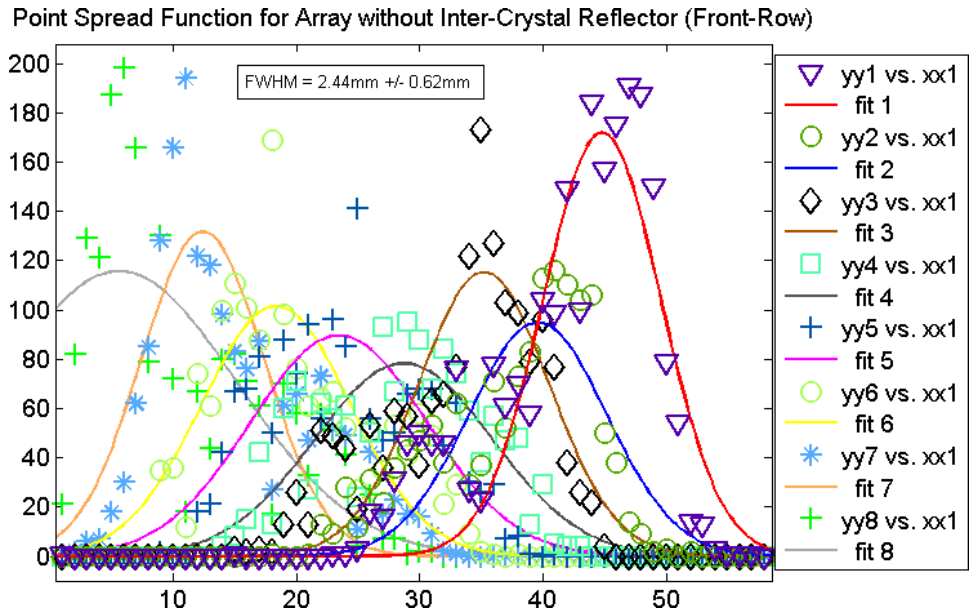

Figure 5.30: Fitted point spread function for the front crystal and opposing row without inter-crystal reflector.

Figure 5.30 shows the fitted point spread function for each front crystal and opposing row of crystals. Again, the markers indicate the measured counts at each scan step and the solid lines indicate a single Gaussian fit to each crystal pair distribution. The average FWHM width of the Gaussians was 2.4 mm ± 0.6 mm.

These results show that the position resolution for the arrays without inter-crystal reflector indicate that neighboring crystals are not resolved from one another, despite the seemingly well separated crystal locations in the crystal flood measurements.

With Intercrystal Reflector

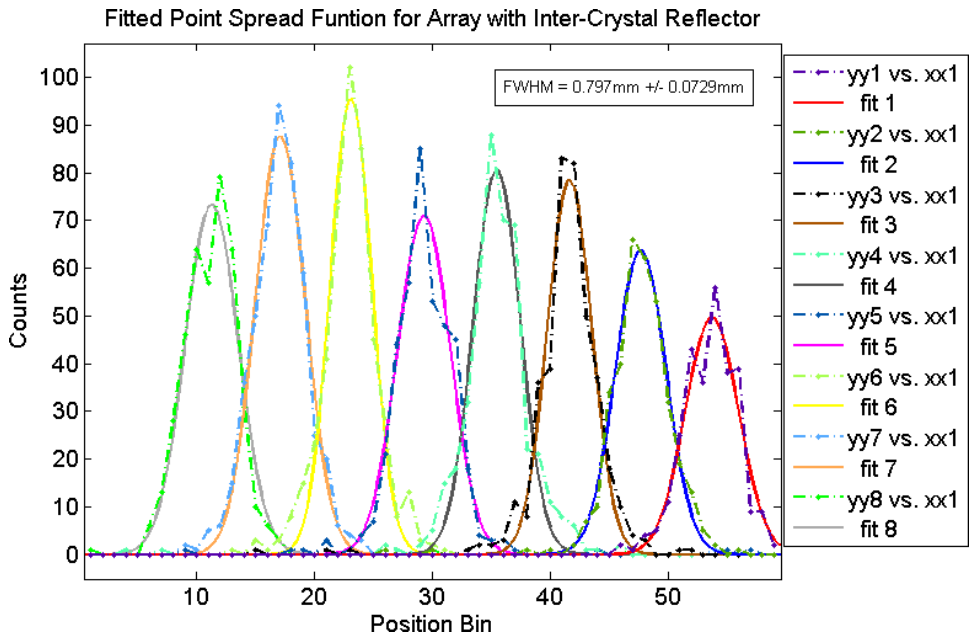

Figure 5.31: Fitted point spread function for the front crystal pairs with VM2000 inter-crystal reflector.

Figure 5.31 shows the fitted point spread function for each front crystal pair. In

the legend, xx1 is the source position (in steps) and yy1-yy8 are the first through eigth rows of the coincident arrays, respectively. The markers indicate the measured counts at each scan step and the solid lines indicate a single Gaussian fit to each crystal pair distribution. The average FWHM width of the Gaussians was 0.80 mm ± 0.07 mm.

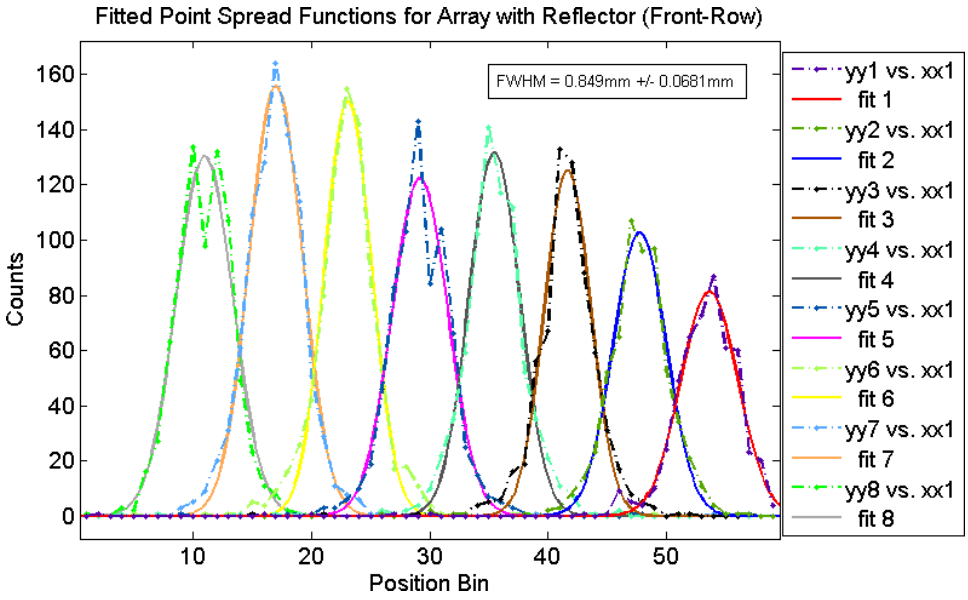

Figure 5.32: Fitted point spread function for the front crystal and opposing row with VM2000 inter-crystal reflector.

Figure 5.32 shows the fitted point spread function for each front crystal and opposing row of crystals. Again, the markers indicate the measured counts at each scan step and the solid lines indicate a single Gaussian fit to each crystal pair distribution. The average FWHM width of the Gaussians was 0.85 mm ± 0.07 mm.

These results show that the crystals in the arrays with inter-crystal reflector are well separated from one another, i.e. that the fitted PSF FWHM is smaller than

the PSF peak separation. This result provides a good argument for choosing to use arrays with inter-crystal reflector for similar segmented crystal designs.

5.6.2 Coincidence Time Resolution

Coincidence time resolution (CTR) was measured for all pairs of crystals in the first three columns and in the same crystal row. The TAC spectra were plotted for each pair and fit to a single Gaussian. All TAC data were energy filtered by the individual crystal energy window.

Without Intercrystal Reflector

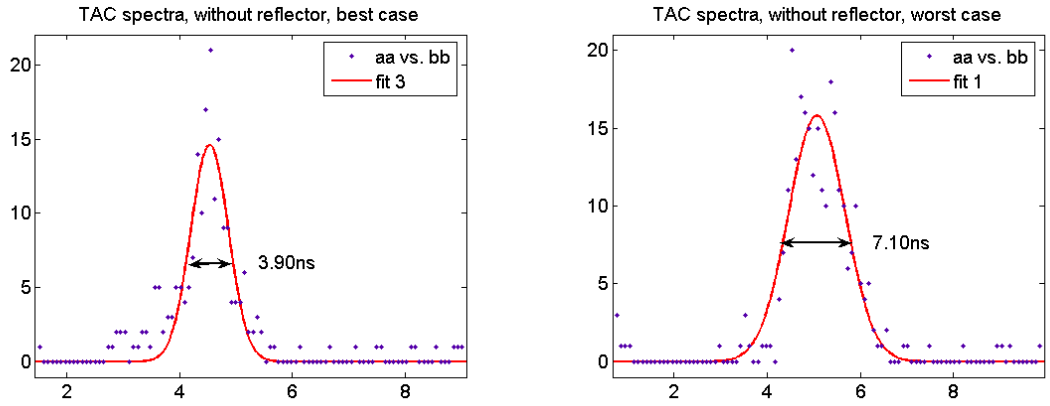

(a) (b)

Figure 5.33: Energy gated coincidence TAC spectra for the best and worst case individual crystal coincidence.

The average coincidence time resolution for the arrays without inter-crystal reflector was 5.6 ns ± 1.0 ns. The best and worst TAC distributions are shown in Figure

5.33. The markers are the acquired, energy filtered data, and the solid lines are the single Gaussian fits. The peak position of the TAC distribution also varied with an average of 16.2 ns ± 2.1 ns.

With Intercrystal Reflector

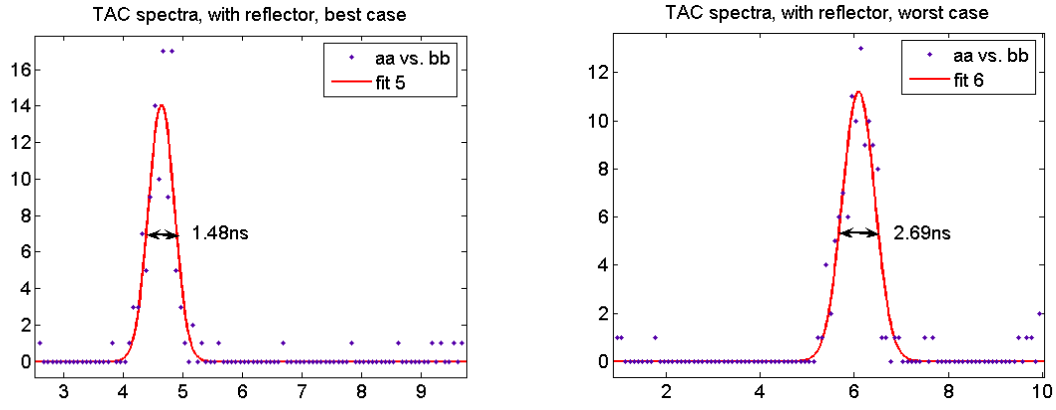

(a) (b)

Figure 5.34: Energy gated coincidence TAC spectra for the best and worst case individual crystal coincidence.

The average coincidence time resolution for the arrays without inter-crystal reflector was 1.9 ns ± 0.3 ns. The best and worst TAC distributions are shown in Figure 5.34. The markers are the acquired, energy filtered data, and the solid lines are the single Gaussian fits. The peak position of the TAC distribution also varied with an average of 18.0 ns ± 3.2 ns. These CTR results do not follow the trend seen in previous experiments where CTR was measured using a PMT in coincidence with an LSO array coupled to a PSAPD. These results indicate that a module design with

inter-crystal reflector would have superior coincidence time resolution.

5.7 Conclusion

Performing scanning coincidence experiments between two LSO-PSAPD modules produced definitive results in determining the superior module design. Although arrays without inter-crystal reflector had on average better energy resolution (13.8%) than those with inter-crystal reflector (15.1%), position resolution (0.8 mm versus 2.8 mm), coincidence time resolution (1.9 ns versus 5.6 ns), and photopeak location (gain, 5.31 V versus 4.62 V) were superior for modules with inter-crystal reflector.

Chapter 6

System Design

6.1 Introduction

The on-going goal for development of imaging systems for molecular imaging is to increase detection sensitivity and resolution. Higher counting statistics along with better precision in event energy, time, and spatial localization directly correlate with feature quantitation and detection in the reconstructed image. In constructing detectors for high-energy photon tomographic imaging, such as positron emission tomography (PET) and single photon emission tomography (SPECT), the scintillator material and shape are chosen to have high effective stopping power, convert high energy photons to energies more efficiently read by photodetectors, and increase the resolution of the detection system. The placement of this scintillation material and how it is read out determines many of the factors important to emission tomography:

sensitivity, energy resolution, time resolution, position resolution; all of which ultimately lead to a system's ability to reject noise, and increase contrast and resolution in the resulting image.

6.2 Mechanical System Design Constraints

6.2.1 Inner Bore Diameter

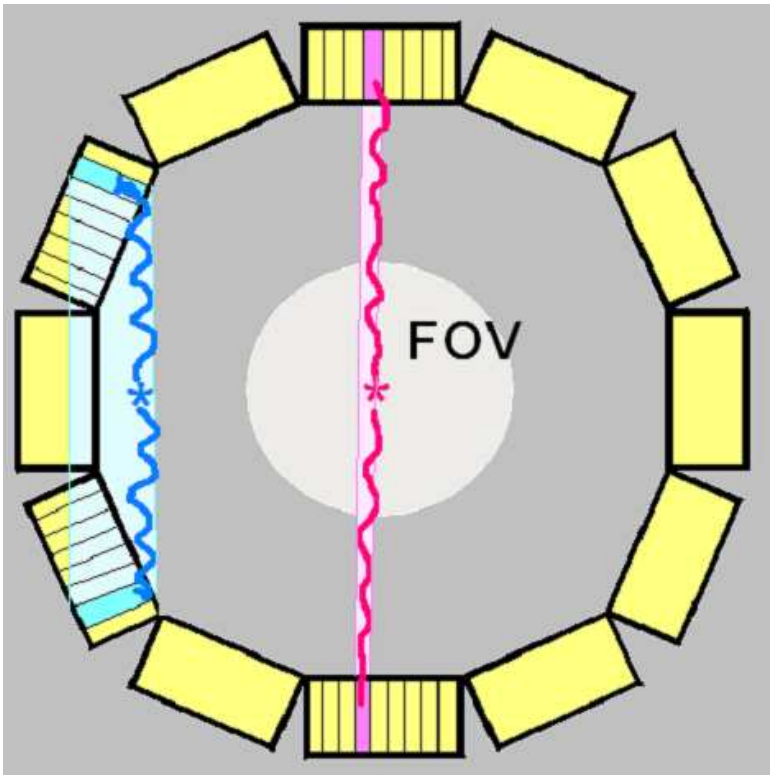

Figure 6.1: An illustration of the depth of interaction blur when detector elements are unable to record a photon's interaction location in the radial direction, as is the case with traditional detector systems.

In traditional PET systems, the inner diameter of a detector system is made large

to reduce the effects of depth of interaction (DOI) blur [186]. Figure 6.1 shows how the location of annihilation inside the system in conjunction with the detector location and orientation can result in varying degrees of positioning accuracy.

A traditional system's field of view (FOV) is chosen to reduce the error from not knowing the radial interaction location. The pink coincident event in Figure 6.1 was created by an annihilation near the center of the system, within the usable FOV, where photons are travelling mostly along the long dimension of the detection crystal. The blue coincident event demonstrates the increase in position blur from events outside this central FOV. This increase in position blur is due to the direction the annihilation photons are travelling relative to the detection crystals, i.e. the blue photons have a large vector component perpendicular to the long dimension of the detection crystal. Because the location of the interaction in the depth direction (long dimension) of the crystal is unknown, it is said to have a depth of interaction blur. To counteract this DOI blur, systems often use a reduced or useful field of view (UFOV) (see Section 1.4.3).

The system that is being investigated in this study inherently measures the depth of interaction location in the detector system by means of segmented scintillation crystals coupled to position sensitive photodetectors. This DOI direct measurement capability greatly expands the possible system designs. Detection elements can be oriented in far more directions with respect to incoming photons and brought in close to the subject being imaged without suffering blur from depth of interaction

uncertainties. Being able to use modules in more orientations (because they can detect in three dimensions), increases the practicality of many system shapes.

Bringing detectors close to the subject has other benefits. A smaller system diameter means the same solid angle can be covered as in traditional systems while using far less system material. Sensitivity can also be increased with a smaller system cost increase because each detector covers a larger solid angle when proximal to the object. As mentioned in Section 1.3.1, a smaller system diameter also reduces the effect of annihilation photon acollinearity, resulting in a smaller deviation of the line of response from a line that goes through the actual annihilation location.

Although depth of interaction concerns were no longer dominating the need to restrict the size of the inner bore of the system, there were physical constraints of which to take note. These constraints are discussed in the following subsections.

Subject Size

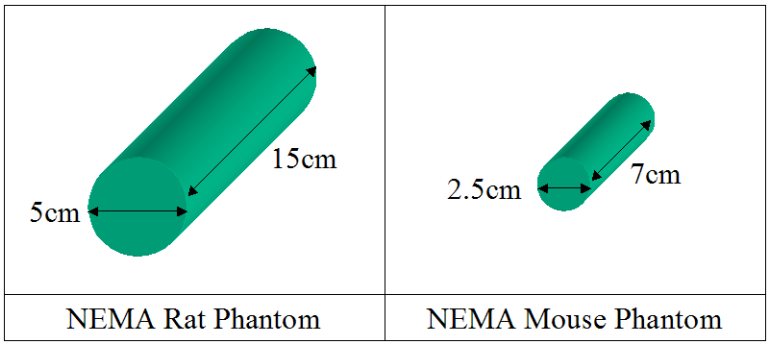

Figure 6.2: An illustration of rat and mouse sized phantoms as defined by NEMA.

The tomographic imaging system designed in this study surrounds the object being imaged, therefore the size of the object must be taken into account when designing the inner bore dimension. Mouse and rat subjects are the primary in-vivo test environment for drug discovery and studies of disease mechanisms. The National Electrical Manufacturers Association (NEMA) introduces standards for the Positron Emission Tomography imaging field and have determined standard mouse and rat dimensions. The simplified geometry of the mouse and rat consist of a cylinder with radius 2.5 cm and 5 cm, and height 7 cm and 15 cm, respectively. Figure 6.2 shows an illustration of the two simulated animal geometries, which are called phantoms.

Anesthesia and Test Bed

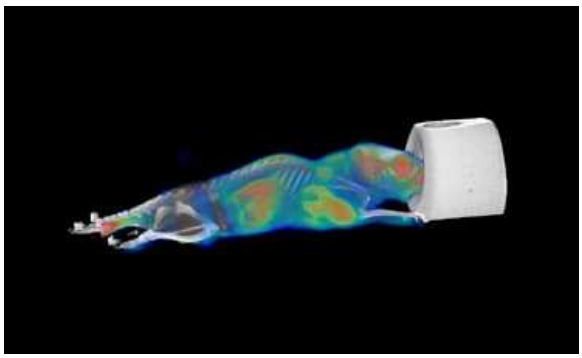

Figure 6.3: A CT image of a mouse with anesthesia nose cone. Courtesy of the Brenda Ogle lab in the BioMedical Engineering Department at Univ. Wisconsin, Madison.

A test bed is used to administer anesthesia, warm the unconscious animal, and position the animal in the center of the system [56]. Figure 6.3 shows the nose cone used for anesthesia delivery to the subject and its relative size to a mouse. Figure

Figure 6.4: A picture of a small animal imaging system with a grey and white phantom resting on a clear test bed.

6.4 shows a microPET small animal system with a cylindrical phantom inside the inner bore of the system, resting on a clear test bed. In order to account for the subject being imaged, test bed and associated equipment, as well as providing some extra room for the end user to manipulate objects within the system, an inner bore diameter of 8 cm was chosen.

6.2.2 Dual-chip PSAPD Module

A novel detection geometry is utilized in this work employing the concept that the light output from a scintillation crystal is optimal when orienting crystal in a large aspect ratio configuration (see Section 4.2.2). This detection geometry was made possible by the compact size of the photodetector.

Figure 6.5 shows the relative size of the position sensitive avalanche photodiode

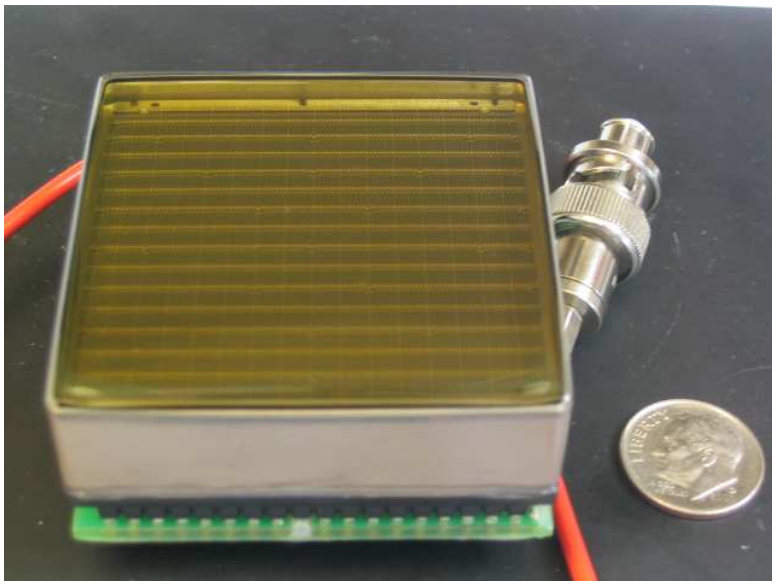

(a)

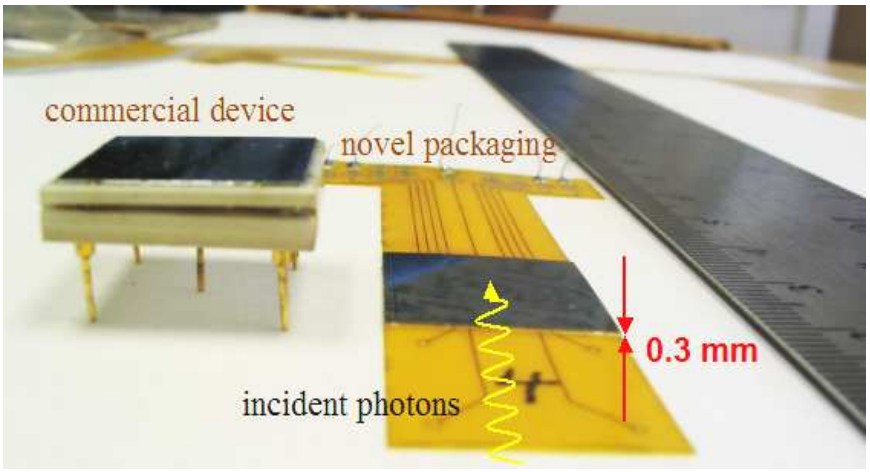

(b)

Figure 6.5: Pictures of photodetection devices. a) Position sensitive photomultiplier tube, and b) two position sensitive avalanche photodiodes.

(PSAPD) used in this work compared to that of a compact position sensitive photomultiplier tube (PSPMT). The PSPMT device and associated electronics (Figure

6.5a) had dimensions 52 x 52 x 30 mm^3. The PSAPD device (the black square chip in Figure 6.5b) had dimensions 11 x 11 mm^2 and a thickness of 300 μm.

The detection module consisted of segmented crystals that were laid down so that their long dimension was in contact with the face of the PSAPD. Because the thickness of the photodetector is negligible, detection modules were oriented so that incident annihilation photons travelled through the crystal along the face of the PSAPD photodetector (as shown in Figure 6.5b). This orientation is called "edge-on" as the detector face is pointing in a direction that was rotated 90^o with respect to the incoming photons. As will be discussed in the next subsection, two LSO-PSAPD detectors could be placed adjacent to one another in the depth of interaction direction, forming modules with a crystal depth of 18 mm, as seen by incoming photons.

Using 1 x 1 x 3 mm^3 crystals forming an 8 x 3 array, the edge-on orientation provided the following advantages: (1) light collection from the scintillation crystals was near 99% efficiency, (2) position resolution in the axial and transaxial directions were $\sim$1 mm, (3) direct depth of interaction position measurement was acquired with $\sim$3 mm resolution, and (4) detection efficiency was still high (18 mm depth of crystal) due to the adjacent detectors within one module. Figure 6.5b shows one such module with only one PSAPD and 8 x 3 LSO crystal array coupled to the read-out circuit. This read-out circuit will be discussed in the next subsection.

6.2.3 Read-out Electronics

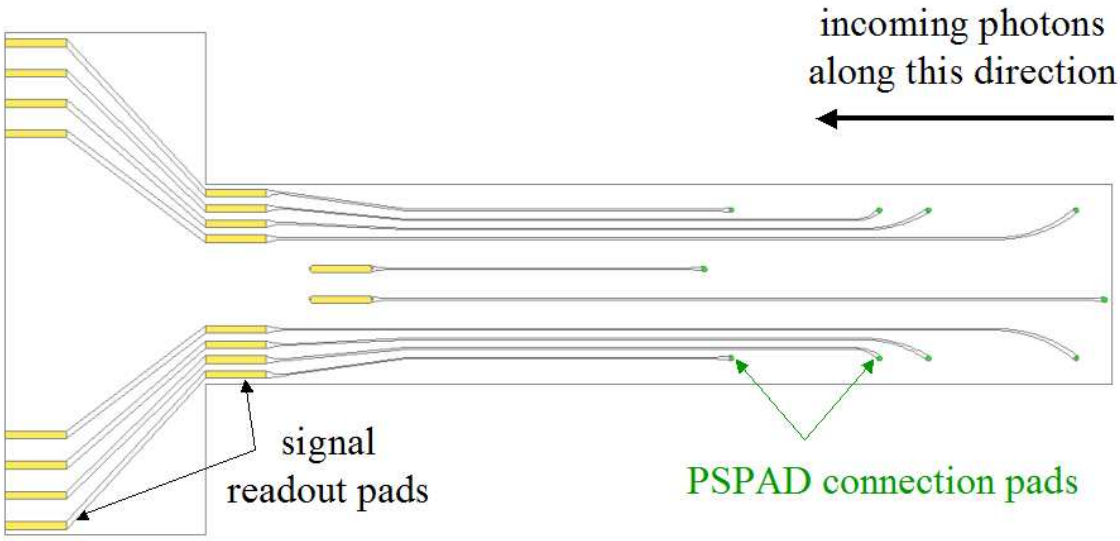

Figure 6.6: A CAD drawing of the flex circuit for the dual-PSAPD module.

A Kapton flex circuit was used to compactly read signals from the PSAPD. Figure 6.6 shows a CAD drawing of the flex circuit. In the figure, the green circular contact pads on the right of the circuit directly connect to the two PSAPDs, and the orange pads on the left of the circuit couple to the read-out electronics. With the orientation of the flex as it is in the figure, the annihilation photons would be moving from outside the figure from the right to the region of the green circular contact pads, where the LSO is coupled to the PSAPDs. The signal traces in the circuit have both low (∼1 Volt) and high (∼1800 Volt) voltage signals transported through the flex circuit. Although Kapton is a high dielectric material, the voltage differences along the signal

paths require spacing between signal traces which limit the number of PSAPDs that can be incorporated into a single flex circuit module. Two PSAPD per flex circuit provide space for contact pads that are 0.36 mm in size and provide photodetectors for enough coupled LSO scintillation crystal to stop ∼80% of annihilation photons (see Section 4.2.1 for a discussion on LSO).

6.3 Methods

6.3.1 Monte Carlo Simulation

A high energy physics Monte Carlo simulation tool, GATE, was utilized to acquire data to evaluate each of the proposed systems. The GEANT4 Application for Tomographic Emission (GATE) environment is an add-on software package to the GEANT family of validated high energy physics simulation software. All high energy transport modeling and other annihilation photon studies in this work used GATE. GATE, as a subset of the entire GEANT modeling environment, has been validated for various Positron Emission Tomography (PET) and Single Photon Emission Computed Tomography (SPECT) systems built and used in both clinical and pre-clinical studies [72].

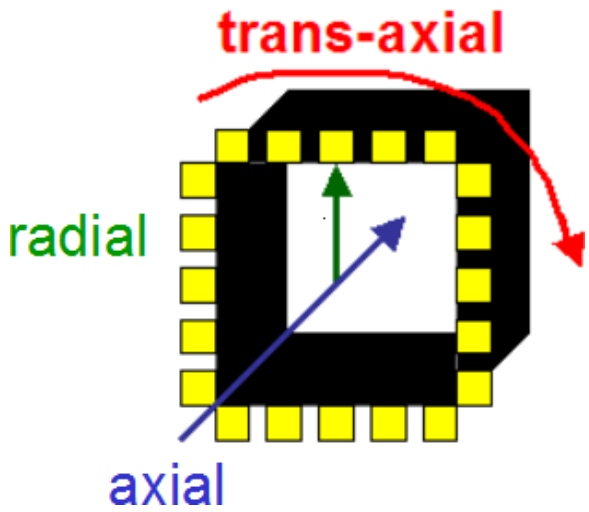

Figure 6.7: An illustration of the directions involved in discussing system space locations. The blue arrow shows the axial direction, the green arrow the radial direction, and the red arrow the trans-axial direction.

6.3.2 Detector System Space Nomenclature

Figure 6.7 shows the nomenclature used when defining locations and directions in detector system space. The trans-axial, axial and radial directions are shown in the figure. The axial direction points along the "barrel" of the detection system, moving along the inner bore from one of the open ends to the other. The trans-axial direction moves along the length of one of the heads of the detector system, and the radial direction points in the depth of interaction (see Section 6.2.1) direction.

6.3.3 Module Construction

The simulated position sensitive avalanche photodiodes (PSAPDs) were modeled based on 11 mm x 11 mm x 190 μm prototypes that were mounted on a thin (50

μm) flex cable for signal acquisition and high voltage. LSO (1 mm x 1 mm x 3 mm) scintillation crystals in an 8 x 3 array were sandwiched between a reflector on one side and optically coupled to the PSAPDs on the sensitive 8 mm x 8 mm area on the other. The total thickness of the flex cable, crystals and reflective film was 1.3 mm. The crystal array-PSAPD structures were configured edge-on with respect to incoming 511 keV photons and were repeated transaxially to form the number of heads in each investigated geometry. These compact scintillation detector modules facilitate the consideration of numerous designs.

6.3.4 Event Processing

From previously reported prototype measurements with the LSO-PSAPD detectors, excellent spatial ($\sim$1 mm FWHM), energy ($\sim$12% FWHM at 511 keV) and coincidence time ($\sim$2 ns FHWM) resolutions were achieved. The software package GATE was used to model the physics of the processes involved in PET detection and incorporated the experimentally determined device resolutions into the detection model. In all simulations, a dead time of 5 μs was used to simulate recovery time between detected events. This dead time was a conservative estimate based on studies performed on similarly sized avalanche photodiodes [61], where dead times were measured to be on the order of 2.5 μs for a 7 x 7 mm^2 active area device. Events were written out in a list mode format and post-processed using analysis code written in

MATLAB.

6.4 Sensitivity

Coincidence detection sensitivity, being a measure of the capability of the system to register events, was utilized as a primary measure for choosing between system configurations. Positron emission tomography is an imaging modality that rarely has the ability to scan long enough, with enough source activity in the field of view, to gather sufficient counts to overcome statistical noise in the reconstructed pixelated image. Image contrast, resolution, quantitation and ultimately feature detectibility are all affected by counting statistics. A detector system with high coincidence detection sensitivity gathers more counts during an experiment, when source activity and scan time are equal.

System configuration, energy spectra, and photon scattering were considered for all designs. Module design and module orientation were studied for specific system designs.

6.4.1 Methods

Theory

The coincidence detection sensitivity for each of the whole systems was evaluated. Sensitivity was defined as the percentage of annihilation events detected:

$$S = 100\% \cdot \frac{N_{\text{filter}}}{N_{\text{ann}}} \tag{6.1}$$

where N_{filter} is the number of filtered detected events and N_{ann} is the number of annihilation events. The number of annihilation events depended on the activity of the source within the detector and the decay rate of the isotope in the detector system. For simplicity, the source of activity used in the experiments isotropically generated back to back (collinear, with opposite momentum) 511 keV photons, with no rate of decay. Therefore the number of annihilation events can be calculated knowing the source activity and the time elapsed during the experiment.

Detected annihilation photons were deemed coincident if their time separation was within the defined time window (4 ns), each of their energies was within the defined energy window (24% of 511 keV, centered at 511 keV), and both detected annihilation photons did not occur in the same detection head (which will be defined in the next subsection).

System Configuration

Because of the compact size of the PSAPD-LSO module (11 mm x 22 mm x 1.3 mm), there was a large amount of flexibility in the construction of the components in the detector system. Ten system configurations were explored in the small animal (SA) imaging system size. The main difference between each of the systems is their number of contiguous blocks of modules, or heads.

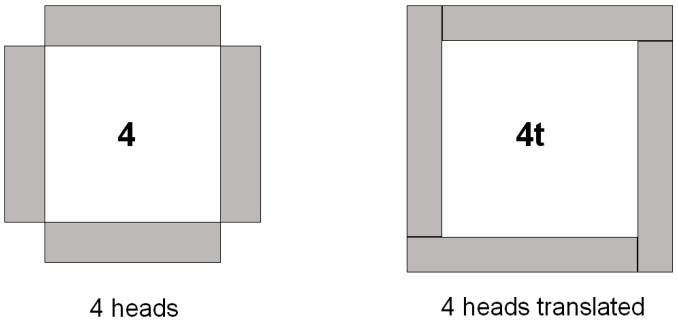

(a) An illustration of the "head" and "translated head" configurations.

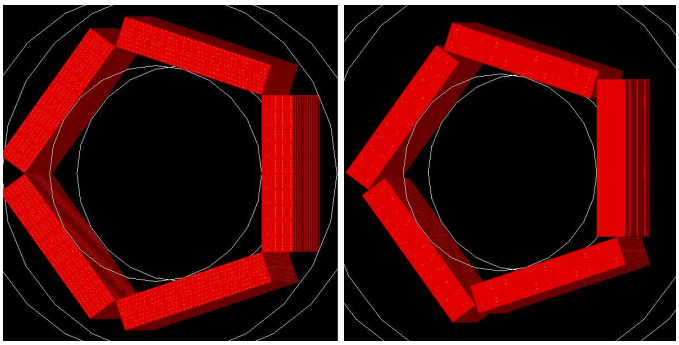

(b) OpenGL image capture of 5-headed and translated-5-headed system configurations.

Figure 6.8: Examples of detector configurations studied.

Most of the systems were studied in two configurations: (1) each head was symmetrically repeated around the field of view to construct the whole system (see left illustrations of Figures 6.8a and 6.8b), or (2) each head was widened and repeated around the field of view with a translation so that all photons within the solid angle of the detectors were directed towards a similar depth of detection crystal (see right illustrations of Figures 6.8a and 6.8b).

The simulated systems are referred to by their number of heads, except in the case of "oring" and "rot" which were cylindrical systems and had 350 and 46 heads in their systems respectively. Systems with a "t" in their name meant the detector heads were larger and translated to provide over-lap where the heads met in an effort to reduce gaps between heads. The "t" systems had the same inner diameter or field of view as those without translation, i.e. the 8 cm specified in Section 6.2.1. A box-shaped system called "4tsm" was also investigated which had a inner bore diameter of only 6 cm at its smallest inter-head distance. Although not 8 cm at its smallest diameter, this system was a design possibility due to the large diameter of the system from corner to corner. The system could be oriented in a diamond position in order to facilitate the animal test bed and associated equipment.

Each configuration was run for 2 minutes with 10 μCi of activity in the form of a point source at the center of the field of view. Using a point source at the center of the system gave an upper limit to the sensitivity of each system. Three energy and time window cases were used. The windows were chosen using traditional and LSO-PSAPD experimental result considerations. The 350-650 keV energy and 20 ns time window case was selected because it is a common energy and time window for traditional systems. It is usually preferred to choose the window that achieves high sensitivity without retaining a significant portion of random events and scatter events (see Section 1.3.4 for a discussion on event types).

The second and third energy and time window study cases investigated were cho-

sen due to the results of detection experiments on the LSO array and PSAPD configuration used in these simulations. A 12% energy resolution and 2 ns coincidence time resolution was measured for this detection module. In order to retain as many true coincidence events, a 25% energy window was used and the time window was chosen to be one or two $\delta\tau$ for cases one and two respectively, where $\delta\tau$ is the coincidence time resolution.

Energy Spectra and Scatter

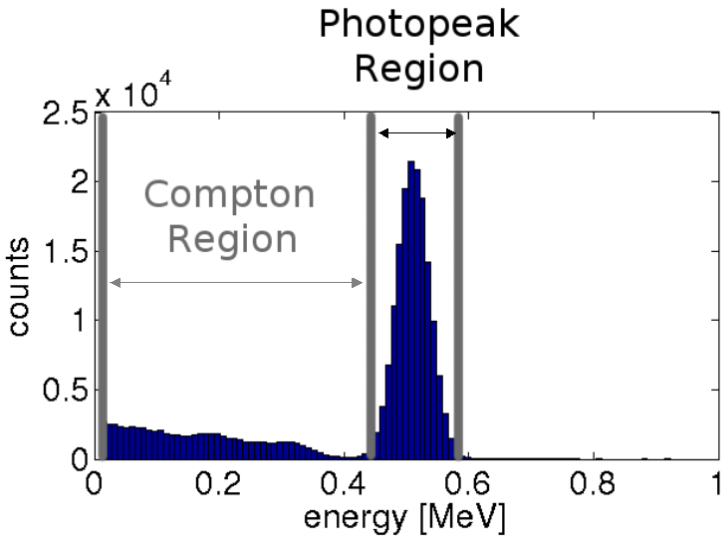

Figure 6.9: A plot showing the two energy regions evaluated for scattering measurements.

Energy spectra of detected events for each system configuration were plotted and evaluated. The energy spectra were binned in a histogram of all collected events where both detected singles were from a time-windowed coincident pair. The resultant

energy spectra were divided into two regions: (1) the photopeak region, 450-572 keV, which was the energy range of singles retained after filtering for sensitivity measurements, and (2) a Compton scattering region, 10 keV - 450keV. Both regions can be seen in Figure 6.9.

Studying the fraction of events that were found in these two regions gives an indication of the fraction of events that interacted by Compton scattering, but left the system before depositing the entirety of their energy. This fraction of events that scattered out of the system can give insight into the relative sensitivity of the systems, as well as the type of head and inter-head gap configuration which would constitute a good detector system design.

Module Design

Two systems were chosen for further study: the system that had the best compromise between ease of construction and highest sensitivity, and one that was the most similar to systems with traditional construction. To understand the effect on sensitivity due to the construction of the constituent modules that made up the system heads, three module parameters were varied and coincidence detection sensitivity was measured at four locations within the field of view. The three parameters investigated were:

- **System radial depth**, or depth of crystal in the depth of interaction direction. The number of LSO-PSAPD detectors was varied from one to three in the depth

of interaction direction, and the amount of crystal for each PSAPD used in the DOI direction was fixed at 9 mm or 11 mm. This produced 6 possible depth of crystal cases: 9 mm, 11 mm, 18 mm, 22 mm, 27 mm and 33 mm.

- **Trans-axial gap size**, or width of crystal in the trans-axial direction coupled to the PSAPD. Array widths of 8 mm, 9.5 mm and 11 mm were simulated, producing an inter-detector gap size of 3 mm, 1.5 mm and 0 mm.

- **System diameter**, or smallest diameter of the inner bore of the system. Three inner bore diameters were investigated: 6 cm, 8 cm and 10 cm.

Module Orientation

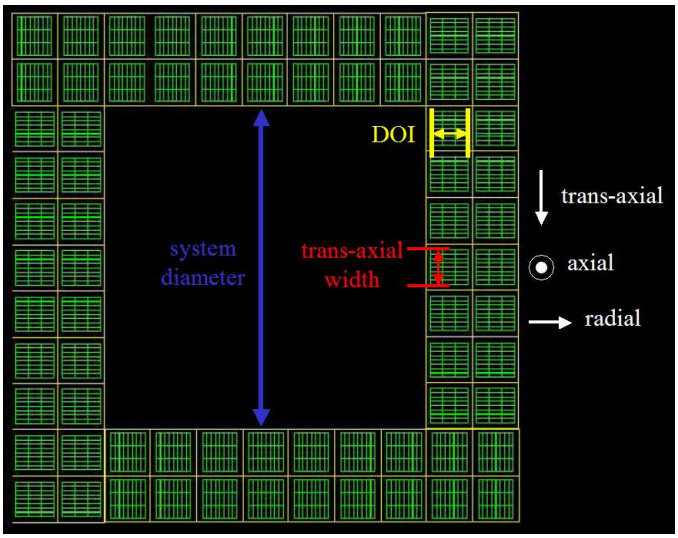

Figure 6.10: An OpenGL image capture of the box-shaped system, illustrating module (white) and crystal (green) placement within the detector system. The transaxial and axial directions with respect to the system are also denoted.

When constructing heads of a system, the compact nature of the detector modules

lend themselves to being oriented in one of two ways. The module can either be oriented so that the normal vector to the face of the photodetector can point axially (as shown in Figure 6.10, where the green lines outline the individual LSO crystals and the white lines outline the PSAPD photodetectors), or point towards the interior of the system. In other words, thinking about the system as a parallelpiped, there are two orientations where the signal pads of the modules exit the system from its outer surface. The two orientations sandwich the modules with their detection surfaces pointing axially or trans-axially.

Since the LSO array area (8 mm x 9 mm) does not fully cover the area of the PSAPD (11 mm x 11 mm), an inter-module gap is formed (again, see Figure 6.10). The orientation of this gap may influence system sensitivity. The system design with the highest sensitivity was simulated to investigate the module orientation dependence.

6.4.2 Results

System Configuration

The data presented in this section was presented at an IEEE workshop (see Reference [51]). Figure 6.11 shows a plot of the coincidence detection sensitivity for each system for the three energy and time window cases investigated versus the amount of crystal used to construct the system. As the number of heads increased, the more

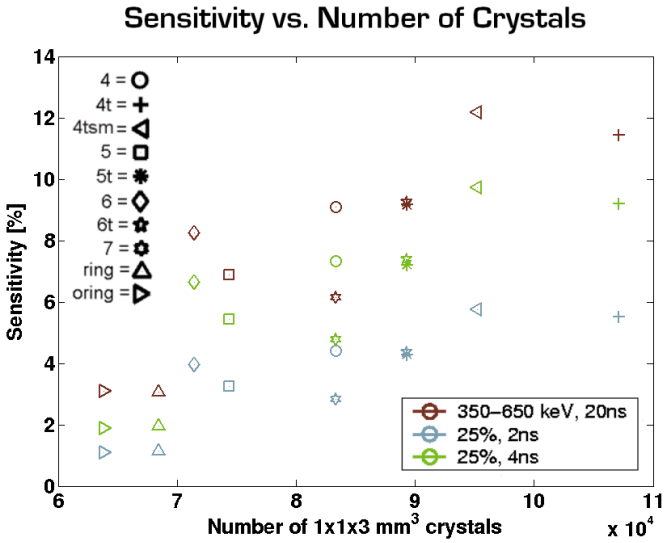

Figure 6.11: Coincidence detection sensitivity versus number of crystals comprising the system for all small animal configurations studied (see Section 6.4.1 for the system naming scheme).

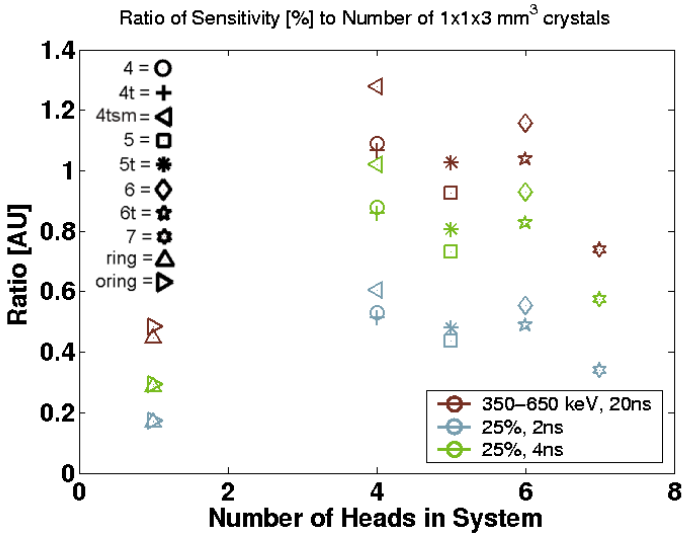

Figure 6.12: Ratio of coincidence detection sensitivity to number of crystals comprising the system versus number of heads used to produce the system for all small animal configurations studied (see Section 6.4.1 for the system naming scheme).

cylindrical the system became, producing a system more efficient at covering solid-angle with the crystal, i.e. the system needed less crystal to construct. However, the more cylindrical the system, the lower in sensitivity, on average, the system was. In particular, when nearly the same amount of crystal was used as in the ring systems, placing the crystals closer together into a smaller number of larger-sized heads as in the 6 headed system, sensitivity increased greatly (from 1% for the ring systems to 4% for the 6 headed system using a 25% energy window, 4ns time window).

The other trend observed was that systems with a "t" configuration, which required more crystal, had higher sensitivity. In order to see if the increase in sensitivity by using a "t" configuration was an efficient use of crystal, the ratio of coincidence detection sensitivity to the number of crystals utilized was plotted versus the number of heads used to construct the system. The cylindrical systems were given a head number of one to compact the plot. The results show that, other than for 6 heads, the "t" configuration at least does as well, if not better in some cases, of linearly increasing sensitivity by increasing crystal used. The general trend of a decrease in sensitivity with the increase in number of heads used can also be seen in this representation of the data. This second trend will be investigated in the next two subsections.

Although the "4tsm" system had the highest overall sensitivity, the ability to construct and utilize such a system would be rather difficult. The "4t" system was chosen as the system to investigate further due to its second highest sensitivity value and simple construction. Although the cost per % sensitivity increase was higher in

the 6 headed system, total coincidence detection sensitivity, or the system's ability to gather counts, affects nearly all aspects of the imaging capability of the system (see section 1.4.1 for a discussion on how acquired counts affects system imaging performance).

Energy Spectra and Scatter

In the previous section, sensitivity versus number of detector heads showed a trend where increasing detectors heads decreased sensitivity. As the number of heads increased so did the spatial frequency of inter-head gaps. In other words, as the number of heads increased, the average distance from a crystal to a gap decreased. Because annihilation photons entering into the detector have a non-negligible path length (~2 cm), annihilation photons that come across a gap have a possibility of leaving a detector before their full energy is deposited. Scattering out of the detector would result in a higher number of counts in the Compton region of the energy spectrum of the detected events, and hence a loss in sensitivity.

Shown in Figure 6.13 are the detected energy spectra for the system configurations investigated. Qualitatively, the fraction of counts in the Compton region of the energy spectra increases with the number of heads in the system.

To quantify the results shown in Figure 6.13, the fraction of detected events in the Compton region of the spectra were plotted for each configuration in Figure 6.14. These results were similar to sensitivity trends, indicating scattering out of the

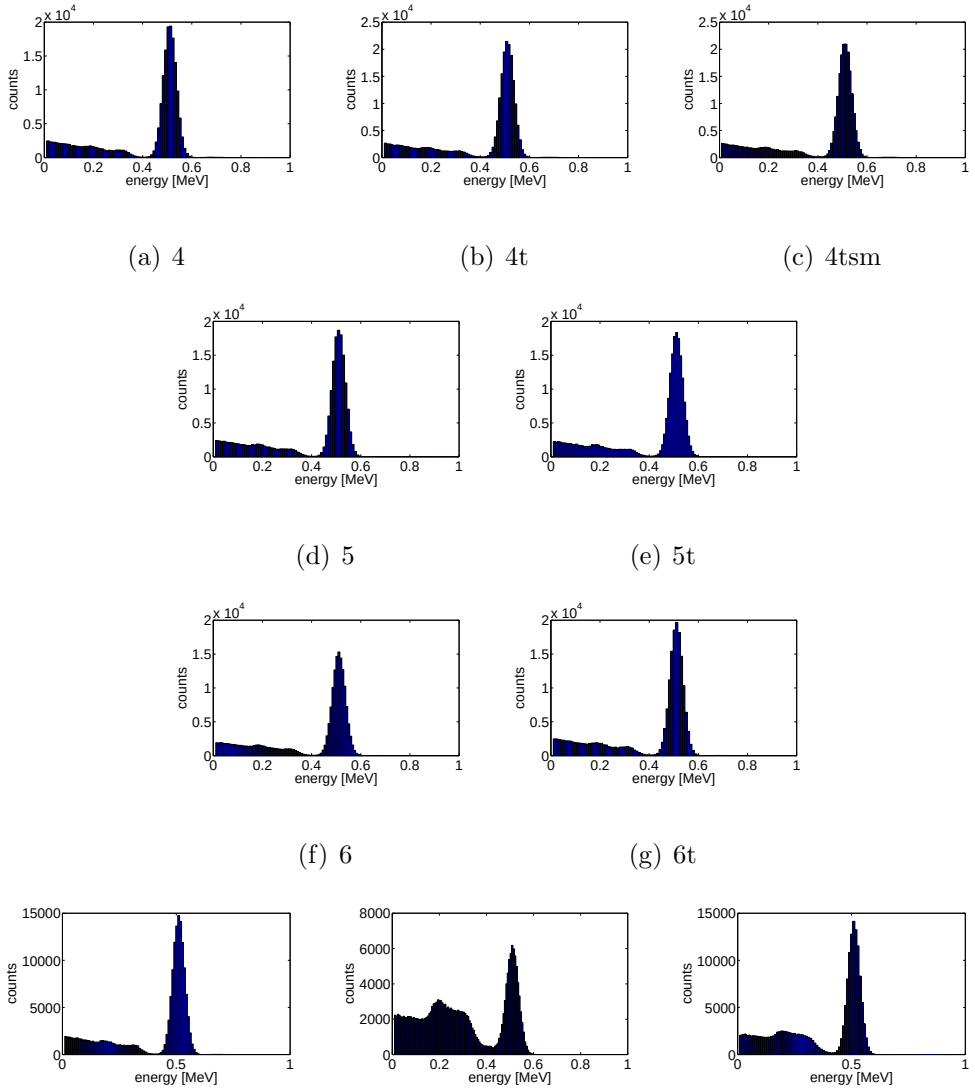

(a) 4 (b) 4t (c) 4tsm

(d) 5 (e) 5t

(f) 6 (g) 6t

(h) 7 (i) oring (j) rot

Figure 6.13: System energy spectra for all small animal system configurations studied.

detector had a large influence on system sensitivity. Further, the systems in the "t" configuration, which had significantly decreased gaps, all had lower scattering fraction than systems with the same number of heads which were not in the "t" configuration. These results provide evidence that the assertion that Compton region event fraction

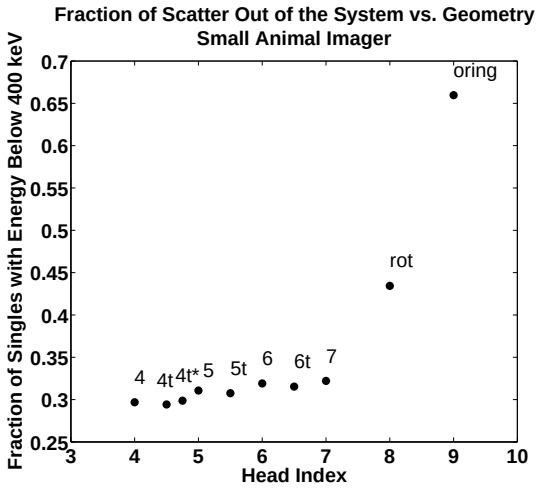

Figure 6.14: Fraction of detected incident 511 keV photons scattering out of the various geometries.

is a good indicator of the amount of scattering out of a system.

Being that the "4t" system had the lowest Compton scattering region event fraction, it was the system that most efficiently stopped annihilation photons that interacted with the system. This result is further evidence that the "4t" or box-like system was a good choice for detector design.

Module Design

The box-shaped system was compared to the cylindrical system with higher sensitivity (previously called "rot", but called "ring" in this section) for the various module designs described in the methods section (Section 6.4.1). The cylindrical system was chosen for comparison because it most approximates a traditional design.

Figure 6.15 shows the results of the coincidence detection sensitivity measurements

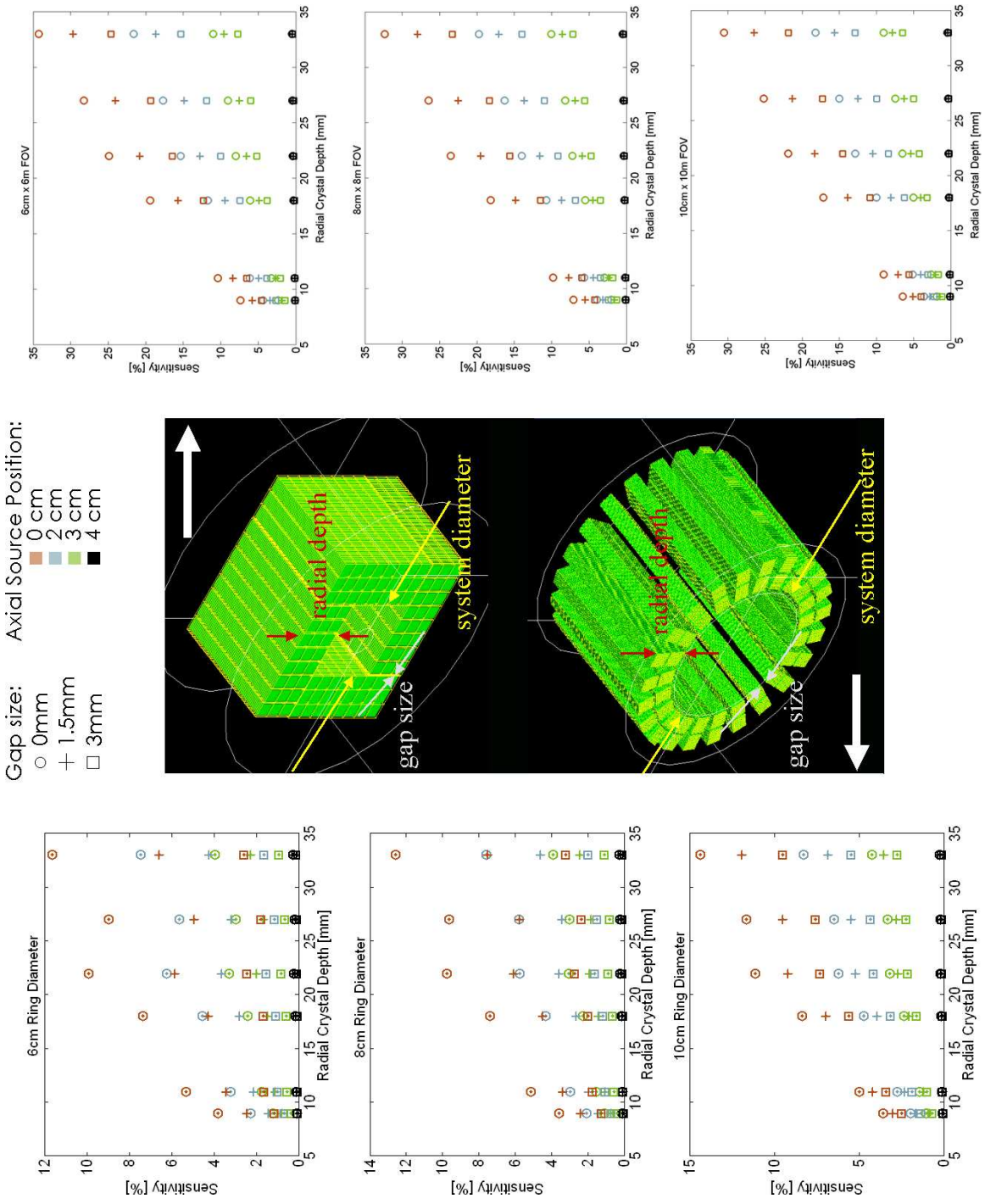

Figure 6.15: Sensitivity for various system configurations.

for all module designs. The general trend was expected: as more crystal was used (going from left to right on the x-coordinate or from bottom to top in markers), sensitivity increased. An interesting result from the box-shaped system is that the sensitivity of a system built of modules consisting of two PSAPDs covered entirely in crystal (11 mm x 1 mm of crystal, signified by the circles at 22 mm of crystal depth) had nearly the same sensitivity as that of a system built of modules consisting of three PSAPDS covered in an 8 mm x 11 mm array (shown by the squares at 33 mm of crystal depth). The results also show that on average, if sheet crystals covering the full area of the PSAPD could be read out as efficiently as the segmented 8 mm x 9 mm array, the coincidence detection sensitivity of the system would increase $\sim$50%.

The results in the cylindrical data showed some evidence of the conclusion previously reached concerning inter-head gaps' influence on detection efficiency. Looking at the 6 cm diameter set of simulations, the cylindrical system showed a *decrease* in sensitivity when replacing a two PSAPD module consisting of 11 mm x 11 mm crystal arrays (242 mm^2 total crystal area, circles at 22 mm crystal depth) with a three PSAPD module consisting of 9 mm x 11 mm arrays (243 mm^2 total crystal area, circles at 27 mm crystal depth). Effectively, the difference in these two systems is the placement and size of each system's gaps. Using the same amount of crystal, packed more loosely with respect to one another, created gaps in which annihilation photons could escape without depositing any or all of their energy.

Module Orientation

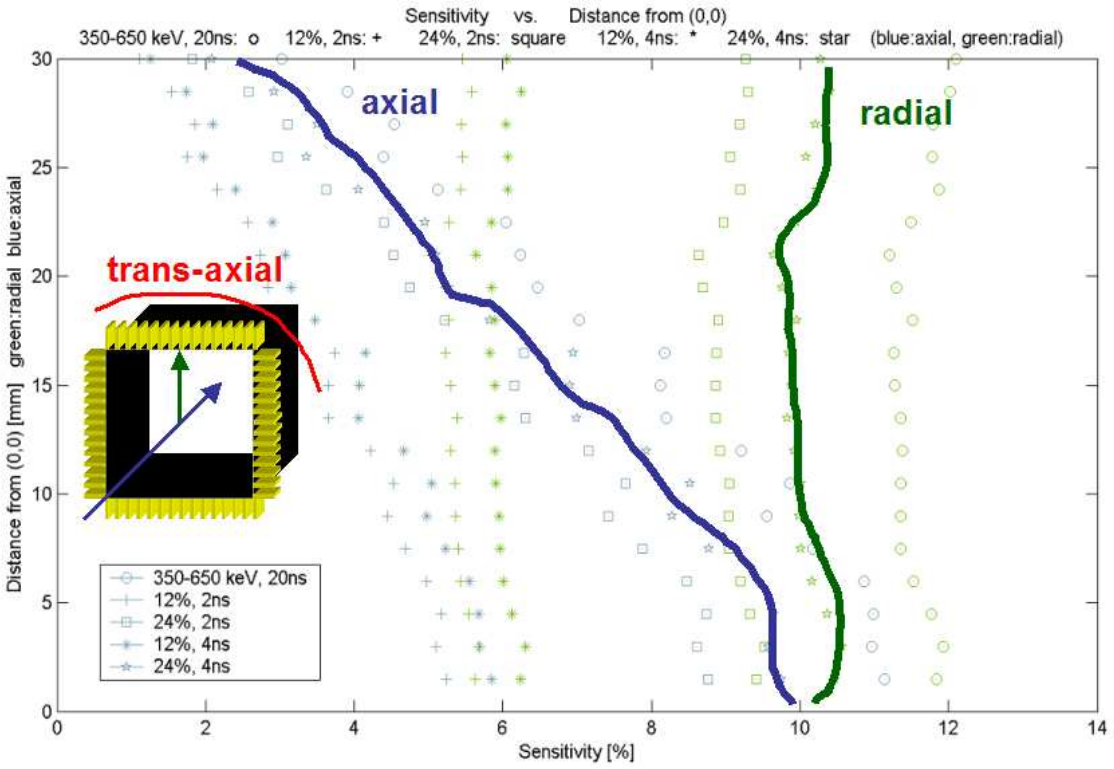

Figure 6.16: Sensitivity measured for axial gap configuration at various source locations throughout the field of view.

Both module orientations were investigated for the box system at various activity source locations throughout the field of view, and for various energy and time window cases. The results for the axial gap orientation are shown in Figure 6.16. An illustration of the crystal array orientation can be seen in the inset. Blue markers indicate locations in the system in an axial direction, and green markers locations in a radial direction (towards the detection heads from the center of the system). Solid lines were drawn through the 24% energy window and 4ns coincidence time window study

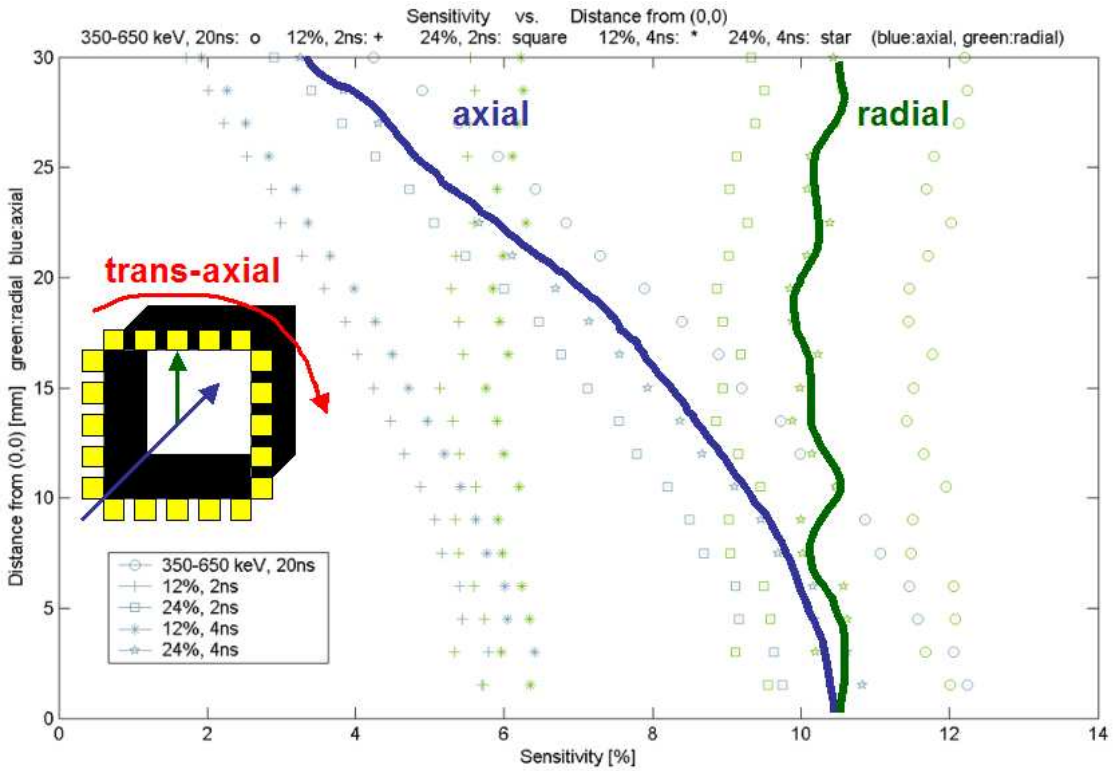

Figure 6.17: Sensitivity measured for trans-axial gap configuration at various source locations throughout the field of view.

for both the axial and radial locations. Radial position did not affect the sensitivity greatly, as it remained near 11% for all positions investigated. As the source moved axially through the system, the sensitivity dropped as expected (from 10% to 2.5%) due to shrinking solid angle coverage of the system.

The results for the module orientation where the large gaps in crystal between arrays was placed along the trans-axial direction are shown in Figure 6.17. An illustration of the crystal array orientation can be seen in the inset. Blue markers again indicate locations in the system in an axial direction, and green markers locations in

a radial direction. Solid lines were also drawn in these data through the 24% energy window and 4ns coincidence time window study for both the axial and radial locations. Radial position did not affect sensitivity greatly, as it remained near 11% for all positions investigated. As the source moved axially through the system, the sensitivity dropped as expected (from 11% to 3.5%) due to shrinking solid angle coverage by the system.

Although both systems performed similarly, the trans-axial gap orientation provided a superior coincidence detection sensitivity throughout the field of view of the system. This is the design of the detector system selected and the one discussed throughout the rest of this and subsequent chapters of this work.

6.5 Noise Equivalent Counts

The data presented in this section was presented at an IEEE workshop (see Reference [51]). Noise equivalent counts (NEC), or a measure of signal to noise, was calculated for the worst-case scenario of a uniformly filled cylindrical phantom that nearly completely filled the detector inner volume (diameter 8 cm, length 8 cm). The following conventional formula was used to calculate NEC [191]:

$$NEC = \frac{T^2}{T + S + 2R} \tag{6.2}$$

where T, S and R are true, scatter and random events respectively, calculated

directly knowing the rates from Monte Carlo generated data. A time resolution of 2 ns and energy resolution of 12% of 511 keV were included in the model. Increasing the coincidence time window (CTW) beyond 4 ns, as expected, further reduced the true (black) to total counts (red) ratio, and thus NEC (magenta). Because of the excellent energy and time resolution of the proposed system, the energy windows (EWs) and CTWs could be narrowed while still maintaining a high true event rate. The use of such a large phantom was to simulate a worst-case, yet possible, scenario for the performance of the detection system.

6.5.1 Operational Parameters

Energy and coincidence time windows were varied to investigate their dependence on NEC, scatter, random and true rate. The left hand side of Figure 6.18 shows each of these rates in a three dimensional plot, varying both energy and coincidence time window in the same plot. The two dimensional plots on the right hand side of the figure show each event type and NEC rate for particular CTWs (markers connected by solid lines) at all EWs tested, and the same data for particular EWs at all CTWs tested in the right 2D plot.

The peak in NEC occured at a 24% energy window and a 3-4 ns CTW. Therefore, a 24% EW and a 4 ns CTW was used for all further simulation experiments to keep sensitivity high while still maintaining the peak NEC rate.

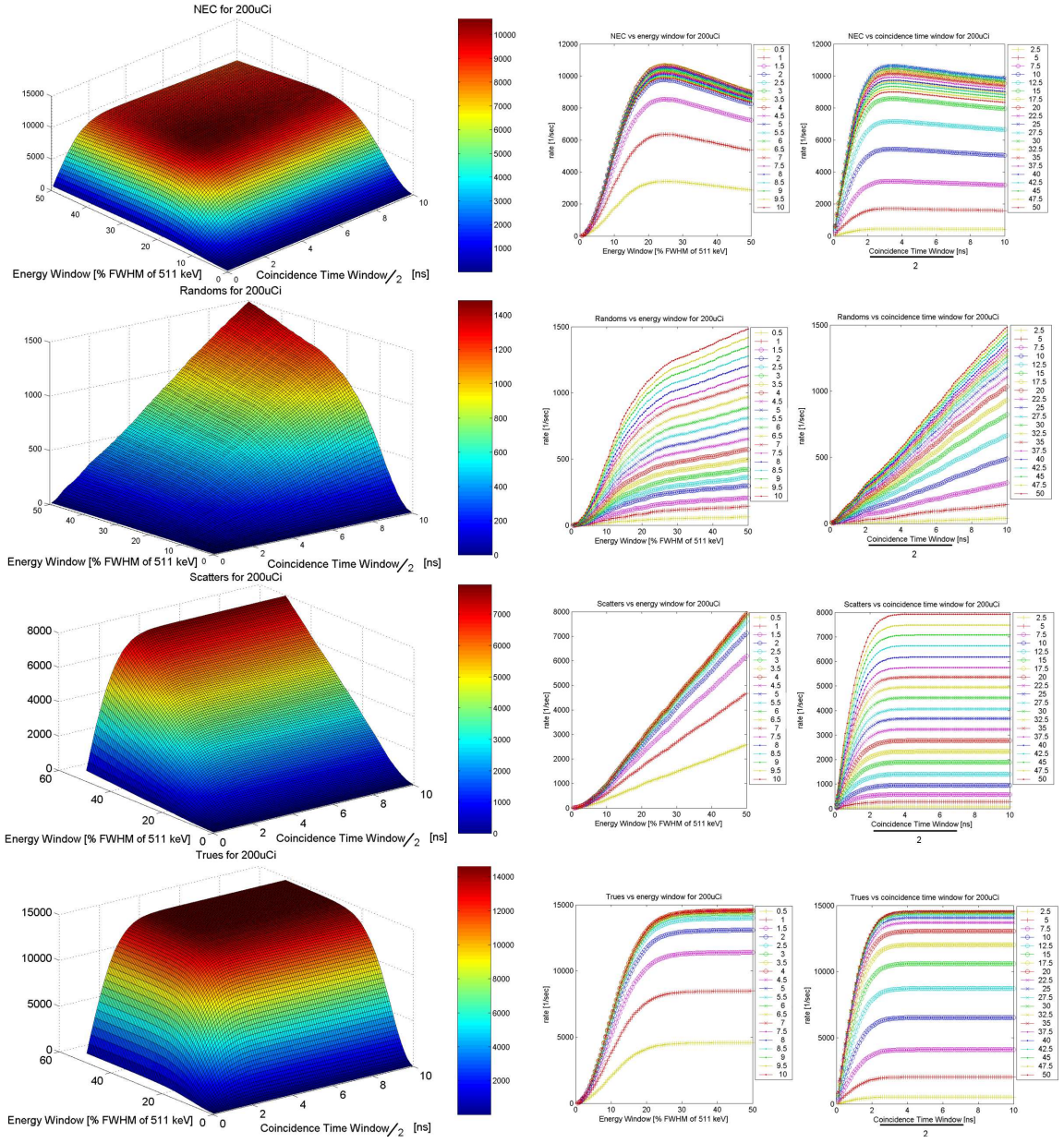

Figure 6.18: NEC, randoms rate, scatter rate, and true rate for various coincidence time and energy windows.

6.5.2 Source Activity

Plotted in Figure 6.19 is the system's response from 10 μCi to 8 mCi of activity for three energy windows: 12%, 24%, an 36% of 511keV, each plot having a coincidence

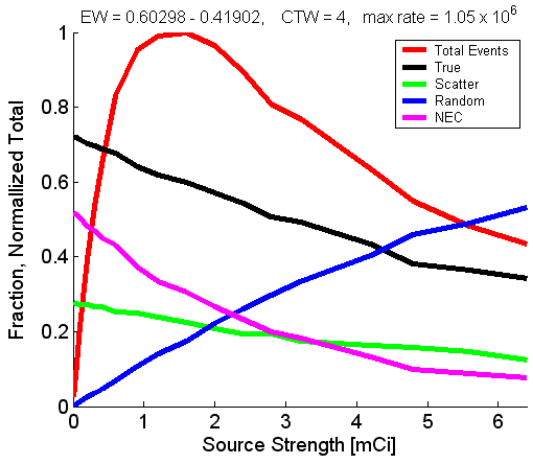

(a) EW: 12% CTW: 4 ns

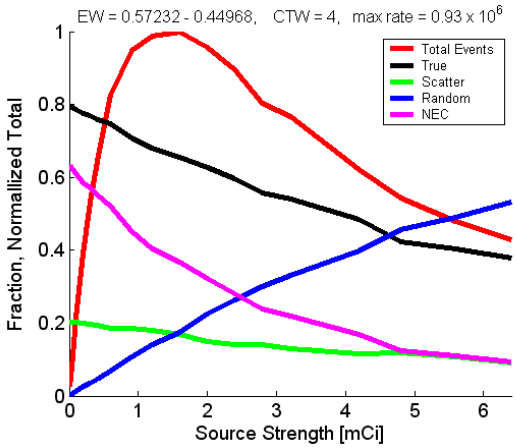

(b) EW: 24% CTW: 4 ns

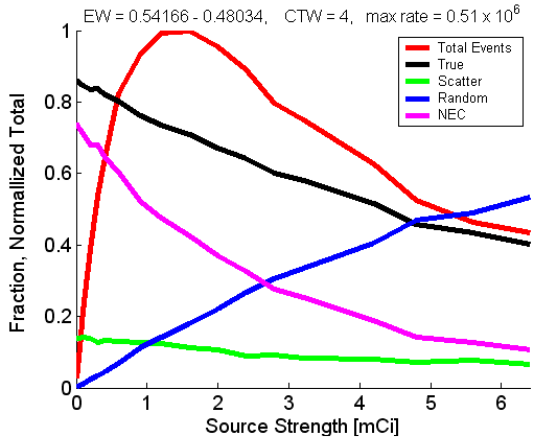

(c) EW: 36% CTW: 4 ns

Figure 6.19: Fraction of random, scatter and true of total, total and NEC rates for various activities and three energy windows.

time window of 4 ns. T, S, R, and NEC are shown for each activity as their fraction of total detected event rate, i.e., T+S+R = 1 for any activity. The total event rate was normalized to one to plot it using the same ordinate axis values. The peak total rate is given in the title of each graph.

These data represent clearly the dominance of each event type at experimentally significant activity ranges. The scatter rate remains nearly unchanged throughout the activity range, but decreases as a fraction of total due to an increase in random events with activity. An increase in randoms rate also reduces the fraction of true rates as activity increases. The total event rate rises in the low activity range of the graph, peaks near 1.7 mCi of activity, and drops off slowly at high source activities.

The peak in the total count rate occured at the point where multiple interactions began to dominate - i.e., the sensitivity of the system was high with more than two annihilation events happening within the time window. For reference, a 2mCi source produces annihilation events on average every 1.39 ns. Recall that the events were gathered using 4 ns time window in each case plotted. If events were acquired with very high activity (higher than investigated), eventually all time windows would have multiple events and the total count rate would reach zero.

6.6 New Complications: Designing the Next Generation PET System

The two fundamental novelties in the detector components developed in this work are: (1) the capability of 3 dimensional positioning of events in the detector and (2) using detector elements smaller than a scattered annihilation photon's path length (see Section 6.6.2).

These two features lead to two major advances in emission tomography detection: punching through previous limitations on how a system must be built (detector configuration versatility leading to higher sensitivity and sampling), and more information gained per detected annihilation photon (advances in event classification, see Reference [53]).

These advances break down the fundamental assumptions about how system quantitation is both measured and realized through detector resolution, sampling, normalization, and event type estimation. These issues will be discussed in Chapters 7 and 8. Chapter 7 discusses more thoroughly the physics and associated modeling necessary to utilize these data further. The following section focuses on a high level discussion on the types of information gathered for one detection event and using this information for positioning events.

6.6.1 Direct Depth of Interaction Measurement

Three dimensional positioning of events in the detector system garners many added advantages. Included in these advtanges are the ability to place detectors close to the object being imaged for high sensitivity, using the increased resolution for better sampling of the object being imaged, and using the small dimension of the detectors and the subsequent novel resultant acquired data to further classify or re-classify events for increased image quantitation.

An added dimension in signal processing and image reconstruction however, add dimensions to the event processing lookup tables, event data representation, and system models, which in turn increase the data storage and computational resources necessary to handle the acquired data. Techniques for dealing with these and other issues are discussed in the next chapters.

6.6.2 Multiple Interaction Detection for One Incident Photon

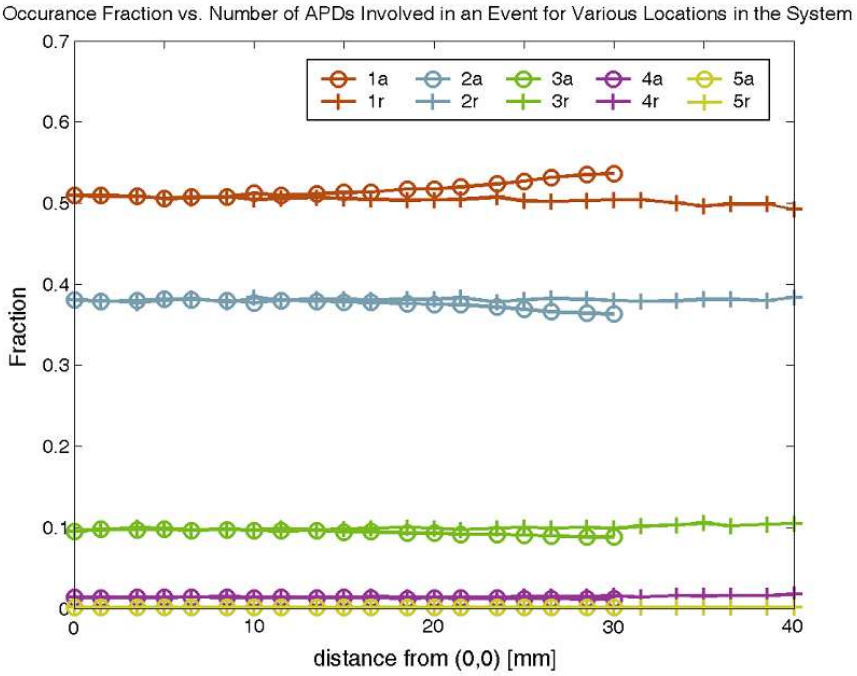

Figure 6.20: Number of PSAPDs involved in the interactions from a single annihilation photon for various locations in the system field of view.

Coincidence simulation experiments using a point source stepped at various radial (cross markers) and axial (circle markers) locations throughout the field of view revealed that nearly half of the annihilation photons that entered the detector system, and deposited their full energy, interacted in two or more PSAPDs. Figure 6.20 shows the fraction of all events that interacted in one (red), two (blue), three (green), four (purple), or five (yellow) PSAPDs before depositing all their initial energy. For clarity, the markers are shown connected by linearly interpolated solid lines.

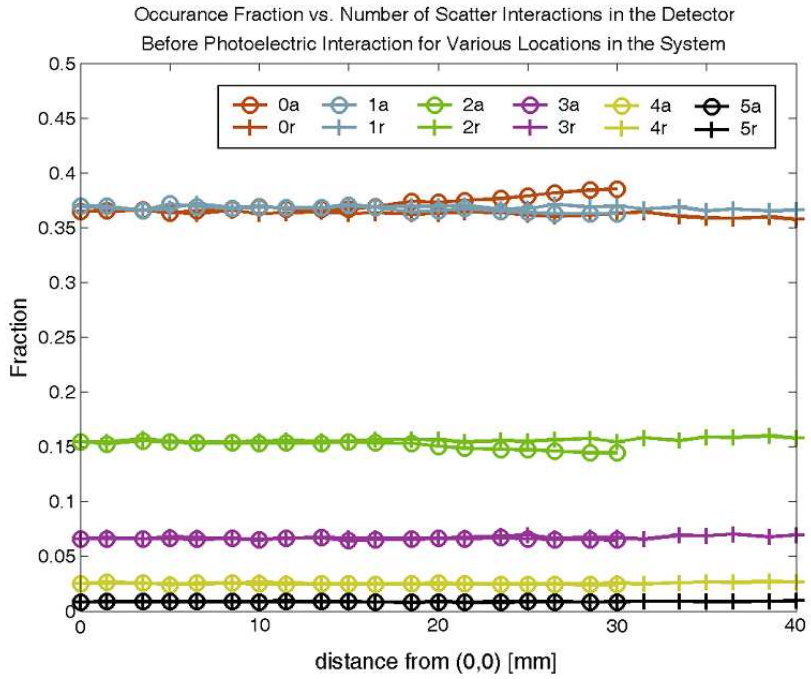

Figure 6.21: The fractional number of Compton interactions in an event (single annihilation photon interaction set) for various locations in the system field of view.

Over most of the field of view, the fractional number of PSAPDs did not vary

greatly (1-2% variation), but a small deviation occurred from the average value when the source was located axially near the end of the system (1-8% variation). The largest deviation was found at an axial location of 30 cm, where there was an increase in the fraction of events when only one PSAPD was involved. This increase was likely due to the direction of photons acquired as coincidence in the system. Annihilation photons were directed, on average, more radially at that location than other locations in the system. This radially preferred annihilation photon direction was due to the smaller coincidence angle range at axial locations far away from the center of the system. Annihilation photons with large radial direction components, in general, are directed at a smaller amount of crystal, increasing the possibility of a scattered photon escaping the system before interacting again and therefore raising the fraction of Photoelectric events. This effect can be seen in Figure 6.21.

Figure 6.21 shows, for the same locations in the field of view, the fractional number of Compton scattering interactions that occurred. These Compton interactions took place before the Photoelectric interaction that fully absorbed the remaining annihilation photon energy. At the 30 cm axial location, the fraction of Photoelectric-only interactions (0 Compton interactions) increased. This increase provides good evidence for the explaination of the divergence seen in Figure 6.20. Another result of note is the nearly identical fraction of events that had either no Compton scattering interactions or just one Compton scattering interaction. Because Photoelectric-only events happened 37% of the time, in the remaining 13+% of all events where only

one PSAPD was involved, one or more Compton interactions must have taken place. This means that there are a measurable number of 1, 2, 3 or 4 Compton scattering events that remain within one PSAPD. This result will be extensively dissected and accounted for in Chapter 7.

6.6.3 Evaluating Simple Positioning Techniques

Knowing that more than one PSAPD may be involved in a single annihilation photon's interactions during the full deposition of it energy, a fundamental question arises. What does detected position mean and how is it determined? Ideally, knowing the location of the very first interaction would give the most accurate representation of the direction the photon entered the detector system. However, since the PSAPDs do not have accurate enough time determination, all interactions from a single annihilation photon appear to have happened at the same time. Therefore, a simple decision rule must be created for positioning.

Using the Compton and Photoelectric interaction data from the simulation, different methods of determining event position pairs, or line of response (LOR), were investigated. The correct line of response should be placed between the first interaction of each of the annihilation photon pair. Three simple methods were investigated to estimate the first detector interaction position. The three algorithms located the event position at the a) minimum energy interaction location, b) maximum energy

interaction location and c) energy-weighted center of mass of the interactions. For all three methods, the distance between the first interaction and the algorithm's calculated position was calculated for each event. A histogram of these position differences can be seen in Figure 6.22.

To be included in position calculations, interactions had to deposit energy above a pre-defined threshold "noise floor" of 10keV. About 30,000 events from 300,000 interactions were included in this study. An EW of 10% (485 - 537 keV) was used. The standard deviation of the difference from the first interaction position for each case was: a) 3.92 mm, b) 5.11 mm and c) 4.25 mm and the mean deviation was: a) 1.12 mm, b) 1.96 mm, and c) 1.85 mm (see Figure 6.22). Of these three positioning algorithms, placing the first interaction where the minimum energy was deposited (above the noise floor) had the lowest standard deviation and mean in positioning error.

However, the more significant measure of positioning accuracy is the algorithm's ability to calculate event positions forming a line of respons closest to the ideal line of response.

The line of response (LOR) was calculated from the detected pair of coincident photons using same three positioning algorithms: each photon's position was calculated from the 1) minimum energy, 2) maximum energy or 3) center of mass (COM) interaction positions. The ideal LOR positions were determined from the first interaction in the crystal - the true position of the event before scattering. To find

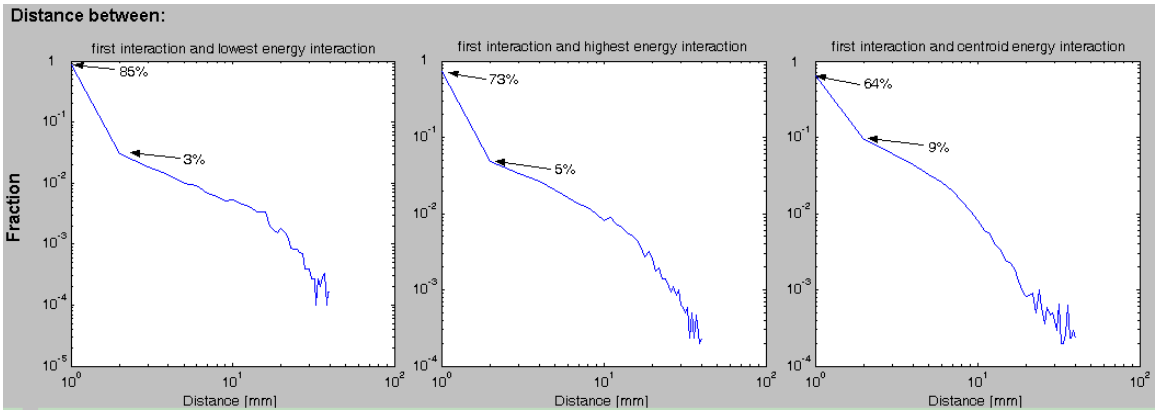

Figure 6.22: Effect of positioning algorithm on prediction of correct position of energy gated events. Plotted is the histogrammed distance from "true position" and a) lowest energy interaction above a prescribed noise floor, b) highest energy interaction (presumably photoelectric interaction), c) centroid of locations of energy deposited. The percentage of the events with error between 0 - 1 mm and between 1 - 2 mm for each positioning algorithm (first two points) are labeled in the plots.

the blurring due to a particular positioning algorithm, the difference between the algorithm positioned LOR (calculated LOR - cLOR) and the ideal LOR (iLOR) was calculated. These calculations were performed for interactions from a point source located at various axial and radial positions. Deviations were calculated in sinogram space where lines of response have an angular (θ), trans-axial (t) and axial (z) component. For a particular positioning algorithm,

$$\delta(\theta, t, z) = cLOR(\theta, t, z) - iLOR(\theta, t, z) \tag{6.3}$$

and for each coordinate

$$\sigma_\theta = \sqrt{\frac{1}{N}\sum_{i=0}^{N}(\delta_i)^2} \tag{6.4}$$

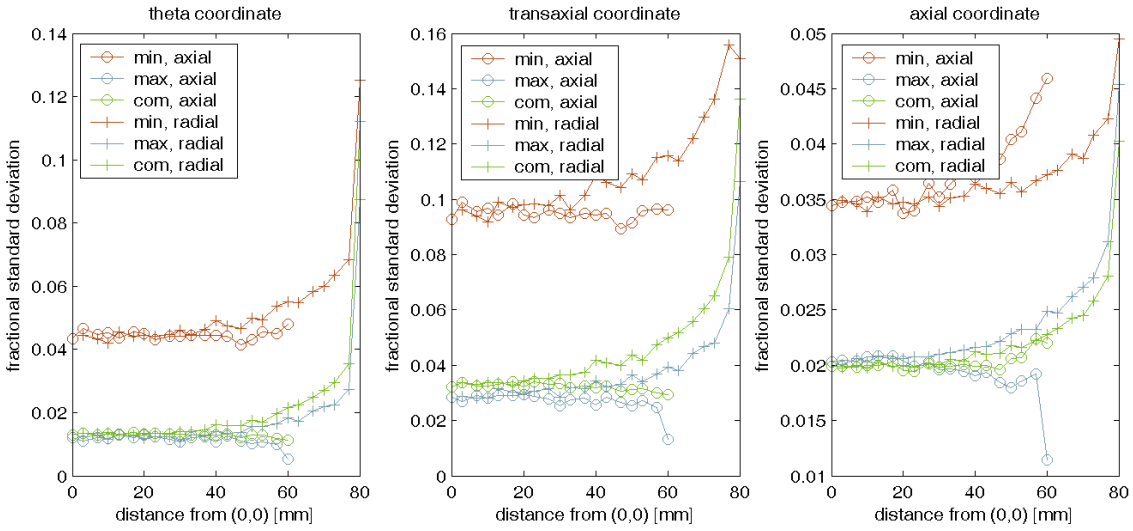

Figure 6.23: Standard deviation of the difference between position algorithm calculated position and the first interaction position for the three positioning algorithms for various locations in the detector system.

The standard deviations of these differences are plotted in Figure 6.23 for each radial and axial field of view location. The events plotted were within a 24% energy window around 511keV. The results clearly show that, although the minimum energy positioning algorithm produced the smallest three dimensional position deviation from the ideal location, the center of mass positioning algorithm has a smaller LOR space deviation for most components. The smaller LOR space deviation for the COM algorithm must mean that although the minimum energy position is closer to the ideal, its vector deviation in LOR space has larger components perpendicular to the line of response direction (see Figure 6.24). The center of mass positioning algorithm will be used in all following chapters.

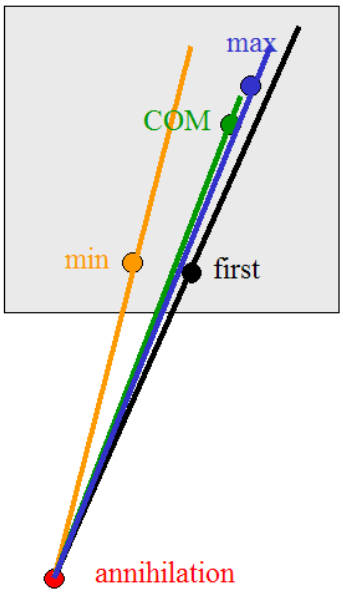

Figure 6.24: Two dimensional illustration of lines of response formed by an example event with three interactions, one that was: 1) the first (black circle), 2) the minimum energy (orange circle) and 3) the maximum energy (blue circle) deposited. The center of mass position (green circle) is also shown. The angular deviation in LOR from the "true" LOR (black line) to the minimum energy interaction (orange line) is the greatest, even though the distance from the minimum energy interaction to the "true"/first interaction is the smallest. Both the maximum energy and COM interaction locations are farther in distance from the first interaction, but have comparable deviation in LOR from the "true" LOR.

6.7 Discussion and Conclusions

A small animal system was designed using LSO scintillation crystals and position sensitive avalanche photodiodes by evaluating various system designs. The box-shaped system was chosen from the designs investigated for its incorporation of necessary specifications for its use in small animal experiments (8 cm inner bore diameter), simplicity of construction and highest coincidence detection sensitivity (~10%).

Energy spectra studies were performed to evaluate how the systems differed in their ability to capture annihilation photons directed at their detection heads. Systems with a high number of detection heads formed larger numbers of inter-head gaps. These gaps lead to a higher number of annihilation photon events that did not deposit the entirety of their energy in the system, but instead scattered out of the detector. Module construction investigations showed similar trends, where more spatially frequent inter-crystal-array gaps decreased the coincidence detection sensitivity, as compared to systems employing the same volume, but more densely packed crystal. Module orientation experiments on the box-shaped detector system determined the final construction variable and indicated the trans-axial gap system design, which was used in all following chapters.

The box-shaped system was further evaluated for determining experimental operational parameters by evaluating Noise Equivalent Counts over a range of energy and coincidence time windows. A 24% energy window and 4 ns coincidence time window gave the peak NEC value, while still maintaining a coincidence sensitivity. The system was studied for a range of source activities to understand how it will perform during small animal experiments. Results showed that multiple interactions began to dominate and therefore produce a peak in acquired events at $\sim$1.7 mCi. This peak is above the 400 μCi activity with which most animal experiments are performed, so multiples are not likely to reduce sensitivity for most experiments.

During the simulations, it was discovered that single annihilation photons entering

the detector system produced interactions in two or more PSAPDs for nearly half of the cases, throughout the field of view. The number of scattering interactions were also investigated for the system. Events with only a Photoelectric interaction were as frequent as events with only one Compton scattering event (∼37% of events).

Knowing that multiple PSAPD photodetectors were involved in nearly half of all events, a final study was performed to investigate how to position annihilation photons. Three positioning algorithms were investigated: positioning based on the (1) lowest energy interaction, (2) highest energy interaction, and (3) center of mass of the interactions. Although the lowest energy interaction positioning scheme proved to have the lowest deviation from the true (first interaction) position, it produced a line of response with the largest deviation from the true (first interactions, paired) line of response. The center of mass positioning algorithm had the lowest deviation from the true line of response, and was used for positioning in all following chapters.

Chapter 6, in part, is a reprint of the material as it appears in Physica Medica 2006. Foudray, AMK, Habte, F, Chinn, G, Zhang, J, Levin, CS. The dissertation author was the primary investigator and author of this paper.

Chapter 7

Development of a Realistic LSO-PSAPD Detector System Signal Model

7.1 Introduction

Many of the studies performed in this work used the Monte Carlo simulation package GEANT4 Application for Tomographic Emission (GATE). GATE is useful tool for understanding the capabilities of detector systems, or to develop algorithms for efficient and effective data usage in parallel to system construction. GATE is a add-on package to GEANT, constructed specifically for medical imaging, and was built for ease of use for any user. In generalizing some features of system implementation for

wide use in the community, some assumptions were built in which break down for the novel detectors employed in this work. One such assumption is that all interactions in the detector from a single annihilation photon are contained in one detection element and can therefore be centroided as the preferred coincidence output.

A model for incorporating the known variations in the detection process and light transport physics in the novel detectors was developed in this chaper. The results from the developed model, discussed later in this chapter, will show that half of the time, annihilation photons interact in two or more PSAPDs before fully depositing all of their energy.

First, a discussion on the transport processes of the particles involved (annihilation and characteristic x-ray photons; electrons) will illustrate the backbone of the phyics integrated into the developed model.

7.2 Interactions in Matter

The interactions of photons that many of us are most familiar with on a day to day basis, deal with photons in the visible region of the spectrum. When the energy of photons become high enough to effect constituent members of the atom, namely inner and outer shell electrons, another set of classes of energy deposition mechanisms arise.

7.2.1 Compton Scattering

One of the primary methods of interaction that the annihilation photon undergoes, because of its energy and the density and atomic number of the material with which it is interacting, is by Compton scattering [146]. Figure 7.1 shows the fractional frequency of three types of interactions for a low density, low atomic number material (aluminum), and a high density, high atomic number material (lead) [82].

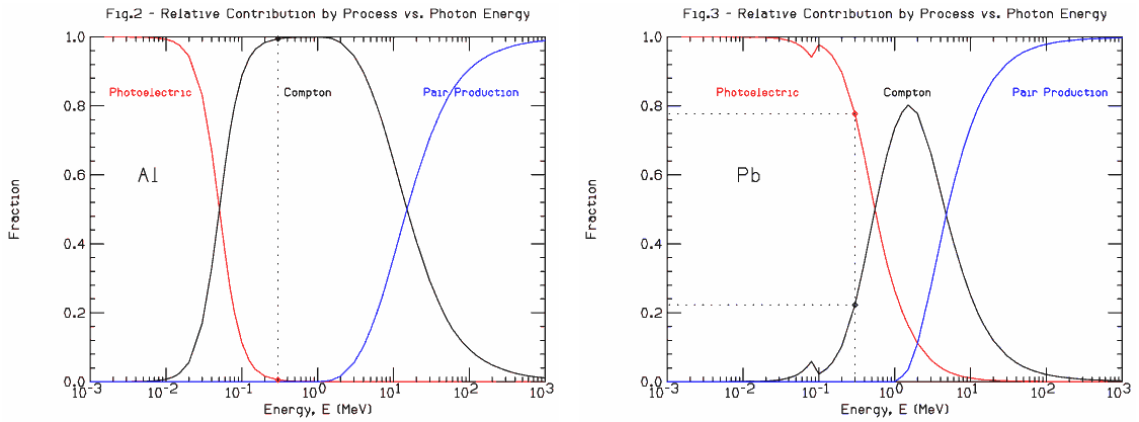

(a) (b)

Figure 7.1: The fractional mode of interaction in (a) aluminum (Z=13, ρ=2.70 g/cm^3) and (b) lead (Z=82, ρ=11.3 g/cm^3) versus incoming photon energy. A dotted reference line is drawn at 200 keV in both figures [82].

When the annihilation photon impacts an outer-shell electron of an atom, it imparts some of its energy to the electron (which can go on to ionize other electrons), and subsequently changes direction. The annihilation photon's energy after a Compton scattering is a function of its pre-interaction energy and the angle at which it scattered [94]:

$$E'(E,\theta) = \frac{E}{1+\alpha(E)(1-cos(\theta))} \tag{7.1}$$

where E and E' are the photon energies before and after scattering respectively, θ is the scattering angle, and α(E) is the relative energy of the photon to the rest mass of an electron. For an unscattered annihilation photon, $\alpha = 1$. This relationship is governed by a probability that the photon will scatter into a particular solid angle, which is also energy dependent [94]:

$$\frac{d\sigma}{d\Omega} = 0.5r_e^2(R(E,\theta) - R(E,\theta)^2 \cdot sin^2(\theta) + R(E,\theta)^3) \tag{7.2}$$

where r_e is the classical electron radius, and

$$R(E,\theta) = \frac{E'(E,\theta)}{E} \tag{7.3}$$

At the higher range of photon energies (350-500 keV), equation 7.2 states that the angular distribution will be weighted along preferred directions, making the scattering process less isotropic (heavily forward-scattering). As the energy of the photon lowers, the process becomes increasingly isotropic. This angular dependence affects the distribution of interactions in the detector.

7.2.2 Photoelectric

As seen in Figure 7.1, the photoelectric effect is the other predominant interaction affecting the transport of the annihilation photon through matter. In the photoelectric effect, the incoming annihilation photon imparts the entirety of its energy to an orbital electron (most frequently an inner shell electron). The electron is ejected from energy levels near the nucleus, and its vacancy is filled by an electron with lower binding energy, producing an x-ray with energy specific to the energy levels of the electon before and after filling the vacancy. The energy of the x-ray is also characteristic of the particular atom from which it was emitted [75].

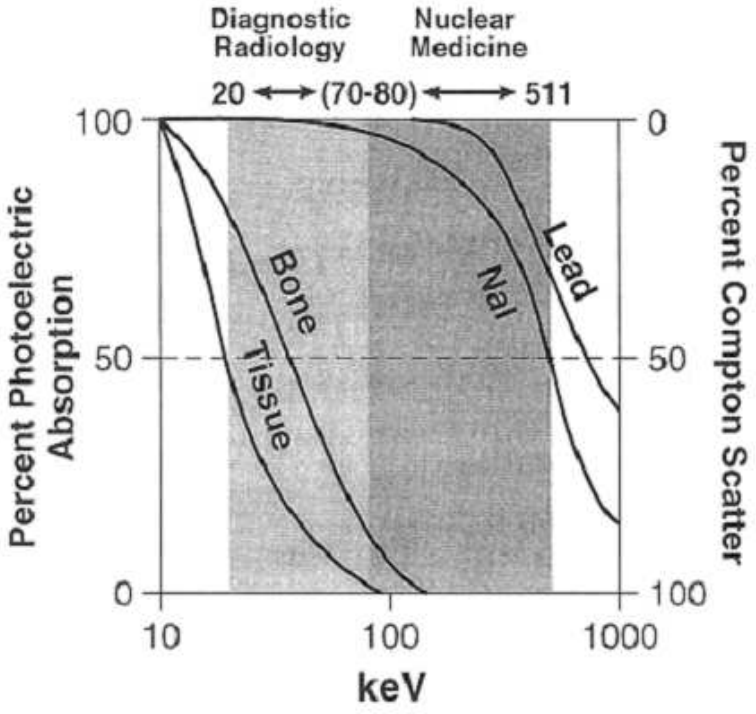

Figure 7.2: Interaction probabilities for various materials and incident photon energies [163].

The probability of Photoelectric interaction is proportional to the atomic number (Z) of the absorber and inversely proportional to the energy (E) of the incident photon (see Figure 7.2 [75]:

$$P \propto \frac{Z^{n(E)}}{E^{3.5}} \tag{7.4}$$

where n is a number between three and four, dependent on the energy of the incident photon.

Both the ejected electron and the emitted characteristic x-ray go on to deposit energy in the detector system. These processes will be discussed momentarily.

7.2.3 Rayleigh Scattering

An annihilation photon can also interact with the nucleus of an atom. This is called Rayleigh (coherent) scattering. Although the photon is deflected in the process, due to the large mass of the nucleus and momentum conservation, very little energy − negligible as far as detector energy resolution can discern − is imparted to the atom.

The scattering cross-section is highly wavelength dependent and generally negligible unless the incident photon's energy is quite low (very apparent in the visible spectrum). The scattering cross-section (σ_S) is computed in the following manner:

$$\sigma_S = \frac{2\pi^5 \cdot d^6}{3\lambda^4} \left(\frac{n^2 - 1}{n^2 + 2} \right)^2 \tag{7.5}$$

where d is the diameter of the atom, λ is the wavelength of the photon, and n is the refractive index of the material.

The effect of Rayleigh scattering in the context of the detector system is that, at the energies that Rayleigh scattering becomes a significant fraction of interactions ($\sim$12% at 30 keV in soft tissue, and $\sim$5% at 30 keV in the detector), the path length is very short ($\ll$1 mm) [83]. Therefore, if direction change occurs due to Rayleigh scattering, the photon does not traverse a sufficient distance to significantly impact position resolution.

7.2.4 Electron Interactions

There are two major methods by which electrons, liberated by previously described processes, deposit their energy into the detector system: collisional and radiative loss mechanisms. These processes will be briefly described in this section.

Radiative Energy Loss

Bremsstrahlung is a relatively low probability radiative energy loss process for electrons that are liberated from Compton scattering and the Photoelectric effect at electron kinetic energies found in PET ($<$ 1 MeV) [63]. Figure 7.3 shows how the Coulomb attraction between the nucleus of the surrounding atoms and the free

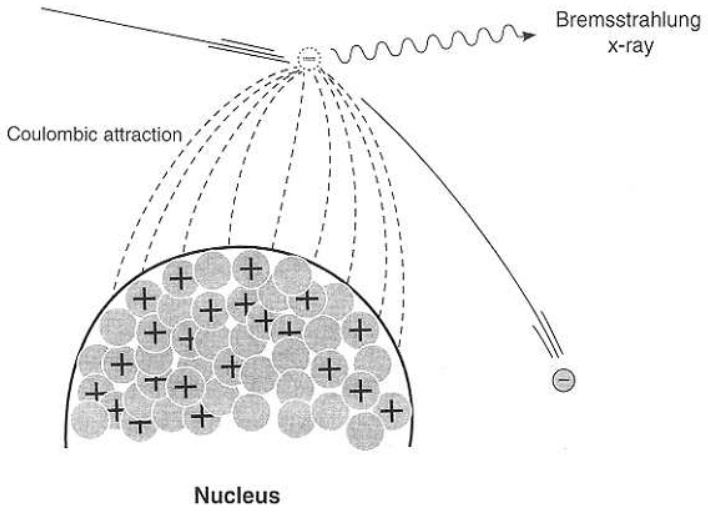

Figure 7.3: Illustration of the interaction mechanisms of Bremsstrahlung.

electron produce an acceleration on the electron. As the electron accelerates (bends) towards the nucleus, some of the photon's energy is released in the form of an x-ray.

Probability of Bremsstrahlung production per atom is proportional to the square of the Z of the absorbing material. For instance, Bremsstrahlung x-ray production accounts for ∼1% of energy loss when 100 keV electrons impinge tungsten (Z = 74) [63].

Collisional Energy Loss

Excitation and ionization, on the other hand, account for the majority of the method Compton- and Photoelectric-process-liberated electrons deposit their energy in the detector system [94]. The produced electron passes through the electron clouds

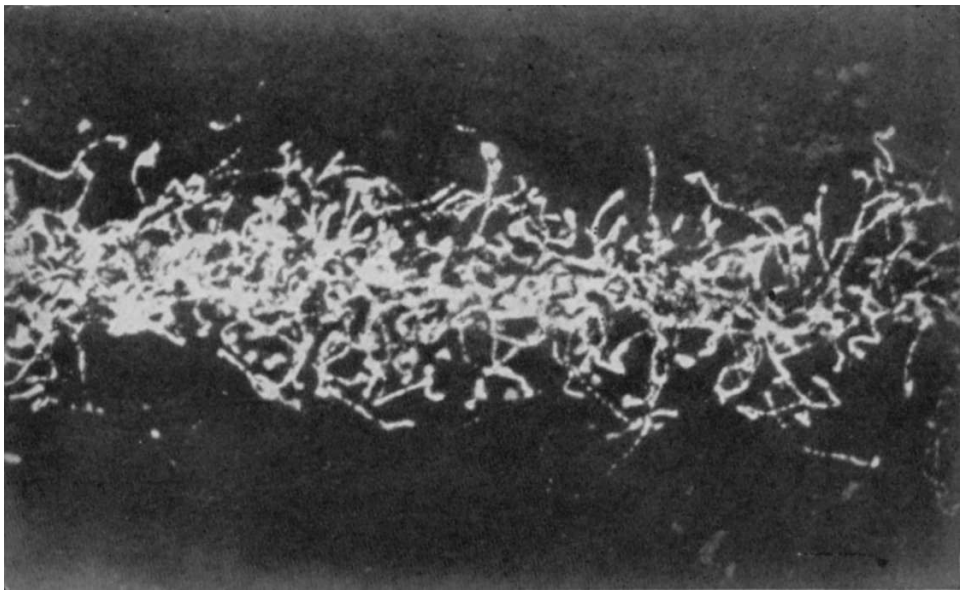

Figure 7.4: A photograph of electron paths resulting from collisions with atoms [176].

of the atoms that make up the absorbing material, ripping off or exciting into higher energy states other loosely bound electrons, as it traverses its path. Colliding with like mass objects, electrons undergoing collisional loss can undergo large angular deviations in direction, creating tortous tracks (see Figure 7.4).

The total stopping power for both radiative and collisional processes are additive and can be computed using the following formula [178]:

$$\left(-\frac{dE}{dx}\right)_{\text{tot}} = \left(-\frac{dE}{dx}\right)_{\text{coll}} + \left(-\frac{dE}{dx}\right)_{\text{rad}} \tag{7.6}$$

7.2.5 Characteristic X-rays

Mean-Free Path

Mean free path (λ) and linear attenuation length (l) have an inverse relationship, and can be computed [86]:

$$\lambda = \frac{1}{l} \tag{7.7}$$

Mass attenuation coefficient (μ), a useful quantity, does not vary with the density (ρ) of the absorber and is defined as:

$$\mu = \frac{l}{\rho} \tag{7.8}$$

Therefore, mean free path with respect to mass attenuation length can be written:

$$\lambda = \frac{1}{\mu\rho} \tag{7.9}$$

and for a chemical compound, the effective mass attenuation length is:

$$\mu_c = \sum_i \frac{w_i}{\mu_i} \tag{7.10}$$

where w_i is the proportion by weight of the element i.

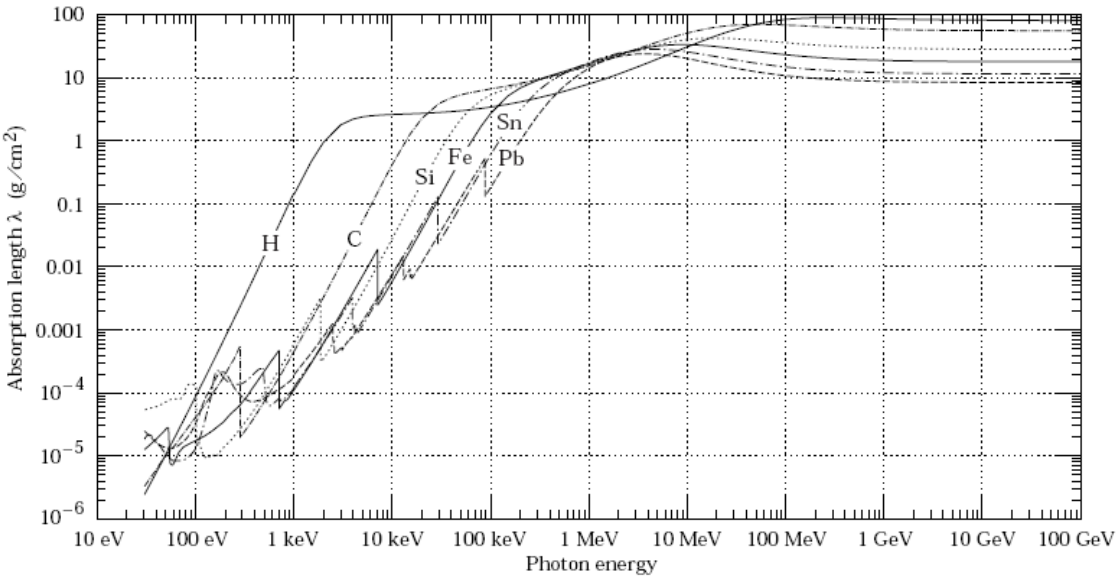

Figure 7.5: Photon attenuation length for multiple elements, over a range of photon energies [94].

X-Ray Escape

As the characteristic x-rays produced have a non-zero path length, there is a finite probability that they will escape the detector element of the interaction that produced them and be absorbed in a neighboring detector element. This "x-ray escape" results in a characteristic energy loss and a non-negligible contribution to the energy spectrum near the 511 keV photopeak. When the energy resolution of the detector system is sufficient, the photopeak and the x-ray escape photopeak can be fit separately, producing a curve that more accurately depicts the data near the photopeak. This information will be utilized in further chapters when evaluating detector components.

7.2.6 G4EMLOW GEANT4 Package

The low energy electromagnetic processes (G4EMLOW) package is the data package of GEANT4 that governs the physics described in this section. All processes that this package handles include: Compton scattering, pair production, photoelectric effect, Rayleigh scattering, Bremstrahlung, ionization, fluorescence, and Auger effect. The original data files and documentation can be retrieved online using Reference [38].

7.3 LSO-PSAPD System Model and Event Clustering

7.3.1 Overview

The input to the developed system model was the unblurred annihilation interaction locations produced by GATE, represented by "Annihilation photon enters the detector system." Each of the process from scintillation photon production to the output of the PSAPD was incorporated into the model. The developed model is specific to the LSO-PSAPD system designed in this thesis and was created to produce a realistic data set from the information gathered using GATE. An overview flow chart can be seen in Figure 7.6, which shows the processes and detector components involved.

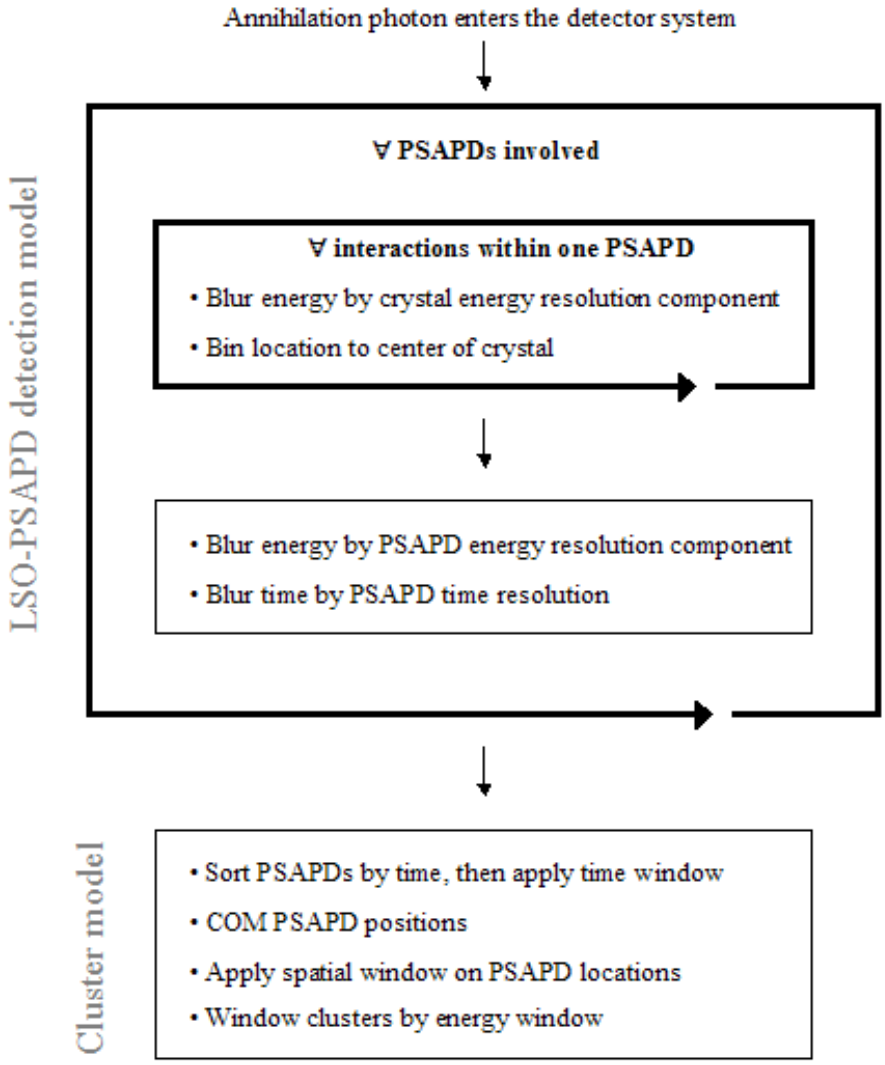

Figure 7.6: A flow chart illustrating the steps involved in the developed detection model where ∀: for all, COM: center of mass. Dark, thick lined boxes that have arrows in their lower right hand corner of their perimeter represent a loop over the process in the title of that box (e.g. in the first, large, outer box, ∀ PSAPDs involved means loop over all PSAPDs that had interactions at any time.

The first box (which contains two boxes) that loops over all PSAPDs (titled "∀ PSAPDs involved" in Figure 7.6) is the heart of the LSO-PSAPD detection model.

It takes into account the factors that affect position, energy and time characteristics of the signal produced from a single PSAPD. The output of the detection model step is a list-mode position, energy, and time "signal" from all PSAPDs in which at least one interaction occurred. The components of this detection process will be discussed in detail in Sections 7.3.2-7.3.7.

The second box shows the steps that are contained in the cluster model for collecting PSAPD signals into a "single". The steps involved in this clustering process are described in Sections 7.3.8 and 7.3.9.

7.3.2 Information Losses and Uncertainties

The characteristics and components of the detector system which produce variations in interaction energy, position, and time are illustrated in the following instrumentation features:

- size, shape, coupling mechanism, and material used for converting annihilation photons into either readable electrical signals directly, or photons detectable by a photodetector device
- the size, shape, photon readout structure, wavelength dependent quantum efficiency, signal amplification, and signal output structure of the photodetector device
- any filtering or multiplexing from front-end electronics reading out signals from

the detectors

Each surface, geometry, device, material, or processing algorithm can affect the transmission of information throughout the detector system. The design-specific components of these blurs were measured in Chapters 3 and 4. Used in conjunction with experimental data gathered by the original authors investigating these materials, the methods for incorporating gathered knowledge into the model are described in the next few subsections.

7.3.3 Optical Photon Binning

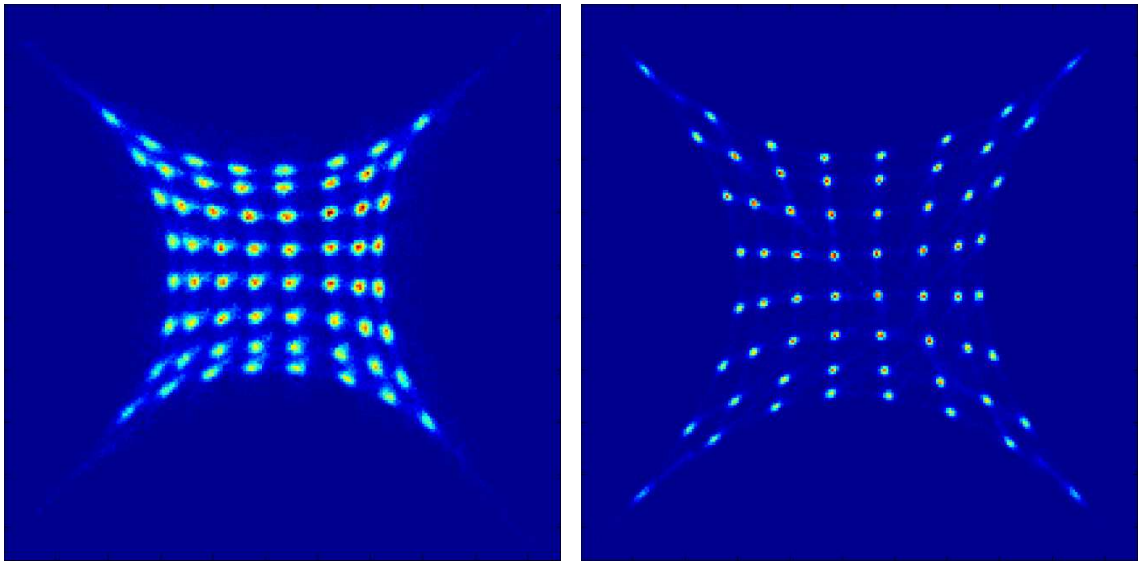

(a) without inter-crystal reflector (b) with inter-crystal reflector

Figure 7.7: Two dimensional flood histograms from a 10 x 10 array consisting of ∼1 x 1 x 1 mm^3 LSO crystals.

Figure 7.7 shows 2-dimensional flood histograms of data taken from a 10 x 10 ar-

ray consisting of ∼1 x 1 x 1 mm^3 LSO crystals, without (left) and with (right) array intercrystal reflector. As evidenced by these flood images, although the array with intercrystal reflector shows smaller diameter crystal feature sizes, the array without intercrystal reflector shows well-separated crystal feature locations for each crystal in the array. This well-localized crystal feature location demonstrates the reflective nature of the surfaces of the crystal, keeping the majority of photons within the crystal with which the annihilation photon interacted. The photons are reflected and directed to the photodetector detection surface and the center-of-massing (centroiding) nature of the PSAPD produces a detected position, on average, at the center of the crystal. Fluctuations about this crystal center location are due mostly to fluctuations in scintillation light production (counting statistics) and noise in the detector. Therefore, a first approximation to the light transport and PSAPD positioning mechanisms is binning the GATE-produced interaction location to the center of the crystal on the detection surface.

7.3.4 Device Centroiding

As mentioned in the previous section, the PSAPD photodetector receives light at its detection surface, and with some efficiency, produces a photocurrent. The photodetector amplifies the photocurrent, and is read out on both the top (common) and bottom (4 corner) contacts. Current signals at the cathode, or common contact,

of the device are produced from the generated hole current. At the bottom of the device, each collected charge from the electron current is directed to the four corner signals via charge division. Therefore, the output signal from each of these corner anodes is a superposition of the individual charges, directed by statistics along their paths. The resultant signal is the energy weighted mean of the positions of all charges, or the energy weighted mean (center of mass, centroid) of all positions. This result not only centroids the gain multiplied photocurrent from all scintillation photons from a single interaction, if two interactions occur in an array coupled to a single photodetector at the same time, they would become indistinguishable. The position of the interaction would be the centroided position, and the energy would be the sum of the interaction energies.

7.3.5 Crystal and PSAPD Energy Resolution

The energy blurring process measured in Chapters 3 and 4 were broken down into (1) scintillation light production variation contributions and (2) PSAPD detector contributions to the experimentally observed energy blur ($\sim$12%).

Each interaction was first blurred by an energy blur due to the variation in scintillation light production. Intrinsic resolution for LSO was estimated from experimental observations and found to be 3.4-8% [12, 91]. A crystal energy blur factor of 5% was used in the developed model.

The rest of the observed 12% energy resolution, measured from the LSO-PSAPD modules in previous chapters, was applied to the energy blurring step of the PSAPD. This resulted in a blur of $\sqrt{12^2 - 5^2} = 10.9\%$. A PSAPD-specific energy blur of 11% was used in the developed model.

7.3.6 PSAPD Time Resolution

Time resolution was observed to be ∼2 ns when in coincidence with a photo-multiplier tube. This time resolution of the PSAPD alone could be estimated by de-convolving the time resolution of the PMT device. For a conservative estimate of PSAPD device function, a time resolution of 2 ns for a single PSAPD device was used.

A Gaussian with 2 ns FWHM, centered on the time given by the GATE simulation, was applied to the first of the interactions that occurred in the PSAPD. The first interaction was chosen as it would initiate the rise time of the PSAPD signal pulse, from which signal time is estimated with electronics. This blurred time stamp was the one reported by the model.

7.3.7 Minimum Detectable Energy

All resulting signals in the PSAPD were subject to an energy threshold, which represented the value above the noise floor at which the PSAPD signals would be

considered a detected annihilation photon interaction. The noise from a 8 x 8 mm^2 PSAPD was measured to be 0.8 keV at room temperature [157]. A conservative 10 keV was used in the developed model.

7.3.8 Time, Energy and Spatial Windows

The output of the detection model is a list of PSAPDs with position and energy signals and a time stamp. This list is then sorted by time (as time stamps have been blurred and are no longer necessarily in order) to be time windowed. A moving time window of 4 ns was used based on NEC calculations for this system performed in Chapter 6. PSAPDs that had signals within this window were then filtered spatially.

PSAPDs that had signals within the time window were used to check to find if there were neighboring PSAPDs within 2 cm in x, y and z locations within the detector system. The groups of PSAPDs that were within this neighborhood were used to find a center of mass. A window of 2 cm in x, y and z was applied, relative to the center of mass of the PSAPDs within the original neighborhood. These PSAPD signals then constituted the resulting cluster.

The energies of the PSAPD signals in the cluster were then summed and subjected to a 24 % of 511 keV energy window, i.e. in order to be kept by the clustering model, the total energy of the cluster had to lie between 450 keV and 572 keV.

7.3.9 Cluster Positioning Algorithm

The cluster at this point contained PSAPDs with individual positions, energies and time. The representative position, energy and time for the cluster was determined in the following way: the position of cluster was the mean of the positions weighted by their energy (center of mass), the energy of the cluster was the sum of the energies, and the time stamp of the cluster was the average time.

7.4 Implications for Data Acquisition System

This LSO-PSAPD model was applied to each interaction produced by GATE, forming a signal blurred by measured experimental positioning effects as well as energy and time resolutions. By using this model, simulated data could be used to estimate full system response in terms of characteristics such as image resolution throughout the detector, effective signal to noise ratio (NEC), and normalization techniques (Chapter 8).

Some initial results of the application of this model are described below and were studied using full system simulations. These results are for the box-shaped 8 cm x 8 cm x 8 cm field of view small animal system.

7.4.1 Devices Involved in One Event

As mentioned in Section 6.6.2, because the size of the detection modules are on the order of the path length of annihilation photons, the number of PSAPDs involved in the interactions from a single annihilation photon could be greater than one. In other words, as an annihilation photon loses its energy to interactions in the detector system, the interactions could potentially occur in multiple independent PSAPD photodetection devices. The fraction of occurance of the number of PSAPDs involved in the interactions from a single annihilation photon was studied in various locations in the detector system's field of view.

Figure 6.20 shows the results for various axial and radial locations measured from the center of the system (0,0). The marker shape denotes the direction of the displacement at the time of measurement: the circle means an axial displacement from the center, and the cross a radial displacement. The color of the marker signifies the number of PSAPDs involved. So, for instance, the data represented by the left-most red circle denotes that about 50% of annihilation photons originating from the center of the system have interactions that occur in only one PSAPD.

As Figure 6.20 shows, the majority ($\sim$90%) of all annihilation photons deposit their energy in either one or two PSAPDs $-$ 50% involve one PSAPD and 40% involve two PSAPDs. Another $\sim$9% of interactions occur in three PSAPDs. This leaves the event fraction of four or more PSAPDs involved nearly negligible.

Because of the PSAPD device centroiding of multiple interactions within a single PSAPD, the fractional occurrence of the number of interactions (regardless of the number of detectable interactions), was also studied for various locations in the field of view of the detector system. The results shown in Figure 6.21 illuminate the centroiding effect by the PSAPD. As can be seen from the data, the fraction of annihilation events that contain a Photoelectric interaction only (1 interaction) and one Compton plus the Photoelectric interaction (2 interactions) are essentially identical throughout most of the field of view.

7.5 Conclusions

A model, specific to the detector module used throughout this thesis, was developed from experimentally acquired material and device measurements in order to translate perfect Monte Carlo interaction simulation measurements to realistic module measurements. The model incorporated position, energy and time blurs, as well as, a realistic noise floor. The developed model was used to characterize system response to realistic PET experiment environments.

The number of PSAPDs involved in a single event was studied for many radial and axial locations in the field of view of the detector system. $\sim$99% of all events took place in three or less PSAPDs, with $\sim$90% occurring in two PSAPDs or less.

Although not all interactions are measured independently in the novel detector

system developed in this thesis, nearly 50% of all events occur in two or more PSAPDs (see Section 7.4.1). This result presents both a challenge and an opportunity to best use the information from the detected signals. These issues will be addressed in the following chapters.

Chapter 8

Development of a Component-Based System Line of Response Normalization Algorithm

8.1 Introduction

In order to achieve high image quality and quantitative accuracy in reconstructed images, the sensitivity of each detector line of response (LOR) must be normalized. If these variations in LOR sensitivity are not resolved prior to reconstruction, artifacts will present themselves as intensity variations and bias in the image. These artifacts confound the ability of the system to represent the actual activity in the object of interest, which is the fundamental purpose of this instrument.

There are two commonly used methods for calculating the weighting factor applied to each LOR in the system: direct normalization and component-based normalization. While utilizing direct normalization is relatively straightforward to calculate after a calibration measurement, using this method, acquisition itself is time consuming and has a few major drawbacks and limitations that will be discussed in Section 8.3.1. The other commonly used approach is component-based normalization, where weighting factors are broken down into separable pieces and symmetries in the system are taken into account. Component-based methods have a much faster measurement time and have the ability to take more system parameters into account, but they do require more data manipulation and careful calculation than the direct method.

The small animal box-shaped and dedicated breast dual-panel detector systems use detectors that can locate energy-depositing interactions in five dimensions: three dimensions of space, one of energy and one of time. Since the detectors are not restricted by the usual depth of interaction (DOI) determination problem as they directly measure interactions in three spatial dimensions (3D), the detectors can be moved in close to the imaging subject for higher sensitivity. This 3D spatial measurement capability offers the possibility of the useful FOV equal to the interior volume of the system. However, this capability introduces many more LORs requiring normalization.

Component based normalization was introduced to measure and take into account all factors that contribute to the efficiency variations over all LORs [10]. The method

used in this study was developed to adapt the component-based normalization model to include depth of interaction (DOI) and large useful FOV considerations without an order of magnitude increase in computational resources.

Some of the data and results presented in this chapter were previously published in Reference [52].

8.2 Quantification in Reconstructed Tomographic Images

The image reconstruction process uses detector acquired data to accurately solve for the object of interest. To understand how detector efficiency information would be used during reconstruction, one must understand how tomography works. This section will only consider basic ideas pertaining to tomography that are necessary to understand to role of normalization in tomographic imaging. A more detailed discussion of tomographic theory can be found in References [20, 23, 66, 79, 131].

8.2.1 Role of Normalization in Tomography

As mentioned previously, at the heart of tomographic imaging is the ability to non-destructively determine information about the interior of an object of interest. In the case of PET, the detected activity distribution in a subject depicts the density

of a particular biomolecular process. Accurately measuring signals emitted from the object is essential to accurately reconstruct activity density in the object. All detector lines of response must act in the same manner when presented with annihilation photon pairs directed at them. The reasons in which line of response efficiency can differ are described in the next section.

8.3 Normalization Methods

8.3.1 Direct Normalization

In order to account for LOR-dependent efficiency differences, one could measure the counts reported by the system when irradiating each line of response in the same manner. The reciprocal of the counts in each LOR produces a weighting factor to apply to future acqusitions. This method of calculating a weighting factor - by directly measuring system response, is called direct normalization (DN). The data for this method can be gathered by using a uniform concentration source, shaped such that each LOR traverses the source volume for either the same path length or known path lengths through the source, for which the counts reported must be compensated. For instance, in a cylindrical detector system, one could use a cylindrical volume source which would need compensation for different activities that each line of response would traverse, or an infinitely thin cylindrical shell source where no activity difference compensation would be necessary (see Figure 8.1).

Since the normalization weight factors, computed from the DN source measurement, will be applied to correct each LOR used in future data measurements, a large number of counts per LOR must be acquired in order to mitigate propagation of error. Multiple experimental difficulties must be overcome or accounted for correctly: (1) efficiency variation of LORs in the system can vary greatly (as much as 2-3 orders of magnitude in some cases − see Figure 8.2), (2) the number of lines of response in a system are generally on the order of $10^7 - 10^9$ making data processing difficult, (3) count rates for most systems are on the order of millions of counts per second [153] making data streaming difficult, (4) gathering sufficient counts can be extremely time consuming, (5) inherent dead-time of a system, the time in which it takes the system to recover from processing and recording an event, limits the count-rate and therefore activity strength of the source used to gather the data, and (6) difficulty to manufacture both uniform activity sources and sources that would extend to the extremities of the field of view.

Other complications arise when trying to use weight factors calculated using a DN technique even after they have been calculated. DN does not account for the difference between the normalization factors for scatter and true coincidence events [129], which may lead to artifacts in the image.

To investigate the range of normalization factors acquired using the DN method, a sinogram was constructed from 10 million counts gathered for a uniform activity cylindrical phantom in the small animal box-shaped tomographic system (Figure 8.2).

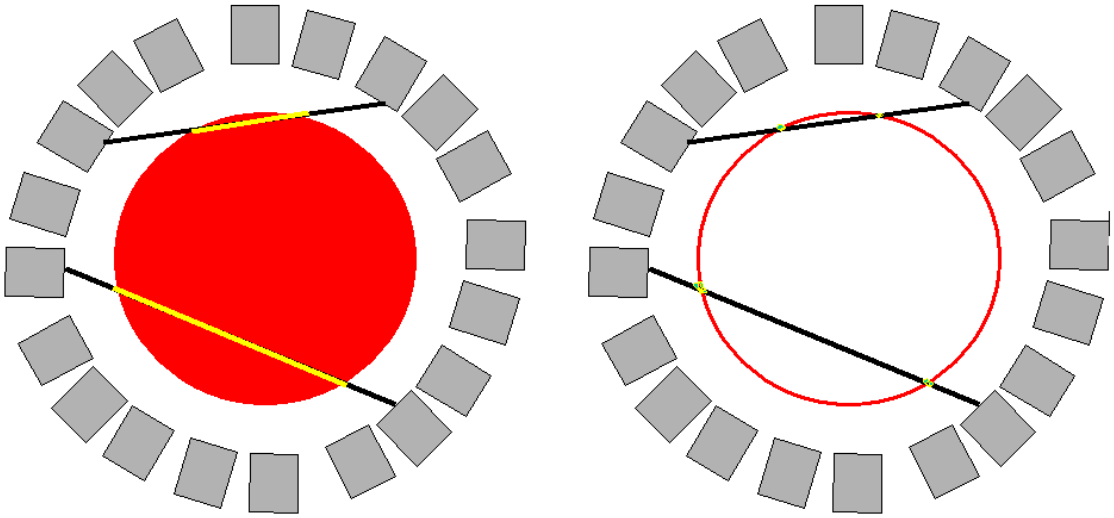

Figure 8.1: Illustration of activity phantoms used in count acquisition for direct normalization. See text for details

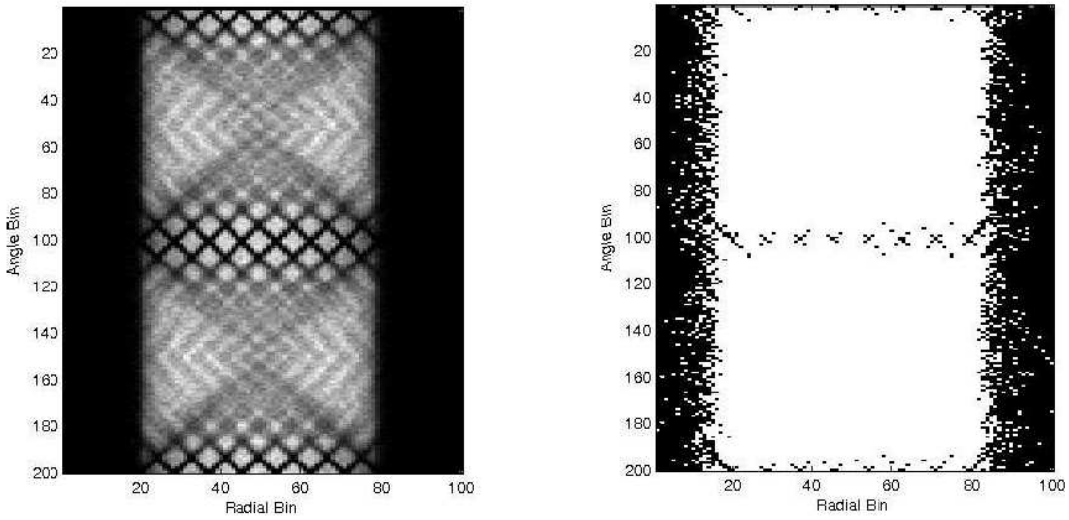

Figure 8.2: Direct-plane sinogram of an infinitely thin annulus 2.5 cm in radius, showing intensity differences between the counts filling each LOR bin. (Left): the intensity weighted sinogram, (right): a binary look at the same data where black = no counts, white = 1 or more counts.

Large gaps are apparent in the direct plane sinogram and there are some bins where there were no counts at all (see the right figure in Figure 8.2). These gaps are due to absence of crystals in the dead regions surrounding each PSAPD photo-detector used in this study. The normalization factor necessary to correct for bins with zero counts would be infinite.

8.3.2 Component Based Normalization Efficiencies

There are numerous ways in which lines of response can vary in sensitivity. Generally, they can be broken down into the following categories: a) geometric and intrinsic differences in detection, and b) any differences in a detector's immediate neighborhood.

Geometric and Interference CBN Efficiencies

Geometric parameters are defined as the variance in efficiency of a detection element to "stop" the incident high energy photon due to the effective shape of the detector - which generally changes as function of incident angle, unless the elements were infinitely small and spherical − which would not be practical. The following are component based normalization (CBN) factors that affect sensitivity of a detector element due to geometric considerations:

- Block Profile factors: the detection element's position in the detector block with respect to the other crystals. In the case of this system, the block profile

factor for a given crystal is a function of is its relative position in two directions: transaxial and depth of interaction.

- Radial and axial geometric factors: crystal depth changes due to variations in incident photon direction in both Θ and Φ.

- Interference factors (radial and axial components): these factors modulate the radial and axial geometric factors due to a crystal being obscured by crystals in other blocks of detectors.

The effects shown in the list above will be the central focus of this study. Gathering representative data and separating and quantifying these efficiencies is the backbone of the calculation of the per-LOR weighting factor. How to combine these factors, the system space in which these factors are applied, the novel measurement method used to calculate these factors, the implementation scheme to normalize each LOR, and results of the application of this algorithm will be described in the next sections.

Intrinsic CBN Efficiencies

Intrinsic parameters in component based normalization sensitivity are defined as the variance in efficiency of each detector with respect to other detectors used in the system. This can include effects such as:

- Magnitude and variance of intensity, spectral and temporal distribution of light output of the scintillation crystals (i.e. variations in material properties of the

scintillation crystals)

- Optical coupling thickness, reflector coverage and reflectivity, edge effects (i.e. variations in optical transport of the photons that are produced)

- Quantum efficiency; index of refraction; temperature; operating voltage; leakage current; gain; energy, position, temporal resolution (i.e. variations in how each photodetector registers photons)

In essence, these variations are properties that would exist even if the crystals that were used were exactly the same size, and were positioned precisely the same on the photo-detectors. Even if these constants could be maintained, there could be variability in the operation of these elements.

These normalization effects were not modeled in the development of this algorithm (as all modules were constructed identically), but possible means of their measurement will be discussed in Section 8.5.

8.4 Component Based Normalization

8.4.1 Nomenclature

Conventional PET detectors, for any application (whole body, dedicated to a particular region or organ, or small animal), consist of finite extent detection elements.

These elements, defined either by physical restrictions (the dimensions of small crystals attached to photodetectors, device centroiding, etc.) or the acquisition scheme (hardware readout configurations or software event positioning schemes), determine the precision of event positioning. As investigated in Chapter 6, the detection elements are arranged such that they form a set D_i (i = 1, 2, ... m) in coincidence with another set D_j (j = 1, 2, ... n). This set of pairs defines end points of lines of response that traverse the field of view. The set of all LOR_{ij} form an m x n 2D interaction or acquisition space D_{ij} (see Figure 8.3 for an example).

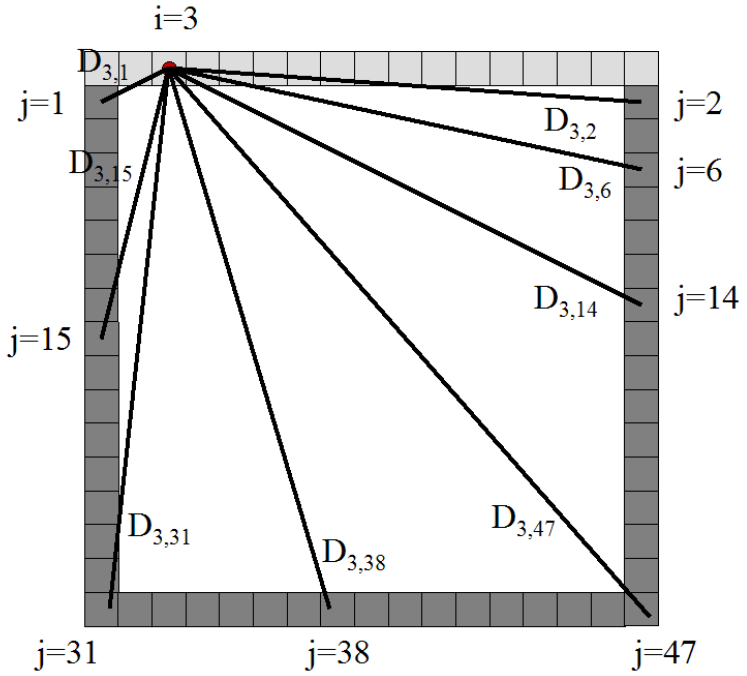

Figure 8.3: An illustration of some possible LORs D_{ij} formed when i=3 in this box-shaped detector design. All light and dark grey boxes are individual detector elements. If the field of view is the entirety of the interior volume of the detector, all dark colored detector elements can possibly form a pair with detector element i=3, but the light colored ones cannot pair.

Count rate in a particular LOR, or number of events detected per second, should be proportional to the amount of activity that lies along that LOR. This leads to the useful definition of the component-based normalization factor.

8.4.2 Definition

Normalization models compute the activity within a LOR using the following relationship [10]:

$$A_{ij} \propto C(P, R, S) \cdot NC(\text{true})_{ij} \cdot att_{ij} \cdot dt_{ij} \tag{8.1}$$

where A is the activity, ij is the index of the LOR; P, R and S are prompt, random and scatter, respectively; C is a count rate factor dependent on the individual count rates of P, R and S; $NC(\text{true})$ is the normalization coefficient for true coincidences; and att and dt are attenuation and dead-time correction factors. The normalization coefficient can be further broken down into components calculated from intrinsic efficiencies (ϵ) and geometric efficiencies (g) that depend on the particular pair of detectors that formed the LOR. These factors can also be represented as multiplicative coefficients to compute the NC:

$$NC_{ij} = \frac{1}{\epsilon_i \cdot \epsilon_j \cdot g_{ij}} \tag{8.2}$$

Equation 8.2 demonstrates the separable nature of intrinsic efficiency components

from geometric components. This relationship is very useful when a detector has many symmetries, and will be integral to the implementation of the method and usage of the acquired data.

For completeness, a cross-term is included in this definition, which depends on the particular detectors involved, and must be calculated knowing both detectors. In the case of this model, the cross term is only a function of distance between detectors, and will be calculated on the fly. The system model used in this novel component based normalization technique is describe more thoroughly in Section 8.5.1.

8.4.3 Implementation

Data Respresentation

All event positions $(x_1, y_1, z_1, x_2, y_2, z_2)$ and computed normalization weight w, were calculated using equations 8.2 and 8.3 on a line-by-line (individual event) basis. This seventuple for each event $(x_1, y_1, z_1, x_2, y_2, z_2, w)$ was then stored in list-mode to be read by the OSEM reconstruction software. As mentioned previously, the reconstruction algorithm-modified counts for a given LOR are backprojected through the image voxels intersecting that line. The sum of distributed counts for all pixels was then normalized to the weight in the seventuple. The weight, or inverse efficiency, was scaled so that it was ≥ 1, weighting LORs of the highest efficiency to one.

Density of Line of Response Image

Independent of the efficiency of each of the lines of response within a detector block (many modules) is a factor dependent on how the system modules are configured.[1] This system dependent component is the density of lines of response (dLOR) through image space. Ideally, a sensitivity image would be formed from one count from all possible lines of response. Because the LOR space is prohibitively large, a subset of the LORs were used to calculate the dLOR sensitivity image. Rotational and mirror symmetries of the system were then employed by adding the symmetric images together, forming a higher count image. The resulting image was inverted and then smoothed to reduce the variations in sampling of each of the image pixels. This image was then used in the reconstruction algorithm as a direct sensitivity correction to the image space. A 2D slice through the 3D dLOR sensitivity image for the small box-shaped animal system can be seen in Figure 8.4.

[1]The density of lines of response in an image is independent of LOR efficiency in the systems studied here because the heads of the system are much larger than the scattering length of photons within the detector head (i.e. each module is essentially equivalent to the one studied). If the heads' size were on the order of the scattering length, many of the system symmetries described in Section 8.5.1 would not be applicable, and the LOR efficiency would have block profile factors. This configuration would couple the density of lines of response image and the weighting factors in that relatively small changes in system configuration would significantly change both weighting factors and the density of lines of response image.

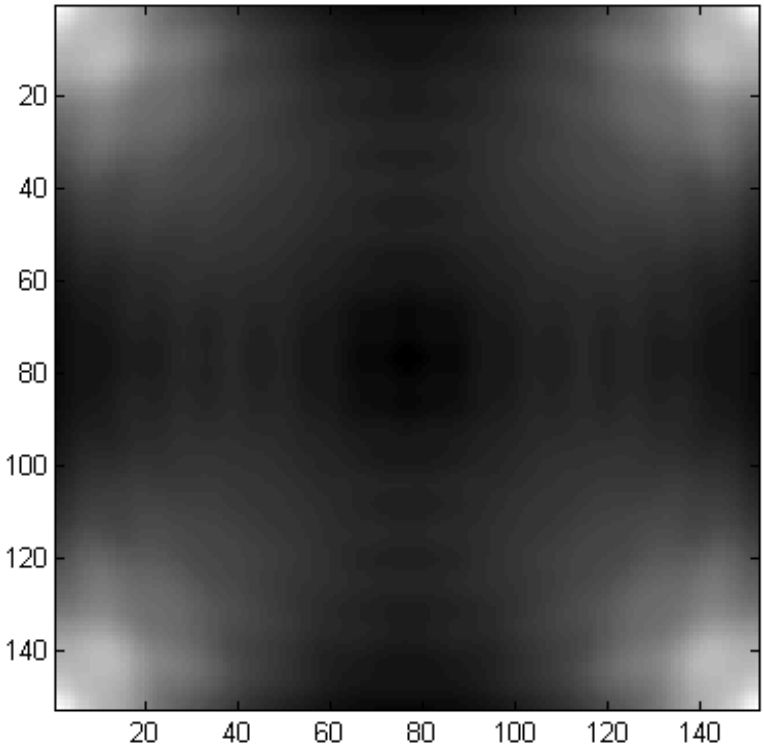

Figure 8.4: The central axial slice through the small animal density of line of response image.

8.5 Component Estimation Techniques

The ultimate goal of this study is to obtain the efficiency for every LOR in the system. Fortunately, by looking at the way in which the system is constructed, inherent symmetries emerge, which become useful to reduce the amount of information that must be gathered. System construction, how the weights were applied to data, component gathering strategies, and results are all described in this section.

8.5.1 System Modeling

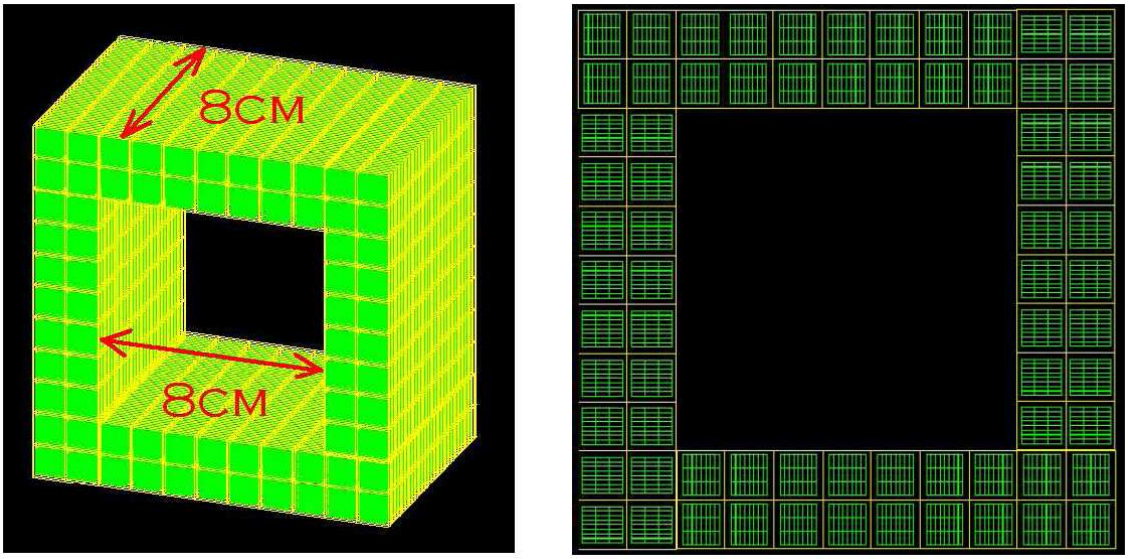

Figure 8.5: Left: Screenshot of the system during GATE simulation showing the 8 cm x 8 cm x 8 cm field of view. Right: Axial cross-section of the system showing crystal placement and distance between crystal arrays. Crystals are outlined in green, PSAPDs are outlined in yellow.

The Monte Carlo package GATE (GEANT4) was used to generate the data reported in these studies. The imaging system simulated is a box-shaped small animal PET system constructed of thin ($\sim$300 μm) position-sensitive avalanche photodiodes (PSAPDs) coupled to 1 mm x 1 mm x 3 mm Lutetium Oxyorthosilicate (LSO) scintillation crystals forming an 8 x 3 array, which gave a crystal volume of 8 mm x 9 mm x 1 mm coupled to each photodetector. Due to this construction, the system had $\sim$1mm trans-axial, 1.3 mm axial and 3 mm depth of interaction positioning capability (see Figure 8.6). Variation of intrinsic efficiency due to factors such as photodetector gain and crystal light output in the detector pairs were not modeled in the Monte Carlo

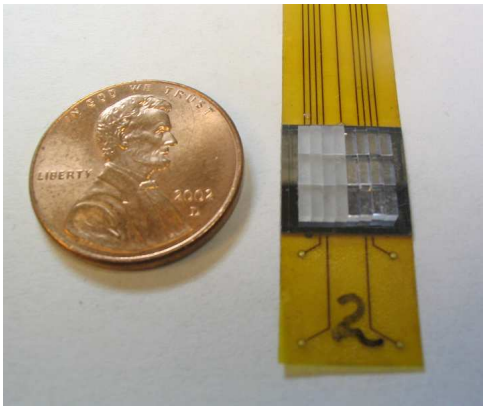

Figure 8.6: A PSAPD module with one photodetector coupled to an 8 x 3 array of crystal. The modeled system comprised modules with both PSAPDs, each with a coupled 8 x 3 array.

except on an individual detector basis using an blurred energy resolution. Therefore, all intrinsic efficiencies were set to one and the normalization coefficient from equation 8.2 reduces to the following cross- and geometric factors:

$$NC_{ij}^{-1} = (g_{\text{rad}})_{ij} \cdot (g_{\text{ax}})_{ij} \cdot (g_{\text{int}})_{ij} \cdot dd_{ij} \tag{8.3}$$

where "rad" is radial, "ax" is axial, "int" is interference, i and j are detectors in LOR_{ij}, and dd is the (x_i,y_i,z_i) to (x_j,y_j,z_j) distance factor.

A module was made up of two PSAPDs lying flat on a single thin readout circuit and were oriented so that they were adjacent to each other in the depth of interaction (DOI) direction (see Chapter 5). The system comprised modules stacked together in the transaxial and axial direction to form the system. A picture of an axial cross-section of the system can be seen on the right side of Figure 8.5, and the whole system can be viewed on the left side of Figure 8.5.

A single module in a section of detectors from the system was probed with single photons. Symmetry was then used to deduce the factors for each detection element over the whole system (see Section 8.5.1). Interaction events were generated in the detector section using a thin pencil beam of single photons which irradiated the detector element for a constant time (20 msec), at a constant activity (10 μCi), in the full range of angles possible, and at a distance of 10 cm from the center of each crystal investigated. Figure 8.7 shows the locations of the pencil beam.

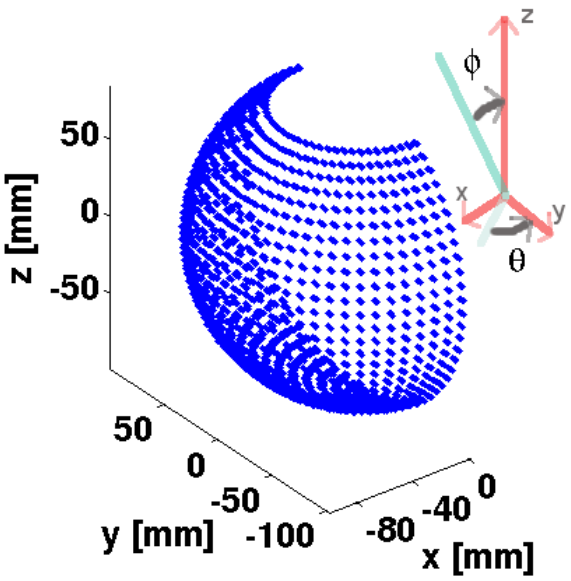

Figure 8.7: Locations of the point source used to acquire data to estimate the efficiency components.

Symmetries

Because of the high fraction of events involving inter-crystal scattering and its subsequent affect on both positioning [53] and sensitivity [52] of this system, a block was

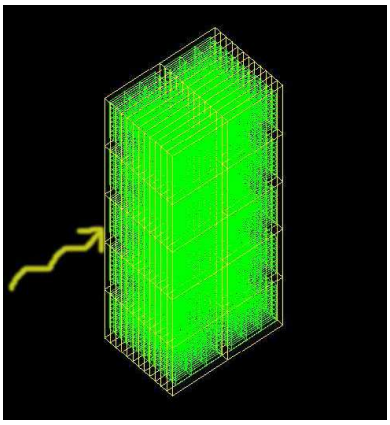

Figure 8.8: An illustration of a section of the system that was modeled. Green lines: outline of the LSO crystals, yellow lines: outline of the PSAPDs, and yellow photon for reference of direction of incident photons.

constructed of multiple modules so that the module being evaluated was surrounded. This construction gave a block size of 2.2 cm in the depth of interaction direction, 5.5 cm in the transaxial direction and 1.6 cm in the axial direction (Figure 8.8). By symmetry then, the module inside the block represented nearly all modules in the system (barring edge effects) and factors calculated for this module were applied to any subsequent modules so constructed.

Line of Response

The line of response for a particular event was determined during acquisition of the data by the two positioned interactions. Interactions were positioned in the manner described in Chapter 6. An energy filter of 24% around 511 keV, a coincidence time filter of 4ns, multiple position filters that required events produced an LOR that traversed the FOV and the composite interactions passed through the cluster filter

(see cluster construction in Chapter 7) were used as selection criteria for usable events. Events with only a pair of usable singles were used to determine useful events. Events with one, three or more usable singles were discarded. For each single in the pair, the theta and phi angles were calculated using the line formed by the LOR constructed from the pair, measured with respect to the face of the system closest to the center of the field of view (see Figure 8.7).

8.5.2 Depth of Interaction

Re-binning for System Space Reduction

With depth of interaction measurement capability, the number of lines of response can require overwhelming amounts of memory and computational resources. For instance, the number of independent LORs in the small animal imaging system investigated here is estimated in equation 8.4. In this estimation, each detector in each head can form a line of response with any other detector in another head (leading to the squared term).

$$\text{LORs} = \frac{3}{4} \cdot \frac{1}{2} \cdot (N_{\text{heads}}) \cdot (N_{\text{heads}} - 1) \cdot (N_{\text{mDOI}} \cdot N_{\text{mAX}} \cdot N_{\text{mTRAX}} \cdot N_{\text{crys}})^2 \qquad (8.4)$$

where N_{heads}, N_{mDOI}, N_{mAX}, N_{mTRAX}, and N_{crys} are the number of detector heads; number of modules in the DOI, axial and transaxial directions within each detector head; and the number of detector elements within a module, respectively. The $\frac{3}{4}$

factor comes from the fact that not all of the possible LORs traverse the imaging volume due to the overlap nature of the system configuration. The sub-elements of the small animal box-shaped system are shown in Table 8.1.

Table 8.1: The number of elements contributing to the number of possible LORs. From equation 8.4, the total number of possible LORs is 3 billion.

SubUnit Name	Quantity
Heads	4
DOI modules	2
Axial modules	62
Trans-axial modules	9
Crystals in a module	24

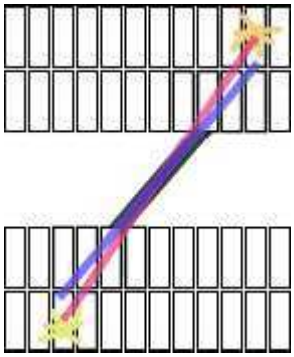

Figure 8.9: Illustration of depth of interaction re-binning. Red line: actual LOR reported by the detectors, purple line: binned LOR to crystal, black line: re-binned DOI LOR

From equation 8.4 and Table 8.1 there are nearly 3 billion LORs in this box-shaped PET system configuration under study. To reduce matrix sizes involved in normalization and reconstruction, LORs involving crystal layers beyond those closest to the center of the detector system can be re-binned to detectors nearest to the field of view (FOV). Figure 8.9 shows this concept: the red line represents the LOR from

the actual interaction position, the purple line shows the binned LOR, and the black line represents the LOR resulting from re-binning to the front crystals. Re-binning the data adds counts, or efficiency to the LOR to which the data has been binned. The per detector NC can then be written as:

$$NC_i = \frac{1}{\epsilon_i \cdot g_i + \sum_{k=1}^{n} \epsilon_k \cdot g_k \alpha_{ik}} \tag{8.5}$$

where $\alpha = 1$, 0 or -1. The α coefficient is 1 if the LOR is re-binned to LOR ij and 0 if there is no correlation between D_i and D_k. This method can also compensate for binning errors made during the LOR calculation for the acquired data by increasing ($\alpha = 1$) or decreasing ($\alpha =$ -1) the normalization coefficient. This method may also be useful during reconstruction if lines of response were grouped for decreasing computation time at the expense of detector resolution.

List-Mode Considerations

A reduction in system space does come at a cost. The precision loss and bias due to binning a LOR to another bin can manifest itself in the reconstructed image. Another consideration is the number of lines of response in the reduced space with respect to the number of counts that are gathered in the study. Most of the studies in this chapter acquired on the order of 100 million counts. If the number of counts were less than the number of lines of response in system space, the system matrix would

be larger than the list mode representation of the data. Ultimately, because the goal for the imaging system described in this study is to resolve image features of $1mm^3$ or less volume, data was reconstructed in this study using in list-mode (not binned to a sinogram) to retain as much accuracy as the system would afford. Reconstruction was performed using the ordered subset expectation maximization algorithm (OSEM).

8.5.3 Detector Element Efficiencies

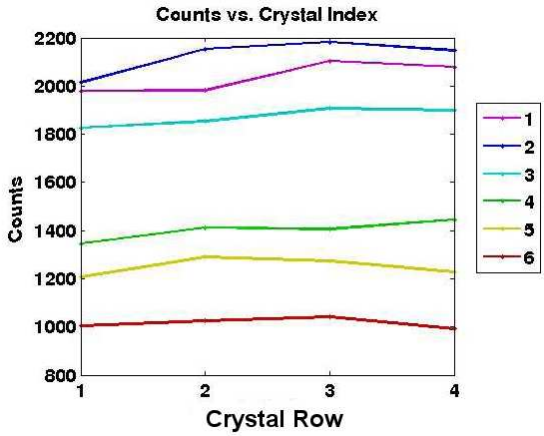

Figure 8.10: Sensitivity of each of the 12 crystals per PSAPD photodetector (12 in the front PSAPD, 12 in the back PSAPD) for a source irradiating each crystal edge-on from a distance of 10 cm. The lines numbered 1-6 in the legend signify the column of the crystal (three columns per array).

Detector element locations were defined as the crystal bin locations (the centers of the crystal). Each crystal array was assembled from 24 individual crystals, forming an 8 x 3 array, as pictured in Figure 3.5. Another symmetry that was exploited was the xz-plane mirror symmetry along the center of the module. This means that the

number of detector element efficiencies that must be measured is cut in half. Shown in Figure 8.10 are the block interference counts (proportional to the inverse of the efficiency factors), which were gathered using a distance of 10 cm from the source to the center of each crystal.

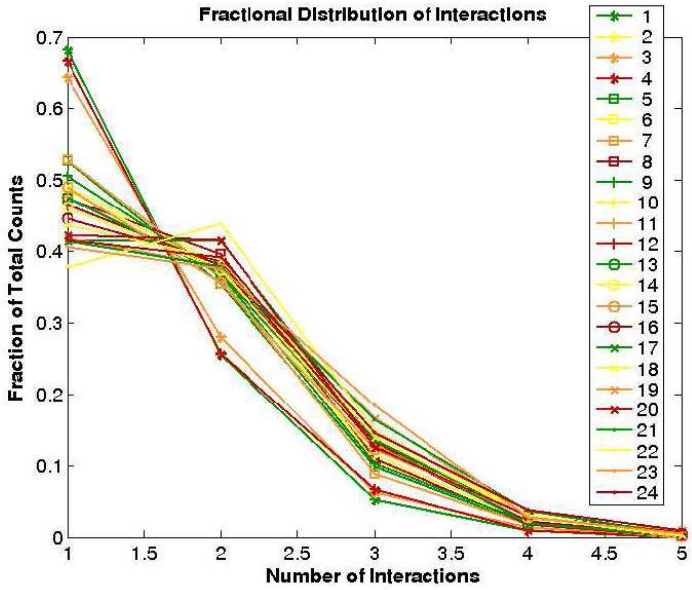

Figure 8.11: Fraction of the events having the indicated number of interactions for each crystal in the module. Crystals 1-4 were in the column nearest to the center of the system, 5-8 were the next columns in the depth of interaction direction, etc. Due to symmetry, only half of the crystals rows needed to be studied.

Having collected data for each crystal, the relationship between crystal location, and fractional number of interactions that went into producing those counts, can be seen in Figure 8.11. The general trend was that crystals near the front of the module had, in general, a lower number of interactions which produced a usable single. This is due to the penetrating nature of annihilation photons and their tendency to scatter into directions which were close to their initial trajectory. This causes a maximal

probability of deposition location offset from the front face of the detector system. On average, the fractional number of interactions agreed with data acquired throughout the detection space of a complete system.

Fits were made for the theta (radial), phi (axial) and module position (interference) dependence on sensitivity and their corresponding weights were generated to produce pre-corrected data for the list-mode reconstruction algorithm. Detector element position dependent results are shown in Figure 8.11.

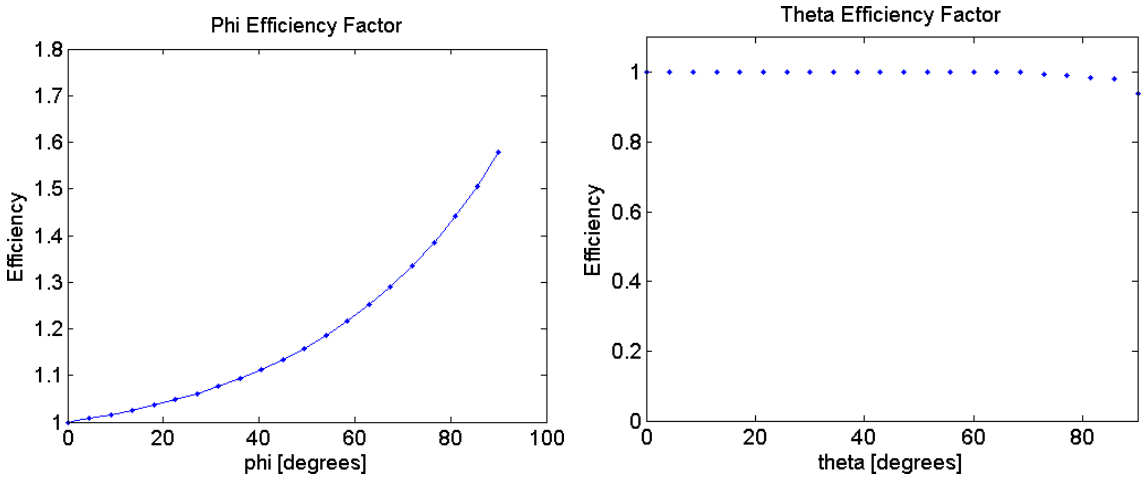

(a) phi dependent efficiency factor

(b) theta dependent efficiency factor

Figure 8.12: Theta (radial) and phi (axial) efficiency factors for the range of LOR angles possible in the system.

The phi efficiency factor was fit to a polynomial equation and was scaled by the sensitivty measurement shown in Figure 8.10. The theta efficiency factor was relatively flat compared to other factors, and was approximated to one for all theta.

In order to form the total normalization efficiency factor given in equation 8.3,

the axial and interference factors were calculated for each single in the coincidence pair separately. The factors were able to be calculated independently by using the resultant angle, formed by the line of response between the two coincident singles, with respect to the front face of the detector in which each single interacted. The individual interference factors were calculated by radiating each crystal in the module and applied using a look up table formed from the data displayed in Figure 8.11. The interference efficiency factors are also shown in Table 8.2.

Table 8.2: Interference efficiency factors for each crystal in a module.

Row	Col 1	Col 2	Col 3	Col 4	Col 5	Col 6
1	114.1	116.1	105.3	77.5	69.5	57.8
2	114.2	124.1	106.9	81.3	74.3	59.0
3	121.2	125.8	109.9	81.0	73.4	60.1
4	119.8	123.7	109.5	83.3	70.8	57.2
5	119.8	123.7	109.5	83.3	70.8	57.2
6	121.2	125.8	109.9	81.0	73.4	60.1
7	114.2	124.1	106.9	81.3	74.3	59.0
8	114.1	116.1	105.3	77.5	69.5	57.8

The axial factor was calculated using an equation, fit to the data shown in Figure 8.12, using the LOR-calculated incident angle for the input angle ϕ (in radians). The equation for the axial efficiency factor is shown in equation 8.6.

$$(g_{\mathrm{ax}})_i = e^{0.0188 \cdot \phi} + 16.35 \tag{8.6}$$

The distance factor was calculated knowing the position of the coincident singles and calculating the Cartesian distance between them (d), using an equation fit to the

data (see equation 8.7).

$$dd_{ij} = 8464 \cdot (d)^{-2.382} + 0.0235 \tag{8.7}$$

All factors were then multiplied to form the total normalization efficiency factor.

8.6 Validation Methods

8.6.1 Uniformity

NEMA Definition

Non-uniformity (U), as defined by the National Electrical Manufacturers Association (NEMA), is calculated in the following manner [11, 39, 47]:

$$U = \frac{N_{\max} - N_{\min}}{N_{\max} + N_{\min}} * 100\% \tag{8.8}$$

where $N_{\max}$ and $N_{\min}$ are the maximum and minimum pixel count value. The region in which this calculation is made breaks down non-uniformity into two categories: (1) integral non-uniformity (IU) which is measured over the whole of the 3D image and (2) differential non-uniformity (DU) which is measured in a region of interest (ROI) in one slice of the image. One can think of the results of these calculations as a measurement of (1) system-wide non-uniformity and (2) local non-unformity, respectively. Some authors prefer to perform smoothing on images before these calculations

are made, but the raw images were used for non-uniformity calculations in studies in this document.

8.6.2 Coefficient of Variation

Another test was used to determine the non-uniformity of reconstructed pixel values, the coefficient of variation (CV), which is a measure of the dispersion of counts in a region of interest, normalized by the mean of the counts (μ) [11, 39, 47]:

$$CV = \frac{\sigma}{\mu} \tag{8.9}$$

where the variation measure, σ, is the standard deviation. μ, σ and the counts themselves, in any region of interest, are all positive numbers. A strictly positive CV value insures that relative standard deviation (RSD) can then be defined as:

$$RSD = CV \cdot 100\% \tag{8.10}$$

RSD was reported for each study in the useful field of view as well as regions of interest.

8.6.3 Visual Inspection

As the eye is a sensitive instrument to features and patterns in images, qualitative comparison of normalized versus un-normalized data can also be made by looking

at 2D slices through the 3D volume. Un-normalized and normalized images reconstructed from data gathered the from same phantom in a warm or cold background was used for inspection.

8.7 Results: Reconstructed Images for a Box-Shaped Small Animal Imager

In order to understand the effects of applying the calculated component based normalization efficiency factors to the lines of response gathered by the detection system, events were reconstructed both using the normalization factor defined in previous sections, these images will be called normalized, as well as using an efficiency weight of one, where the images are labelled un-normalized.

To calculate non-uniformity and coefficient of variation validation measurements for both normalized and un-normalized images resulting from the small animal imager shown in Figure 8.5, two phantoms were used. The first phantom consisted of a uniformly filled cylinder, the size of a rat truncated in length, with a plane of spheres at the center axial plane. The cylinder was 6 cm long, 5 cm in diameter and filled with water and 400 μCi of activity. Because the center axial planes contain spheres with 10:1 sphere:background concentration ratio, planes containing any portion of spheres were removed from calculation (see Figure 8.13). Nearly 10 billion counts were acquired for this phantom, making it a high counting statistics data set.

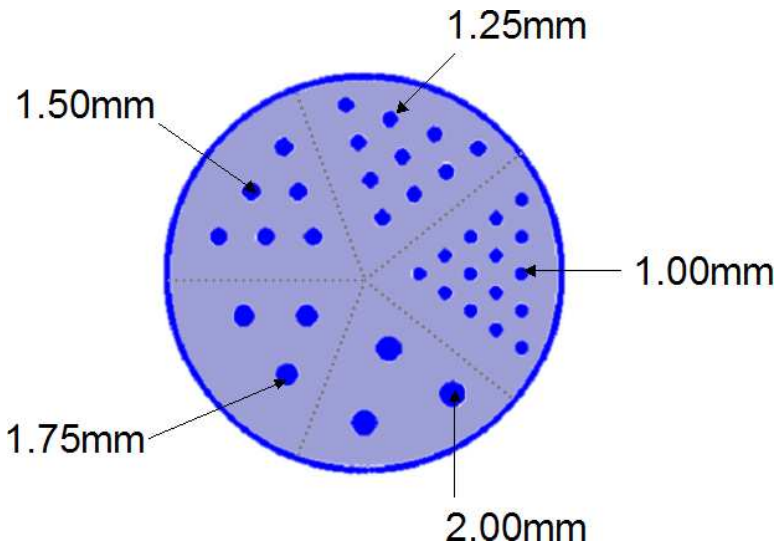

Figure 8.13: The high-count phantom used in the small animal imager uniformity studies. The dark blue dots show the cross section of the spheres through their centers, and the thick dark blue line on the circumference shows the extent of the cylinder. The light blue color represents the background where the activity density was 1/10th of the activity of the dark blue spheres. The light grey dotted lines are there simply to provide a visual border for different regions of sphere sizes, it does not represent any physical attribute of the phantom.

To observe the effect of counting statistics on the quantitative results, a lower counting statistics study was also studied. This lower counting statistics study utilized the 3:1 contrast ratio phantom, for which 50 million counts were gathered. This phantom consisted of a uniformly filled cylinder, the size of a large truncated rat, with a thin rod containing three times the activity at the center axial plane (see Figure 8.15). The cylinder was 6 cm long, 7 cm in diameter and filled with water and 400 μCi of activity.

The data gathered were filtered with a 24% energy window around 511 keV and a 4ns coincidence time window. Images were reconstructed with list-mode OSEM using

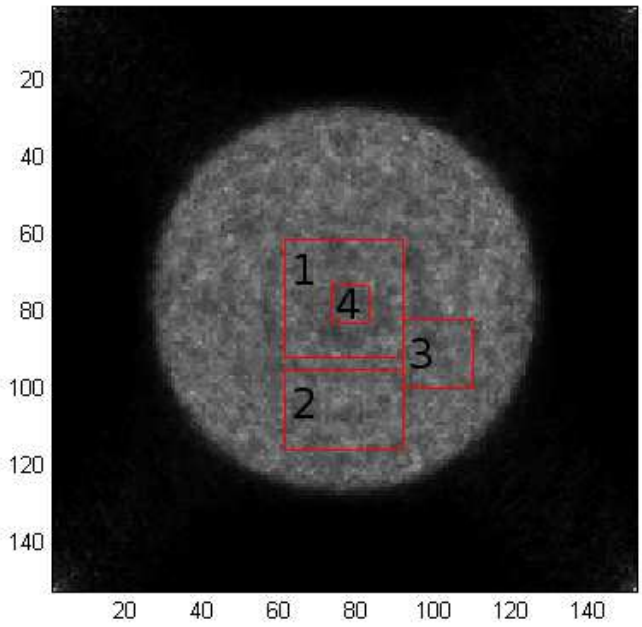

Figure 8.14: High count phantom: the four local ROIs used to evalute non-uniformity in normalized and un-normalized reconstructed images.

1 iteration and 22 subsets for the high count phantom, and 16 subsets for the low count phantom. Reconstructed images had 152 x 152 x 156 pixels, or were 0.5mm in size, which filled the entire interior volume of the box detector system. All image slices shown were made in the yz-plane.

Four local regions of interest were chosen to investigate non-uniformity and relative standard deviation of images in different subsections of the image. For the high count statistics phantom, these four regions, are depicted in Figure 8.14. A fifth region of interest, the field of view, was chosen to be a circle with radius 2.1 cm, positioned at the center of each axial slice. Error was estimated for uniformity and relative

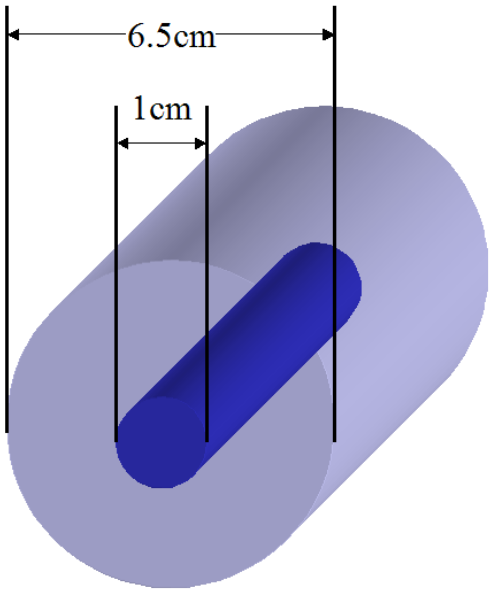

Figure 8.15: An illustration of the phantom used in the contrast-only studies. The dark blue inner rod was studied with 3 times the activity concentration with respect to the light blue surrounding cylinder.

standard deviation in each ROI using propagation of error and an equivalency of spatial ensemble variation with temporal (trial) ensemble variation.

The low count statistics phantom also had 4 local and one field of view regions of interest. Three of four local ROIs are depicted in Figure 8.16. The first local ROI was circular, with a radius of 4mm, positioned over the center of the image. This central local ROI was the region which coincided with the cross-section of the hot rod which went through the center of the warm cylinder. The fifth FOV ROI was chosen to be an annulus with an inner radius of 0.8 cm and an outer radius of 2.8 cm, located at the center of each axial slice.

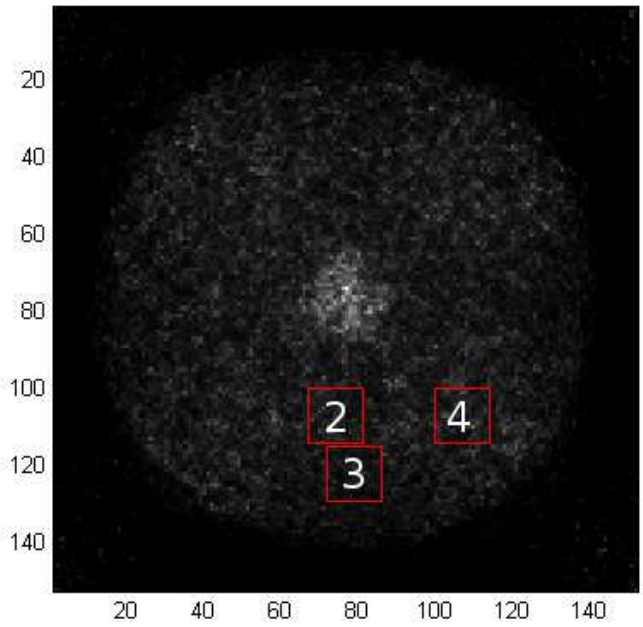

Figure 8.16: Low count phantom: shown are the three square-shaped local ROIs used to evalute non-uniformity in normalized and un-normalized reconstructed images. The fourth local ROI was a 0.8 cm diameter circle located at the center of the image, containing the high activity concentration region.

8.7.1 Uniformity

Local Regions of Interest - High Count Statistics

Non-uniformity results for both un-normalized and normalized (Figure 8.17) cases for local regions of interest are calculated for each axial slice through the phantom. The count-independence of this result will be investigated further in Section 8.7.1, after all of the non-unformity data for this phantom have been presented.

Non-uniformity for each plane decreased when using the normalization algorithm,

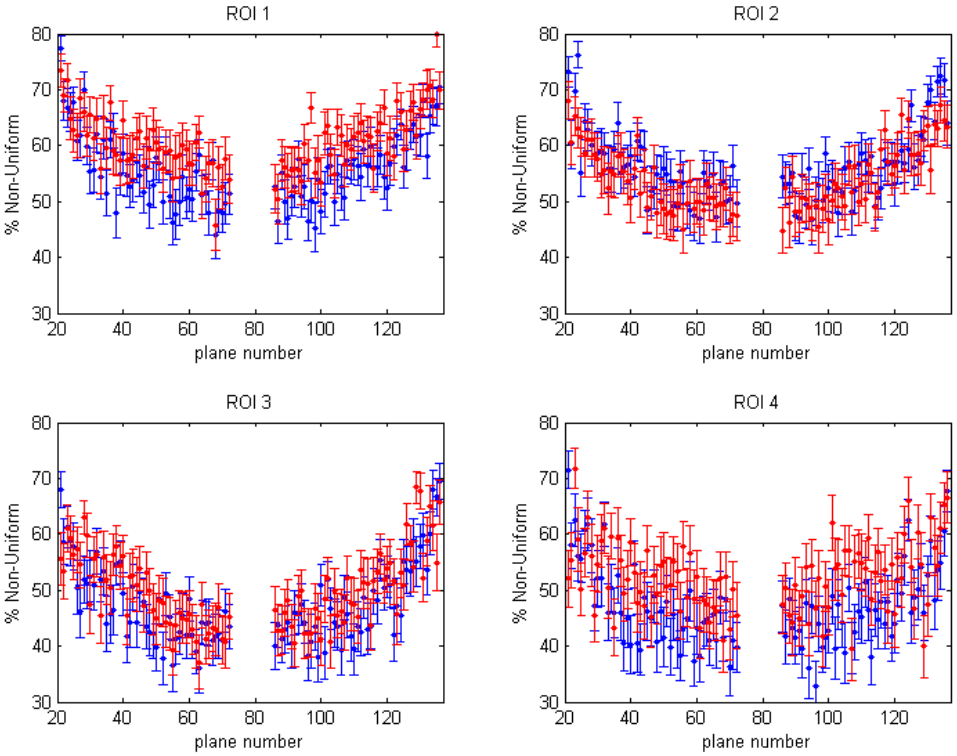

Figure 8.17: Normalized (blue) and un-normalized (red) reconstructed image non-uniformity measurements for the four regions of interest in the high-count statistics phantom depicted in Figure 8.14. Measurements for each plane are shown.

for most of the regions of interest. As a summary of the data, the mean of each region of interest, averaged over the planes, is shown in Table 8.3. The general trend of non-uniformity results versus plane number followed the sensitivity trend in image space, i.e., as the axial plane moved away from the center of the system, the sensitivity decreased and non-uniformity increased. This increase in variation is in part due to the amplification of noise from using a non-uniform density of lines of response prior image during reconstruction.

Non-uniformity in the axial direction in ROI 1 (Figure 8.14) was also investigated. Non-uniformity decreased from 88.1% to 84.3%, an improvement of 4.3%.

Field of View Region of Interest - High Count Statistics

Table 8.3: Mean and standard deviation (StDev) of the percent non-uniformity (U) for five regions of interest in the high-count statistics phantom (four local and the FOV), for both normalized (Norm) and un-normalized (UN) reconstructed images.

Value	Region 1	Region 2	Region 3	Region 4	FOV
U UN Mean [%]	60.7	54.1	50.0	52.4	63.1
U UN StDev [%]	5.4	5.7	6.7	6.2	5.8
U Norm Mean [%]	56.0	56.1	47.7	47.1	59.9
U Norm StDev [%]	6.3	6.3	7.2	7.2	6.7

Non-uniformity results for both un-normalized and normalized (Figure 8.18) cases for the field of view were calculated for each axial slice through the phantom.

Table 8.3 shows that non-uniformity decreased by 4.7% in the ROIs, and decreased by 4.9% in the FOV. Variation in non-uniformity over the planes increased by 12.5% in the ROIs, and 26.4% in the FOV, though the statistical maximum value of normalized non-uniformity is less than un-normalized non-uniformity.

To simulate a higher count image, three scenarios were investigated: summing (1) two, (2) five, (3) ten, (4) fifteen, (5) half of all, and (6) all of the planes together throughout the FOV. Then mean non-uniformity, averaging over summed planes, is shown in Figure 8.19. For comparison, data included in Table 8.3 for the single plane case are also shown.

It is clear from these data that counting statistics were playing a role in the

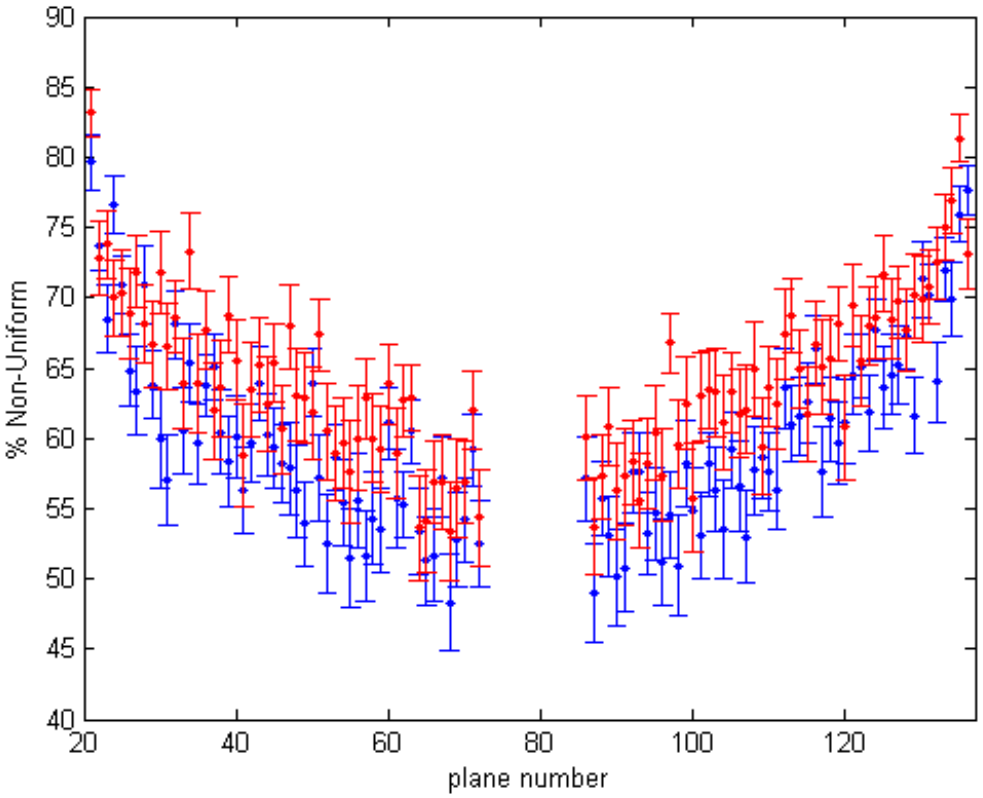

Figure 8.18: Normalized (blue) and un-normalized (red) reconstructed image non-uniformity measurements for the field of view in the high-count statistics phantom. Measurements for each plane are shown.

number reported by the non-uniformity calculation. Non-uniformity in the planes continued to decrease until half of the planes were used for a single image, when non-uniformity in each ROI was ∼0.5% different than summing all of the planes. This finding suggests that to reduce the effect of counts in the non-uniformity calculation, all other parameters being equal, gathering on the order of 15 times the number of counts produces an image with non-uniformity within 10% of the count-independent value. This comparison was also made for relative standard devation measurements,

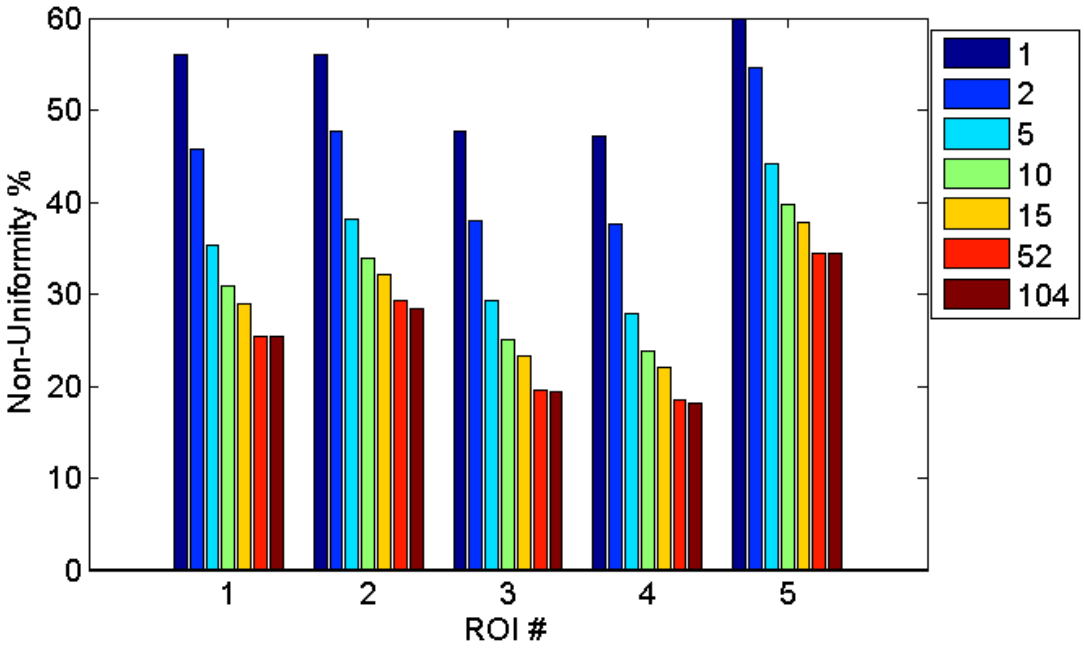

Figure 8.19: Normalized reconstructed image non-uniformity measurements for four regions of interest in the high-count statistics phantom depicted in Figure 8.16 and the FOV ROI, called ROI 5. Shown in the legend is the number of planes summed together to form the image on which calculations were performed.

and is reported with the relative standard deviation results.

Local Regions of Interest - Low Count Statistics

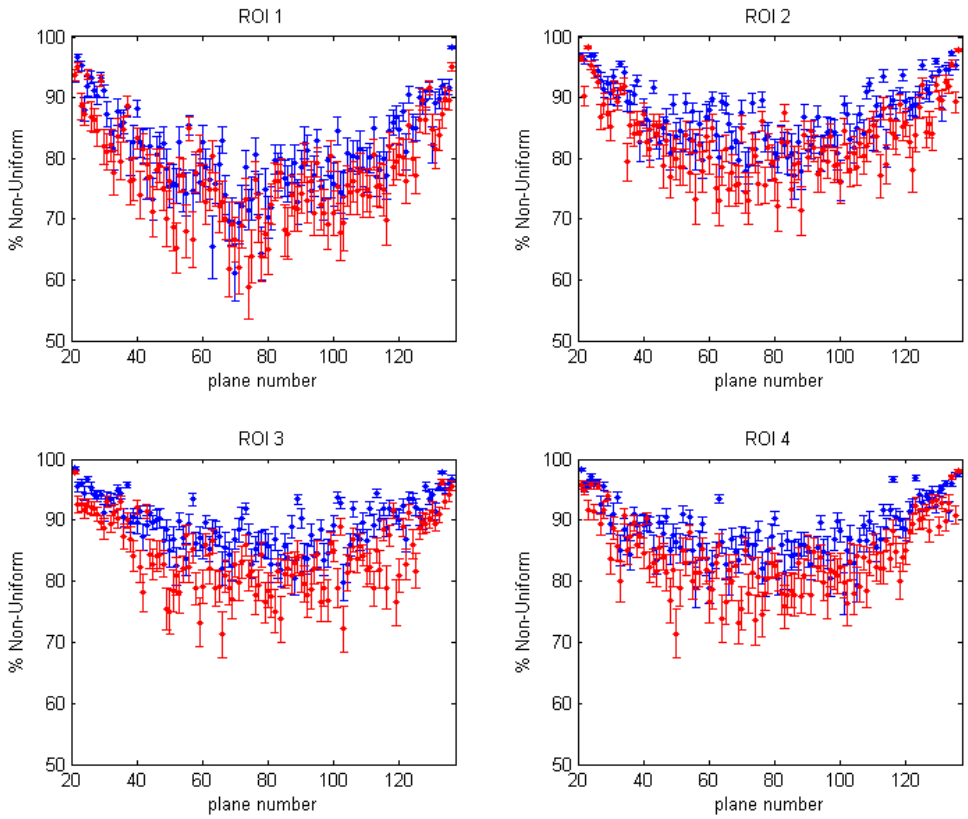

Figure 8.20: Normalized (blue) and un-normalized (red) reconstructed image non-uniformity measurements for the four regions of interest in the low-count statistics phantom depicted in Figure 8.16. Measurements from all planes are shown.

Looking now at the low count statistics results for both un-normalized and normalized reconstructed images, non-uniformity measurements are shown in Figure 8.20 for local regions of interest, for each axial slice through the phantom. Non-uniformity for each plane increased when using the normalization algorithm for most of the regions of interest. As a summary of the data, the mean of each region of interest, averaged

over the planes, is shown in Table 8.4. The general trend of the non-uniformity results versus plane number, as with the high count phantom, followed the sensitivity trend in image space. As mentioned in the previous section, there was an added component of noise from using a non-uniform density of lines of response efficiency image during reconstruction.

Field of View Region of Interest - Low Count Statistics

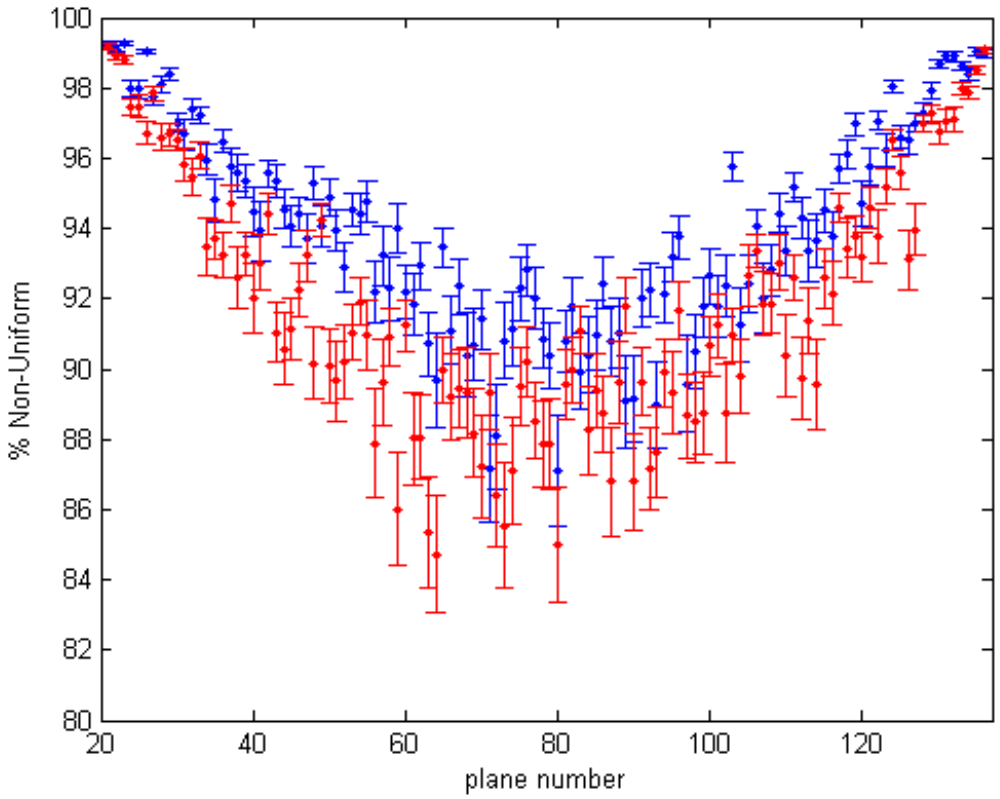

Figure 8.21: Normalized (blue) and un-normalized (red) reconstructed image non-uniformity measurements for the field of view of the low-count statistics phantom. Measurements for each plane are shown.

The general trend across the axial planes was similar to the results obtained in the high count statistics case - non-uniformity for both normalized and un-normalized images was the largest at the edges of the system and decreased uniformly towards the center of the system, where the density of lines of lines of response was the greatest.

Table 8.4: Mean and standard deviation (StDev) of the percent non-uniformity (U) for five regions of interest in the low-count statistics phantom (four local and the FOV), for both normalized (Norm) and un-normalized (UN) reconstructed images.

Value	Region 1	Region 2	Region 3	Region 4	FOV
U UN Mean [%]	77.1	83.1	84.1	84.0	91.9
U UN StDev [%]	7.6	5.8	5.8	5.7	3.6
U Norm Mean [%]	81.0	87.0	89.3	88.2	94.0
U Norm StDev [%]	7.1	5.5	4.2	4.7	3.0

Table 8.4 shows that non-uniformity increased by 5.2% in the ROIs, and increased by 2.3% in the FOV. Variation in non-uniformity over the planes increased by 13.7% in the ROIs, and 16.7% in the FOV.

The result in the low statistics scenario suggested that the normalization algorithm increased rather than decreased non-uniformity in reconstructed images. To the eye, however, the images looked more uniform in the normalized case versus un-normalized, barring high frequency variations in pixel values due to low counts. The plane at the axial center of the system for both un-normalized (Figure 8.22a) and normalized (Figure 8.22b) reconstructions are shown for illustration.

To simulate many more counts, all image planes were summed together and the same equations were applied to the single resultant plane. Table 8.5 shows the results

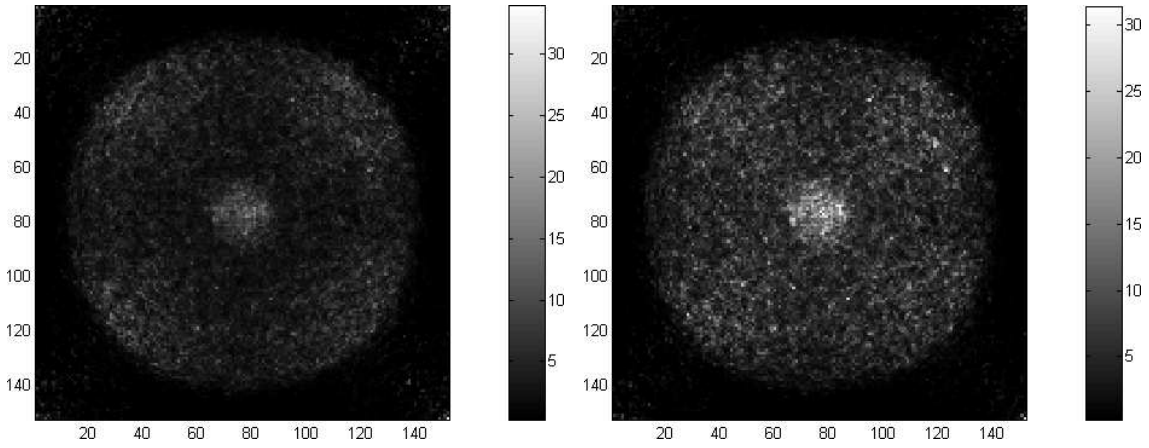

(a) Un-normalized (b) Normalized

Figure 8.22: Reconstruction of center axial plane for un-normalized and normalized data gathered using the low-count statistics phantom.

of the measurements for each region.

Table 8.5: Non-uniformity for five regions of interest in the low-count statistics phantom (four local and the FOV), for both normalized (Norm) and un-normalized (UN) plane-wise summed reconstructed images.

Value	Region 1	Region 2	Region 3	Region 4	FOV
U UN Mean [%]	28.5	28.9	26.1	29.2	40.7
U Norm Mean [%]	23.3	23.4	30.1	25.7	35.9

For the plane summed images, non-unformity decreased by 9.1% in the ROIs and by 11.8% in the FOV. The observable differences in Figures 8.22a and 8.22b, coupled with the calculations for the plane-wise summed images, show a reversal of trends when more counts were added to the pixels (i.e. non-uniformity decreased in normalized reconstructed images).

8.7.2 Coefficient of Variation

The same regions of interest, as shown in Figure 8.14 were used to compute relative standard deviation (equation 8.10).

Local Regions of Interest - High Count Statistics

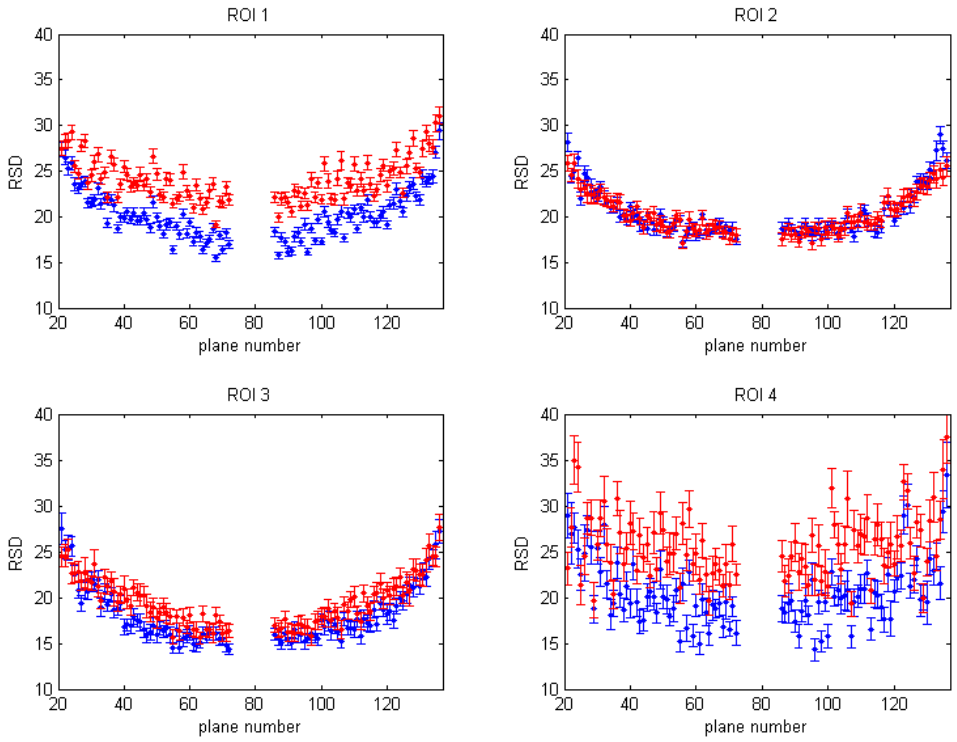

Figure 8.23: Normalized (blue) and un-normalized (red) reconstructed image relative standard deviation measurements for the local regions of interest in the high-count statistics phantom. Measurements from all planes are shown.

Relative standard deviation results for both un-normalized and normalized (Figure 8.23) cases for local regions of interest were calculated for each axial slice through the

phantom. The blue markers represent the standard non-uniformity measure and red markers represent those accounting for counting statistics. RSD count-independence result will be investigated further in Section 8.7.2, after all of relative standard deviation data for this phantom have been presented.

Relative standard deviation, as with non-uniformity, for each plane decreased when using the normalization algorithm for ROIs 1-3. No clear trend was seen in ROI 4, as the planes were traversed. As a summary of the data, the mean of each region of interest, averaged over the planes, is shown in Table 8.6. The general trend of RSD results versus plane number followed the sensitivity trend in image space as well, i.e., as the axial plane moved away from the center of the system, sensitivity decreased and RSD increased. This increase in variation, again, is in part due to the amplification of noise from using a non-uniform density of lines of response sensitivity image during reconstruction.

Field of View Region of Interest - High Count Statistics

Table 8.6: Mean and standard deviation (StDev) of relative standard deviation for five regions of interest (four local and the FOV), for both normalized (Norm) and un-normalized (UN) reconstructed images.

Value	Region 1	Region 2	Region 3	Region 4	FOV
RSD UN Mean [%]	22.8	20.2	19.4	23.2	21.5
RSD UN StDev [%]	2.2	2.0	2.4	3.4	2.1
RSD Norm Mean [%]	20.2	20.5	18.1	20.6	19.4
RSD Norm StDev [%]	2.7	2.6	3.1	3.6	2.7

Relative standard deviation results for both un-normalized and normalized (Fig-

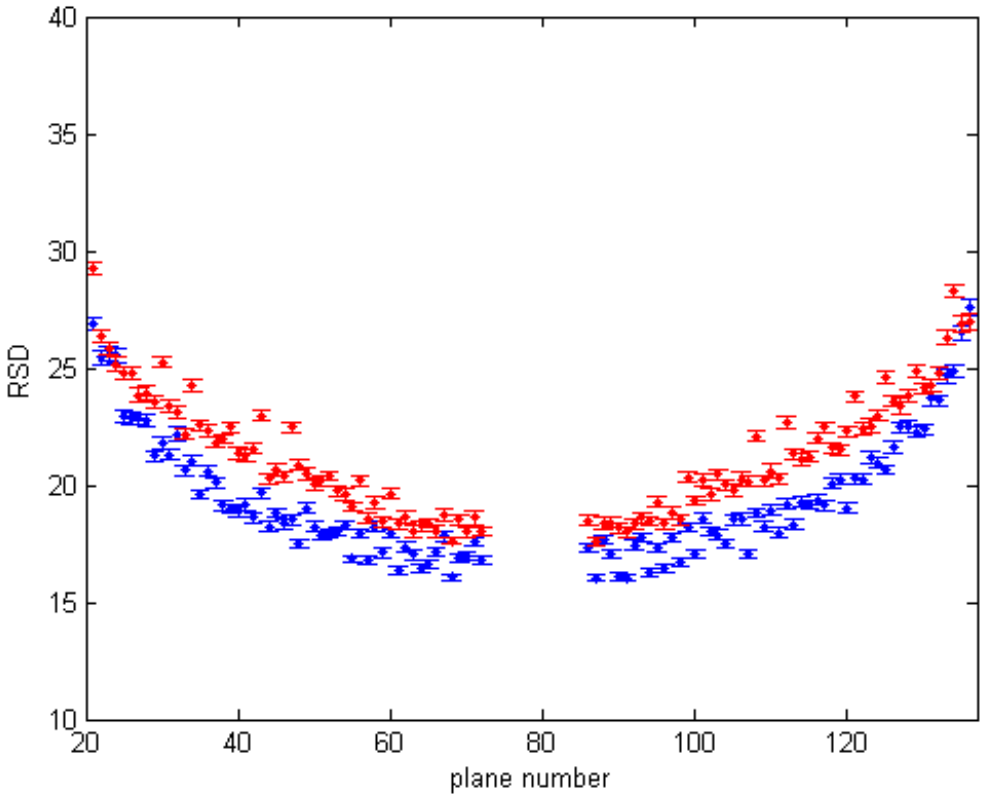

Figure 8.24: Normalized (blue) and un-normalized (red) reconstructed image relative standard deviation measurements for the field of view in the high-count statistics phantom. Measurements from all planes are shown.

ure 8.24) cases were calculated for the field of view for each axial slice through the phantom. Table 8.3 shows that relative standard deviation decreased by 7.4% in the ROIs, and decreased by 9.8% in the FOV. Variation in RSD over the planes increased by 16.7% in the ROIs, and 22.2% in the FOV, though the statistical max value of the normalized RSD is less than un-normalized RSD.

To simulate a higher count image, three scenarios were investigated: summing (1) two, (2) five, (3) ten, (4) fifteen, (5) half of all, and (6) all of the planes together

throughout the FOV. Then the mean relative standard deviation, averaging over the new summed planes in each case, is shown in Figure 8.25. For comparison, the data included in Table 8.6 for the single plane case is also shown.

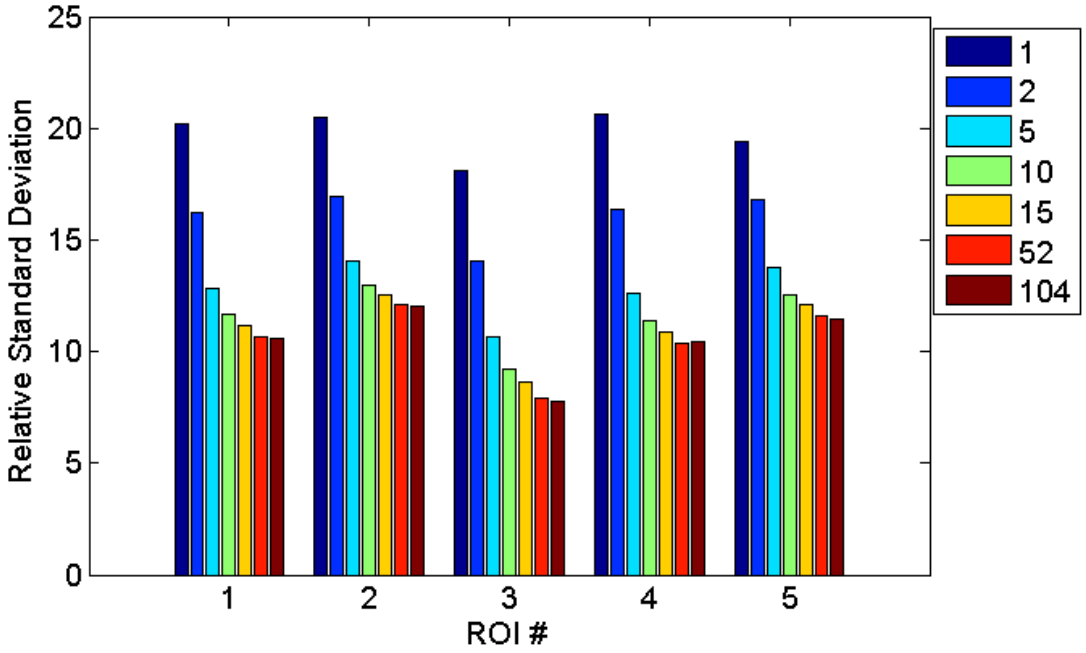

Figure 8.25: Normalized reconstructed image relative standard deviation measurements for the four regions of interest in the low-count statistics phantom depicted in Figure 8.16 and the FOV ROI, called ROI 5. Shown in the legend is the number of planes summed together to form the image on which the calculations were performed.

It is clear from these data that counting statistics are playing a role in the number reported by the relative standard deviation calculation. The RSD in the planes continue to decrease until half of the planes are used for a single image, when RSD in each ROI is ∼1% different than summing all of the planes. This seems to suggest that to reduce the effect of counts in relative standard deviation calculation, all other

parameters being equal, gathering on the order of 10 times the number of counts produce an image with RSD within 10% of the count independent value.

Local Regions of Interest - Low Count Statistics

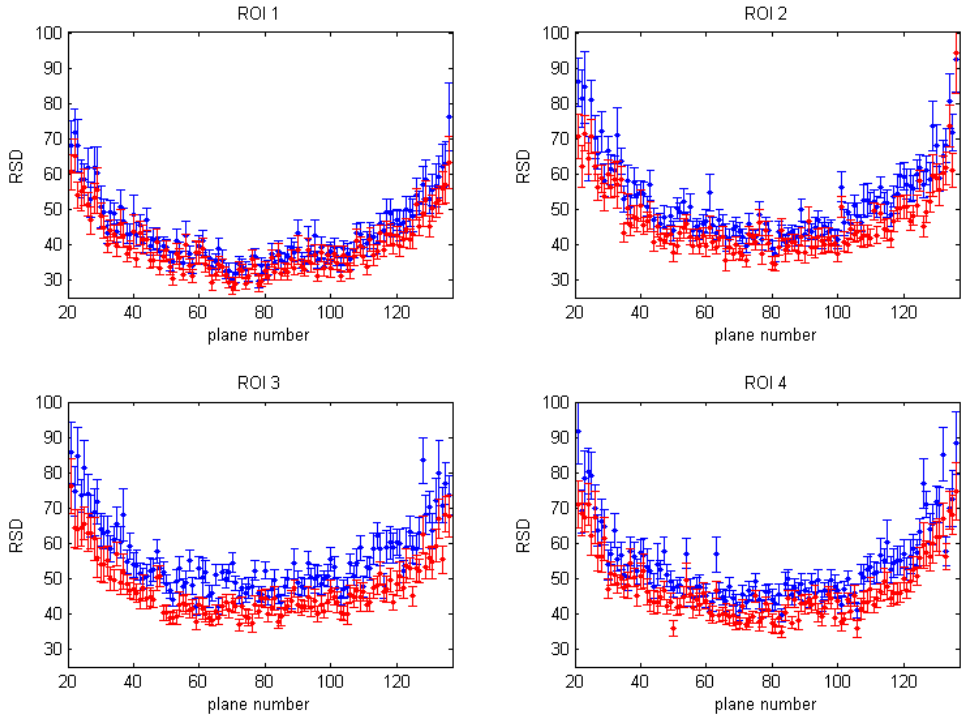

Figure 8.26: Normalized (blue) and un-normalized (red) reconstructed image relative standard deviation measurements for the location regions of interest in the low-count statistics phantom. Measurements from all planes are shown.

The low count statistics results for both un-normalized and normalized (Figure 8.26) cases are shown for local regions of interest, for each axial slice through the phantom. Relative standard deviation for each plane increased when using the normalization algorithm, for most of the regions of interest. As a summary of the data,

the mean of each region of interest, averaged over the planes, is shown in Table 8.4. The general trend of RSD results versus plane number, as with the high count phantom, follows the sensitivity trend in image space.

Field of View Region of Interest - Low Count Statistics

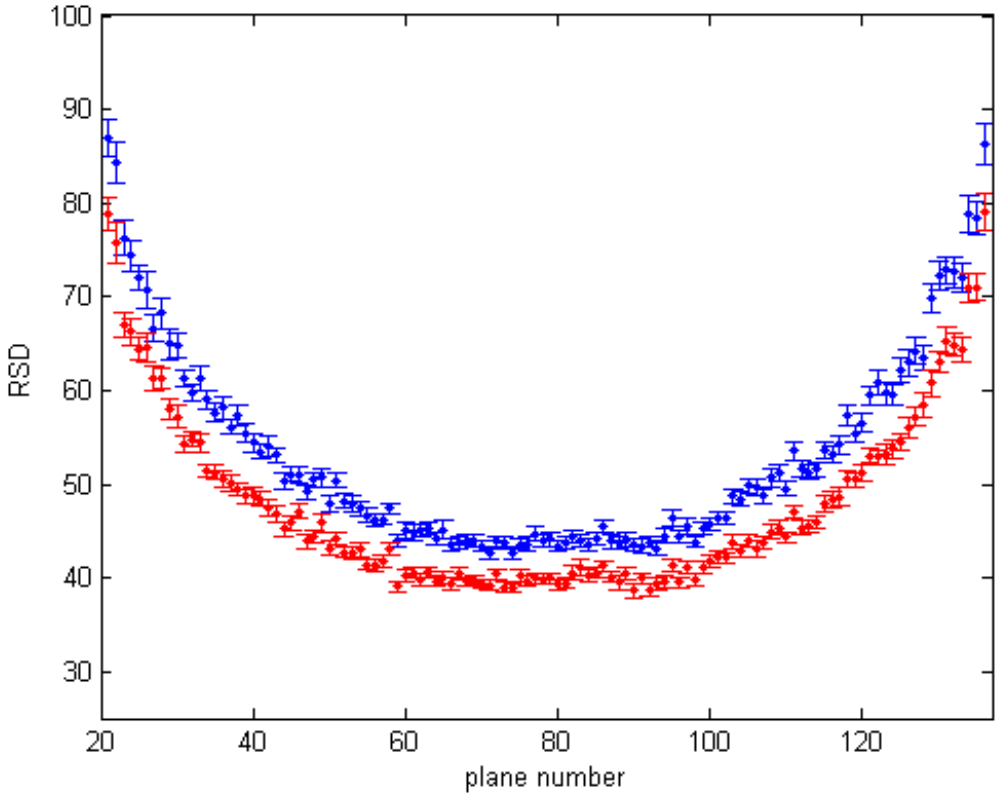

Figure 8.27: Normalized (blue) and un-normalized (red) reconstructed image relative standard deviation measurements for the field of view of the low-count statistics phantom. Measurements from all planes are shown.

Table 8.7 shows that relative standard deviation increased by 5.2% in the ROIs, and increased by 2.3% in the FOV. variation in RSD over the planes increased by

Table 8.7: Mean and standard deviation (StDev) of relative standard deviation for five regions of interest (four local and the FOV), for both normalized (Norm) and un-normalized (UN) reconstructed images.

Value	Region 1	Region 2	Region 3	Region 4	FOV
RSD UN Mean [%]	39.4	46.8	47.1	47.0	47.8
RSD UN StDev [%]	8.0	9.6	8.0	8.9	9.6
RSD Norm Mean [%]	43.3	52.6	55.7	53.6	55.3
RSD Norm StDev [%]	9.6	11.2	10.0	10.7	10.8

13.7% in the ROIs, and 16.7% in the FOV.

The result in the low statistics scenario for relative standard deviation calculation also suggested that the normalization algorithm actually increased RSD in reconstructed images. Being that uniformity in the images looked better for normalized images versus un-normalized, a similar high-count simulation study was performed.

Table 8.8: Relative standard deviation for five regions of interest in the low-count statistics phantom (four local and the FOV), for both normalized (Norm) and un-normalized (UN) plane-wise summed reconstructed images.

Value	Region 1	Region 2	Region 3	Region 4	FOV
RSD UN Mean [%]	12.0	12.2	9.7	9.9	11.5
RSD Norm Mean [%]	9.1	10.3	10.0	9.0	9.9

To simulate many more counts, all of the image planes were summed together and the same equations were applied to the single resultant plane. Table 8.8 shows the results for the corrected and standard RSD calculations. These data now show what we would expect from looking at Figure 8.22, that the coefficient of variation decreased using the developed normalization method by 12.3% in the ROIs and 13.9% in the FOV.

8.7.3 Visual Inspection - Reconstructed Images

To visualize the effect of the normalization algorithm, a three dimensional resolution phantom was used, consisting of three axial planes of sources. Each plane consists of spheres separated by twice their diameter. The diameter of the spheres for each quadrant are 1, 1.25, 1.5, 1.75 mm. The total activity in the phantom was 10 μCi, distributed between the three planes of spheres (in a cold background), with constant concentration for all spheres. The list-mode OS-EM algorithm was used with 1 iteration and 16 subsets. For the sphere phantom images, a 1 mm voxel size was chosen.

Un-normalized and normalized reconstructed images for the three planes with sources are shown in Figures 8.28-8.30. In the raw reconstructed images, the effect of the proximal detectors in the corners of the system produced hot reconstructed spheres as well as inter-sphere background. The inter-crystal gaps in the system contributed to the depression of the uncorrected spheres in the center of the system. After application of the normalization weights to the events, a more uniform and streak-free image was produced.

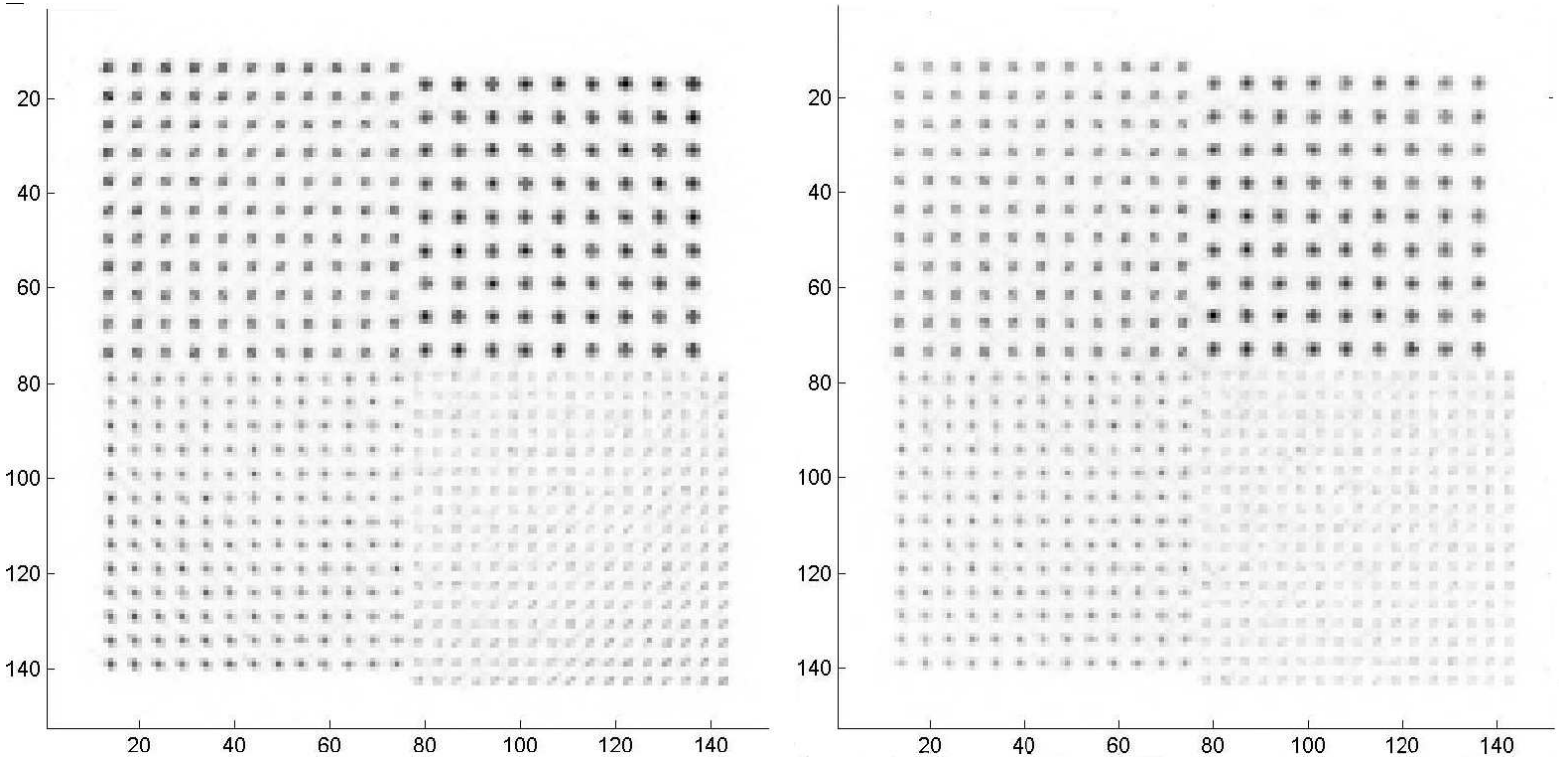

(a) UNorm: center

(b) Norm: center

Figure 8.28: Left: raw, right: normalized reconstructed images.

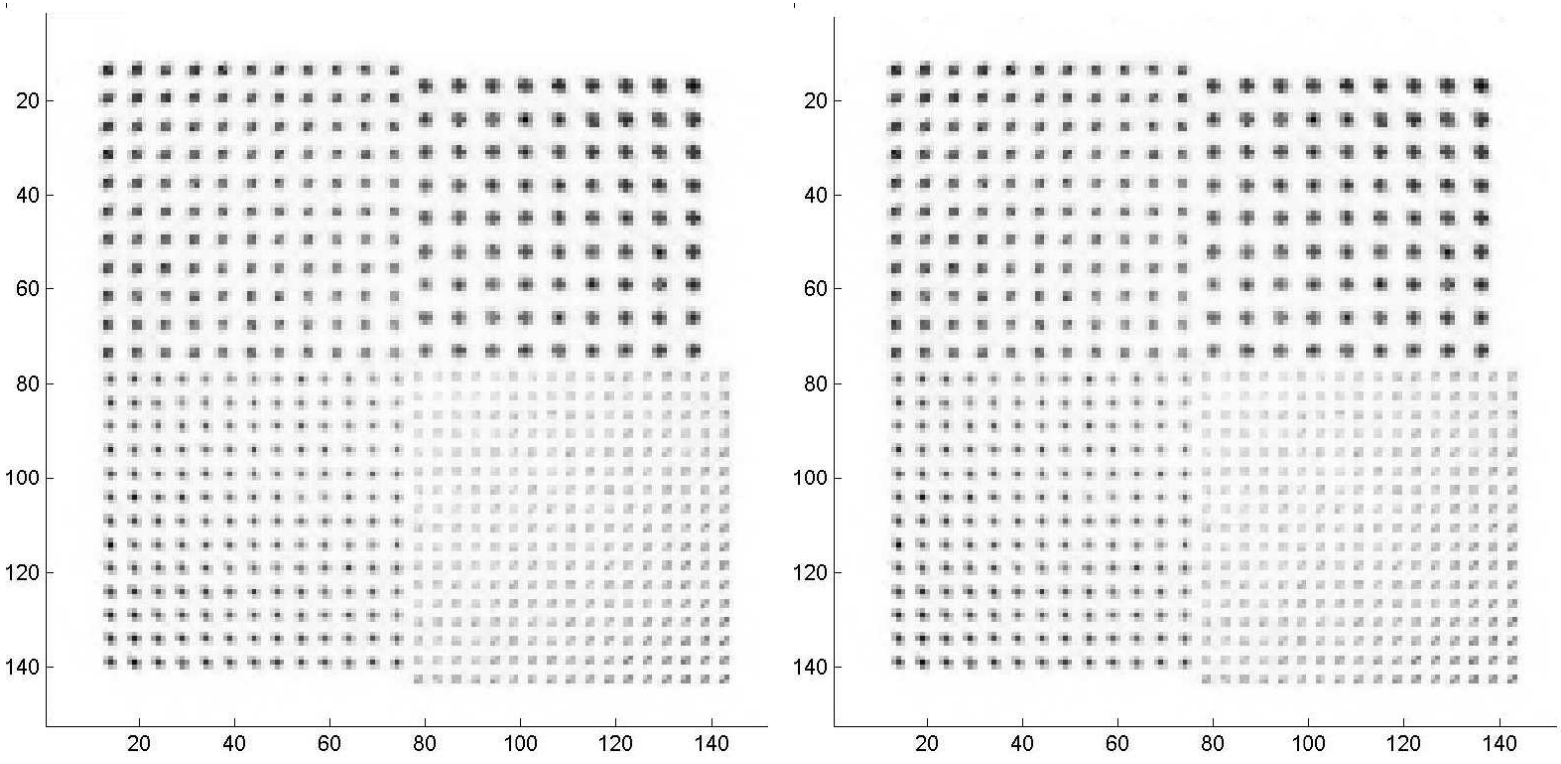

(a) UNorm: 1.5 cm

(b) Norm: 1.5 cm

Figure 8.29: Left: raw, right: normalized reconstructed images.

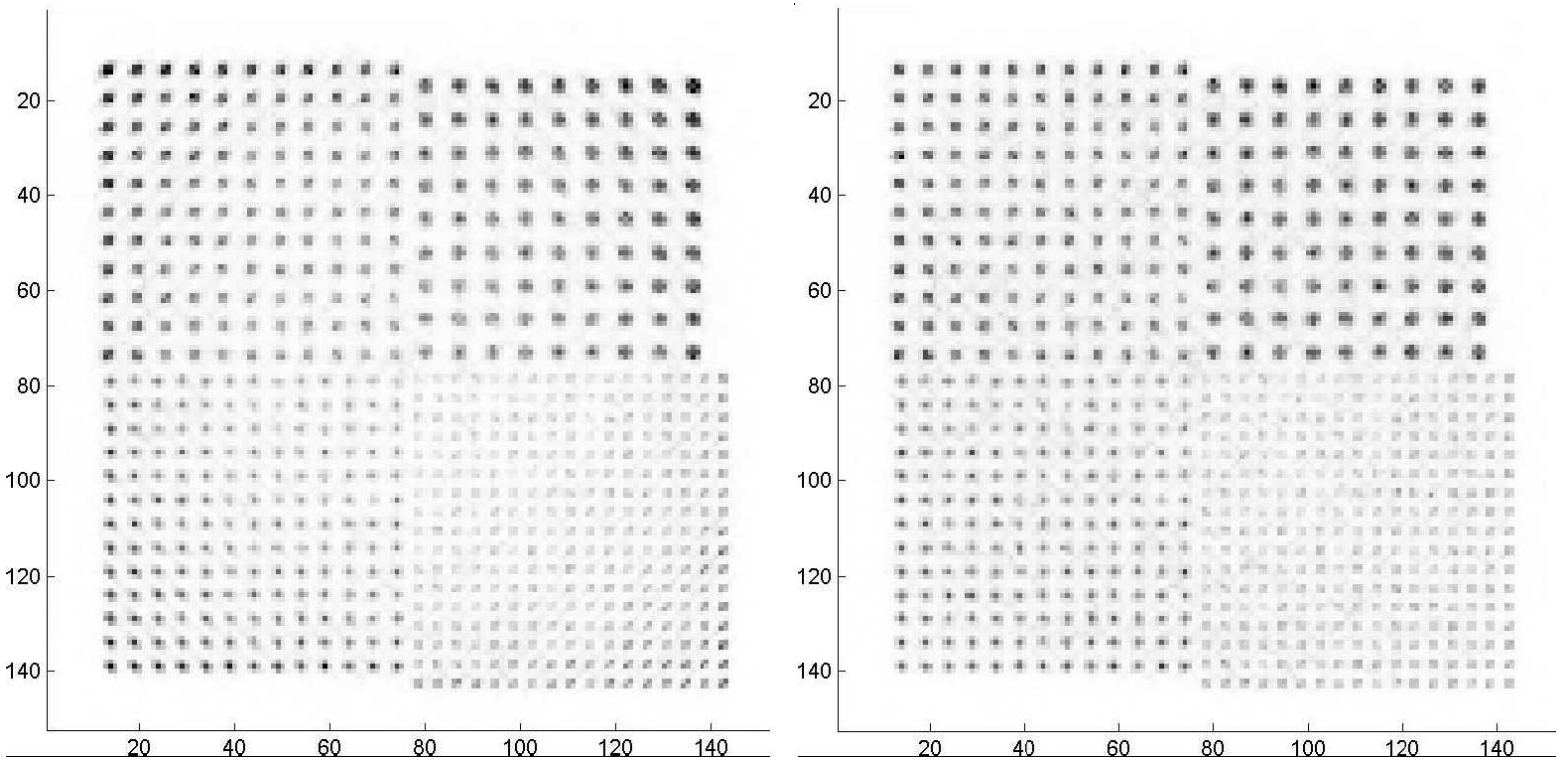

(a) UNorm: 3.0 cm

(b) Norm: 3.0 cm

Figure 8.30: Left: raw, right: normalized reconstructed images.

8.8 Results: Reconstructed Images for a Dual-Panel Breast Imager

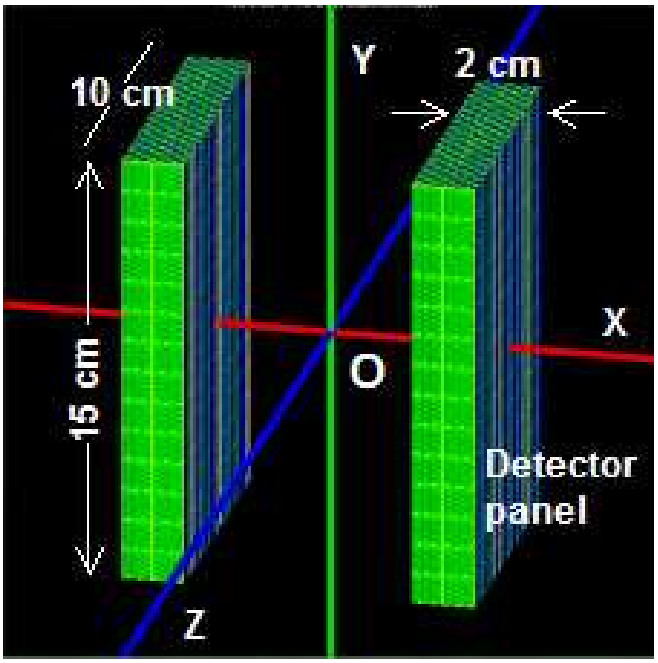

Figure 8.31: An illustration of the dual panel breast imaging system.

The normalization algorithm's ability to correct data acquired from a similar system in a different configuration was evaluted. Images were reconstructed with and without normalization, acquired using a dedicated breast imager with two flat panel detection heads. The system panels were constructed of modules identical to the small animal imaging system, but the most noteworthy differences in system space was the slightly larger field of view (15 cm x 10 cm x 4 cm for the breast imager, versus 8 cm x 8 cm x 8 cm for the small animal imager), and the increased sampling

non-uniformities in the inter-panel dimension created by the removal of transaxial detectors, and subsequent lowering of 4π coverage. The removal of detectors was to afford versatility in imaging with different inter-panel distances and to create a configuration intended to image axial nodes as well as breast tissue.

The panels used for this study were 10 cm x 15 cm in the transaxial (y) and axial (z) dimensions respectively, 2 cm deep in the depth of interaction (x) direction (see Figure 8.31). The way in which the modules were layered to construct the system is described in Table 8.9.

Table 8.9: Quantitation of the number of elements contributing to the number of possible LORs in the dual-panel dedicated breast imaging system.

SubUnit Name	Quantity
Heads	2
DOI modules (x)	2
Axial modules (z)	77
Trans-axial modules (y)	14
Crystals in a module	24

Data were acquired when the panels were seperated by 4 cm in the x-direction, gathering 96 million counts over 23 minutes, with a total activity in the FOV being 200 uCi. The data gathered were filtered, as with the small animal imaging system, with a 24% energy window around 511 keV and a 4ns coincidence time window. Images were reconstructed with the same list-mode OSEM algorithm as the small animal imaging system data, using 1 iteration and 14 subsets. Reconstructed images had 80 x 300 x 200 pixels, or were 0.5mm in size, which filled the entirety of the

volume between the two panels. All image slices shown were made in the yz-plane.

8.8.1 Uniformity

Four local regions of interest were chosen to investigate the uniformity of images in portions of the image (see Figure 8.32). A fifth region of interest, the field of view, was chosen to be a 8 cm x 13 cm rectangle, centered at the center of each axial slice.

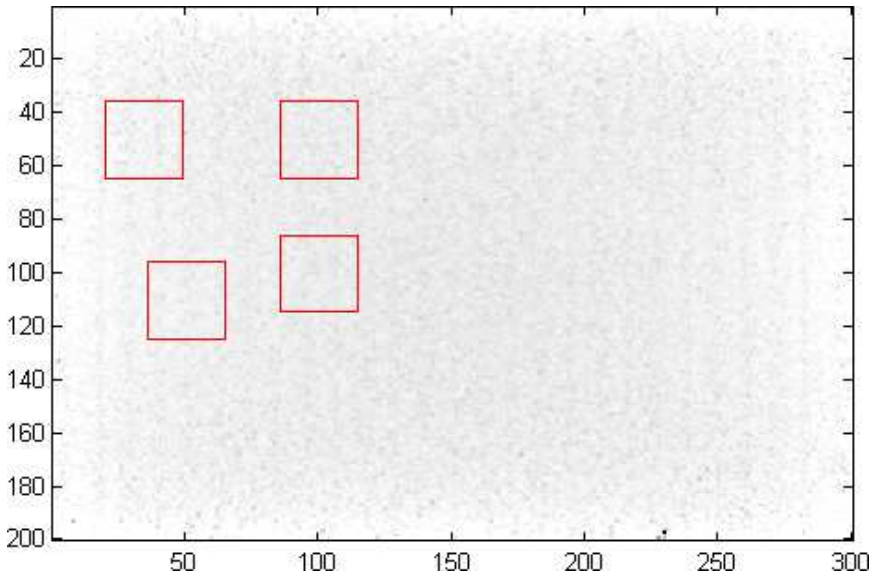

Figure 8.32: Four local ROIs used to evalute non-uniformity in normalized and un-normalized reconstructed images in the dedicated breast imager.

Local Regions of Interest

Non-uniformity results for both un-normalized and normalized (Figure 8.33) cases for local regions of interest were calculated for each axial slice through the phantom. Non-uniformity for each plane decreased when using the normalization algorithm, for

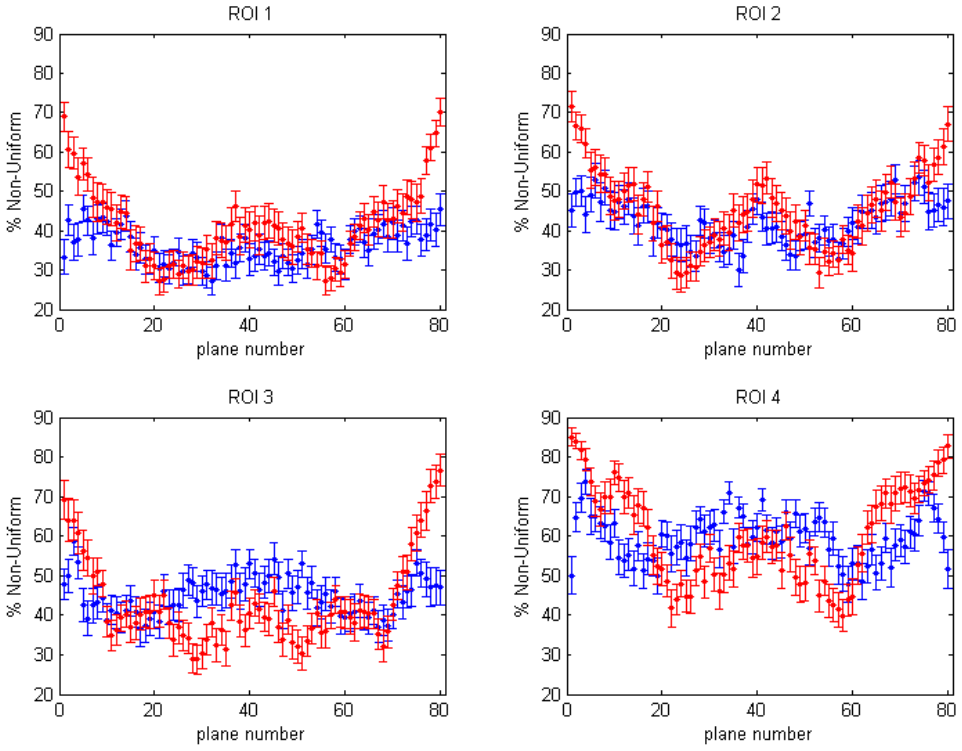

Figure 8.33: Normalized (blue) and un-normalized (red) reconstructed image non-uniformity measurements for the four 30 x 30 regions of interest in the dedicated breast imaging system depicted in Figure 8.32. Measurements from all planes are shown.

most of the regions of interest. As a summary of the data, the mean of each region of interest, averaged over the planes, is shown in Table 8.10. The general trend of non-uniformity results versus plane number had a different shape than the one seen for the small animal imager. This trend will be discussed in the next section.

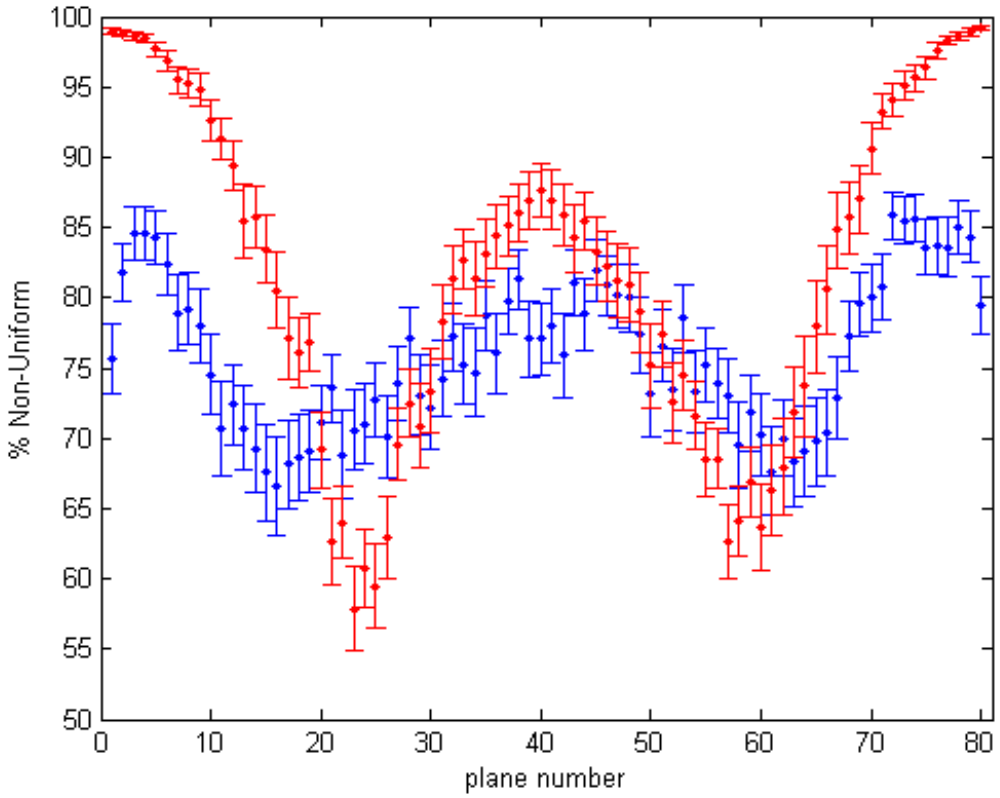

Figure 8.34: Normalized (blue) and un-normalized (red) reconstructed image non-uniformity measurements for the center 8 cm x 13 cm field of view of the dedicated breast imaging system. Measurements from all planes are shown.

Field of View Region of Interest

Non-uniformity results for both un-normalized and normalized (Figure 8.34) cases for the field of view were calculated for each axial slice through the phantom. The normalization algorithm decreased non-uniformity across most regions of interest, particularly at the center of the FOV and the whole FOV (see Table 8.10). The most marked improvement was in the variation across the axial planes in all regions

Table 8.10: Mean and standard deviation (StDev) of the percent non-uniformity (U) for five regions of interest (four local and the FOV), for both normalized (Norm) and un-normalized (UN) reconstructed images for the dedicated breast imager.

Value	Region 1	Region 2	Region 3	Region 4	FOV
U UN Mean [%]	41.1	45.3	43.1	60.2	81.8
U UN StDev [%]	9.7	9.8	11.0	12.0	11.7
U Norm Mean [%]	36.2	42.4	44.9	59.5	76.0
U Norm StDev [%]	4.5	5.5	4.7	5.8	5.3

of interest. The normalization algorithm decreased non-uniformity by 3.5% in the ROIs, and by 7.1% in the FOV. Variation in non-uniformity across planes decreased by 51.8% in the ROIs, and 54.7% in the FOV, using the normalization algorithm.

The trend in the local and FOV ROIs for un-normalized data was that the variation in counts went through a local maximum at the center of the system. This trend was likely due to the same phenomenon as the depression of counts in the center of the reconstruted images for the small animal system: the orientation of the detectors produces a gap of about 25% of the cross-section for direct plane LORs; i.e. the LORs, if in vector form, which have only an x-component (see Figure 8.7). The only lines of response traversing this region of the image are longer than the direct plane LORs. These oblique lines of response in the un-normalized case do not have a sensitivity-compensated weight applied to them. Therefore, although many lines are traversing the region, without normalization, the counts are spread out over more pixels, creating a dip.

8.8.2 Coefficient of Variation

The same regions of interest, as shown in Figure 8.32 are used here to compute relative standard deviation (equation 8.10).

Local Regions of Interest

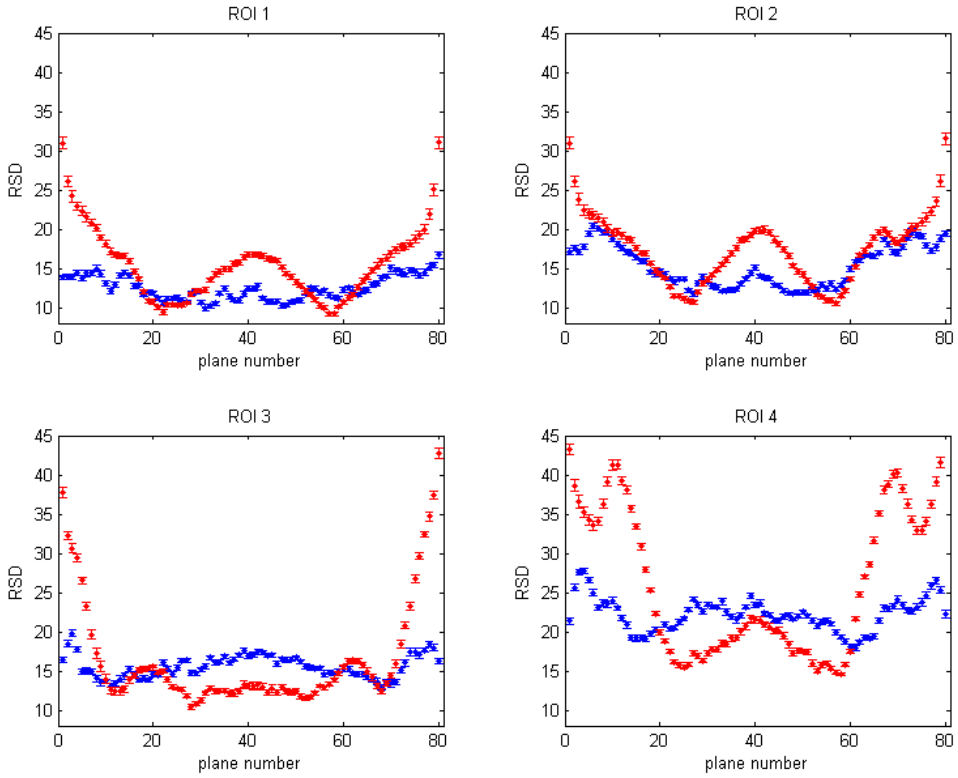

Figure 8.35: Normalized (blue) and un-normalized (red) reconstructed image relative standard deviation measurements for the four 30 x 30 regions of interest in the dedicated breast imaging system depicted in Figure 8.32. Measurements from all planes are shown.

Relative standard deviation results for both un-normalized and normalized (Figure

8.35) cases for local regions of interest were calculated for each axial slice through the phantom. Relative standard deviation for each plane decreased when using the normalization algorithm, for most of the regions of interest. As a summary of the data, the mean of each region of interest, averaged over the planes, is shown in Table 8.11. The general trend of non-uniformity results versus plane number had a different shape than the one seen for the small animal imager, and similar to non-uniformity calculations. This trend was discussed in Section 8.8.1.

Field of View Region of Interest

Table 8.11: Mean and standard deviation (StDev) of relative standard deviation (RSD) for five regions of interest (four local and the FOV), for both normalized (Norm) and un-normalized (UN) reconstructed images for the dedicated breast imager.

Value	Region 1	Region 2	Region 3	Region 4	FOV
RSD UN Mean [%]	15.5	17.4	16.6	26.2	40.9
RSD UN StDev [%]	4.6	4.4	7.1	9.6	19.9
RSD Norm Mean [%]	12.5	15.3	15.6	22.2	24.0
RSD Norm StDev [%]	1.5	2.6	1.5	2.1	2.2

Relative standard deviation results for both un-normalized and normalized (Figure 8.36) cases for the field of view were calculated for each axial slice through the phantom. The normalization algorithm decreased relative standard deviation across most regions of interest, particularly at the center of the FOV and the whole FOV (see Table 8.11). The normalization algorithm decreased relative standard deviation by 13.3% in the ROIs, and decreased RSD by 41.3% in the FOV. Variation in RSD

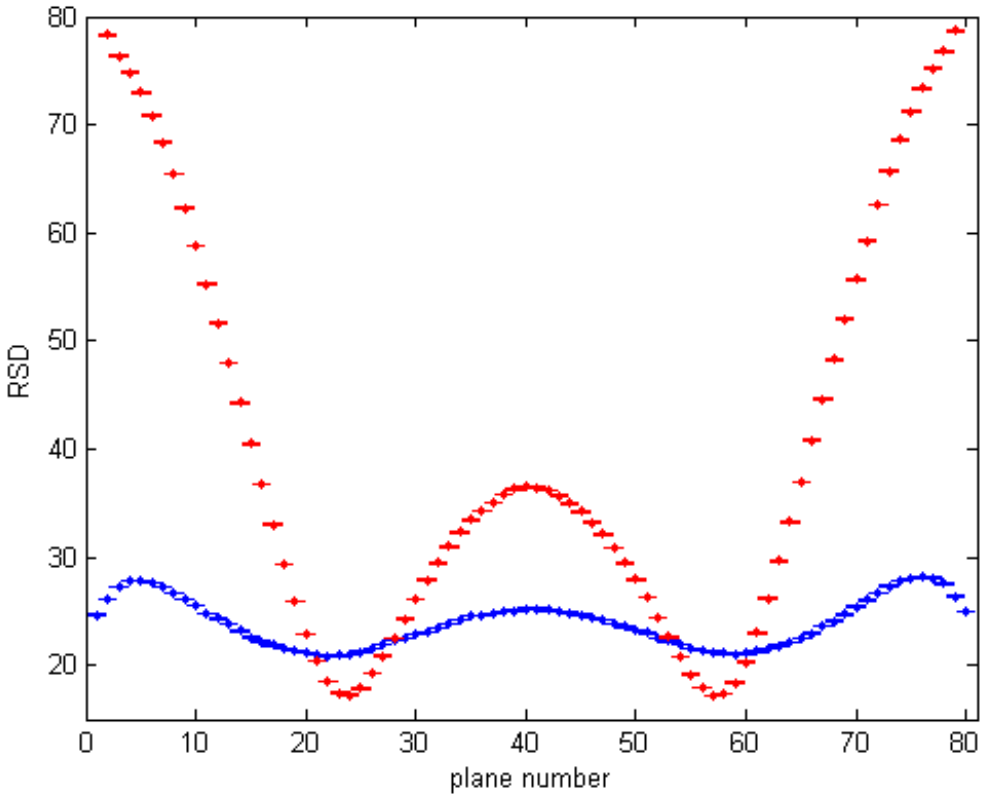

Figure 8.36: Normalized (blue) and un-normalized (red) reconstructed image non-uniformity measurements for the center 8 cm x 13 cm field of view in the dedicated breast imaging system. Measurements from all planes are shown.

across planes significantly decreased by 70.0% in the ROIs, and 88.9% in the FOV, using the normalization algorithm.

8.8.3 Visual Inspection - Reconstructed Images

To visualize the effect of the normalization algorithm, a three dimensional resolution phantom was used, consisting of three axial planes of sources. Each plane had a 5 x 5 spheres, at locations described in the caption of Figure 8.37. The radius of

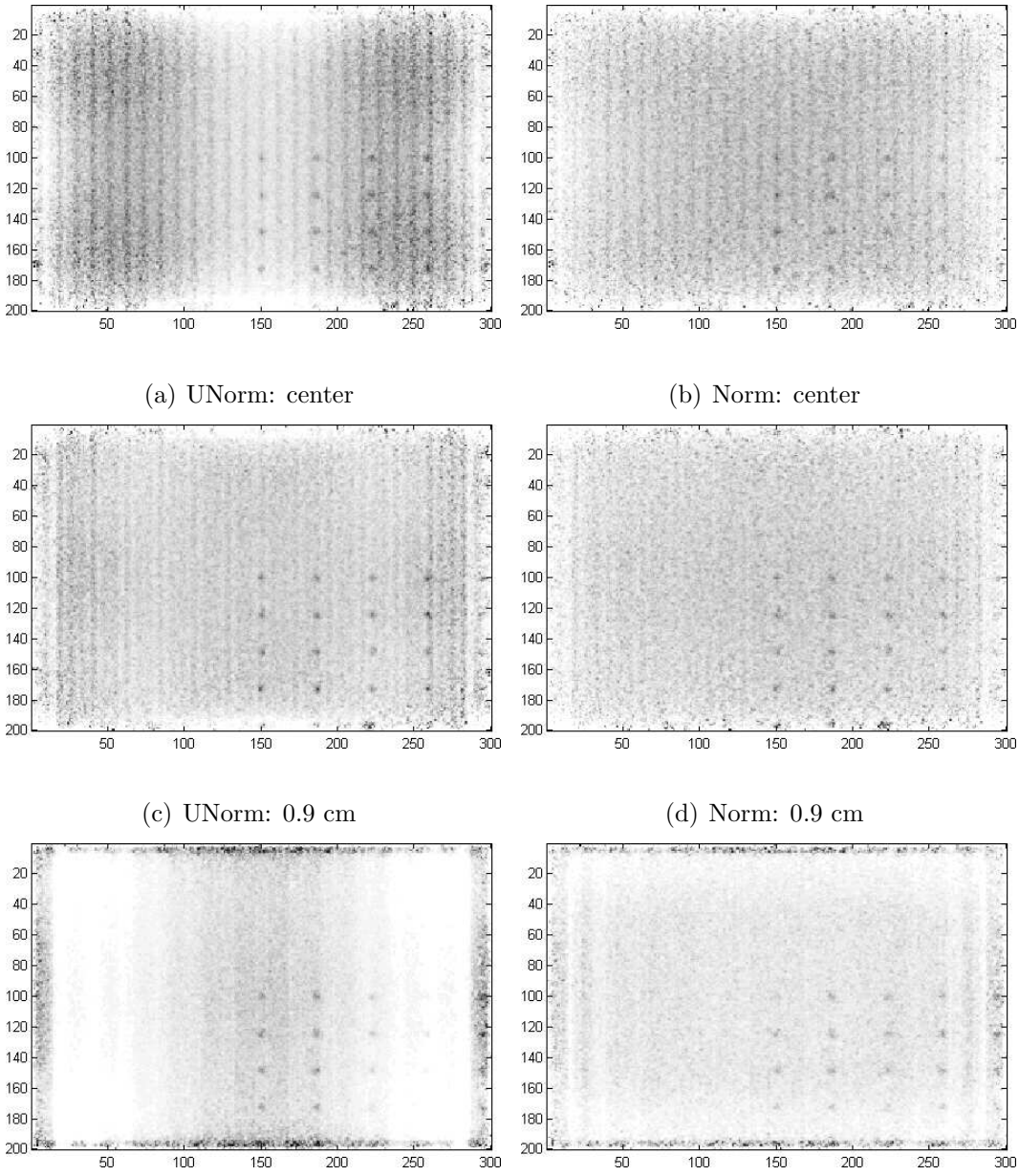

(a) UNorm: center

(b) Norm: center

(c) UNorm: 0.9 cm

(d) Norm: 0.9 cm

(e) UNorm: 1.8 cm

(f) Norm: 1.8 cm

Figure 8.37: Reconstructed images for a 5 x 5 sphere phantom with uniform background, at three planes in the field of view in the dedicated breast imaging system: (top) at the center of the system, (middle) 0.9 cm away from the center or 1.1 cm from the edge, (bottom) 1.8 cm away from the center or 0.2 cm from the edge. Shown are both the Left: un-normalized (Unorm) images and Right: normalized (Norm) images.

each sphere was 1.25mm, at a 10:1 concentration ration with respect to the uniform background. The total activity in the phantom was 200 μCi, distributed between the three planes of spheres and the uniform background. Images were reconstructed with the same list-mode OSEM algorithm as the small animal imaging system data, using 1 iteration and 14 subsets. Reconstructed images had 80 x 300 x 200 pixels, or were 0.5mm in size, which filled the entirety of the volume between the two panels. All image slices shown will be made in the yz-plane.

At the very edge of the field of view, low numbers of lines of response created a prior with a large sensitivity compensation. In the raw reconstructed images, small fluctuations in counts produced high frequency, high amplitude variations and large non-uniformity. After application of the normalization weights to the events, a more uniform and streak-free image was produced.

8.9 Discussion

The efficiency factors determination method developed in this study was quick to compute and simple to implement. The separable nature of the efficiency components for component-based normalization method, along with system symmetries, led to efficiency factor determination with relatively few acquired counts and a relatively simple source configuration. These efficiency factors were used to calculate a line of response (LOR) normalization weighting factor on the fly in a line-by-line, or

list mode, basis. As the systems and source used in these studies are simulated, a discussion on the means of determining these factors in a constructed system can be found in Section 8.9.2.

The component based normalization algorithm developed in this work was successful at reducing non-uniformities (U) and relative standard deviation (RSD), as well as their variation across planes for all sufficiently high count studies using differing system configurations. The line of response density variation and image space sampling in the two studied systems were vastly different. The ability of the algorithm to achieve higher quantification in both systems demonstrates its versatility and applicability.

Reconstructed images using the normalization algorithm had fewer streaks and artefacts. In the low count small animal system study however, the U and RSD results seemed to defy the general trend in non-uniformity and relative standard deviation improvement when using the normalization algorithm that were seen in the other studies. Under further inspection, this discrepancy disappeared when larger numbers of counts were added to each pixel, and the general trend returned.

Separating the factors of normalization coefficients can be used to accurately weight each line of response in order to obtain quantitative reconstructed images and to help illuminate factors affecting design of a detector system.

8.9.1 Implications of Results

Small Animal System

There was a large effect on sensitivity from axial geometric factors, distance between detectors, and amount of crystal surrounding a particular crystal in the box-shaped system. This effect on sensitivity resulted in the raw reconstructed images having regions of higher than average reconstructed counts in the corner and lower than average reconstructed counts in the center of the system, as well as small streaks in regions of high sensitivity due to the repetitive structure of the sphere phantom and the EM reconstruction algorithm used.

The component-based normalization weight was calculated and added to the listmode reconstruction algorithm. The list-mode applied weight improved non-uniformity and relative standard deviation for all sufficiently high count studies. In both the raw and normalized images shown for visual inspection, the 1mm diameter spheres in cold background were resolved throughout the relatively large useful field of view (the spheres extend to within 3mm from the edge of the detector system).

Non-uniformity for normalized images improved by 5 to 10 % on average in regions of interest and a similar amount in the useful field of view. Variation in non-uniformity across the planes was improved to a greater degree, by $\sim$20% on average. The relative standard deviation also saw a large improvement using the normalization algorithm. It improved by $\sim$15% in the ROIs and by $\sim$20% in the FOV.

Breast Imaging System

Because the LOR density variation was very high in the dual panel system, the density of lines of reponse (dLOR) correction added high frequency, high amplitude noise near edges of the system. The lines of response (LORs) variation, coupled with geometric sensitivity variations created large scale high count regions of un-normalized images (in the corners of the central plane, in the center of the off-center planes). Edge noise was significantly reduced using the normalization algorithm and the hot regions were nearly removed.

In only normalized images shown for visual inspection, the 1.5mm radius spheres in warm background were resolved throughout the relatively large useful field of view (the spheres extend to within 3mm from the edge of the detector system), with the exception of the last row and column of spheres near the edge in the central plane, which did not resolve. In un-normalized reconstructed images, uniformity variations were large enough so that most of the visualized planes had at least one column of spheres that was difficult to detect.

Non-uniformity for normalized images improved by 4 to 7% on average in regions of interest and a similar amount in the useful field of view. Variation in non-uniformity across the planes was improved to a much greater degree, by ∼52% on average. Relative standard deviation also saw a large improvement using the normalization algorithm. It improved by ∼13% in the ROIs and by ∼41% in the FOV. variation in

relative standard deviation was greatly reduced using the normalization algorithm, it decreased by ∼70% in the ROIs and by ∼89% in the FOV.

The efficiency factors in this system were the same as in the small animal imaging system, but the distance between detector cross-term had a larger range, which increased the normalization factor range. The large system sampling variations provided a means to test the bounds of the accuracy of the novel normalization algorithm. Relatively small miscalculations in weighting factors that may have been masked by relatively uniform sampling in the small animal system, would have become readily apparent in the dual panel breast imaging system.

General Technique

The component based normalization method proved to be a useful, versatile, and efficient means of producing a line of response weighting factor to apply to list mode data. The difficulty in this method of reconstruction was in calculating the density of line of response sensitivity image. This difficuly developed due to the method of positioning utilized in the studies. For singles that contained interactions in more than one detector, the method of positioning was to use the center of mass of the positions which made up the single (see Section 7.3 for a more thorough discussion). The center of mass position was not binned further once the calculation was made. Therefore, determining a representative subset of all LORs to create the image (as creating all possible LORs would be prohibitively costly) was difficult. Binning the

center of massed events to a fine (500 μm) bin size would likely reduce the difficulty in calculating the dLOR prior image.

8.9.2 Efficiency Determination in a Built System

The geometric factors described and calculated in this work were done using the Geant4 add-on package Geant4 Application for Emission Tomography (GATE). This Monte Carlo simulation package has been validated by the high energy physics and emission tomography community for many constructed systems. Once a system is constructed, data obtained using this simulation package could provide a basis, essentially an approximate value, for the geometric efficiency factors of the built system. The components of the system; e.g. the crystal, photodetector, reflector, etc.; are manufactured to specified dimensions and associated tolerances. A simulation would aid in finding the geometric factors by modeling the average component dimension, as this is a good approximation for the modules in the contructed system. These geometric efficiency factors attained through simulation could then be modified for each of the constructed system detectors, using data acquired with the built system. The system acquisition data would account for small, but inevitable, variations in manufactured module construction. The method in which these factors would be modified can be done using equipment that currently exists for similar functions.

A quality control scan that is currently performed on positron emission tomogra-

phy systems is the Geometric Distortion Removal (GDR) scan. This scan is performed at different intervals (∼daily) using a point source at several locations in the field of view, inspecting any kind of shift in system position determination. This scan would be ideal for calculating system-wide deviations from the average geometric detection efficiency. The point source would produce annihilation events along specific known lines of response, probing most or all detectors for every point source position. Since there are three geometric factors for each detector, at least three source locations per detector would be necessary to separate the deviations in each geometric component. To account for possible statistical variations, and to ensure accurate fitting, 6 or more locations would be preferred.

This GDR scan setup is also useful for determining the intrinsic efficiency components as well. The geometric efficiencies are scaled by intrinsic detector efficiency factors. Stored on a per detector basis, the intrinsic efficiencies can be regarded as a single scaling efficiency, which is not angle dependent. The light output, reflector reflectivity, quantum efficiency of the photodetector, etc., do not change based on which line of response produced the event in the detector. If a single is constructed of interactions in multiple photo-detectors, each of the detector efficiencies would ideally be used. If the detector system hardware or software construction does not allow for tracking the detectors involved in a multi-interaction single event, a mean intrinsic efficiency value based on the probability of detectors invovled can be utilized instead. This would require per-detector measurements performed on the system

before assembly as well as modeling for the interaction density around each detector.

The GDR method is nearly identical in execution to methods currently used to determine component based normalization factors [49]. In the case presented here, the efficiency factor determination is expedited by simulation, but this need not be the case. Component based normalization factors can be completely determined using the method described above (as it is in nearly every system using CBN), though more point source location acquisitions would be required.

Chapter 8, in part, is a reprint of the material as it appears in Nuclear Science Symposium Conference Record, 2005 IEEE Volume 4, October 23 - 29, 2005 Page(s):2108 - 2111, Foudray AMK, Chinn, G, Levin, CS. The dissertation author was the primary investigator and author of this paper.

Chapter 9

Summary of this Work and Future Directions

9.1 Knowledge Gained from this Work

The position-sensitive avalanche photodiodes (PSAPDs), used as optical photon detection devices in conjunction with lutetium oxyorthosilicate (LSO) scintillation crystals, were characterized for position, energy and timing information as well as operating voltage ranges and gain. In our design, the photodetector had to be very thin to maintain a high crystal packaging fraction. In order to acheive this, novel packaging components were also determined. A Kapton flex circuit was utilized for high and low voltage signal extraction and inter-signal passivation, protection from moisture, power delivery to the PSAPDs, and module orientation flexibility. An aluminum

nitride (AlN) structure was constructed for temperature conduction, structural support, LSO array positioning and inter-PSAPD electrical passivation (see Figure 9.1). Cross-talk and individual device characteristics were measured for the modules with two devices packaged on a single flex circuit. Dual-chip module results showed little to no signal generation in the un-irradiated bundled PSAPD device when the other PSAPD was irradiated. The humidity of the environment during the testing of the devices was shown to be a factor in the operation of the novelly packaged devices.

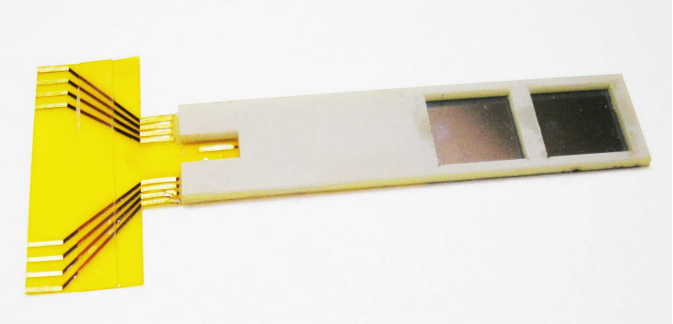

Figure 9.1: A picture of the novel detector module with LSO arrays removed.

System parameters such as module orientation and configuration were also studied, revealing high-sensitivity configurations using a smaller volume of detector as compared to traditional systems. Systematic observations included system construction rules of thumb such as placement of detector heads with respect to one another (i.e. local crystal packing density) and its effect on system sensitivity. Energy and coincidence time windows were determined using standard figures of merit (NEC). The type of signal acquired by the detector system was also estimated for two types

of constructed systems: one in a small animal dedicated formation, one in a dedicated human breast imaging configuration.

System performance was evaluated including achievable detectability, usable field of view, and system detection sensitivity. Quantitation was addressed by developing a novel component based normalization algorithm for detectors with direct depth of interaction measurement and observing its applicability to two different detector system configurations (small animal and dedicated human breast imaging).

The device (Chapters 3-5) and system (Chapter 6.1) characterization performed in studies, and the developed algorithms (Chapters 7-8) for the device utilization contained in this work have been shown to be applicable to different system configurations. The next steps leading to the building and evaluation of systems consisting of these novel detector modules for dedicated imaging are very exciting and have already begun. These studies will be discussed in the next section.

9.2 Future System Realization

9.2.1 Quality Assurance Procedures

Systems built from the LSO-PSAPD modules characterized in this work will require many modules stacked together. Each of the modules must have position identification, energy resolution, time resolution, gain, and optimal bias voltage characteristics known before complete system operation. Current efforts are being made

to correlate quickly measureable physical and electronic parameters with the needed device operational parameters. For instance, positioning capabilities of the devices have been investigated by using the quickly acquired unbiased corner signal so that positioning capabilities might be able to be estimated using finite element analysis [128]. Further parameter estimation, using corner signal acquisition, under no bias voltage is currently being investigated.

9.2.2 Mechanical Design

The design of the assembly for module incorporation into robust yet separable groups has already begun. The robustness needs to be in the form of mechanical, thermal, electrical considerations, as well as ambient radio-frequency, humidity, and optical isolation. The design must be able to be taken apart so that individual modules that need to be replaced can be extracted.

9.2.3 Acquisition Design

Electronics

Active work is also underway in terms of an electronics design for the system [127, 138]. Application specific integrated chips (ASICs) for signal amplification and shaping in the built system have been tested with individual detector modules [180]. Further work will include final PCB design and connection techniques for power

delivery and signal acquisition of detectors in the configuration of the final built system.

Signal Processing

An analog signal multiplexing scheme has been developed to reduce the number of channels required to be collected by the system, and thus reducing the complexity, size and cost of the data acquisition system [90]. Further signal processing studies are currently being performed, such as methods for more accurately determining interaction time in order to reduce coincidence time jitter [148].

9.3 Future Reconstruction Methodologies

Methods for utilizing multiple interactions in the detector for processing data acquired from a single incident annihilation photon have begun to take shape. These methods call for re-thinking many components of reconstruction: the shape of the volume of response (traditionally the line of response is represented by a tube of thickness determined by the resolution of the detectors), the order in which information is used, normalization, etc. Some of these issues have been explored in the studies mentioned below.

Instead of throwing out scattering events, we are looking into studying how the direction of the incoming annihilation photons to reduce the volume from which the

annihilation occurred [33]. Results show that using scattering events, along with physical models of annihilation photon scattering and multiple interaction collimation, regions with high source activity concentration become evident in reconstructed images. Using these models, the likely volume in image space in which annihilation events took place are not contained any longer along a line. This impacts how the normalization must be applied, and how to incorporate this data with traditional data gathered in parallel (electronically collimated "true" coincidence events). Further studies considering how to best use this new information are under way.

Annihilation photons that have multiple interactions and cannot be paired with another detected annihilation photon (Singles) are also being investigated for use in reconstruction [34]. Images have been reconstructed using Singles whose likely angles of incidence were determined via Compton Kinematics and gathered with a simulated CZT detector system. The result of the Compton Kinematics algorithm for Singles provides yet another likely volume in which annihilation occurred, impacting normalization and data utilization methods. The techniques used in this reconstruction scheme can likely be modified to be used in the LSO-PSAPD based detector system presented in this work.

A method that can be investigated to improve noise in reconstructed images is to apply the line of response normalization factors directly in the image space along with the density of line of response sensitivity image [145]. This technique can incorporate importance sampling of the detector space as well as smoothing of the image to reduce

computation time of the normalization image. Combining these factors together in a single image also enables the full sensitivity map to be calculated once for a particular system as long as the line of response normalization factors and detector element locations remain constant.

Graphical processor units (GPUs) are the processors used in commercially available video cards. These processors are not nearly as flexible as the CPUs used for general processing in modern computers, but have the following distinct advantages: 1) they are optimized to perform the same tasks as the list-mode geometrical steps used in iterative reconstruction, i.e. lines or tubes of response filling a volume, 2) they are highly parallel, being able to perform on the order of 24 geometrical operations in one clock cycle (instead of just one or two operations per processing unit), 3) they have fast clock cycles and have high bandwidth access to memory to perform each geometrical operation. GPU OSEM reconstruction algorithms have been developed [141] to utilize the cost and computation advantages offered by this off-the-shelf technology. Reconstruction using GPU harware and software will greatly aid in reducing the time it takes to produce images from data gathered using the constructed detector system.

Appendix A

Final Design Crystal Array Data

A.1 8 x 8 Agile Crystal Arrays without Inter-crystal Reflector

A.1.1 Crystal Identification

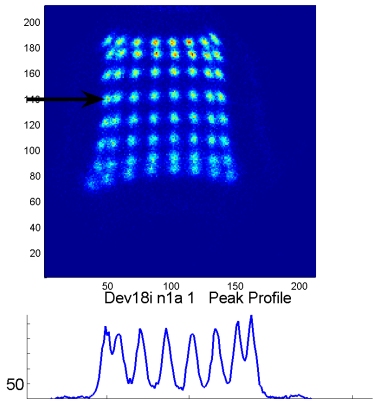

Peak	PVR
1	1.65
2	4.37
3	6.25
4	7.90
5	6.95
6	6.07
7	4.94
8	2.15
Mean	5.04
StDev	2.23

(a)

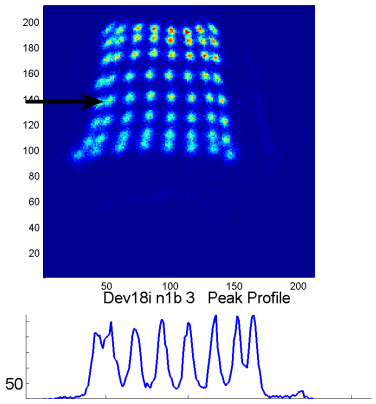

Peak	PVR
1	1.35
2	6.37
3	6.81
4	7.84
5	7.57
6	8.84
7	6.70
8	2.81
Mean	6.04
StDev	2.59

(b)

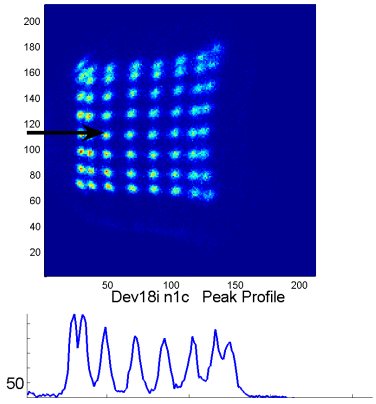

Peak	PVR
1	1.71
2	7.74
3	14.37
4	16.68
5	13.54
6	6.97
7	4.12
8	1.49
Mean	8.33
StDev	5.90

(c)

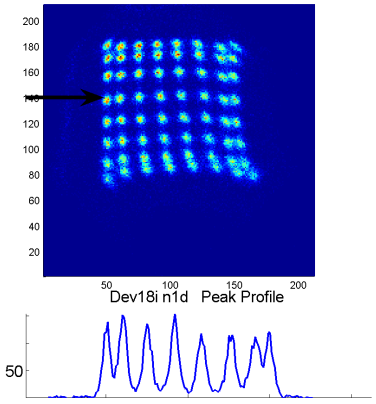

Peak	PVR
1	3.80
2	13.23
3	11.00
4	15.84
5	13.20
6	10.49
7	6.33
8	2.17
Mean	9.51
StDev	4.89

(d)

Figure A.1: Flood (upper left), profile (lower left), and peak to valley ratio (right table) for 8 x 8 Agile crystal arrays 1-4 without inter-crystal reflector.

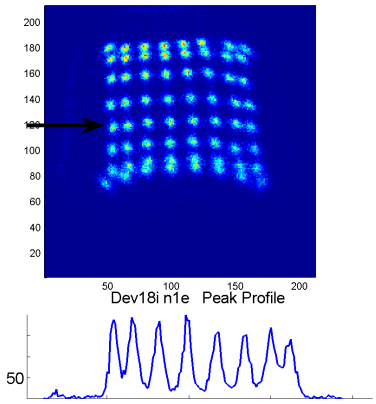

Peak	PVR
1	3.84
2	7.79
3	10.45
4	10.88
5	9.12
6	5.85
7	6.13
8	2.01
Mean	7.01
StDev	3.14

(a)

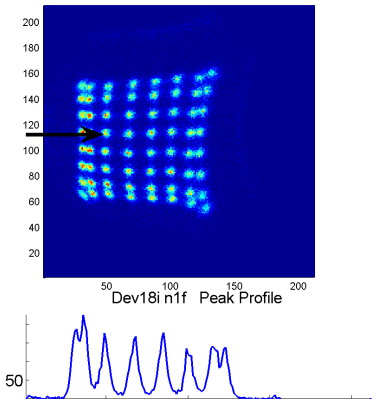

Peak	PVR
1	1.22
2	7.52
3	20.76
4	12.17
5	15.11
6	11.40
7	6.80
8	1.71
Mean	9.59
StDev	6.65

(b)

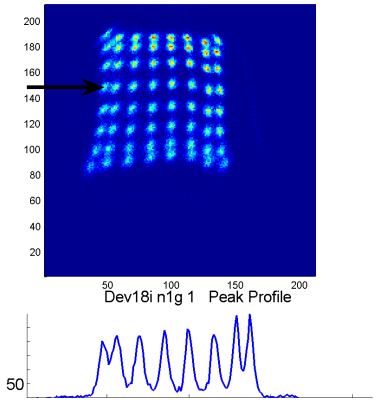

Peak	PVR
1	1.72
2	5.84
3	8.32
4	11.04
5	9.72
6	7.90
7	8.71
8	3.18
Mean	7.05
StDev	3.23

(c)

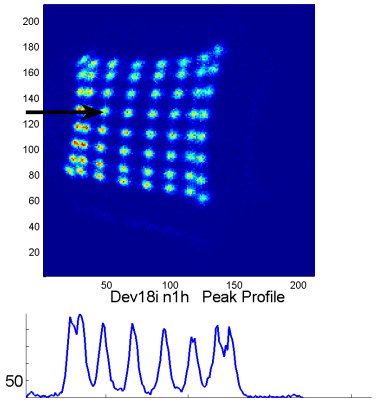

Peak	PVR
1	1.27
2	7.10
3	10.17
4	23.59
5	16.03
6	9.83
7	5.88
8	1.72
Mean	9.45
StDev	7.45

(d)

Figure A.2: Flood (upper left), profile (lower left), and peak to valley ratio (right table) for 8 x 8 Agile crystal arrays 5-8 without inter-crystal reflector.

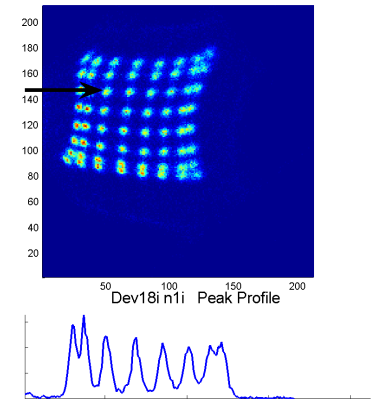

Peak	PVR
1	1.85
2	6.67
3	10.02
4	8.05
5	7.19
6	5.27
7	3.61
8	1.27
Mean	5.49
StDev	3.07

(a)

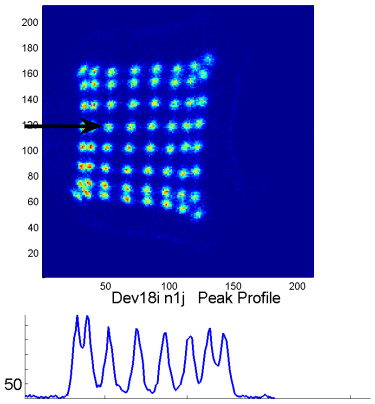

Peak	PVR
1	1.64
2	7.74
3	12.22
4	11.55
5	9.98
6	6.92
7	4.79
8	2.01
Mean	7.11
StDev	4.07

(b)

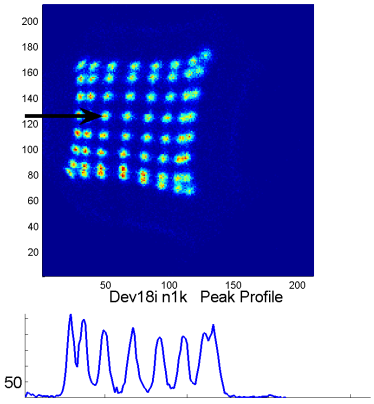

Peak	PVR
1	2.69
2	6.41
3	15.73
4	11.33
5	10.47
6	7.03
7	4.85
8	1.29
Mean	7.47
StDev	4.80

(c)

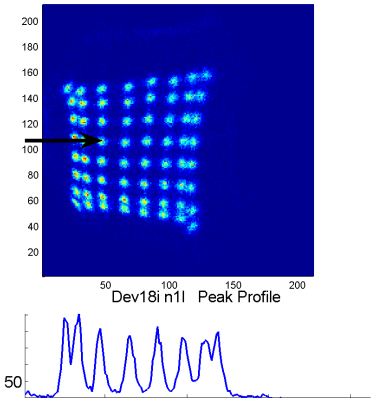

Peak	PVR
1	2.40
2	11.60
3	12.32
4	11.87
5	14.19
6	9.68
7	3.46
8	1.77
Mean	8.41
StDev	5.03

(d)

Figure A.3: Flood (upper left), profile (lower left), and peak to valley ratio (right table) for 8 x 8 Agile crystal arrays 9-12 without inter-crystal reflector.

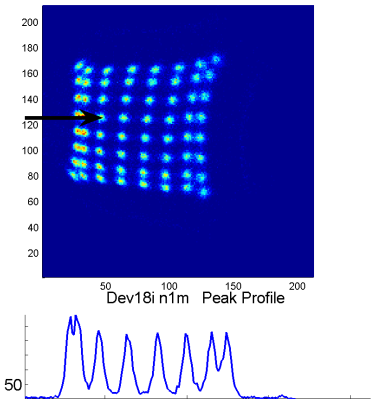

Peak	PVR
1	1.29
2	8.92
3	12.06
4	10.65
5	12.33
6	11.45
7	9.13
8	2.38
Mean	8.53
StDev	4.32

(a)

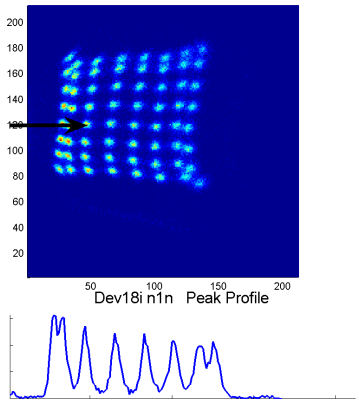

Peak	PVR
1	1.35
2	8.44
3	12.15
4	15.73
5	16.29
6	7.52
7	5.59
8	1.93
Mean	8.62
StDev	5.73

(b)

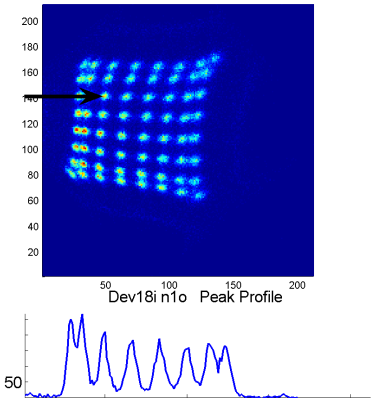

Peak	PVR
1	1.59
2	6.34
3	10.51
4	7.78
5	7.35
6	5.41
7	4.69
8	2.16
Mean	5.73
StDev	2.95

(c)

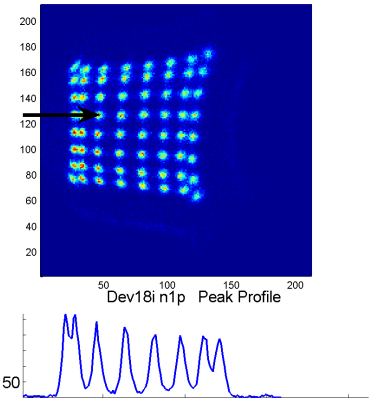

Peak	PVR
1	1.45
2	9.20
3	17.42
4	15.69
5	15.84
6	8.19
7	6.06
8	2.20
Mean	9.51
StDev	6.25

(d)

Figure A.4: Flood (upper left), profile (lower left), and peak to valley ratio (right table) for 8 x 8 Agile crystal arrays 13-16 without inter-crystal reflector.

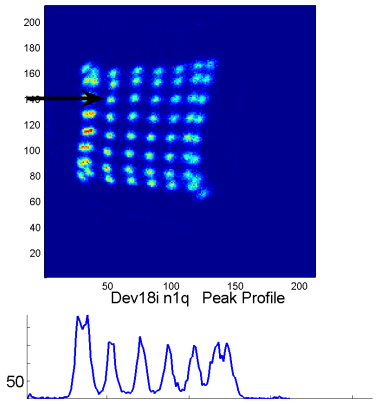

Peak	PVR
1	1.22
2	16.16
3	10.60
4	10.55
5	10.49
6	7.41
7	4.45
8	1.50
Mean	7.80
StDev	5.17

(a)

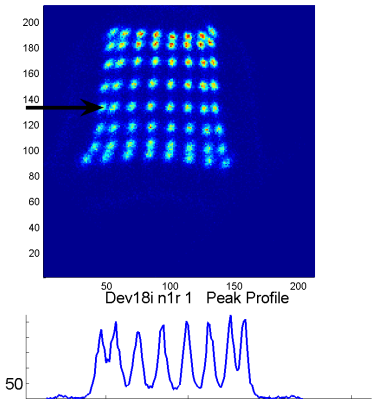

Peak	PVR
1	1.93
2	6.46
3	7.00
4	7.58
5	8.31
6	6.71
7	7.49
8	2.81
Mean	6.04
StDev	2.34

(b)

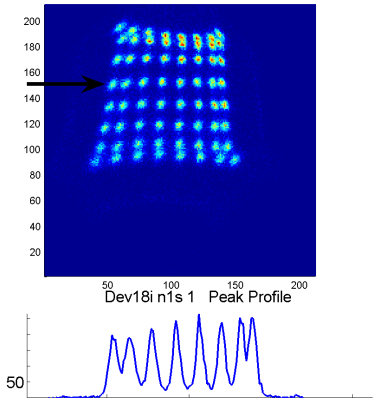

Peak	PVR
1	2.51
2	5.11
3	10.13
4	8.46
5	9.14
6	8.79
7	6.07
8	2.13
Mean	6.54
StDev	3.08

(c)

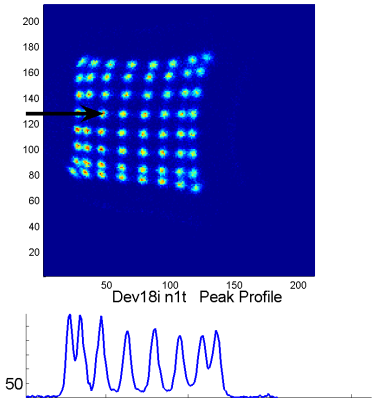

Peak	PVR
1	2.27
2	10.85
3	12.40
4	10.53
5	11.67
6	9.69
7	5.52
8	2.34
Mean	8.16
StDev	4.16

(d)

Figure A.5: Flood (upper left), profile (lower left), and peak to valley ratio (right table) for 8 x 8 Agile crystal arrays 17-20 without inter-crystal reflector.

A.1.2 Energy Resolution

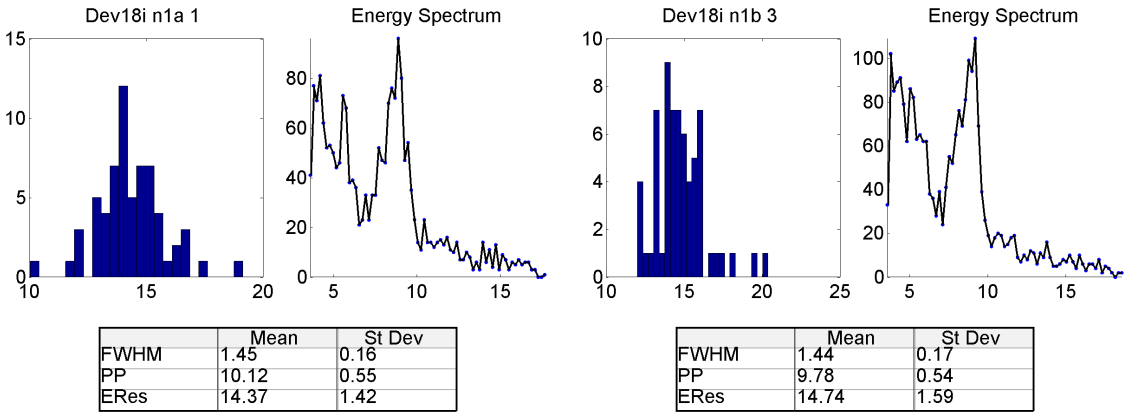

	Mean	St Dev
FWHM	1.45	0.16
PP	10.12	0.55
ERes	14.37	1.42

(a)

	Mean	St Dev
FWHM	1.44	0.17
PP	9.78	0.54
ERes	14.74	1.59

(b)

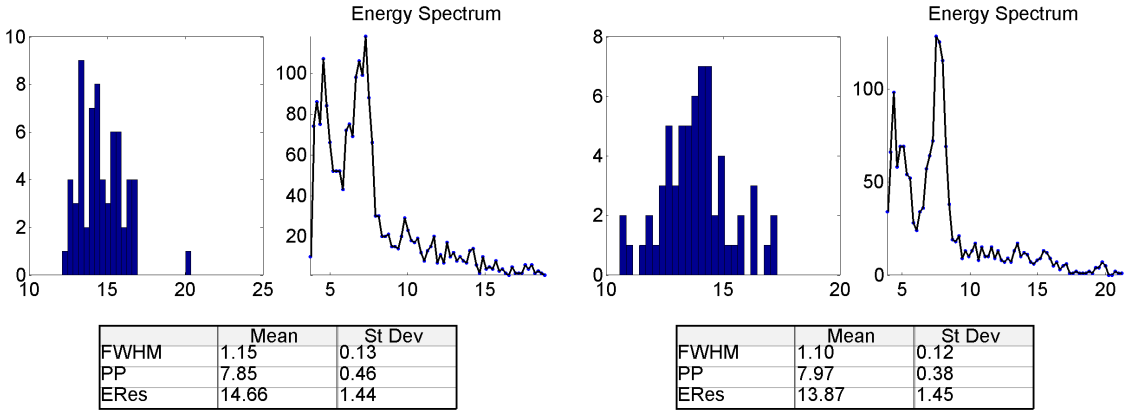

	Mean	St Dev
FWHM	1.15	0.13
PP	7.85	0.46
ERes	14.66	1.44

(c)

	Mean	St Dev
FWHM	1.10	0.12
PP	7.97	0.38
ERes	13.87	1.45

(d)

Figure A.6: For Agile crystal arrays without inter-crystal reflector 1-4, energy resolution histograms for all 64 crystals (bar plot, upper left) as well as a representative energy spectrum (blue line, upper right), and the mean and standard deviation of energy parameters obtained from the 64 crystals (bottom table).

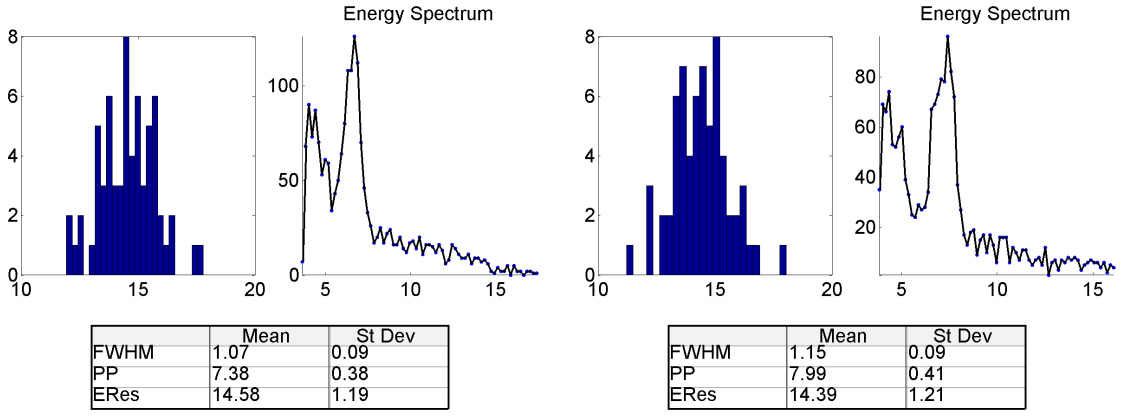

(a)

(b)

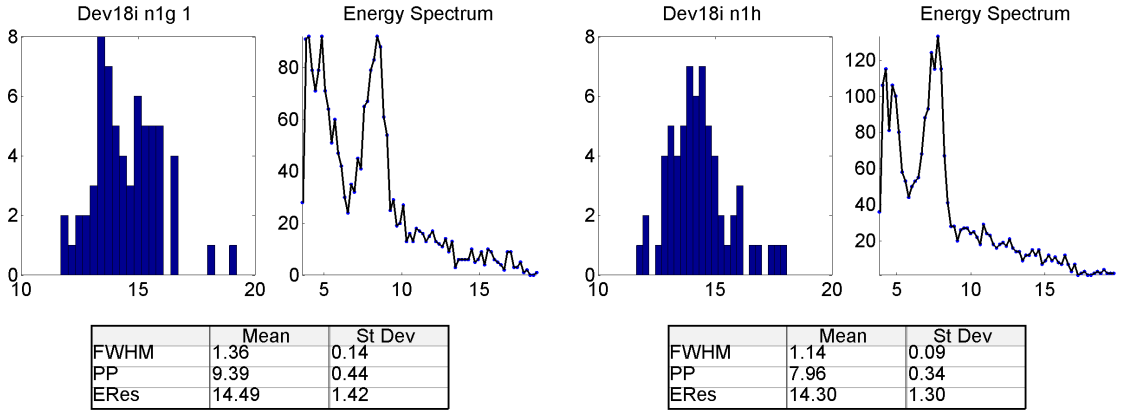

(c)

(d)

Figure A.7: For Agile crystal arrays without inter-crystal reflector 5-8, energy resolution histograms for all 64 crystals (bar plot, upper left) as well as a representative energy spectrum (blue line, upper right), and the mean and standard deviation of energy parameters obtained from the 64 crystals (bottom table).

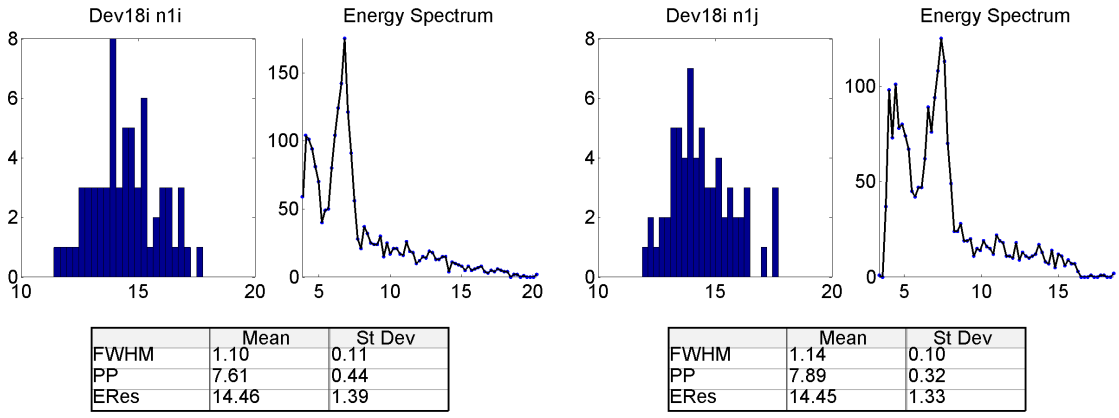

	Mean	St Dev
FWHM	1.10	0.11
PP	7.61	0.44
ERes	14.46	1.39

(a)

	Mean	St Dev
FWHM	1.14	0.10
PP	7.89	0.32
ERes	14.45	1.33

(b)

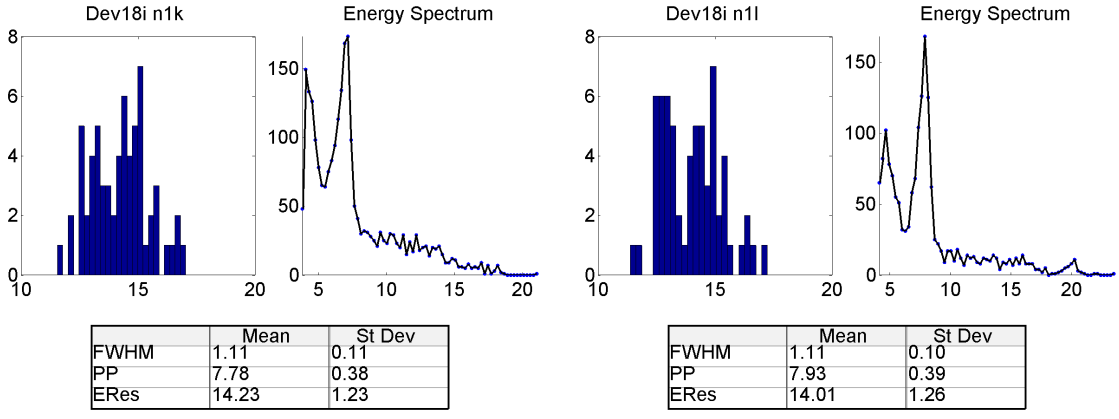

	Mean	St Dev
FWHM	1.11	0.11
PP	7.78	0.38
ERes	14.23	1.23

(c)

	Mean	St Dev
FWHM	1.11	0.10
PP	7.93	0.39
ERes	14.01	1.26

(d)

Figure A.8: For Agile crystal arrays without inter-crystal reflector 9-12, energy resolution histograms for all 64 crystals (bar plot, upper left) as well as a representative energy spectrum (blue line, upper right), and the mean and standard deviation of energy parameters obtained from the 64 crystals (bottom table).

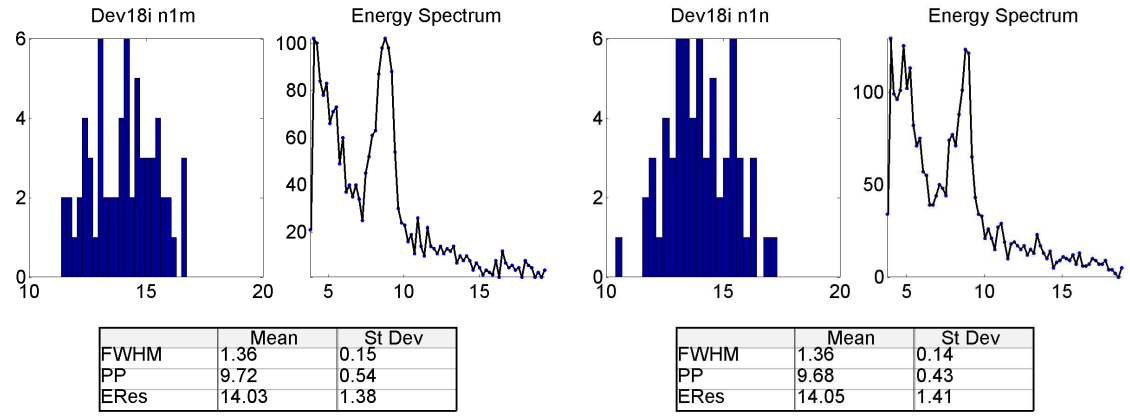

	Mean	St Dev
FWHM	1.36	0.15
PP	9.72	0.54
ERes	14.03	1.38

(a)

	Mean	St Dev
FWHM	1.36	0.14
PP	9.68	0.43
ERes	14.05	1.41

(b)

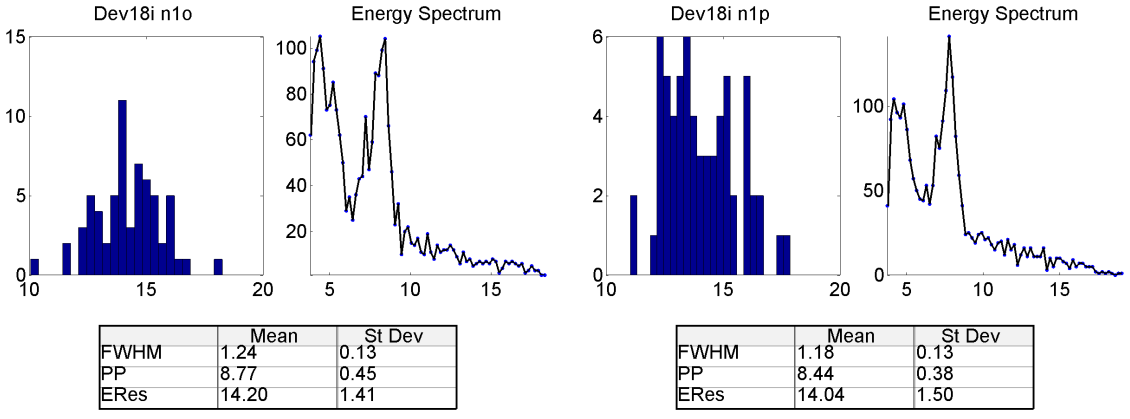

	Mean	St Dev
FWHM	1.24	0.13
PP	8.77	0.45
ERes	14.20	1.41

(c)

	Mean	St Dev
FWHM	1.18	0.13
PP	8.44	0.38
ERes	14.04	1.50

(d)

Figure A.9: For Agile crystal arrays without inter-crystal reflector 13-16, energy resolution histograms for all 64 crystals (bar plot, upper left) as well as a representative energy spectrum (blue line, upper right), and the mean and standard deviation of energy parameters obtained from the 64 crystals (bottom table).

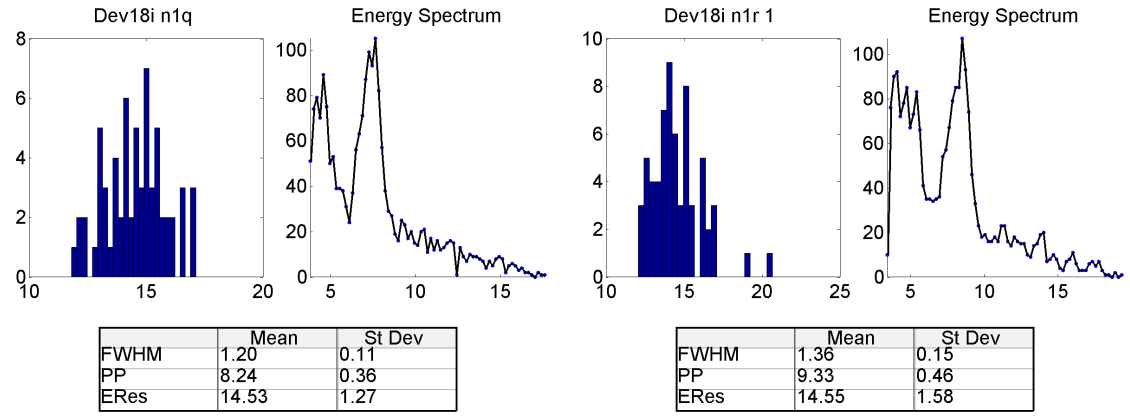

	Mean	St Dev
FWHM	1.20	0.11
PP	8.24	0.36
ERes	14.53	1.27

(a)

	Mean	St Dev
FWHM	1.36	0.15
PP	9.33	0.46
ERes	14.55	1.58

(b)

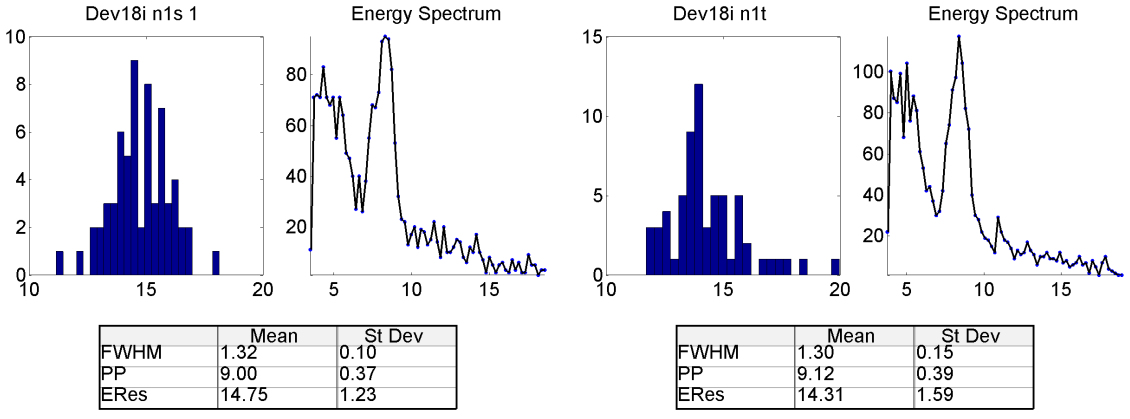

	Mean	St Dev
FWHM	1.32	0.10
PP	9.00	0.37
ERes	14.75	1.23

(c)

	Mean	St Dev
FWHM	1.30	0.15
PP	9.12	0.39
ERes	14.31	1.59

(d)

Figure A.10: For Agile crystal arrays without inter-crystal reflector 17-20, energy resolution histograms for all 64 crystals (bar plot, upper left) as well as a representative energy spectrum (blue line, upper right), and the mean and standard deviation of energy parameters obtained from the 64 crystals (bottom table).

A.2 8 x 8 Agile Crystal Arrays with VM2000 Inter-crystal Reflector

A.2.1 Crystal Identification

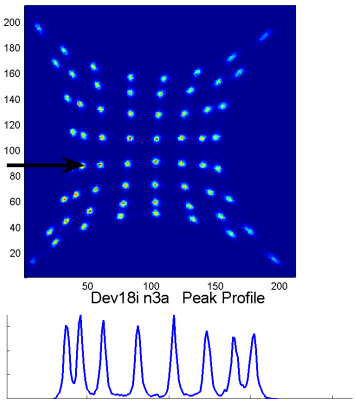

Peak	PVR
1	4.92
2	25.14
3	27.48
4	42.47
5	34.90
6	26.04
7	18.86
8	5.89
Mean	23.21
StDev	13.04

(a)

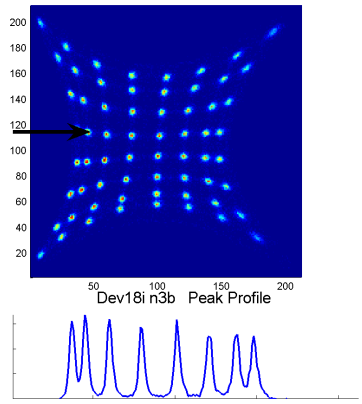

Peak	PVR
1	4.82
2	24.59
3	35.42
4	31.63
5	44.73
6	25.19
7	16.39
8	5.13
Mean	23.49
StDev	14.14

(b)

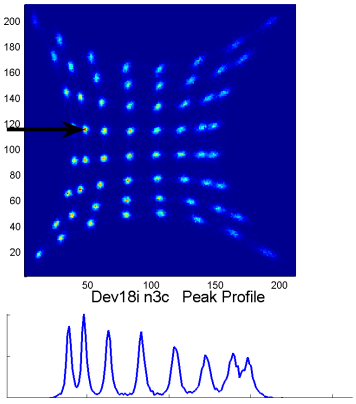

Peak	PVR
1	6.86
2	21.32
3	25.38
4	25.00
5	16.60
6	9.32
7	7.20
8	2.12
Mean	14.23
StDev	9.03

(c)

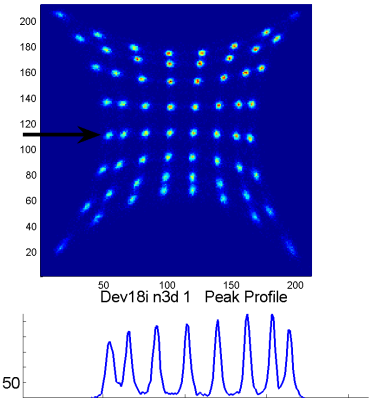

Peak	PVR
1	5.00
2	18.31
3	18.48
4	25.78
5	36.88
6	29.09
7	19.17
8	6.52
Mean	19.90
StDev	10.78

(d)

Figure A.11: Flood (upper left), profile (lower left), and peak to valley ratio (right table) for 8 x 8 Agile crystal arrays 1-4 with VM2000 inter-crystal reflector.

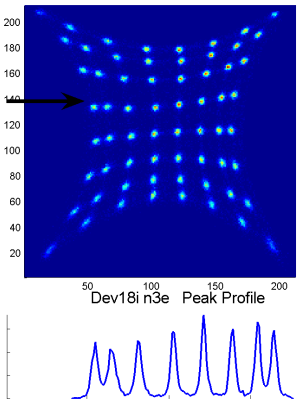

Peak	PVR
1	4.03
2	21.11
3	30.87
4	25.48
5	26.52
6	22.12
7	21.07
8	5.42
Mean	19.57
StDev	9.74

(a)

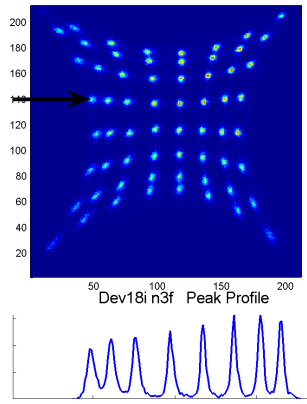

Peak	PVR
1	4.49
2	9.08
3	22.90
4	21.64
5	27.57
6	38.65
7	26.60
8	14.26
Mean	20.65
StDev	11.01

(b)

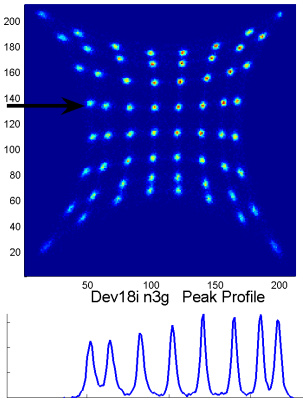

Peak	PVR
1	4.98
2	23.19
3	25.95
4	46.85
5	54.08
6	25.00
7	27.80
8	10.84
Mean	27.34
StDev	16.44

(c)

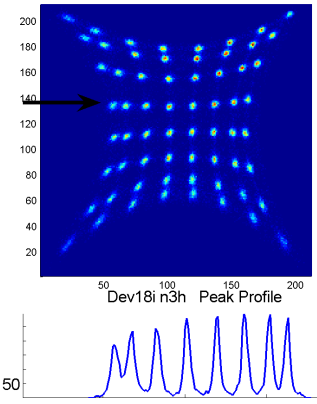

Peak	PVR
1	2.56
2	11.35
3	23.80
4	20.82
5	21.30
6	26.85
7	23.06
8	9.21
Mean	17.37
StDev	8.56

(d)

Figure A.12: Flood (upper left), profile (lower left), and peak to valley ratio (right table) for 8 x 8 Agile crystal arrays 5-8 with VM2000 inter-crystal reflector.

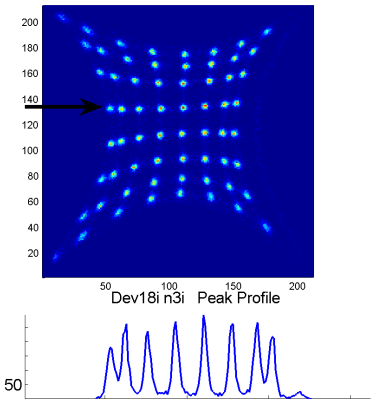

Peak	PVR
1	2.75
2	12.61
3	11.43
4	22.86
5	21.85
6	25.80
7	15.33
8	3.89
Mean	14.56
StDev	8.59

(a)

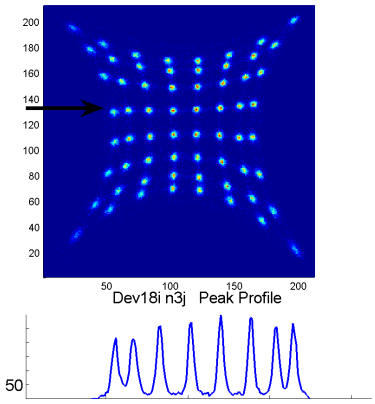

Peak	PVR
1	4.61
2	13.36
3	14.86
4	26.44
5	21.79
6	20.20
7	16.18
8	6.87
Mean	15.54
StDev	7.37

(b)

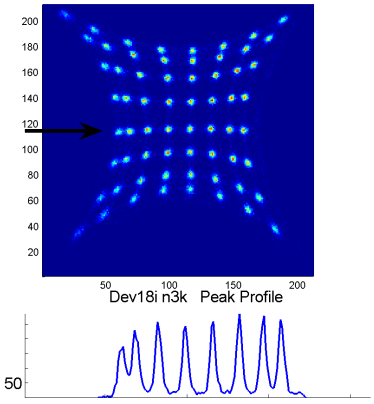

Peak	PVR
1	2.30
2	10.58
3	19.18
4	18.15
5	25.24
6	17.05
7	20.58
8	7.87
Mean	15.12
StDev	7.55

(c)

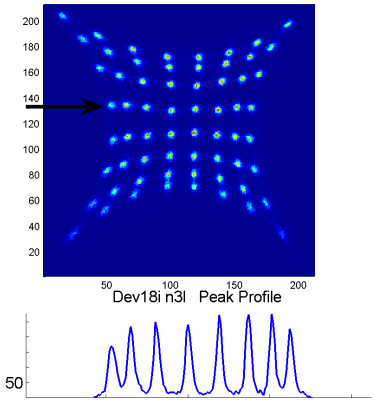

Peak	PVR
1	4.79
2	14.74
3	18.58
4	21.81
5	26.60
6	21.77
7	25.15
8	7.23
Mean	17.59
StDev	8.05

(d)

Figure A.13: Flood (upper left), profile (lower left), and peak to valley ratio (right table) for 8 x 8 Agile crystal arrays 9-12 with VM2000 inter-crystal reflector.

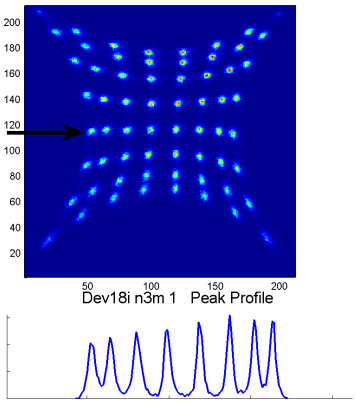

Peak	PVR
1	4.35
2	11.09
3	20.84
4	25.48
5	22.04
6	25.96
7	11.90
8	6.95
Mean	16.08
StDev	8.51

(a)

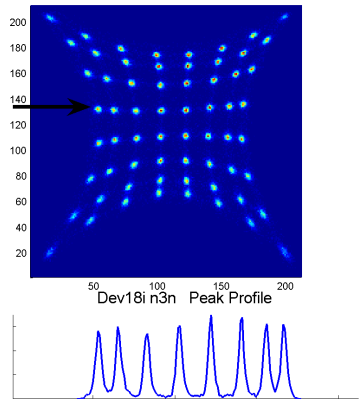

Peak	PVR
1	9.38
2	25.56
3	27.29
4	22.10
5	25.21
6	37.42
7	34.68
8	11.03
Mean	24.08
StDev	9.96

(b)

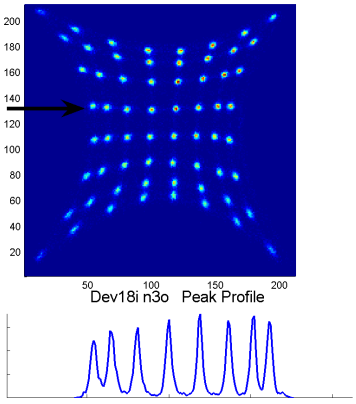

Peak	PVR
1	5.43
2	15.97
3	26.05
4	31.95
5	28.48
6	22.04
7	30.43
8	8.68
Mean	21.13
StDev	10.07

(c)

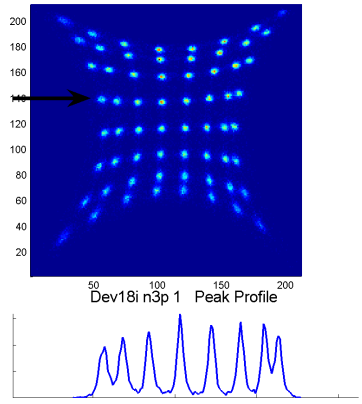

Peak	PVR
1	3.80
2	11.73
3	14.35
4	23.00
5	25.35
6	20.86
7	15.15
8	2.49
Mean	14.59
StDev	8.43

(d)

Figure A.14: Flood (upper left), profile (lower left), and peak to valley ratio (right table) for 8 x 8 Agile crystal arrays 13-16 with VM2000 inter-crystal reflector.

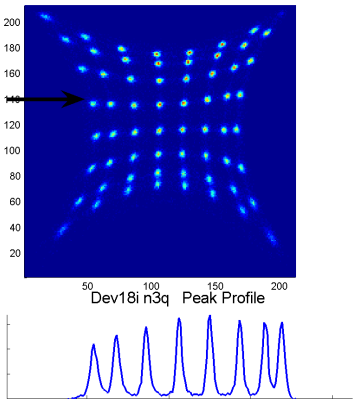

Peak	PVR
1	8.70
2	18.45
3	21.07
4	23.83
5	24.66
6	29.00
7	20.55
8	7.11
Mean	19.17
StDev	7.65

(a)

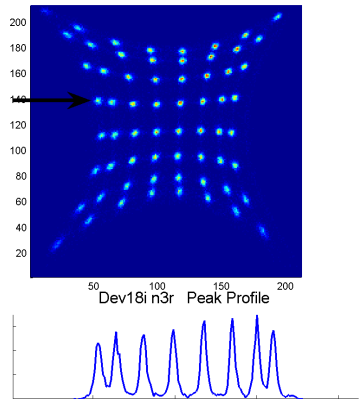

Peak	PVR
1	4.60
2	15.10
3	22.52
4	67.22
5	61.55
6	21.30
7	48.33
8	6.69
Mean	30.91
StDev	24.65

(b)

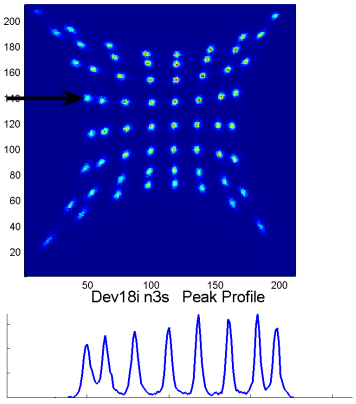

Peak	PVR
1	3.78
2	17.26
3	19.48
4	19.19
5	22.94
6	21.58
7	19.43
8	8.88
Mean	16.57
StDev	6.68

(c)

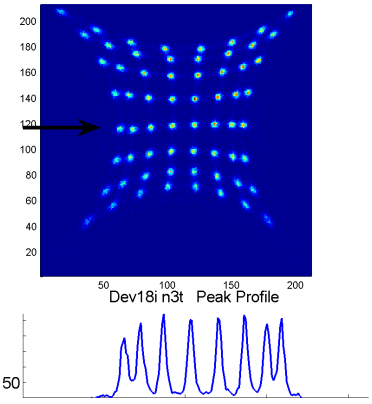

Peak	PVR
1	3.60
2	19.45
3	19.11
4	22.85
5	21.90
6	34.47
7	11.94
8	4.47
Mean	17.22
StDev	10.25

(d)

Figure A.15: Flood (upper left), profile (lower left), and peak to valley ratio (right table) for 8 x 8 Agile crystal arrays 17-20 with VM2000 inter-crystal reflector.

A.2.2 Energy Resolution

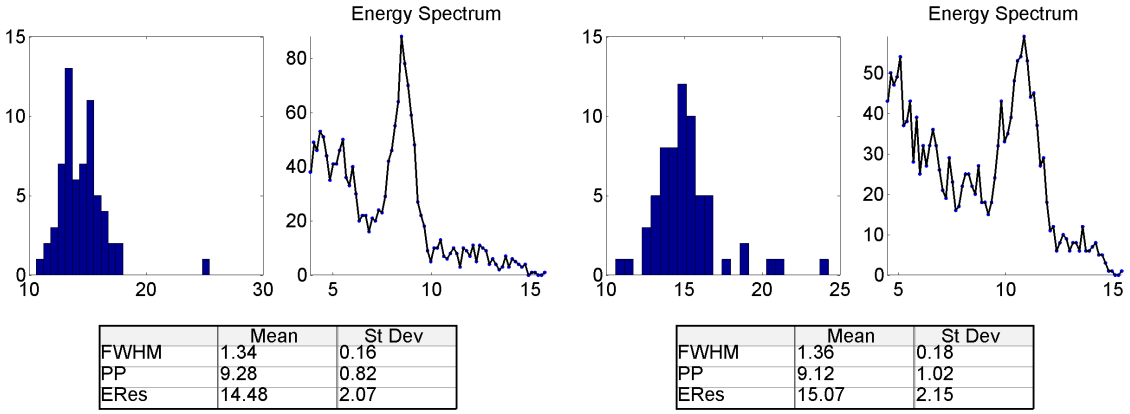

	Mean	St Dev
FWHM	1.34	0.16
PP	9.28	0.82
ERes	14.48	2.07

(a)

	Mean	St Dev
FWHM	1.36	0.18
PP	9.12	1.02
ERes	15.07	2.15

(b)

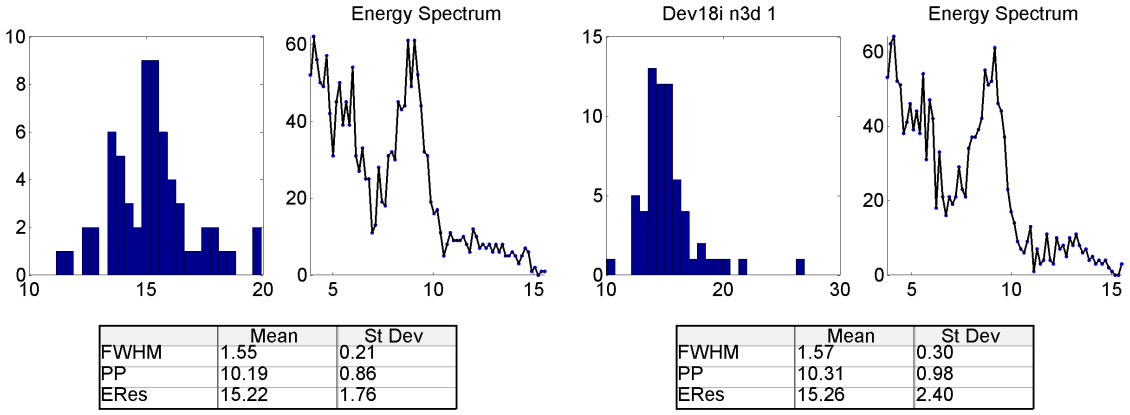

	Mean	St Dev
FWHM	1.55	0.21
PP	10.19	0.86
ERes	15.22	1.76

(c)

	Mean	St Dev
FWHM	1.57	0.30
PP	10.31	0.98
ERes	15.26	2.40

(d)

Figure A.16: For Agile crystal arrays with VM2000 inter-crystal reflector 1-4, energy resolution histograms for all 64 crystals (bar plot, upper left) as well as a representative energy spectrum (blue line, upper right), and the mean and standard deviation of energy parameters obtained from the 64 crystals (bottom table).

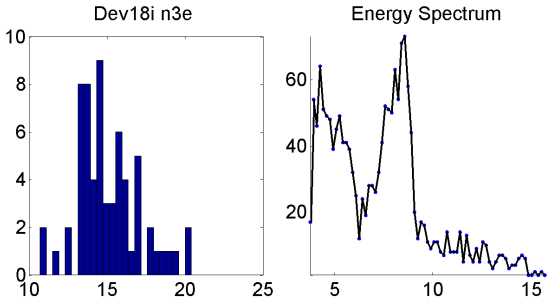

	Mean	St Dev
FWHM	1.37	0.21
PP	9.07	0.69
ERes	15.07	2.00

(a)

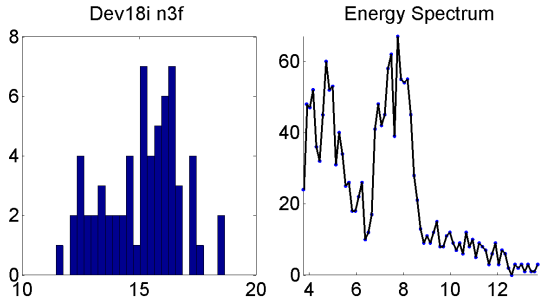

	Mean	St Dev
FWHM	1.33	0.16
PP	8.85	0.78
ERes	15.13	1.65

(b)

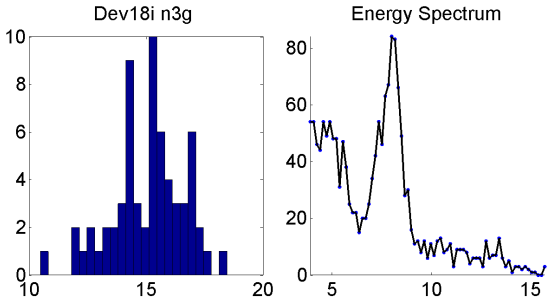

	Mean	St Dev
FWHM	1.33	0.16
PP	8.87	0.71
ERes	15.08	1.55

(c)

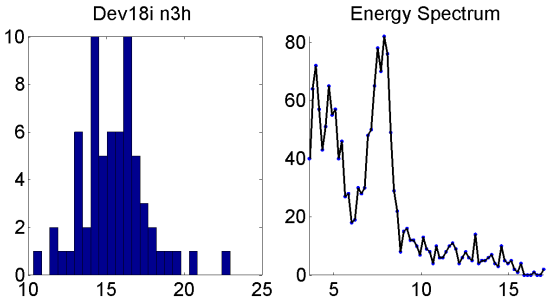

	Mean	St Dev
FWHM	1.36	0.20
PP	8.81	0.70
ERes	15.48	2.10

(d)

Figure A.17: For Agile crystal arrays with VM2000 inter-crystal reflector 5-8, energy resolution histograms for all 64 crystals (bar plot, upper left) as well as a representative energy spectrum (blue line, upper right), and the mean and standard deviation of energy parameters obtained from the 64 crystals (bottom table).

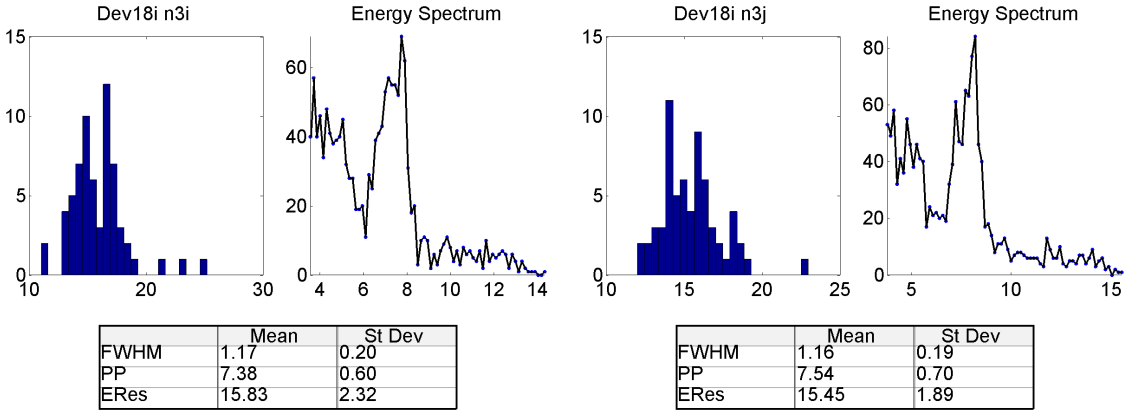

	Mean	St Dev
FWHM	1.17	0.20
PP	7.38	0.60
ERes	15.83	2.32

(a)

	Mean	St Dev
FWHM	1.16	0.19
PP	7.54	0.70
ERes	15.45	1.89

(b)

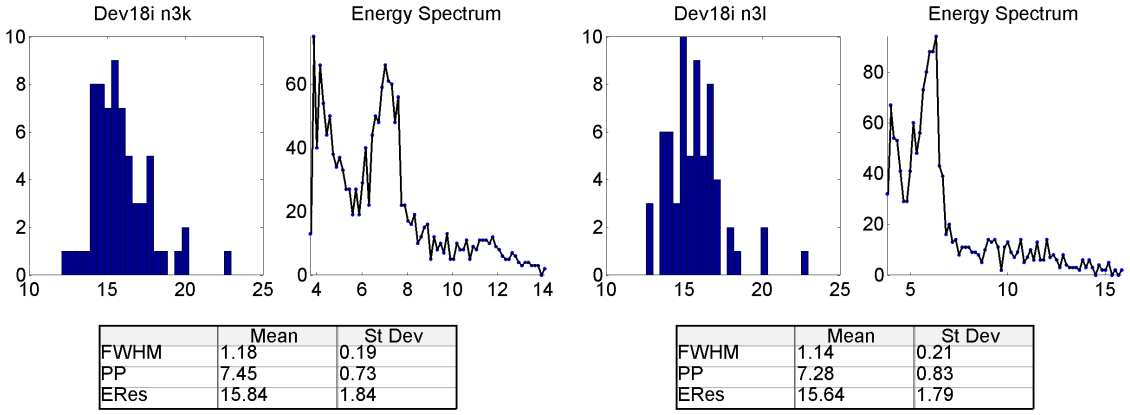

	Mean	St Dev
FWHM	1.18	0.19
PP	7.45	0.73
ERes	15.84	1.84

(c)

	Mean	St Dev
FWHM	1.14	0.21
PP	7.28	0.83
ERes	15.64	1.79

(d)

Figure A.18: For Agile crystal arrays with VM2000 inter-crystal reflector 9-12, energy resolution histograms for all 64 crystals (bar plot, upper left) as well as a representative energy spectrum (blue line, upper right), and the mean and standard deviation of energy parameters obtained from the 64 crystals (bottom table).

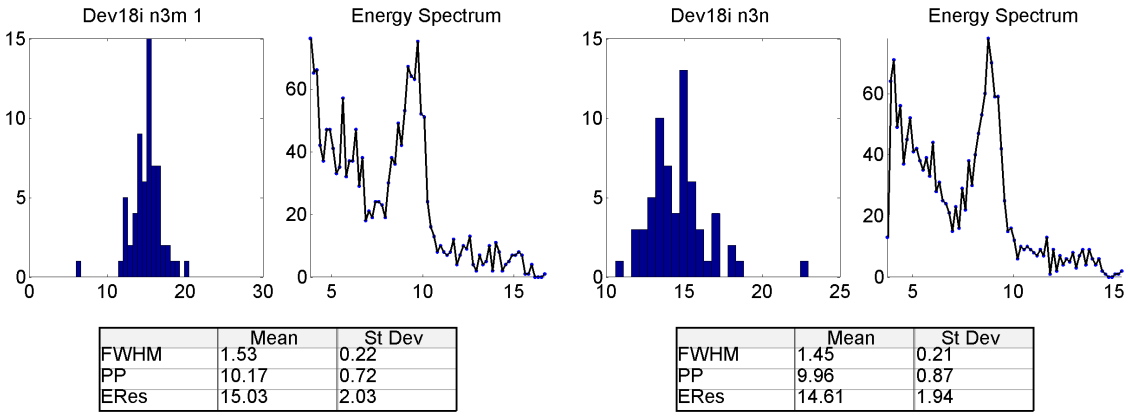

	Mean	St Dev
FWHM	1.53	0.22
PP	10.17	0.72
ERes	15.03	2.03

(a)

	Mean	St Dev
FWHM	1.45	0.21
PP	9.96	0.87
ERes	14.61	1.94

(b)

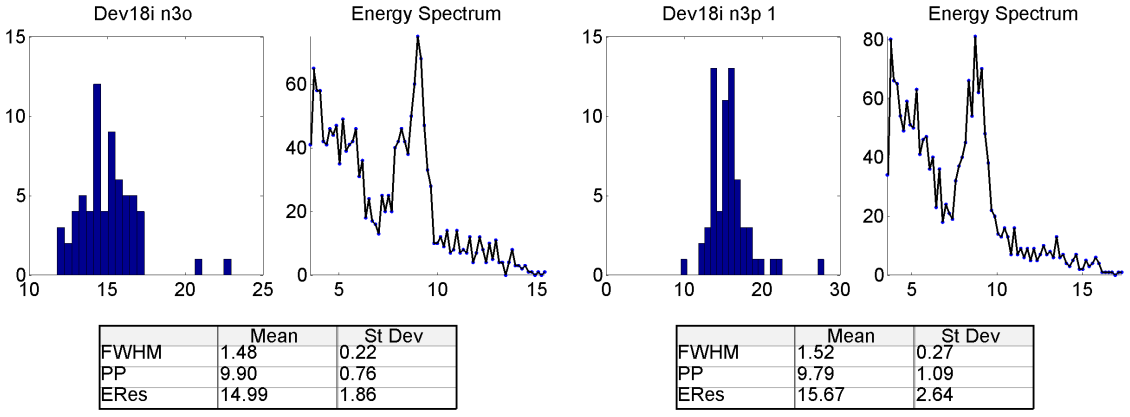

	Mean	St Dev
FWHM	1.48	0.22
PP	9.90	0.76
ERes	14.99	1.86

(c)

	Mean	St Dev
FWHM	1.52	0.27
PP	9.79	1.09
ERes	15.67	2.64

(d)

Figure A.19: For Agile crystal arrays with VM2000 inter-crystal reflector 13-16, energy resolution histograms for all 64 crystals (bar plot, upper left) as well as a representative energy spectrum (blue line, upper right), and the mean and standard deviation of energy parameters obtained from the 64 crystals (bottom table).

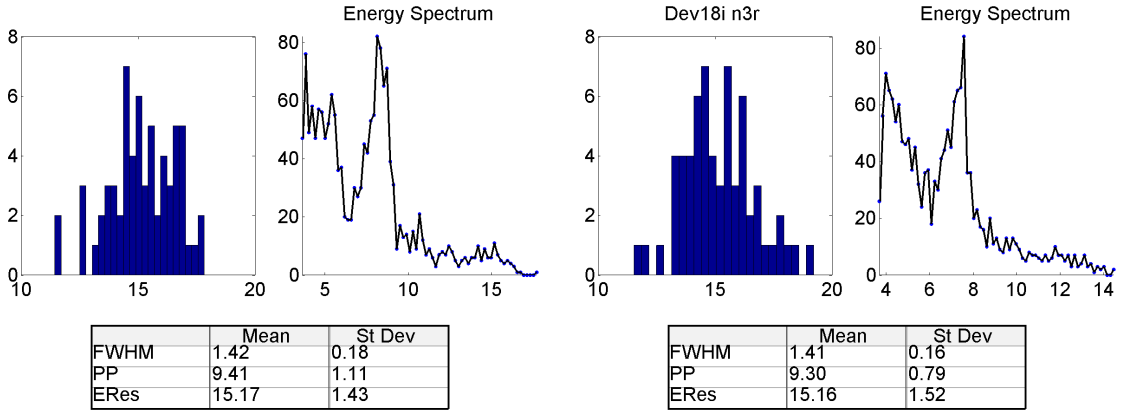

	Mean	St Dev
FWHM	1.42	0.18
PP	9.41	1.11
ERes	15.17	1.43

(a)

	Mean	St Dev
FWHM	1.41	0.16
PP	9.30	0.79
ERes	15.16	1.52

(b)

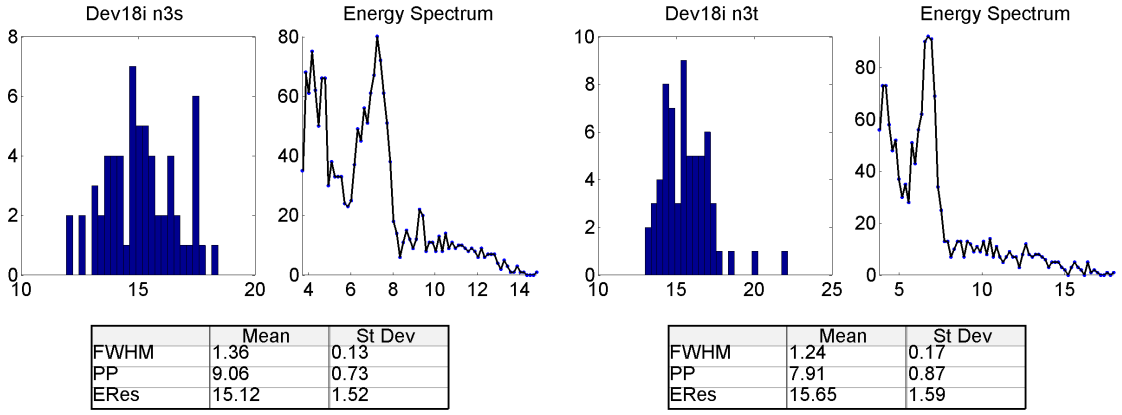

	Mean	St Dev
FWHM	1.36	0.13
PP	9.06	0.73
ERes	15.12	1.52

(c)

	Mean	St Dev
FWHM	1.24	0.17
PP	7.91	0.87
ERes	15.65	1.59

(d)

Figure A.20: For Agile crystal arrays with VM2000 inter-crystal reflector 17-20, energy resolution histograms for all 64 crystals (bar plot, upper left) as well as a representative energy spectrum (blue line, upper right), and the mean and standard deviation of energy parameters obtained from the 64 crystals (bottom table).

Bibliography

[1] http://micro.magnet.fsu.edu/primer/digitalimaging/concepts/photomultiplier, JUL 2004. Concepts in Digital Imaging Technology.

[2] http://www.gehealthcare.com/usen/funimg/pcimaging/products/vista.html, 2008. GE Healthcare.

[3] The clearpet lyso/luyap phoswich scanner a high performance small animal pet system. http://www.raytest.de/index2.html/pet/clearPET/clearPET.html, 2008. The ClearPET Collaboration.

[4] Simulations of preclinical and clinical scans in emission tomography. http://opengatecollaboration.healthgrid.org/, 2008. OpenGATE collaboration.

[5] Elfatih Abuelhia, K. Kacperski, and N. Spyrou. Three-photon annihilation in pet: 2d imaging experiments. *Journal of Radioanalytical and Nuclear Chemistry*, 271(2):489–495, Feb 2007.

[6] Bruce Alberts, Dennis Bray, Julian Lewis, Martin Raff, Keith Roberts, and James D Watson. *Molecular Biology of the Cell*. Garland Publishing Inc, 2nd edition, 1989.

[7] Adam Alessio, Ken Sauer, and Paul Kinahan. Analytical reconstruction of deconvolved fourier rebinned pet sinograms. *Phys. Med. Biol.*, 51:77–93, 2006.

[8] H. O. Anger. Scintillation camera with multichannel collimators. *Journal of Nuclear Medicine*, 65:515–531, JUL 1964.

[9] K Assi, I Gardin, P Vera, and I Buvat. Validation of the monte carlo simulator gate for indium 111 imaging. *Physics in Medicine and Biology*, 50:3113–3125, 2005.

[10] R. D. Badawi and P. K. Marsden. Developments in component-based normalization for 3d pet. *Phys Med Bio*, 44:571–594, 1999.

[11] Dale L. Bailey, David W. Townsend, Paul E. Kinahan, Sylke Grootoonk, and Terry Jones. An investigation of factors affecting detector and geometric correction in normalization of 3-d pet data. *IEEE Transactions on Nuclear Science*, 43(6):3300–3307, 1996.

[12] M. Balcerzyk, M. Moszynski, M. Kapusta, D. Wolski, J. Pawelke, and C. L. Melcher. Yso, lso, gso and lgso. a study of energy resolution and nonproportionality. *IEEE TRANSACTIONS ON NUCLEAR SCIENCE*, 47(4):1319–1323, 2000.

[13] W. C. Barber, T. Funk, M. McClish, K. S. Shah, and B. H. Hasegawa. Psapd gamma camera for spect imaging. *IEEE Nucl Sci Symp Conf Rec*, pages 2815 – 2817, Oct 2004.

[14] Catherine Beckers, Clio Ribbens, Batrice Andr, Stefaan Marcelis, Olivier Kaye, Luc Mathy, Marie-Jolle Kaiser, Roland Hustinx, Jacqueline Foidart, and Michel G. Malaise. Assessment of disease activity in rheumatoid arthritis with 18f-fdg pet. *Journal of Nuclear Medicine*, 45(6):956–964, 2004.

[15] M A Bedell, N A Jenkins, and N G Copeland. Mouse models of human disease. part i: techniques and resources for genetic analysis in mice. *Genes and Development*, 11:1–10, 1997.

[16] EL Berg, E Hytopoulos, I Plavec, and EJ Kunkel. Approaches to the analysis of cell signaling networks and their application in drug discovery. *Current Opinion in Drug Discovery and Development*, 8:107–114, 2005.

[17] Sandip Biswal, Donald L. Resnick, John M. Hoffman, and Sanjiv S. Gambhir. Molecular imaging: Integration of molecular imaging into the musculoskeletal imaging practice. *Radiology*, 244(3):651–671, 2007.

[18] R Boellaard, A van Lingen, and A A Lammertsma. Experimental and clinical evaluation of iterative reconstruction (osem) in dynamic pet: quantitative characteristics and effects on kinetic modeling. *Journal of Nuclear Medicine*, 42(5):808–817, May 2001.

[19] A. Braem, M. Chamizo, E. Chesi, N. Colonna, F. Cusanno, R. De Leo, F. Garibaldi, C. Joram, S. Marrone, S. Mathot, E. Nappi, F. Schoenahl, J. Seguinot, P. Weilhammer, and H. Zaidi. Novel design of a parallax free compton enhanced pet scanner. *Nuclear Instruments and Methods in Physics Research A*, 525:268–274, 2004.

[20] Philippe P Bruyant. Analytic and iterative reconstruction algorithms in spect. *Journal of Nuclear Medicine*, 43(10):1343–1358, 2002.

[21] K. C. Burr, A. Ivan, J. LeBlanc, S. Zelakiewicz, D. L.McDaniel, C. L. Kim, A. Ganinand K. S. Shah, R. Grazioso, R. Farrell, and J. Glodo. Evaluation of a position sensitive avalanche photodiode for pet. *IEEE Trans Nucl Sci*, 50(4):792–796, Aug 2003. Part 1.

[22] Kent C. Burr, Adrian Ivan, Donald E. Castleberry, Richard A. Thompson, James W. LeBlanc, Kanai S. Shah, and Richard Farrell. Depth-of-interaction-encoding high-resolution pet detector with sub-nanosecond timing. *IEEE Nuclear Science Symposium Conference Record*, pages 3880–3884, 2004.

[23] Charles Byrne. Likelihood maximization for list-mode emission tomographic image reconstruction. *IEEE Transactions on Medical Imaging*, pages 1084–1092, 2001.

[24] Franois Cayouette, Denis Laurendeau, and Christian Moisan. Detect2000: An improved monte-carlo simulator for the computer aided design of photon sensing devices. *Proc. SPIE*, 4833(69):69–76, 2003.

[25] M. T. Chan, R. M. Leahy, E. U. Mumcuoglul, S. R. Cherry, J. Czernin, and A. Chatziioannou. Comparing lesion detection performance for pet image reconstruction algorithms: a case study. *IEEE TRANSACTIONS ON NUCLEAR SCIENCE*, 44(4):1558–1563, Aug 1997.

[26] Guo-Ping Chang, Tinsu Pan, Feng Qiao, John Clark, and Osama Mawlawi. Improving pet image resolution and snr with super resolution post-processing. *Journal of Nuclear Medicine*, 48, 2007.

[27] A. Chatziioannou, J. Qi, A. Moore, A. Annala, K. Nguyen, R. Leahy, and S. R. Cherry. Comparison of 3-d maximum a posteriori and filtered backprojection algorithms for high-resolution animal imaging with micropet. *IEEE TRANSACTIONS ON MEDICAL IMAGING*, 19(5):507–512, 2000.

[28] A. F. Chatziioannou, Simon R. Cherry, Y. P. Shao, R. W. Silverman, K. Meadors, T. H. Farquhar, and M. Pedarsani amd M. E. Phelps. Performance evaluation of micropet: A high-resolution lutetium oxyorthosilicate pet scanner for animal imaging. *J. Nucl. Med.*, 40(7):1164–1175, Jul 1999.

[29] Jiaming Chen, Liyuan Zhang, , and Ren yuan Zhu. A further study on large size lso and lyso crystal samples. *IEEE Nuclear Science Symposium Record*, 2005.

[30] Simon R. Cherry, Yiping Shao, Stefan Siegel, Robert W. Silverman, Erkan Mumcuoglu, Ken Meadors, and Michael E. Phelps. Optical fiber readout of

scintillator arrays using a multi-channel pmt: A high resolution pet detector for animal imaging. *IEEE Trans Nucl Sci*, pages 1766–1770, 1996.

[31] Simon R Cherry, James A Sorenson, and Michael E Phelps. *Physics in Nuclear Medicine*. Saunders, 3rd edition, 2003.

[32] SR Cherry, S Siegel, AR Ricci, L Eriksson, EJ Hoffman, and ME Phelps. Development of position sensitive detectors for use in positron emission tomography of small laboratory animals. *Nuclear Instruments & Methods in Physics Research, Section A: Accelerators, Spectrometers, Detectors and Associated Equipment*, 348(2-3):613–617, Sept 1 1994.

[33] G. Chinn, A. M. K. Foudray, and C. S. Levin. Accurately positioning and incorporating large-angle tissue-scattered photons into pet image reconstruction. *IEEE Nuclear Science Symposium and Medical Imaging Conference Record*, pages 1746–1751, 2006.

[34] G. Chinn, A. M. K. Foudray, and C. S. Levin. A method to include single photon events in image reconstruction for a 1 mm resolution pet system built with advanced 3d positioning detectors. *IEEE Nuclear Science Symposium and Medical Imaging Conference Record*, pages 1740–1745, 2006.

[35] Giovanni Di Chiro, Robert L. DeLaPaz, Rodney A. Brooks, Louis Sokoloff, Paul L. Kornblith, Barry H. Smith, Nicholas J. Patronas, Conrad V. Kufta, Robert M. Kessler, Gerald S. Johnston, Ronald G. Manning, and Alfred P. Wolf. Glucose utilization of cerebral gliomas measured by [18f] fluorodeoxyglucose and positron emission tomography. *Neurology*, 32:1323–1329, 1982.

[36] Guido Di Cocco, Giuseppe Malaguti, Ezio Caroli, Gianclaudio Ferro, D. Grassi, Claudio Labanti, A. Mauri, Elio Rossi, Filomena Schiavone, Aldo Spizzichino, and Alessandro Traci. Use of compton kinematics on the ibis telescope. *Proc. SPIE*, 2806, 2004.

[37] Cremat. *CR-110 charge sensitive preamplifier: application guide*. 45 Union St., Watertown, MA 02472. http://cremat.com/CR-100.pdf.

[38] Dermott E. Cullen. Nuclear and atomic data. https://wci.llnl.gov/codes/tart/nuclearatomic.html, 1997.

[39] Margaret E. Daube-Witherspoon, Joel S. Karp, Michael E. Casey, Frank P. DiFilippo, Horace Hines, Gerd Muehllehner, Vilim Simcic, Charles W. Stearns, Lars-Eric Adam, Steve Kohlmyer, and Vesna Sossi. Pet performance measurements using the nema nu 2-2001 standard. *J. Nuc. Med.*, 43(10):1398–1409, 2002.

[40] Hugo de Jong, Ronald Boellaard, Christof Knoess, Mark Lenox, Christiaan Michel, Mike Casey, and Adriaan Lammertsma. Correction methods for missing data in sinograms of the hrrt pet scanner. *IEEE Trans on Nucl Sci*, 50(5):1452–1456, Oct 2003. Part 2.

[41] Arthur Dempster, Nan Laird, and Donald Rubin. Likelihood from incomplete data via the em algorithm. *Journal of the Royal Statistical Society*, 39(1):1–38, 1977.

[42] P. Despres, W. C. Barber, T. Funk, M. McClish, K. S. Shah, and B. H. Hasegawa. Investigation of a continuous crystal psapd-based gamma camera. *IEEE Transactions on Nuclear Science*, 53(3):1643–1649, 2006.

[43] Philippe Despres, William C. Barber, Tobias Funk, Mickel McClish, Kanai S. Shah, and Bruce H. Hasegawa. Pincushion distortion correction in position-sensitive avalanche photodiodes. *IEEE Nuclear Science Symposium Conference Record*, pages 2031–2035, 2005.

[44] Andrew P. Dhanasopon, Craig S. Levin, Angela M. K. Foudray, Peter D. Olcott, and Frezghi Habte. Scintillation crystal design features for a miniature gamma ray camera. *IEEE Transactions on Nuclear Science*, 52(5):1439–1446, 2005.

[45] P. A. Dokhale, R. W. Silverman, Kanai S. Shah, R. Grazioso, Richard Farrell, J. Glodo, M. A. McClish, G. Entine, V. H. Tran, and Simon R. Cherry. Performance measurements of a depth-encoding pet detector module based on position-sensitive avalanche photodiode read-out. *Phys. Med. Bio,*, 49(18):4293–4304, Sep 2004.

[46] Tyler Dumouchel, Vitali Selivanov, Jules Cadorette, Roger Lecomte, and Robert A. deKemp. Mlem reconstructed image resolution from the labpet animal scanner. *IEEE Nuclear Science Symposium and Medical Imaging Conference Record*, 2006.

[47] Yusuf E. Erdi, Sadek A. Nehmeh, Tim Mulnix, John L. Humm, and Charles C. Watson. Pet performance measurements for an lsobased combined pet/ct scanner using the national electrical manufacturers association nu 2-2001 standard. *J. Nuc. Med.*, 45(5), 2004.

[48] T. H. Farquhar, A. Chatziioannou, and S. R. Cherry. An evaluation of exact and approximate 3-d reconstruction algorithms for a high- resolution, small-animal pet scanner. *IEEE TRANSACTIONS ON MEDICAL IMAGING*, 17(6):1073–1080, 1998.

[49] N. C. Ferreira, R. Trbossen, C. Comtat, M.-C. Grgoire, and B. Bendriem. Iterative crystal efficiency calculation in fully 3-d pet. *IEEE Transactions on Medical Imaging*, 19(5):485–492, 2000.

[50] A.M.K. Foudray, R. Farrell, P.D. Olcott, K.S. Shah, and C.S. Levin. Characterization of two thin postion-sensitive avalanche photodiodes on a single flex circuit for use in 3-d positioning pet detectors. *IEEE NSS-MIC Conference Record*, 4:2008–2010, Nov 2006.

[51] Angela M. K. Foudray, Frezghi Habte, Garry Chinn, Jin Zhang, Craig S. Levin, and Peter D. Olcott. Optimization of a pet breast imaging system comprised of position sensitive avalanche photodiodes utilizing monte carlo simulation. *Presented at the 2004 IEEE NSS-MIC Breast Cancer Workshop*, 2004.

[52] Angela M. K. Foudray, Frezghi Habte, Craig S. Levin, and Peter D. Olcott. Positioning annihilation photon interactions in a thin lso crystal sheet with a position-sensitive avalanche photodiode. *IEEE Trans Nucl Sci*, 2005. accepted.

[53] Angela M. K. Foudray and Craig S. Levin. Bayesian estimator for angle recovery: Event classification and reconstruction in positron emission tomography. *to appear in AIP Maximum Entropy and Bayesian Interference (accepted with minor revisions)*, 2007.

[54] Anna Fredriksson, Karin Ekberg, Martin Ingvar, Bo-Lennart Johansson, John Wahren, and Sharon Stone-Elander. In vivo biodistribution and pharmacokinetics of 18f-labeled human c-peptide: evaluation in monkeys using positron emission tomography. *Life Sciences*, 71(12):1361–1370, Aug 2002.

[55] D L Fried. Noise in photoemission current. *Applied Optics*, 4(1):79–80, 1965.

[56] Sanjiv S. Gambhir, Jorge R. Barrio, Michael E. Phelps, Meera Iyer, Mohammad Namavari, Nagichettiar Satyamurthy, Lily Wu, Leeta A. Green, Eileen Bauer, Duncan C. MacLaren, Khoi Nguyen, Arnold J. Berk, Simon R. Cherry, and Harvey R. Herschman. Imaging adenoviral-directed reporter gene expression in living animals with positron emission tomography. *Proceedings of the National Academy of Sciences of the United States of America*, 96(5):2333–2338, Mar 1999.

[57] A. Garson, H. Krawczynski, J. Grindlay, G. J. Fishman, and C. A. Wilson. Using the active collimator and shield assembly of an exist-type mission as a gamma-ray burst spectrometer. *Astronomy and Astrophysics*, 456:379–387, 2006.

[58] P Gonias, N Berysekas, P Liaparinos, D Cavouras, I Kandarakis, G Panayiotakis, G Saatsakis, D Nikolopoulos, G Loudos, n Sakelios, N Karakatsanis, A Gaitanis, L Papaspyrou, and A Daskalakis. Validation of a gate model for the simulation of the siemens pet/ct biograph 6 scanner. *Nucl. Instr. Meth. Phys. Res.*, 571:263–266, 2007.

[59] Alberto Del Guerra, Antonietta Bartoli, Nicola Belcari, Deborah Herbert, Alfonso Motta, Angela Vaiano, Giovanni Di Domenico, Nicola Sabba, Elena Moretti, Guido Zavattini, Marco Lazzarotti, Luca Sensi, Michele Larobina, and Licia Uccelli. Performance evaluation of the fully engineered yap-(s)pet scanner for small animal imaging. *IEEE TRANSACTIONS ON NUCLEAR SCIENCE*, 53(3):1078–1083, 2006.

[60] Pedro Guerra, Jose L. Rubio, Juan E. Ortuno, Georgios Kontaxakis, Maria J. Ledesma, and Andres Santos. Performance analysis of a low-cost small animal pet/spect scanner. *Nuclear Instruments and Methods in Physics Research A*, 571:98–101, 2007.

[61] I. R. Gulakov, V. B. Zalesskii, A. O. Zenevich, and T. R. Leonova. A study of avalanche photodetectors with a large photosensitive surface in the photon counting mode. *Instruments and Experimental Techniques*, 50(2):249–252, 2007.

[62] F. Habte, Peter D. Olcott, Angela M. K. Foudray, Craig S. Levin, Jin Zhang, and Garry Chinn. Simulation and measurement of gamma ray and annihilation photon imaging detectors. *IEEE Trans. Nucl. Sci.*, 6:4019–4022, 2004.

[63] Eberhard Haug and Werner Nakel. *The Elementary Process of Bremsstrahlung*, volume Lecture Notes in Physics, 73. World Scientific Publishing Company, May 2004.

[64] R. J. Hicks, D. Dorow, and P. Roselt. Pet tracer development–a tale of mice and men. *Cancer Imaging*, 31(6):S102–S106, Oct 2006.

[65] J D Hove, R Rasmussen, J Freiberg, S Holm, H Kelbaek, and K E Kofoed. Clinical evaluation of iterative reconstruction (ordered-subset expectation maximization) in dynamic positron emission tomography: quantitative effects on kinetic modeling with n-13 ammonia in healthy subjects. *Journal of Nuclear Cardiology*, 2008.

[66] H. Malcom Hudson and Richard S Larkin. Accelerated image reconstruction using ordered subsets of projection data. *IEEE Trans. Med. Imag.*, 13(4):601–609, 1994.

[67] Buvat I and Lazaro D. Monte carlo simulations in emission tomography and gate: an overview. *Nucl. Instr. Meth. Phys. Res.*, 569:323–329, 2006.

[68] Masayuki Inubushi, Joseph C. Wu, Sanjiv S. Gambhir, Gobalakrishnan Sundaresan, Nagichettiar Satyamurthy, Mohammad Namavari, Simon Yee, Jorge R. Barrio, David Stout, Arion F. Chatziioannou, Lily Wu, and Heinrich R. Schelbert. Positron-emission tomography reporter gene expression imaging in rat myocardium. *Circulation*, 107(2):326–332, 2002.

[69] Bernd Jahne. *Digital Image Processing*. Springer, 5th edition edition, 2001.

[70] S Jan, C Comtat, D Strul, G Santin, and R Trbossen. Monte carlo simulation for the ecat exact hr+ system using gate. *IEEE Trans. Nucl. Sci.*, 52:627–633, 2005.

[71] S. Jan, A. Desbre, F. Pain, D. Guez, C. Comtat, H. Gurden, S. Kerhoas, P. Lanice, F. Lefebvre, R. Mastrippolito, and R. Trebossen. Monte carlo simulation of the micropet focus system for small rodents imaging applications. *IEEE Nuclear Science Symposium Conference Record*, 2005.

[72] S. Jan, G. Santin, D. Strul, S. Staelens, K. Assie, D. Autret, S. Avner, R. Barbier, M. Bardies, P. M. Bloomfield, D. Brasse, V. Breton, P. Bruyndonckx, I. Buvat, A. F. Chatziioannou, Y. Choi, Y. H. Chung, C. Comtat, D. Donnarieix, L. Ferrer, S. J. Glick, C. J. Groiselle, D. Guez, P. F. Honore, S. Kerhoas-Cavata, A. S. Kirov, V. Kohli, M. Koole, M. Krieguer, D. J. van der Laan, F. Lamare, G. Largeron, C. Lartizien, D. Lazaro M. C. Maas, L. Maigne, F. Mayet, F. Melot, C. Merheb, E. Pennacchio, J. Perez, U. Pietrzyk, F. R. Rannou, M. Rey, D. R. Schaart, C. R. Schmidtlein, L. Simon, T. Y. Song, J. M. Vieira, D. Visvikis, R. V. de Walle, E. Wieers, and C. Morel. Gate: a simulation toolkit for pet and spect. *Phys. Med. Bio.*, 49(19):4543–4561, Oct 2004.

[73] Martin Janecek and William W. Moses. Design of an instrument to measure optical reflectance of scintillating crystal surfaces. *IEEE Transactions on Nuclear Science*, 55(3):1381–1386, Jun 2008.

[74] A. P. Jeavons, R. A. Chandler, and C. A. Dettmar. A 3d hidac-pet camera with sub-millimetre resolution for imaging small animals. *IEEE Trans. Nucl. Sci.*, 46(3):468–473, Jun 1999. Part 2.

[75] Ron Jenkins, R. W. Gould, and Dale Gedcke. *Quantitative X-ray Spectrometry (Practical Spectroscopy)*. Marcel Dekker, 2nd edition, Apr 1995.

[76] J. Joung, R. S. Miyaoka, and T. K. Lewellen. cmice:a high resolution animal pet using continuous lso with a statistics based positioning scheme. *Nucl. Instr. Meth. Phys. Res. Sect. A*, 489(1–3):584–598, Aug 2002.

[77] Katrin Kaarstad, Dirk Bender, Lise Bentzen, Ole Lajord Munk, and Susanne Keiding. Metabolic fate of 18f-fdg in mice bearing either sccvii squamous cell carcinoma or c3h mammary carcinoma. *Journal of Nuclear Medicine*, 43(7):940–947, 2002.

[78] Krzysztof Kacperski, Nicholas M. Spyrou, and F. Alan Smith. Three-gamma annihilation imaging in positron emission tomography. *IEEE TRANSACTIONS ON MEDICAL IMAGING*, 23(4):525–529, Apr 2004.

[79] Avinash C Kak and Malcom Slaney. *Principles of Computerized Tomographic Imaging*. IEEE Press, online edition, 1999.

[80] L. A. Kappers, R. H. Bartram, D. S. Hamilton, A. Lempicki, and J. Glodo. Thermal quenching and electron traps in lso. *Journal of Luminescence*, 102–103:162–165, May 2003.

[81] Hidefumi Kawashima, Yuji Kuge, Kazuyoshi Yajima, Yoshihiro Miyake, and Naoto Hashimoto. Development of step-specific pet tracers for studying fatty acid ?-oxidation: biodistribution of [1-11c] octanoate analogs in rats and a cat. *Nuclear Medicine and Biology*, 25(6):543–548, 1998.

[82] I. Kawrakow and D.W.O. Rogers. The egsnrc code system: Monte carlo simulation of electron and photon transport. Technical report, Ionizing Radiation Standards, National Research Council of Canada, SEP 2006. NRCC Report PIRS-701.

[83] Iwan Kawrakow, Krassimir Mitev, Georgi Gerganov, Jordan Madzhunkov, and Assen Kirov. Efficient photon transport in positron emission tomography simulations using vmc++. *Journal of Physics: Conference Series*, 102, 2008.

[84] Karin Kneaurek and Josef Machac. Comparison of 18f spect with pet in myocardial imaging: A realistic thorax-cardiac phantom study. *BMC Nuclear Medicine*, 6(5), 2006.

[85] Karin Knesaurek and Josef Machac. Improving 3d pet imaging by restoration: a phantom study. *Computerized Medical Imaging and Graphics*, 29(1):15–19, Jan 2004.

[86] Glenn F Knoll. *Radiation Detection and Measurement*. John Wiley and Sons, Inc., 3rd edition, 1999.

[87] Richard Laforest, Desmond Longford, Stefan Siegel, Danny F. Newport, and Jeffrey Yap. Performance evaluation of the micropet-focus - f120. *IEEE Nuclear Science Symposium Conference Record*, 2004.

[88] F Lamare, A Turzo, Y Bizais, C C Le Rest, and D Visvikis. Validation of a monte carlo simulation of the philips allegro/gemini pet systems using gate. *Phys. Med. Biol.*, 51:943–962, 2006.

[89] Michele Larobina, Arturo Brunetti, and Marco Salvatore. Small animal pet: A review of commercially available imaging systems. *Current Medical Imaging Reviews*, 2:187–192, 2006.

[90] F. W. Y. Lau, P. D. Olcott, M. A. Horowitz, Hao Peng, and C. S. Levin. Noise analysis of lso-psapd pet detector front-end multiplexing circuits. *IEEE Nuclear Science Symposium Conference Record*, 5:3206–3211, 2007.

[91] R. Lecomte, C. Pepin, D. Rouleau, A. Saoudil, M.S. Andreaco, M. Casey, R. Nutt, H. Dautet, and P.P. Webb. Investigation of gso, lso and yso scintillators using reverse avalanche photodiodes. *IEEE Trans Nucl Sci*, 45:478–482, Jun 1998.

[92] Kisung Lee, Paul E. Kinahan, Robert S. Miyaoka, Jae-Seung Kim, and Tom K. Lewellen. Impact of system design parameters on image figures of merit for a mouse pet scanner. *IEEE Transactions on Nuclear Science*, 51(1):27–33, Feb 2004.

[93] Ch Lerche, JM Benlloch, F Sanchez, N Pavon, EN Gimeneza, M Gimenez, M Fernandez, J Cerdaa nd J Martinez, and A Sebastia. Depth of interaction measurement in gamma ray imaging detectors with continuous scintillation crystals. *IEEE Nuclear Science Symposium Conference Record*, 3:2169–2173, 2003.

[94] Claude Leroy and Pier-Giorgio Rancoita. *Principles Of Radiation Interaction In Matter And Detection*. World Scientific Publishing Company, 1998.

[95] C. S. Levin. Design of a high-resolution and high-sensitivity scintillation crystal array for pet with nearly complete light collection. *IEEE Trans Nucl Sci*, 49(5):2236 – 2243, Oct 2002. Part 1.

[96] C. S. Levin, A. M. K. Foudray, P. D. Olcott, and F. Habte. Investigation of position sensitive avalanche photodiodes for a new high resolution pet detector design. *IEEE Nucl Sci Symp Conf Rec*, 4:2262 – 2266, Oct 2003.

[97] C. S. Levin, A. M. K. Foudray, P. D. Olcott, and F. Habte. Investigation of position sensitive avalanche photodiodes for a new high resolution pet detector design. *IEEE Trans. Nucl. Sci.*, 51(3):805–810, June 2004.

[98] Craig S. Levin, Frezghi Habte, and Angela M. K. Foudray. Methods to extract more light from minute scintillation crystals used in an ultra-high resolution positron emission tomography detector. *Nucl. Instr. Meth. Phys. Res. Sect. A*, 527(1–2):35–40, Jul 2004.

[99] Craig S Levin and Edward J Hoffman. Calculation of positron range and its effect on the fundamental limit of positron emission tomography system spatial resolution. *Phys. Med. Biol.*, 44:781–799, 1999.

[100] Hongdi Li, Yaqiang Liu, Tao Xing, Yu Wang, Jorge Uribe, Hossain Baghaei, Shuping Xie, Soonseok Kim, Rocio Ramirez, and Wai-Hoi Wong. An instantaneous photomultiplier tube gain-tuning method for pet or gamma camera detectors using an led network. *IEEE TRANSACTIONS ON NUCLEAR SCIENCE*, 52(5):1295–1299, OCT 2005.

[101] Wen Ping Li, Laura A. Meyer, David A. Capretto, Christopher D. Sherman, and Carolyn J. Anderson. Receptor-binding, biodistribution, and metabolism studies of 64cu-dota-cetuximab, a pet-imaging agent for epidermal growth-factor receptor-positive tumors. *Cancer Biotherapy and Radiopharmaceuticals*, 23(2):158–171, 2008.

[102] T Ling, TH Burnett, TK Lewellen, and RS Miyaoka. Parametric positioning of a continuous crystal pet detector with depth of interaction decoding. *Physics in Medicine and Biology*, 2008.

[103] Bo Liu, Chaoshu Shia, Min Yina, Yibin Fub, Guobin Zhangb, and Guohao Renc. Luminescence and energy transfer processes in lu2sio5:ce3+ scintillator. *Journal of Luminescence*, 117:129–134, Jun 2005.

[104] A Lohstroh1, P J Sellin, and A Simon. High-resolution mapping of the mobility-lifetime product in cdznte using a nuclear microprobe. *J. Phys.: Condens. Matter*, 16:S67–S73, 2004.

[105] T. Ludziejewski, K. Moszyriska, M. Moszynski, D. Wolski, W. Klamra, L.O. Norlin, E. Devitsin, and V. Kozlov. Advantages and limitations of lso scintillator in nuclear physics experiments. *IEEE TRANSACTIONS ON NUCLEAR SCIENCE*, 42(4):328–336, AUG 1995.

[106] P Mahy, M De Bast, T de Groot, A Cheguillaume, J Gillart, K Haustermans, D Labar, and V Grgoire. Comparative pharmacokinetics, biodistribution, metabolism and hypoxia-dependent uptake of [(18)f]-ef3 and [(18)f]-miso in rodent tumor models. *Radiother Oncol.*, 2008.

[107] I. Makkonen, M. Hakala, , and M. J. Puska. Modeling the momentum distributions of annihilating electron-positron pairs in solids. *Physical Review B*, 73:1–12, 2006.

[108] Ravindra M. Manjeshwar, Yiping Shao, and Floris P Jansen. Image quality improvements with time-of-flight positron emission tomography for molecular imaging. *IEEE Trans. Nucl. Sci.*, NS-28(853–856), 2005.

[109] Norma V.S. Marinho, Bruce E. Keogh, Durval C. Costa, Adriaan A. Lammerstma, Peter J. Ell, and Paolo G. Camici. Pathophysiology of chronic left ventricular dysfunction: New insights from the measurement of absolute myocardial blood flow and glucose utilization. *Circulation*, 93:737–744, 1996.

[110] C. J. Marrioitt, J. E. Cadorette, R. Lecomte, V. Scasnar, J. Rousseaau, and J.E. van Lier. High-resolution pet imaging and quantitation of pharmaceutical biodistributions in a small animal using avalanche photodiode detectors. *J. Nucl. Med.*, 35(8):1390–1396, Aug 1994.

[111] C. L. Melcher and J. S. Schweitzer. Cerium-doped lutetium oxyorthosilicate: a fast, efficient new scintillator. *IEEE Trans Nucl Sci*, 39(4):502 – 505, Aug 1992.

[112] C Merheb, S Nicol, Y Petegnief, J N Talbot, and I Buvat. ssessment of the mosaic animal pet system response using list-mode data for validation of gate monte carlo modelling. *Nucl. Instrum. Meth. A*, 569:220–224, 2006.

[113] John Missimer, Zoltan Madi, Michael Honer, Claudia Keller, August Schubiger, and Simon-Mensah Ametamey. Performance evaluation of the 16-module quadhidac small animal pet camera. *Physics in Medicine and Biology*, 49:2069–2081, 2004.

[114] Gregory S. Mitchell, Shrabani Sinha, Jennifer R. Stickel, Spencer L. Bowen, Leonard J. Cirignano, Purushottam Dokhale, Hadong Kim, Kanai S. Shah, and Simon R. Cherry. Cdte strip detector characterization for high resolution small animal pet. *IEEE TRANSACTIONS ON NUCLEAR SCIENCE*, 55(3):870–876, Jun 2008.

[115] Robert S. Miyaoka, Sung-Kwan Joo, and Kisung Lee. Detector light response modeling for a thick continuous slab detector. *Journal of Nuclear Science and Technology*, 45(7):634–638, 2008.

[116] Seng-Peng Mok, Chao-Hsing Wang, Jyh-Cheng Chen, and Ren-Shyan Liu. Performance evaluation of the high resolution small animal pet scanner. *BIOMEDICAL ENGINEERING APPLICATIONS, BASIS AND COMMUNICATIONS*, 15:143–149, Aug 2003.

[117] William W. Moses. Trends in pet imaging. *Nuclear Instruments and Methods A*, 471:209–214, 2001.

[118] Erkan U. Mumcuoglu, Richard Leahy, Simon R. Cherry, and Zhenyu Zhou. Fast gradient-based methods for bayesian reconstruction of transmission and emission pet images. *IEEE TRANSACTTONS ON MEDICAL IMAGING*, 13(4):687–701, Dec 1998.

[119] S Naidoo-Variawa, A J Hey-Cunningham, WLehnert, P L Kench, M Kassiou, R Banati, and S R Meikle. High-resolution imaging of the large non-human primate brain using micropet: a feasibility study. *Phys. Med. Biol.*, 52:6627–6638, 2007.

[120] M. Nakayamaa, N. Andoa, J. Hiraia, and H. Nishimura. Scintillation activated bynanoparticle formation in csi:na thin films. *Journal of Luninescence*, 108:359–363, 2004.

[121] Frank Natterer. Numerical methods in tomography. *Acta Numerica*, pages 107–141, 1999.

[122] Olivier Christiaan Neels. *Tracer development for detection and characterization of neuroendocrine tumors with PET*. PhD thesis, University of Groningen, 2008.

[123] Y. Nemirovsky, G. Asa, A. Ruzin, J. Gorelik, and R. Sudharsanan. Characterization of dark noise in cdznte spectrometers. *Journal of Electronic Materials*, 27(6):807–812, 1998.

[124] Damian OConnell and David Roblin. Translational research in the pharmaceutical industry: from bench to bedside. *Drug Discovery Today*, 11(17/18):833–838, 2006.

[125] Yuu Okada, Tadayuki Takahashi, Goro Sato, Shin Watanabe, Kazuhiro Nakazawa, Kunishiro Mori, and Kazuo Makishima. Cdte and cdznte detectors for timing measurements. *IEEE TRANSACTIONS ON NUCLEAR SCIENCE*, 49(4):1986–1992, APR 2002.

[126] Shinichi Okazumi, Kaichi Isono, Kazuo Enomoto, Toshiyuki Kikuchi, Masahiko Ozaki, Hiroshi Yamamoto, Haruyuki Hayashi, Takehide Asano, and Munemasa Ryu. Evaluation of liver tumors using fluorine- 18-fluorodeoxyglucose pet: Characterization of tumor and assessment of effect of treatment. *Journal of Nuclear Medicine*, 33(3):333–339, 1992.

[127] P. D. Olcott, F. W. Y. Lau, and C. S. Levin. Data acquisition system design for a 1 mm3 resolution psapd-based pet system. *IEEE Nuclear Science Symposium Conference Record*, 5:3206–3211, 2007.

[128] Peter D. Olcott, Jin Zhang, Craig S. Levin, Frezghi Habte, and Angela M. K. Foudray. Finite element model based spatial linearity correction for scintillation detectors that use position sensitive avalanche photodiodes. *IEEE Nuclear Science Symposium Conference Record*, pages 2459–2462, 2005.

[129] J. M. Ollinger. Detector efficiency and compton scatter in fully 3d pet. *IEEE Trans Nucl Sci*, 42(4), 1995.

[130] Beth W. Orenstein. New tracers - beyond fdg. *Radiology Today*, 6(2):8, 2005.

[131] Joseph A O'Sullivan, Richard E Blahut, and Donald A Snyder. Information-theoretic image formation. *IEEE Transactions on Information Theory*, 44(6):2094–2123, 1998.

[132] Anne M. J. Paans and Jan Pruim. Tissue-specific differences in 2-fluoro-2-deoxyglucose metabolism beyond fdg-6-p: a 19f nmr spectroscopy study in the rat. *NMR Biosci.*, 17(4):206–207, Jun 2004.

[133] Sang-June Park, W Leslie Rogers, and Neal H Clinthorne. Improvement of noise equivalent count rate using compton kinematics in a compton pet. *IEEE Transactions on Nuclear Science*, 54(5):1589–1598, Oct 2007.

[134] Sang-June Park, W Leslie Rogers, Sam Huh, Harris Kagan, Klaus Honscheid, Don Burdette, Enrico Chesi, Carlos Lacasta, Gabriela Llosa, Marko Mikuz, Andrej Studen, Peter Weilhammer, and Neal H Clinthorne. Performance evaluation of a very high resolution small animal pet imager using silicon scatter detectors. *Phys Med Biol*, 52:2807–2826, 2007.

[135] Giovanni Paternostro, Paolo G. Camici, Adriaan A. Lammerstma, Norma Marinho, Ragavendra R. Baliga, Jaspal S. Kooner, George K. Radda, and Ele Ferrannini. Cardiac and skeletal muscle insulin resistance in patients with coronary heart disease: A study with positron emission tomography. *J. Clin. Invest.*, 98(9):2094–2099, Nov 1996.

[136] A. Pauchard, P. A. Bessea, M. Bartek, R. F. Wolffenbuttel, and R. S. Popovic. Ultraviolet-selective avalanche photodiode. *Sensors and Actuators A: Physical*, 82(1-3):128–134, May 2000.

[137] C. Pedrini. Scintillation mechanisms and limiting factors on each step of relaxation of electronic excitations. *Physics of the Solid State*, 47:1406–1411, 2005.

[138] H Peng, P D Olcott, A M K Foudray, and C S Levin. Evaluation of free-running adcs for high resolution pet data acquisition. *IEEE Nuclear Science Symposium Conference Record*, 5:3328–3331, 2007.

[139] B. J. Pichler, B. K. Swann, J. Rochelle, R. E. Nutt, Simon R. Cherry, and S. B. Siegel. Lutetium oxyorthosilicate block detector readout by avalanche photodiode arrays for high resolution animal pet. *Phys. Med. Bio.*, 49(18):4305–4319, Sep 2004.

[140] E Ponty, G Favre, R Benaniba, A Boneu, G Soula, and M Carton. Biodistribution study of 99mtc labeled low density lipoprotein in b16 melanoma rearing mice. visualization of a differential fixation in tumoral tissue. *IEEE Engineering in Medicine and Biology*, 14:1809–1810, 1992.

[141] G. Pratx, G. Chinn, F. Habte, P. D. Olcott, and C. S. Levin. Fully 3-d list-mode osem accelerated by graphics processing units. *IEEE Nuclear Science Symposium Conference Record*, 4:2196–2202, 2006.

[142] J. Qi and Richard M. Leahy. A theoretical study of the contrast recovery and variance of map reconstructions from pet data. *IEEE Transactions on Medical Imaging*, 18(4):293–305, April 1999.

[143] Jinyi Qi. Comparison of statistical reconstructions with isotropic and anisotropic resolution. *IEEE Trans. Nucl. Sci*, 53(1):147–151, February 2006.

[144] Jinyi Qi, Richard M. Leahy, Chinghan Hsu, Thomas H. Farquhar, and Simon R. Cherry. Fully 3d bayesian image reconstruction for the egat exact hr+. *IEEE TRANSACTIONS ON NUCLEAR SCIENCE*, 45(3):1096–1103, Jun 1998.

[145] A Rahmim, M Lenox, A J Reader, C Michel, Z Burbar, T J Ruth, and V Sossi. Statistical list-mode image reconstruction for the high resolution research tomograph. *Physics in Medicine and Biology*, 49:4239–4258, 2004.

[146] D.V. Rao, S.M. Seltzer, and P.M. Bergstrom Jr. Compton scattering cross-sections for individual subshells for a few elements of biological interest in the energy region 5 kev-10mev. *Radiation Physics and Chemistry*, 70:479–489, 2004.

[147] M Reivich, D Kuhl, A Wolf, J Greenberg, M Phelps, T Ido, V Casella, J Fowler, E Hoffman, A Alavi, P Som, and L Sokoloff. The [18f]fluorodeoxyglucose method for the measurement of local cerebral glucose utilization in man. *Circulation Research*, 44(1):127–137, 1979.

[148] P. D. Reynolds, P. D. Olcott, G. Pratx, F. W. Y. Lau, and C. S. Levin. Convex optimization of coincidence time resolution for high resolution pet systems. *IEEE Nuclear Science Symposium Conference Record*, 2008.

[149] Sean L. Riggin, Kevin J. Kilroy, and Robin J. Smith. Clinical pet imaging with the c-pet camera. *Journal of Nuclear Medicine Technology*, 28(1):23–28, 2000.

[150] Eric L. Rosen, Timothy G. Turkington, Mary Scott Soo, Jay A. Baker, and R. Edward Coleman. Detection of primary breast carcinoma with a dedicated, large-field-of-view fdg pet mammography device: Initial experience. *Radiology*, 234:527–534, 2005.

[151] Ned C Rouze, Matthias Schmand, Stefan Siegel, and Gary D. Hutchins. Design of a small animal pet imaging system with 1 microliter volume resolution. *IEEE Transactions on Nuclear Science*, 51(3):757–763, JUN 2004.

[152] Branco S, Jan S, and Almeida P. Monte carlo simulations in small animal pet imaging. *Nucl. Instr. Meth. Phys. Res.*, 580:1127–1130, 2007.

[153] C. Comtat S. Jan, R. Boisgard, and R. Trbossen. Comparative study of micropet focus and ecat hrrt pet systems for small rodents imaging. *IEEE Nuclear Science Symposium Conference Record*, 6:3430–3432, 2004.

[154] Gopal B. Saha. *Basics of PET Imaging: Physics, Chemistry and Regulations*. Springer, 2004.

[155] A Sayeed, M Petrou, N Spyrou, A Kadyrov, and T Spinks. Diagnostic features of alzheimer's disease extracted from pet sinograms. *Physics in Medicine and Biology*, 47(1):137–148, Jan 2002.

[156] Jurgen Seidel, Juan J. Vaquero, Javier Pascau, Manuel Desco, Calvin A. Johnson, and Michael V. Green. Features of the nih atlas small animal pet scanner and its use with a coaxial small animal volume ct scanner. *IEEE International Symposium on Biomedical Imaging*, pages 545–548, 2002.

[157] K. S. Shah. A novel position sensitive detector for nuclear radiation. Technical report, Radiation Monitoring Devices, Inc., 44 Hunt Street, Watertown, MA 02472, May 2005. Submitted to Department of Energy, Contract Number DE-FG02-01ER83269.

[158] K S Shah, R Farrell, L Cirignan R Grazioso, P Bennett, S R Cherry, and Yiping Shao. Planar apd arrays for high resolution pet. *SPIE Proceedings: Medical Application of Penetrating Radiation*, 3770:104–111, Jul 1999.

[159] K. S. Shah, R. Farrell, R. Grazioso, E. S. Harmon, and E. Karplus. Position-sensitive avalanche photodiodes for gamma-ray imaging. *IEEE Trans Nucl Sci*, 49(4):1687 – 1692, Aug 2002. Part 1.

[160] K. S. Shah, R. Farrell, R. Grazioso, R. Myers, and L. Cirignano. Large-area apds and monolithic apd arrays. *IEEE Trans Nucl Sci*, 48(6):2352 – 2356, Dec 2001.

[161] K. S. Shah, R. Grazioso, R. Farrell, J. Glodo, M. McClish, G. Entine, P. Dokhale, and S. R. Cherry. Position sensitive apds for small animal pet imaging. *IEEE Trans Nucl Sci*, 51(1):91–95, Feb 2004. Part 1.

[162] Y. P. Shao, Simon R. Cherry SR, and A. F. Chatziioannou. Design and development of 1 mm resolution pet detectors with position-sensitive pmts. *Nucl. Instr. Meth. Phys Res. Sect. A*, 477(1–3):486–490, Jan 2002.

[163] H. Smith. *The Encyclopaedia of Medical Imaging*. Informa HealthCare, 1 edition, NOV 1998.

[164] R Southworth, CR Parry, HG Parkes, RA Medina, and PB Garlick. Tissue-specific differences in 2-fluoro-2-deoxyglucose metabolism beyond fdg-6-p: a 19f nmr spectroscopy study in the rat. *NMR Biomed.*, 16(8):494–502, Dec 2003.

[165] Jennifer R. Stickel and Simon R. Cherry. High-resolution pet detector design: modelling components of intrinsic spatial resolution. *Phys. Med. Bio.*, 50(2):179–195, Jan 2005.

[166] Jennifer R Stickel and Simon R Cherry. High-resolution pet detector design: modelling components of intrinsic spatial resolution. *Physics in Medicine and Biology*, 50:179–195, 2005.

[167] Jennifer R. Stickel, Jinyi Qi, and Simon R. Cherry. Fabrication and characterization of a 0.5-mm lutetium oxyorthosilicate detector array for high-resolution pet applications. *Journal of Nuclear Medicine*, 48(1):115–121, 2007.

[168] S. Surti, J. S. Karp, A. E. Perkins, C. A. Cardi, M. E. Daube-Witherspoon, A. Kuhn, and G. Muehllehner. Imaging performance of a-pet: A small animal pet camera. *IEEE Transactions on Medical Imaging*, 24(7):844–852, Jul 2005.

[169] Y. C. Tai, A. Chatziioannou, S. Siegel, J. Young, D. Newport, R. N. Goble, R. E. Nutt, and Simon R. Cherry. Performance evaluation of the micropet p4: a pet system dedicated to animal imaging. *Phys. Med. Bio.*, 46(7):1845–1862, Jul 2001.

[170] Y. C. Tai, A. F. Chatziioannou, M. Dahlbom, and S. R. Cherry. System design for a $1mm^3$ resolution animal pet scanner: micropet ii. *IEEE Nuclear Science Symposium and Medical Imaging Conference Record*, 3:51–52, 2000.

[171] Y-C Tai, AF Chatziioannou, RW Silverman, K Meadors, S Siegel, DF Newport, Y Yang, J Stickel, and SR Cherry. micropet ii: An ultra-high resolution small animal pet system. *IEEE Nuclear Science Symposium Conference Record*, 3:1848–1853, 2002.

[172] Hiroyasu Tajima, Grzegorz Madejski, Takefumi Mitani, Takaaki Tanaka, Hidehito Nakamura, Kazuhiro Nakazawa, Tadayuki Takahashi, Yasushi Fukazawa, Tuneyoshi Kamae, Motohide Kokubun, Daniel Marlow, Masaharu Nomachi, and Eduardo do Couto e Silva. Gamma-ray polarimetry with compton telescope. Technical report, SLAC, Jul 2004.

[173] Noriaki Tawa, Kenji Mukai, Kazuhiro Ikegami, Emi Miyata, Naohisa Anabuki, Hiroshi Tsunemia, and Kazuhisa Miyaguchi. Optimization of a scintillator-deposited charge-coupled device with monte-carlo simulation. *Nuclear Instruments and Methods in Physics Research Section A: Accelerators, Spectrometers, Detectors and Associated Equipment*, 573(1–2):119–121, 2006.

[174] M.-A. Tetrault, N. Viscogliosi, J. Riendeau, F. Blanger, J. B. Michaud, H. Semmaoui, P. Brard, F. Lemieux, L. Arpin, J. Cadorette, C. M. Pepin, G. Robert, M. D. Lepage, R. Lecomte, and R. Fontaine. System integration of the labpet small animal pet scanner. *IEEE NSS-MIC Conference Record*, pages 1880–1884, 2006.

[175] C O Thiam, V Breton, D Donnarieix, B Habib, and L Maigne. Validation of a dose deposited by low energy photons using gate/geant4. *Phys. Med. Biol.*, 53:3039–3055, 2008.

[176] J. Arthur Thomson. *The Outline of Science*, volume 1. The Knickerbocker Press, 1922.

[177] N Y Tse, C K Hoh, R A Hawkins, M J Zinner, M Dahlbom, Y Choi, J Maddahi, F C Brunicardi, M E Phelps, and J A Glaspy. The application of positron emission tomographic imaging with fluorodeoxyglucose to the evaluation of breast disease. *Ann Surg.*, 216(1):27–34, Jul 1992.

[178] James E. Turner. *Atoms, Radiation, and Radiation Protection.* Wiley-Interscience, 2nd edition, Apr 1995.

[179] Floris H P van Velden, Reina W Kloet, Bart N M van Berckel, Saskia P A Wolfensberger, Adriaan A Lammertsma, and Ronald Boellaard. Comparison of 3d-op-osem and 3d-fbp reconstruction algorithms for high-resolution research tomograph studies: effects of randoms estimation methods. *Physics in Medicine and Biology*, 53:3217–3230, 2008.

[180] A. Vandenbroucke, A. M. K. Foudray, F. W. Y. Lau, C. S. Levin, P. D. Olcott, and P. D. Reynolds. Performance characterization of a new ultra-high resolution, 3-d positioning pet scintillator detector. *IEEE Nuclear Science Symposium Conference Record*, 2008.

[181] P. Vaska, A. Dragone, D. H. Kim W. Lee, J. F. Pratte, Y.G. Cui, J. Fried, S. Krishnamoorthy, A. Bolotnikov, S. J. Park, P. OConnor, F.A. Dilmanian, and R. B. James. A prototype czt-based pet scanner for high resolution mouse brain imaging. *Nuclear Science Symposium Conference Record, 2007. NSS '07. IEEE*, 5:3816–3819, Oct 2007.

[182] D. Visvikis, T. Lefevre, F. Lamare, G. Kontaxakis, A. Santos, and D. Darambara. Monte carlo based performance assessment of different animal pet architectures using pixellated czt detectors. *Nuclear Instruments and Methods in Physics Research Section A: Accelerators, Spectrometers, Detectors and Associated Equipment*, 569(2):225–229, Dec 2006.

[183] S. Waldherr, M. Doszczak, M. Schliemann, J. Schreiner, P. Scheurich, and F. Allgwer. The tnf receptor signalling network: Modular modelling and cell-type specific analysis. *2nd Conference on Systems Biology of the Mammalian Cell*, 2008.

[184] Otto Warburg, Franz Wind, and Erwin Negelein. The metabolism of tumors in the body. *J Gen Physiol.*, 8(6):519–530, 1927.

[185] Lu Weiguo and Thomas R. Mackie. Tomographic motion detection and correction directly in sinogram space. *Physics in medicine and biology*, 47(8):1267–1284, 2002.

[186] Miles N Wernick and John N Aarsvold, editors. *Emission Tomography: The Fundamentals of PET and SPECT*. Elsevier Academic Press, 1st edition, 2004.

[187] C. Woody, A. Kriplani, P. OConnor, J. F. Pratte, V. Radeka, S. Rescia, D. Schlyer, S. Shokouhi, S. Stoll, P. Vaska, A. Villaneuva, N. Volkow, and B. Yu. Ratcap: a small, head-mounted pet tomograph for imaging the brain of an awake rat. *Nuclear Instruments and Methods in Physics Research Section A: Accelerators, Spectrometers, Detectors and Associated Equipment*, 527(1-2):166–170, Jul 2004.

[188] C. Woody, P. Vaska, D. Schlyer, J.-F. Pratte, S. Junnarkar, S.-J. Park, S. Stoll, M. Purschke, S. Southekal, A. Kriplani, S. Krishnamoorthy, S. Maramraju, D. Lee, W. Schiffer, S. Dewey, J. Neill, A. Kandasamy, P. OConnor, V. Radeka, R. Fontaine, and R. Lecomte. Initial studies using the ratcap conscious animal pet tomograph. *Nuclear Instruments and Methods in Physics Research Section A: Accelerators, Spectrometers, Detectors and Associated Equipment*, 571(1–2):14–17, Feb 2007.

[189] Taiga Yamaya, Takashi Obi, Masahiro Yamaguchi, and Nagaaki Ohyama. High-resolution image reconstruction method for time-of-flight positron emission tomography. *Phys. Med. Biol.*, 45:3125–3134, 2000.

[190] Y. F. Yang, Y. C. Tai, S. Siegel, D. F. Newport, B. Bai, Q. Z. Li, R. M. Leahy, and Simon R. Cherry. Optimization and performance evaluation of the micropet ii scanner for in vivo small-animal imaging. *Phys. Med. Bio.*, 49(12):2527–2545, Jun 2004.

[191] Yongfeng Yang and Simon R. Cherry. Observations regarding scatter fraction and nec measurements for small animal pet. *IEEE TRANSACTIONS ON NUCLEAR SCIENCE*, 53(1):127–132, Feb 2006.

[192] Yongfeng Yang, Purushottam A. Dokhale, Robert W. Silverman, Kanai S. Shah, Mickel A. McClish, Richard Farrell, Gerald Entine, and Simon R. Cherry. Depth of interaction resolution measurements for a high resolution pet detector using position sensitive avalanche photodiodes. *Phys. Med. Bio.*, 51:2131–2142, Apr 2006.

[193] Jin Zhang, Angela M. K. Foudray, Peter D. Olcott, and Craig S. Levin. Performance characterization of a novel thin position-sensitive avalanche photodiode for a high resolution pet camera. *IEEE Nuclear Science Symposium and Medical Imaging Conference Record*, 2005.

[194] K. Ziemonsa, E. Auffray, R. Barbier, G. Brandenburg, P. Bruyndonckx, Y. Choi, D. Christ, N. Costes, Y. Declais, O. Devroede, C. Dujardin, A. Fedorovd, U. Heinrichs, M. Korjik, M. Krieguer, C. Kuntner, G. Largeron, C. Lartizien, H. Larue, P. Lecoq, S. Leonard, J. Marteau, Ch. Morel, J.B. Mosset, Ch. Parl, Ch. Pedrini, A.G. Petrosyan, U. Pietrzyk, M. Rey, S. Saladino, D. Sappey-Marinier, L. Simon, M. Streun, S. Tavernier, and J.M. Vieira. The clearpet project: development of a 2nd generation high-performance small animal pet scanner. *Nuclear Instruments and Methods in Physics Research Section A: Accelerators, Spectrometers, Detectors and Associated Equipment*, 537(1-2):307–311, Jan 2004.

[195] H J Zweig. Detective quantum efficiency of photodetectors with some amplification mechanisms. *Journal of the Optical Society of America*, 55(5):525–528, 1965.